Universidade de Aveiro
2021

Rui Miguel da Silva Sampaio

Sensores Electroquímicos para Monitorização de Cloretos e pH em Estruturas de Betão Armado

Universidade de Aveiro
2021

Rui Miguel da Silva Sampaio

Sensores Electroquímicos para Monitorização de Cloretos e pH em Estruturas de Betão Armado

Electrochemical Sensors for Chloride and pH Monitoring in Reinforced Concrete Structures

Tese apresentada à Universidade de Aveiro para cumprimento dos requisitos necessários à obtenção do grau de Doutor em Ciência e Engenharia de Materiais, realizada sob a orientação científica do Doutor Mário Guerreiro Silva Ferreira, Professor Catedrático do Departamento de Engenharia de Materiais e Cerâmica da Universidade de Aveiro, e do Doutor António Alexandre da Cunha Bastos, Investigador do Departamento de Engenharia de Materiais e Cerâmica da Universidade de Aveiro.

Dedico este trabalho aos meus avós pela enorme inspiração.

o júri

presidente

Prof. Doutor Vitor Brás de Sequeira Amaral
professor catedrático da Universidade de Aveiro

Prof. Doutora Maria de Fátima Grilo da Costa Montemor
professora catedrática da Universidade de Lisboa

Prof. Doutor João António Labrincha Baptista
professor associado com agregação da Universidade de Aveiro

Prof. Doutor Carlos Manuel de Melo Pereira
professor associado da Universidade do Porto

Doutor Jorge Manuel Palma Correia
investigador auxiliar da Universidade de Lisboa

Doutor António Alexandre da Cunha Bastos
investigador auxiliar da Universidade de Aveiro (coorientador)

agradecimentos

Em primeiro lugar gostaria de expressar o meu sincero agradecimento aos meus orientadores, Professor Mário e Doutor Alexandre, pelo conhecimento transmitido e espírito crítico no decurso deste trabalho. Não poderia deixar de agradecer à Violeta pela análise microscópica e, sobretudo, pela amizade. Um enorme agradecimento ao Professor Jorge Correia pela disponibilização do elipsómetro e, acima de tudo, pela confiança depositada em mim.

No plano pessoal, gostaria de começar por agradecer aos meus pais, sobretudo à minha mãe, pelo constante apoio. Aos meus avós pela inspiração. Ao meu irmão pelo interesse constantemente manifestado. Ao meu tio Fernando pela motivação dada. E por fim, à Cecília pelo apoio incondicional, paciência e amor.

No círculo da amizade, começo por agradecer ao Celestino e à Marina pela amizade e companheirismo ao longo desta caminhada. Um agradecimento ao Filipe, à Rosa e ao Matias pela enorme amizade e constante preocupação no desenvolvimento do trabalho. E, por último, a todos os não enunciados aqui que, directamente ou indirectamente, fizeram parte desta jornada, um enorme obrigado.

palavras-chave sensores electroquímicos, prata/cloreto de prata, óxido de irídio, monitorização de argamassa, difusão de cloretos, carbonatação, ataque ácido.

resumo

O presente trabalho teve como objetivo o desenvolvimento de sensores electroquímicos para a monitorização do ingresso de cloretos e da variação de pH da solução de poro de materiais cimentícios devido ao processo de carbonatação e ao ataque com ácido sulfúrico.

Para a deteção de cloretos foram testados dois materiais: Ag/AgCl e Lucigenina. O filme de Lucigenina crescido potenciodinamicamente sobre aço inox não apresentou uma resposta potenciométrica aceitável. A síntese dos eléctrodos de Ag/AgCl foi realizada através de voltametria cíclica e de regimes potenciostáticos e galvanostáticos. Os eléctrodos modificados electroquimicamente apresentaram uma resposta potenciométrica para a detecção de cloretos com um declive sub-Nernstiano que depende principalmente da concentração de electrólito utilizada no crescimento dos filmes. Ambientes muito alcalinos levam à degradação precoce dos eléctrodos de Ag/AgCl.

Para a determinação de pH foram testados vários óxidos metálicos — MnO_2, IrO_x e IrO_x + RuO_2 — e um polímero electronicamente conductor — polipirrole. Os filmes de MnO_2 crescidos electroquimicamente apresentaram uma resposta linear no intervalo de pH entre 13 e 8 com um declive próximo do Nernstiano. Contudo, estes filmes dissolvem em ambientes ácidos (pH<6). O estudo de elipsometria identificou a formação da uma camada interna mais resistiva composta por MnOOH.

A síntese de IrO_x foi efectuada potenciodinamicamente e através de um regime potenciostático de singular e de duplo impulso. Os eléctrodos de IrO_x crescidos por voltametria cíclica apresentaram a resposta com maior potencial para a aplicação em materiais cimentícios, exibindo uma resposta potenciométrica linear na região de pH entre 13 e 5, com um declive super-Nernstiano. A adição de 5 e 10 mM de $RuCl_3$ à solução de crescimento levou à diminuição do declive da resposta potenciométrica dos eléctrodos modificados para valores mais próximos do Nernstiano. Os eléctrodos modificados potenciostaticamente apresentaram uma resposta potenciométrica linear na região de pH entre 10 e 2, com um declive mais próximo do Nernstiano que os filmes crescidos por voltametria.

Por último, os filmes de polipirrole sintetizados potenciostaticamente exibiram uma resposta linear na região de pH entre 11 e 5.

O estudo elipsométrico da passivação do aço em 0.1 M NaOH mostrou a formação de uma camada interna de $Fe(OH)_2$ seguida do crescimento de duas camadas mais porosas subsequentes compostas por hidróxidos de ferro.

Os sensores de Ag/AgCl foram utilizados com sucesso no estudo da penetração de cloretos em amostras de argamassa com e sem um aditivo com potencial capacidade de remover cloretos de solução (LDH). A presença de LDH na argamassa levou à diminuição do teor de cloretos na solução de poro. Contudo, a análise destrutiva levada a cabo mostrou a presença de uma maior quantidade de cloretos totais na amostra com LDH, o que evidencia um aumento da quantidade de cloretos imobilizados na matriz cimentícia. A remoção de cloretos da solução de poro pode ser consequência da troca iónica com o LDH ou devido à formação de sais de Friedel na presença de iões alumínio provenientes da dissolução do LDH. Os resultados com os eléctrodos de ferro corroboraram os resultados obtidos com os sensores do efeito do LDH na captura de cloretos.

Os sensores de IrO_x foram aplicados com sucesso no estudo da variação de pH da solução de poro de amostras cimentícias devido aos processos de carbonatação e de ataque ácido.

O estudo da carbonatação mostrou uma alteração imediata do pH da solução de poro perto da superfície depois da libertação inicial de dióxido de carbono, mas gradualmente realcalinizada após a libertação do gás. Contudo, o regime de CO_2 puro promoveu a obstrução da rede porosa superficial, o que levou ao bloqueio da entrada de dióxido de carbono até maiores profundidades.

Por fim, os sensores de IrO_x mostraram que a variação de pH da solução de poro devido à exposição a ácido sulfúrico concentrado é limitada a uma camada de apenas 1 a 2 mm de espessura. A variação de pH em profundidade acontece à medida que a frente de ataque progride.

keywords electrochemical sensors, silver/silver chloride, iridium oxide, mortar monitoring, chloride ingress, carbonation, acid attack.

abstract

The present work had as objective the development of electrochemical sensors to monitor the ingress of chlorides. and the pH variation of the pore solution of cementitious materials due to the carbonation process and attack with sulfuric acid.

For the detection of chlorides, two materials were tested: Ag/AgCl and Lucigenin. The Lucigenin film grown potentiodynamically on stainless steel did not present an acceptable potentiometric response. The synthesis of the Ag/AgCl electrodes was performed using cyclic voltammetry and potentiostatic and galvanostatic regimes. The electrochemically modified electrodes showed a potentiometric response for the detection of chlorides with a sub-Nernstian slope which mainly depends on the concentration of electrolyte used in film growth. Very alkaline environments lead to early degradation of Ag/AgCl electrodes.

For pH determination, several metal oxides were tested — MnO_2, IrO_x and IrO_x + RuO_2 — and an electronically conducting polymer — polypyrrole. The electrochemically grown MnO_2 films showed a linear response in the pH range between 13 and 8 with a slope close to Nernstian. However, these films dissolve in acidic environments (pH<6). The ellipsometry study identified the formation of a more resistive inner layer composed of MnOOH.

The IrO_x synthesis was carried out potentiodynamically and through a potentiostatic regime of single and double impulse. The IrO_x electrodes grown by cyclic voltammetry showed the response with the greatest potential for application in environments as aggressive as cementitious materials, exhibiting a linear potentiometric response in the pH region between 13 and 5, with a super-Nernstian slope. The addition of 5 and 10 mM $RuCl_3$ to the growth solution led to a decrease in the slope of the potentiometric response of the modified electrodes towards values closer to Nernstian. The potentiostatically modified electrodes showed a linear potentiometric response in the pH region between 10 and 2, with a slope closer to Nernstian than the films grown by voltammetry.

Finally, the potentiostatically synthesized polypyrrole films exhibited a linear response in the pH region between 11 and 5.

The ellipsometric study of steel passivation in 0.1 M NaOH showed the formation of an inner layer of $Fe(OH)_2$ followed by the growth of two subsequent more porous layers composed of iron hydroxides.

Ag/AgCl sensors have been successfully used to study chloride penetration in mortar samples with and without an additive with the potential to remove chlorides from solution (LDH). The presence of LDH in the mortar led to a decrease in the chloride content in the pore solution. However, the destructive analysis carried out showed the presence of a greater amount of total chlorides in the sample with LDH, which shows an increase in the amount of chlorides immobilized in the cement matrix. The removal of chlorides from the pore solution can be a consequence of ion exchange with the LDH or due to the formation of Friedel salts in the presence of aluminum ions from the dissolution of the LDH. The results with the iron electrodes corroborated the results obtained with the sensors about the effect of LDH on chloride capture.

IrO_x sensors have been successfully applied to study the pH variation of the pore solution of cementitious samples due to carbonation and acid etching processes. The carbonation study showed an immediate change in the pH of the pore solution near the surface after the initial release of carbon dioxide, but gradually recalinized after the release of the gas. However, the pure carbon dioxide regime promoted the obstruction of the superficial porous network, which led to the blocking of carbon dioxide entry to greater depths.

Finally, IrO_x sensors showed that the pH variation of the pore solution due to exposure to concentrated sulfuric acid is limited to a layer only 1 to 2 mm thick. The pH variation in depth happens as the attack front progresses.

Contents

Abbreviations and symbols

Abbreviations

AA	Acid attack
AIROF	Anodic iridium oxide film
CE	Counter electrode
CV	Cyclic voltammetry
C2S	Dicalcium silicate
C3S	Tricalcium silicate
C-S-H	Calcium-silicate hydrates
DPCA	Double pulse chronoamperometry
ECP	Electronically conducting polymer
EDS	Energy-dispersive X-ray spectroscopy
EIROF	Electrodeposited iridium oxide film
EIS	Electrochemical impedance spectroscopy
FR	Friedel's salt
HLOD	Higher limit of detection
ISE	Ion-selective electrode
LDH	Layered double hydroxide
LDH-NO_2	Layered double hydroxide loaded with nitrite
LDH-NO_3	Layered double hydroxide loaded with nitrate
LLOD	Lower limit of detection
LOD	Limit of detection
OCP	Open circuit potential
PDA	Peripheral differential amplifier
PEDOT	Poly(3,4-ethylenedioxythiophene)
PPy	Polypyrrole
RE	Reference electrode
RRE	Red rod electrode
SCC	Stress corrosion cracking
SCE	Saturated calomel electrode
SHE	Standard hydrogen electrode
SEM	Scanning electron microscopy
SS	Stainless steel
WE	Working electrode
WNS	Wood's nickel strike
XRD	X-ray diffraction

Symbols

a_i	Activity of the species i (mol cm^{-3})
a_i^*	Intersection of the extrapolated linear portions of the potential-activity plot
a.u.	Arbitrary units

A	Geometric area of electrode (cm^2)
	or Nucleation rate constant (s^{-1})
b	E-intercept (V)
B	Stern-Geary constant (V)
c_i	Concentration of species i (mol cm^{-3})
c_i^*	Concentration of species i in the bulk solution (mol cm^{-3})
$c_i(0,t)$	Concentration of species i at the electrode surface (x=0) (mol cm^{-3})
C	Capacitance (F cm^{-2})
C_{dl}	Double layer capacitance (F cm^{-2})
C_S	Pseudo-capacitance (F cm^{-2})
d	Film thickness (Å)
d_{hkl}	Spacing between planes of atoms (Å)
D_i	Diffusion coefficient of species i (cm^2 s^{-1})
e	Charge on the electron (C)
E	Potential *vs*. a reference electrode (V)
E^0	Standard equilibrium potential (V)
E_{corr}	Corrosion potential (V)
$E_{p,a}$	Anodic peak potential (V)
$E_{p,c}$	Cathodic peak potential (V)
E_p^{inc}	Parallel component of electric field vector of incident beam
E_p^{ref}	Parallel component of electric field vector of reflected beam
E_s^{inc}	Perpendicular component of electric field vector of incident beam
E_s^{ref}	Perpendicular component of electric field vector of reflected beam
f	Frequency (s^{-1})
F	Faraday constant (C mol^{-1})
i	Current (A)
i_{corr}	Corrosion current (A)
i_0	Exchange current (A)
I	Fluorescence intensity after quenching
I_0	Original fluorescence intensity
j	Current density (A cm^{-2})
j_0	Exchange current density (A cm^{-2})
$j_{p,a}$	Anodic peak current density (A cm^{-2})
$j_{p,c}$	Cathodic peak current density (A cm^{-2})
j_{max}	Current density at maximum in an j-t transient (A cm^{-2})
k	Extinction coefficient
$K_{A,B}^{pot}$	Selectivity coefficient of specie A in the presence of specie B
K_{SV}	Quenching constant
m	Slope (mV pH^{-1})
n	Number of electrons involved in overall electrode reaction
	or Refractive index
N_0	Number of sites where nucleation can occur (cm^{-2})
$N(t)$	Number of nuclei at time t (cm^{-2})
p	Component parallel to the incidence plane
q	Charge (C)
Q	Charge density (C cm^{-2})

	or Quenching agent
r_p	Fresnel reflection coefficient of the parallel component
r_s	Fresnel reflection coefficient of the perpendicular component
R	Universal constant of ideal gas (J K^{-1} mol^{-1})
	or Resistance (Ω)
R_{ct}	Charge transfer resistance (Ω cm^2)
R_p	Polarization resistance (Ω cm^2)
R_S	Uncompensated resistance between reference electrode probe and working electrode (Ω)
s	Component perpendicular to the incidence plane
t	Time (s)
t_{max}	Maximum time in j-t transient (s)
T	Temperature (K)
x	Distance perpendicular to the electrode surface (cm)
z_i	Charge number on ion i
Z	Impedance (Ω)
Z_W	Warburg impedance (Ω)
Z'	Real component of impedance (Ω)
Z''	Imaginary component of impedance (Ω)
α_a	Anodic transfer coefficient
α_c	Cathodic transfer coefficient
β	Phase change due to propagation of the light wave through the film
β_a	Anodic Tafel constant
β_c	Cathodic Tafel constant
Δ	Change in phase difference (°)
η	Overpotential (V)
θ	Angle of incidence
λ	Wavelength of light (nm)
μ_i	Chemical potential of species i (J mol^{-1})
υ	Potential scan rate (V s^{-1})
ρ	Density (g cm^{-3})
	or Complex ratio of the total reflection coefficients
ρ_c	Concrete resistivity (Ω cm)
σ	Warburg coefficient (Ω $s^{-1/2}$)
τ	Transition time (s)
	or Step width (s)
$ø$	Angle of incidence
Ψ	Azimuth angle (°)

The IUPAC convention is followed. Anodic currents are positive and moving to more positive potentials corresponds to increasing the driving force for an oxidation process. Otherwise, cathodic currents are negative and moving to more negative potentials promotes an increasing driving force for reduction.

List of Figures

List of Tables

Objectives of the work

The main objectives of this thesis were the development of electrochemical sensors for monitoring the main agents responsible for the corrosion of concrete reinforcement, and its, subsequent, embedment in mortar samples under different conditions: presence of chlorides, carbon dioxide, sulfuric acid, with and without corrosion inhibitors, in order to determine the variation with time of the penetration of these agents and the viability of inhibitors. The principal tasks for this work were:

- Identification of sensitive materials for chloride and pH detection, and optimization of their electrochemical synthesis in order to achieve the best potentiometric or amperometric response.
- Characterization of the sensors and determination of their reversibility and degradation when exposed to extreme media for a long time.
- Morphologic and optical characterization of the synthetized films in order to determine properties, such as porosity and thickness, and correlate with calibration curve parameters.
- Design and construction of a sufficiently robust but non-invasive electrode to be embedded in concrete structures.
- Construction of several mortar samples with the developed embedded sensors for the different conditions (ingress of chloride ions, carbonation and acid medium) and monitoring their signals with time.
- Use of similar mortar samples, but with embedded iron wires, to simulate reinforced concrete, and validate the sensor results.
- Effect of the use of LDH in mortars to control the chloride attack of the iron.

This thesis consists of 7 chapters. The first 2 chapters present the state of the art contextualizing the thesis, as well as the techniques used to carry out the experimental work. Chapter 1 gives an overview of the processes involved in the degradation of reinforced cementitious structures, due to the ingress of chlorides and the decrease in the pH of the pore solution, and describes the electrochemical sensors, for the determination of the chloride content and pH, that were studied in this experimental work. Chapter 2 describes the techniques used for the synthesis and characterization of the modified electrodes. The experimental procedure adopted for carrying out the experimental work is explained in Chapter 3.
Results and their discussion are presented in Chapters 4 to 6. Each experimental chapter ends with a section of partial conclusions to facilitate the reader's work. The synthesis and characterization of chloride and pH sensors can be found respectively in Chapters 4 and 5. Chapter 6 presents the application of the sensors for the study of chloride ingress and pH variation in mortar samples. In the previous chapter, mortar samples with embedded iron wires and the effect of the addition of LDH to the mortar in presence of chloride ions were also studied.
The main global conclusions drawn from this work, as well as suggestions for immediate future work, are described in Chapter 7.

This thesis was integrated in a European project — Long Lasting Reinforced Concrete for Energy Infrastructure under Severe Operating Conditions (LORCENIS, grant agreement n° 685445, H2020 EU) — that had as main objective to double the lifetime of reinforced concrete structures under harsh conditions. The tasks of University of Aveiro were the development of tools to monitor and predict the ingress of aggressive agents that are responsible for the degradation of reinforced concrete structures. Thus, the purpose of this thesis was to develop electrochemical sensors capable to monitor

the ingress of chlorides and the variation of the pH in the pore solution due to carbon dioxide ingress and acid attack.

CHAPTER 1 Reinforced concrete and monitoring of aggressive agents

In the first chapter of this doctoral thesis, the main concepts to be used along the work will be subject to a detailed analysis. Initially, the phenomenon of degradation of reinforced cementitious structures caused by the reinforcement corrosion is exposed. The processes of penetration of chlorides, carbon dioxide and exposure to acidic environments are subject of a complete description. Then, the main methods of monitoring cementitious materials are described. Finally, the working principle of an electrochemical sensor is explained, and the materials exploited as potentiometric sensors are described. This will set the table for the presentation of the scientific work carried out.

1.1. Introduction

Concrete is nowadays the most used construction material, being part of many building structures due to its ability to be moulded to the desired shape, high durability, excellent mechanical properties and fire resistance [1]. However, these structures have a limited lifetime, which represents a major economic and environmental impact. The degradation of reinforced concrete structures is caused by several processes, such as physical (freeze-thaw cycles, fire), mechanical (abrasion, erosion, impacts), structural (overloading, cyclic loading, settlement), chemical (acid attack, alkali-aggregate reactions, pure water attack, sulfate attack), biological (fouling) and corrosion of steel reinforcement (carbonation, oxygen and chlorides ingression) [2]. Corrosion of steel reinforcement represents the main cause of deterioration of these structures. The evolution of the reinforced structures deterioration due to rebar corrosion is shown in Figure 1.1: (i) before corrosion, (ii) during cover delamination, (iii) and after total reinforcement exposure. In fact, metallic corrosion is a major problem in the services and industry sectors. The global cost of corrosion is equivalent to 3-4% of the global gross domestic product (2013) [3]. In addition to economic issues, the growing demand for concrete infrastructures combined with their limited lifetime causes a high increase in greenhouse gas emissions [4]. The industrial sector responsible for production and transportation of cement is responsible for about 8% of total global CO_2 emissions and contributes 7.8% of nitrogen oxide emissions and 4.8% of sulfur oxide emissions [5].

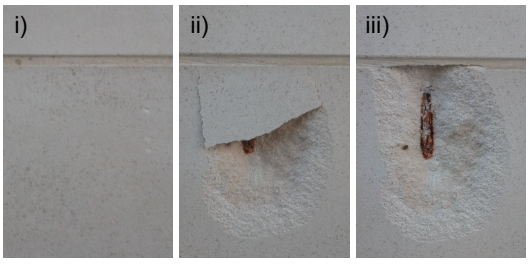

Figure 1.1: Example of corrosion initiation of steel rebar in cementitious materials: (i) before corrosion, (ii) cover delamination, (iii) and reinforcement total exposure. From the building of Department of Materials and Ceramic Engineering, Aveiro.

Corrosion is an irreversible interfacial process of a material (metal, ceramic, polymer) with its surrounding environment, which results in the destruction of the material [6]. The types of metallic corrosion can be grouped into uniform attack and localized corrosion. General corrosion is the most common type in which the corrosive attack occurs on the entire exposed surface being, therefore, more predictable and easier to prevent. In the case of non-uniform corrosion, it can be divided into galvanic, crevice, pitting, stress corrosion cracking (SCC), intergranular, de-alloying, microbial and fatigue. These localized types of corrosion have a complex monitoring and are more difficult to predict. The corrosion protection, depending on the system, can be achieved by different methods: cathodic protection (connected to a sacrificial anode or by applying an external current source), anodic protection, coatings (e.g., metallic, vitreous, inorganic and organic), through preventive actions (e.g., better design of the structures and selection of better materials), and by changing environment when possible.

The fresh concrete promotes the formation of a protecting passive layer on the steel reinforcement due to its high alkalinity. However, concrete is a porous material, which can be penetrated by liquids and gases from the surrounding atmosphere [2] and, over time, the ingress of aggressive agents, such as chloride ions and carbon dioxide, through concrete will promote the creation of the ideal conditions for the destruction of the protective layer of steel and, therefore, corrosion processes will start. Offshore constructions (bridges, floating platforms, dams or harbour structures) are very susceptible to chloride penetration, which when reaches a certain critical limit will promote localized corrosion attack (e.g., pitting, crevice and SCC. On the other hand, buildings located in an environment with a high content of carbon dioxide are highly susceptible to deterioration of the reinforcement due to the decrease of concrete alkalinity that leads to the destruction of the passive oxide layer of steel rebars. For submerged structures, the oxygen availability is also an important factor for the corrosion of steel in concrete since its corrosion rate is mainly controlled by diffusion of dissolved oxygen through concrete network.

The internal condition — mechanical, physical and chemical properties — of reinforced concrete structures can be monitored by different methods, which can be divided into destructive or non-destructive. In destructive methods it is necessary to extract a sample from the structure under study to analyse qualitatively or quantitively its composition. Non-destructive methods, such as monitoring through embedded sensors, can provide useful information on continuous real-time about the depassivation of the steel rebars, changes in the concrete cover resistivity, and the ingress of aggressive agents — chlorides, molecular oxygen or carbon dioxide.

1.2. Corrosion of steel reinforcement in concrete

Concrete presents good resistance to compressive forces, but does not resist to tensile forces, needing a reinforcement. Several materials have been tested as reinforcement for concrete, however, steel is the most used for this purpose due to the lower price, improvement of the mechanical properties of concrete, and to its expansion coefficient, which is very similar to that of concrete. The biggest problem with the use of steel as reinforcement is its corrosion under certain conditions, which leads to a decrease in the strength of the cementitious structure. A more expensive alternative would be to use a corrosion resistant reinforcement, such as stainless steels, galvanized steel, and fibre reinforced polymers, or to increase the corrosion resistance of the common carbon steel rebars by applying an organic or metallic coating or by modifying the chemical composition of the steel [2].

1.2.1. Passivation of steel rebar

Concrete is a composite material made by several elements such as different sized aggregates, cement and water. The high alkalinity of pore solution — pH between 12.5 and 14 [7] — is due to the presence of different types of hydroxides — sodium, potassium and calcium hydroxides — and depends mainly on the composition of the cement. At the beginning, the high pH is mostly due to calcium hydroxides formed in the hydration reactions of the calcium silicates present in the cement and of the alkalis of the clinker. However, as the hydration process continues, leaching of the calcium hydroxides occurs and, consequently, the high alkalinity of concrete becomes mainly due to the sodium and potassium hydroxides. The alkaline environment promotes a spontaneous growth of a protective layer on the steel surface. Passive films are compact and resistive layers with only a few nanometers of thickness that are constituted by an inner layer mainly composed of Fe^{2+} oxides and an outer layer consisting of Fe^{3+} oxides and hydroxides [8,9]. The passivation process of the steel rebar starts with the adsorption of hydroxyl ions on the steel surface to form iron(II) hydroxide, $Fe(OH)_2$, which reaction is represented in the following equation:

$$Fe + 2OH^- \rightarrow Fe(OH)_2 + 2e^- \quad (1)$$

Then, an additional oxidation of iron(II) hydroxide leads to the formation of magnetite:

$$3Fe(OH)_2 + 2OH^- \rightarrow Fe_3O_4 + 4H_2O + 2e^- \quad (2)$$

Finally, for even more anodic potentials, magnetite is oxidized to maghemite ($\gamma.Fe_2O_3$) or to goethite (α.FeOOH), as represented in the following equations, respectively:

$$2Fe_3O_4 + 2OH^- \rightarrow 3\gamma.Fe_2O_3 + H_2O + 2e^- \quad (3)$$

$$Fe_3O_4 + OH^- + H_2O \rightarrow 3\alpha.FeOOH + e^- \quad (4)$$

The quality of the passive layer — electrical resistivity and thickness — depends on the availability of oxygen during the curing period, time of curing [10], composition of pore solution [11] and oxidation state of the steel rebar surface before embedment in cementitious materials [9]. The passivation process of steel is different in simulated pore solution and in hardened cementitious samples. In the case of hardened samples, the steel rebar takes about 7 days to reach an acceptable passivation, whereas in the case of immersion in pore solution, it only needs 3 days [9,12]. Passive films grown in $Ca(OH)_2$ solution present a higher stability than those grown in NaOH with the same pH [12,13]. The passivation process can be accelerated by the presence of some metallic cations, such as Ca, Mg and Ba [12], due to the absorption of such cations at the outer plane of the inner layer of the passivating film [14]. A longer passivation time also increases the film resistivity due to the enrichment of iron(III) oxides, which are less conducting compared to magnetite [15].

1.2.2. Microstructure of cementitious materials

Cementitious materials have a porous microstructure that allows a mass transfer with the outside environment and is in constant transformation, as shown in Figure 1.2. The pores can be air-filled or filled with pore solution. The structure of the pore network is mainly affected by curing conditions, water/cement ratio and use of supplementary materials (pozzolanic active materials or superplasticizers).

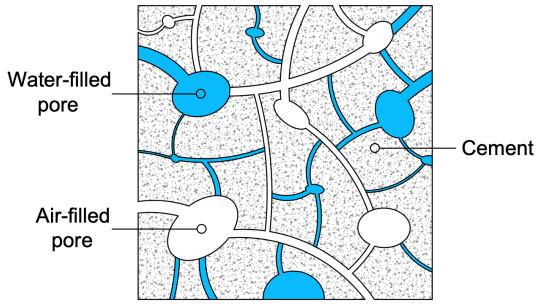

Figure 1.2: Illustration of pore network of cementitious materials.

In the case of curing conditions, on the one hand, water curing reduces air-filled pore network and the size of capillary pores, and on the other hand, longer curing periods decreases the porosity of the microstructure due to increased hydration degree [16]. The decrease in the water/clinker ratio also increases the density of cementitious materials [17,18].

The transport of water and aggressive agents into the porous matrix of cementitious materials occurs through different mechanisms — diffusion, migration, permeation and capillary suction. The penetration of aggressive agents by diffusion is the main transport mechanism through the porous network of cementitious materials. Diffusion of species is driven by a concentration gradient, in the case of ions, or a partial pressure gradient, in the case of gases. The main factors that influence the diffusion of species through cementitious materials are the porous microstructure, water content and the binding capacity of hydration products. The interconnectivity and pore filling are essential for the diffusion of species into the concrete. Ionic species, such as chlorides and sulfates, only diffuse when the pore network is partial or completely filled with water. The diffusion of gases is much faster through air-filled pores than through water-filled ones. Relatively to migration mechanism, the transport of ions is driven by an electrical field. This mechanism is not very common in real cases, but is often applied to accelerate the chloride penetration experiments [19] and for electrochemical chloride extraction from concrete structures [20–22]. The chloride migration coefficient decreases with increasing tortuosity of pore network and with decreasing porosity [23]. In the case of permeation, the transport of liquids is done by pressure gradient, for saturation conditions, or by hydraulic gradient, in the case of submerged conditions. The saturated water permeability of concrete depends on the porous microstructure and the presence of cracks. Permeability through cracks is correlated with the square of crack width [24]. The decrease of porosity leads to a decrease of gas permeability in a natural tidal environment [25]. The aggregate particle size affects the water permeability of concrete [26]. Lastly, capillary suction is the absorption of a liquid in the pore network due to its hydrostatic pressure. This transport mechanism depends on liquid properties (surface tension, viscosity and density) and pore network characteristics (pore dimension and tortuosity). The tortuosity, which is caused by the presence of aggregates, decreases the sorptivity of

concrete [27], which is a measure of the capillarity of the material. The water/cement ratio, which affects the porous microstructure, consequently, influences the capillary coefficient and sorptivity of cementitious materials, as well as changes the distribution of adsorbed water in the pore network [28]. The frost damage accelerates the capillary water absorption and the coefficient of capillary absorption increases with increasing number of freeze-thaw cycles [29]. The sorptivity decreases with age (continuous curing) and with carbonation process [30].

1.2.3. Corrosion of steel rebar

Corrosion of steel reinforcement in concrete is an electrochemical process, in which the steel surface in contact with pore solution is composed by several anodic and cathodic zones that are electrically connected by the metallic phase. There are several possible anodic reactions, which, depending on the pH of pore solution, availability of aggressive agents, and the intrinsic potential of steel rebar, promotes the formation of different iron oxides:

$$3Fe + 4H_2O \rightarrow Fe_3O_4 + 8H^+ + 8e^- \quad (5)$$

$$2Fe + 3H_2O \rightarrow Fe_2O_3 + 6H^+ + 6e^- \quad (6)$$

$$Fe + 2H_2O \rightarrow HFeO_2^- + 3H^+ + 2e^- \quad (7)$$

$$Fe \rightarrow Fe^{2+} + 2e^- \quad (8)$$

The dissolved oxygen reduction or the hydrogen evolution are the possible cathodic reactions depending on the pore solution pH and on the availability of molecular oxygen [31]

$$2H_2O + O_2 + 4e^- \rightarrow 4OH^- \quad (9)$$

$$2H^+ + 2e^- \rightarrow H_2 \quad (10)$$

The formation of a rust layer on the steel reinforcement promotes the formation of cracks on the concrete cover and its subsequent detachment, which consequently leads to accelerated deterioration of the structures, as represented in Figure 1.3.

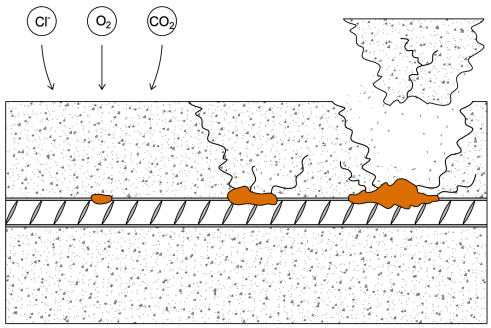

Figure 1.3: Illustration of corrosion process of the steel rebar and consequent delamination of concrete cover.

Corrosion products of iron present a relative volume to the pure metal about 2 times greater in the case of oxides, and about 3 to 6 times greater in the case of hydroxides. Figure 1.4 presents the corrosion products of iron inside a cementitious matrix due to oxygen-induced corrosion, which are represented in decreasing order of their expansion volume in relation to pure metal.
The formation of a corrosion layer and the transport of corrosion products through the concrete proceed simultaneously after the initiation of corrosion process [32]. The transport of corrosion products from the corrosion area decreases the level of concrete degradation [33].

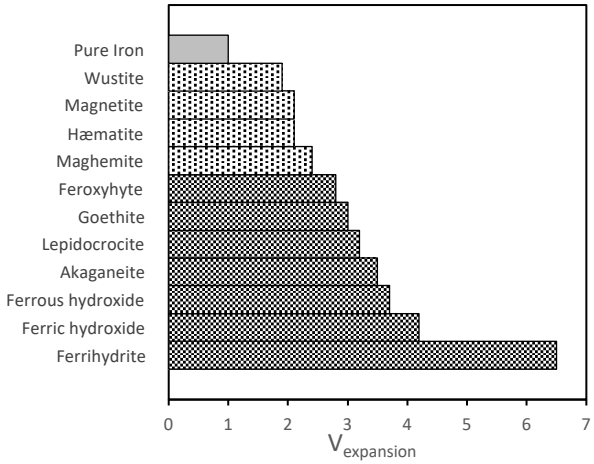

Figure 1.4: Corrosion products of iron inside concrete and their expansion volume relatively to pure metal (oxides with pointed area and hydroxides with meshed area). Adapted from [34].

Corrosion of the steel reinforcement can endanger the safety of those structures. The reduction in cross section of steel rebars causes a decrease of its tensile strength, elongation and fatigue strength. The formation of corrosion products will decrease the adhesion between steel and concrete and will produce tensile stresses that will promote the cracking of concrete cover and its, subsequent, localized spalling. Delamination of the concrete cover leaves the steel reinforcement directly exposed to environmental conditions leading to an increase of corrosion rate and, consequent deterioration of the structure. Besides that, if the very specific conditions that lead to the cathodic reaction of hydrogen evolution are met, there will be hydrogen embrittlement of steel rebars.
The composition of corrosion products depends on the nature of the rebar and exposure conditions. In the case of marine environments where corrosion is essentially chloride-induced, the rust that forms on steel rebar within concrete is mainly composed by crystalline magnetite, goethite and lepidocrocite [35]. In addition to these corrosion products, chloride-induced corrosion can also produce several intermediates, such as ferrous hydroxychloride or chloride green rust (hydrous iron oxides with mixed valence iron and chloride). In the case of carbonation-induced corrosion, which is more related to industrial and large metropolitan areas, the presence of dissolved carbon dioxide in the pore solution promotes the formation of several iron carbonates, such as chukanovite ($Fe_2(OH)_2CO_3$), siderite ($FeCO_3$) and carbonate green rust. The main corrosion products that form under these conditions are lepidocrocite, goethite and feroxyhyte, which result from the oxidation of chukanovite [36].
The corrosion process of steel reinforcement is mainly influenced by the microstructure of concrete (porosity and water content), chemical composition of pore solution (pH, aggressive species content), steel rebar composition and the state of its surface before casting, environmental conditions (temperature, oxygen availability, exposure period and wet-dry cycles) and type of corrosion

products. The porosity facilitates the penetration of aggressive agents through the cementitious matrix and leads to an increase in the amount of corrosion products [37]. The water content is directly related to the electrical resistivity of cementitious materials. The use of supplementary materials in concrete, such as silica fume, can improve corrosion resistance due to decrease of water absorptivity and increase of electrical resistivity [38]. The chemical composition of the pore solution is fundamental in the electrochemical state of the steel reinforcement. In fact, it is widely common to relate the beginning of the corrosion process to the molar ratio between the concentrations of the chloride and hydroxyl ions — $[Cl^-]/[OH^-]$. The open circuit potential decreases and the corrosion rate — i_{corr} — increases with the increase of $[Cl^-]/[OH^-]$ [39,40]. The variation of i_{corr} as a function of $[Cl^-]/[OH^-]$ ratio presents two regions. The region of $[Cl^-]/[OH^-] < 10^2$ (pH > 9.5) presents a more pronounced dependence of mean i_{corr} with $[Cl^-]/[OH^-]$ due to higher competition between the chloride and hydroxyl ions when the steel rebar is still passivated. In the region of $[Cl^-]/[OH^-] > 10^2$ (pH < 9.5) the mean corrosion rate decreases slightly with lower $[Cl^-]/[OH^-]$. In the case of the specific influence of pH on i_{corr} variation, there are 3 distinct regions. In the acid region, with pH < 5, the corrosion process occurs with water reduction and the i_{corr} increases as the pH of the medium decreases, which is related to the increase in H^+ concentration, easy removal of corrosion products from the steel surface due to the stirring effect of gas evolution (H_2) and, in the case of oxygen availability, enhanced cathodic process, which is fed simultaneously by the reductions of oxygen and H^+. In the neutral region, with pH between 5 and 9.5, the corrosion rate remains almost constant due to the precipitation of $Fe(OH)_2$ on the metal surface, which reduces the total active area for the anodic process. Finally, in the alkaline region, with pH > 9.5, the corrosion rate decreases steeply as the pH increases due to effective passivation of the steel rebar [39]. The state of the steel rebar surface before casting also affects its corrosion behaviour [40]. On the one hand, the presence of rust promotes an increase in the corrosion rate due to an increase of the pore solution conductivity at the metal-concrete interface and the decrease of repassivation ability [41]. On the other hand, the mill scale largely affects the distribution and penetration of corrosion products through cementitious matrix [42]. Relatively to exposure conditions, the temperature affects the kinetic parameters of corrosion rate [43,44] and presents an exponential dependence with conductivity of concrete [45]. The corrosion rate of structures that are exposed to wet and dry cycles, such as tidal and splash zones of offshore structures, increases during wetting cycle and decreases during drying, which can be explained by a change in the electrochemically active area due to the presence of water [46]. The presence of molecular oxygen in the cathodic zone is essential to initiate the corrosion process and can be a limiting factor to the global reaction of corrosion. The availability of molecular oxygen depends on the moisture content and the interconnectivity of the porous matrix of the concrete [47–49]. Finally, the corrosion products can also act as an oxidizing agent in the cathodic reaction of steel corrosion. After the corrosion process starts, the corrosion product FeOOH, present in the corrosion layer can be reduced and contribute to the total cathodic current, or even replace oxygen in the cathodic process under conditions of high water saturation [50,51].

1.2.4. Steel corrosion monitoring

The electrochemical state of the steel reinforcement can be accessed by determining the main parameters related to the corrosion process: corrosion potential — E_{corr} —, polarization resistance — R_p — and concrete resistivity — ρ_c. In the case of parameters directly related to the steel

reinforcement, it may be necessary to remove the concrete cover over the rebar in order to make the electrical contact with it, as illustrated in Figure 1.5 (left). The determination of E_{corr} can be carried out by measuring the open circuit potential of the steel rebar with a high impedance voltameter using a two-electrode configuration [52]. The contact between the concrete surface and the reference electrode is usually made using a wet sponge with an electrolytic solution with a pH similar to that of the pore solution in order to minimize possible junction potentials [53]. The open circuit potential reflects the electrochemical state of the steel rebar, which depends mainly on the pH of the pore solution and the composition of the reinforcement. According to the ASTM C876 standard, for values of open circuit potential above -125 mV *vs*. SCE (about 116 mV *vs*. SHE) the probability of steel corrosion activity is less than 10%, and for values under -275 mV *vs*. SCE (about -34 mV *vs*. SHE), the probability of steel corrosion activity is greater than 90% [34]. The electrical resistivity of cementitious materials is the ability to withstand ionic movement. This fundamental property of concrete is inversely proportional to the corrosion rate of the steel rebar [54] and is mainly influenced by the degree of saturation of the pore network. The resistivity of concrete varies between 10 and 10^6 Ω m for saturated and dry concrete, respectively [54]. In the case of the absence of electrodes embedded in the structure under analysis, its resistivity can be determined through the Wenner method (also known as 4-point method), which uses a four-electrode configuration, with the probes equally spaced [55], as represented in Figure 1.5 (right).

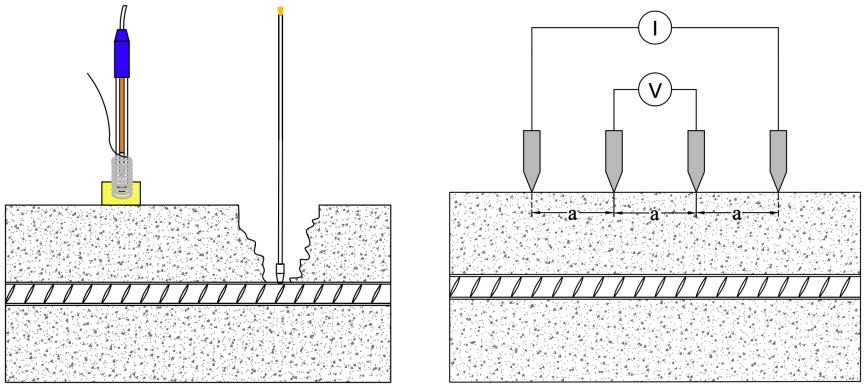

Figure 1.5: Illustration of 3-electrode configuration for determination of polarization resistance and 4-point method for determination of concrete resistivity.

This technique consists in the application of a determined current in the outer electrodes and in the measurement of the resulting potential drop in the inner electrodes. The resistance of the concrete — R_c — is the quotient between the potential drop and the current induced [56]. Finally, the resistivity is directly proportional to resistance with a geometric factor as proportionality constant, which depends on the sample (size and shape) and the experimental device. For concrete with Portland cement, the risk of corrosion is considered negligible for a resistivity higher than 10^3 Ω m and high for a resistivity lower than 10^2 Ω m [56]. The polarization resistance of a given material is defined as the opposition to the deviation from its equilibrium potential. The main techniques used for the determination of the resistance polarization are linear and transient polarization resistance methods and electrochemical impedance spectroscopy (EIS), which are based on the application of an external perturbation to the equilibrium state of the steel rebar. The polarization resistance can be used to determine the corrosion current — i_{corr} — by the Stern-Geary equation [57]:

$$i_{corr} = \frac{B}{R_p} \quad (11)$$

where B is the Stern-Geary constant and can be determined according to the following equation:

$$B = \frac{\beta_a \beta_c}{2.3(\beta_a + \beta_c)} \quad (12)$$

with β_a and β_c denoting the anodic and cathodic Tafel constants, respectively.

1.2.5. Carbonation of cementitious materials

Carbonation of cementitious materials is a complex process that involves several steps until the formation of carbonation products in the pores of concrete. The penetration of atmospheric carbon dioxide into concrete matrix occurs mainly by diffusion through the air-filled pores. Then, the carbon dioxide dissolves in the pore solution and reacts with the calcium hydroxide present in the medium leading to the formation of calcium carbonate, which reaction is described by:

$$CO_2 + Ca(OH)_2 \rightarrow CaCO_3 + H_2O \quad (13)$$

In addition to calcium hydroxide, there are other species in the pore solution that are susceptible to carbonation, such as calcium-silicate hydrates (C-S-H) and their dehydrated constituents — dicalcium silicate (C_2S) and tricalcium silicate (C_3S) —, aluminates and other hydroxides. However, these species are usually neglected in prediction models due to their small influence on the overall carbonation process [58]. Finally, the carbonates precipitate inside the pores. Carbonation leads to a change in the microstructure of the cement matrix and the chemical composition of the pore solution. In the case of Portland cements, the structural changes are mainly due to the precipitation of calcium carbonate which, by reducing the total pore volume, leads to a decrease in ionic transport and water absorption, and improves compressive and tensile strength of cementitious matrix [59], as shown in Figure 1.6. In compositional terms, carbonation decreases the pH and can contribute to increasing the content of chlorides and sulfates in the pore solution [7].

The main factors affecting the carbonation process in cementitious materials are environmental conditions — CO_2 partial pressure, relative humidity, temperature and presence of other aggressive species — and the microstructure of the materials. The diffusion of CO_2 through the cement matrix depends on the interconnection of air-filled pores. Regarding the use of supplementary materials, the increase of partial replacement of aggregates by pozzolanic active materials — silica fume, low- and high-calcium fly ash — decreases the carbonation depth [60]. Conversely, the increase of the cement replacement by these additives leads to an increase of the carbonation depth [60,61]. Layered double hydroxides evidenced the ability to capture CO_2 and fix it in concrete [62,63]. Finally, superplasticizers can improve carbonation resistance of cementitious materials due to decreased porosity and the production of hydration products with less susceptibility to carbonation [64]. Environmental exposure has a fundamental influence on the carbonation process. The relative humidity of the environment affects the internal relative humidity of the cement, which is essential for the carbonation reaction to occur. The carbonation reactions of portlandite, ettringite and C-S-H

with 0.7 of Ca/Si are significantly faster at high relative humidity of 91 % compared to 57 % [65]. In the case of very dry environments, the water present in the pore network is not sufficient for the carbonation reaction to occur. In the case of saturated environments, such as tidal and splash zones, most of the porous structure is filled with water, which obstructs the penetration of CO_2. The optimum range of environmental relative humidity for the carbonation process is between 50 and 80 %, depending on the microstructural state of the cementitious material. In addition to the relative humidity, the partial pressure of CO_2 also affects carbonation rate of the cementitious matrix. For low CO_2 concentrations (2-20 %), the increase of the partial pressure of CO_2 leads to a marked increase of carbonation depth. For higher concentrations (50-100 %), the increase of the partial pressure practically does not affect the carbonation depth due to the decrease of pore interconnectivity and the increase of microstructural density of the carbonated layer [66].

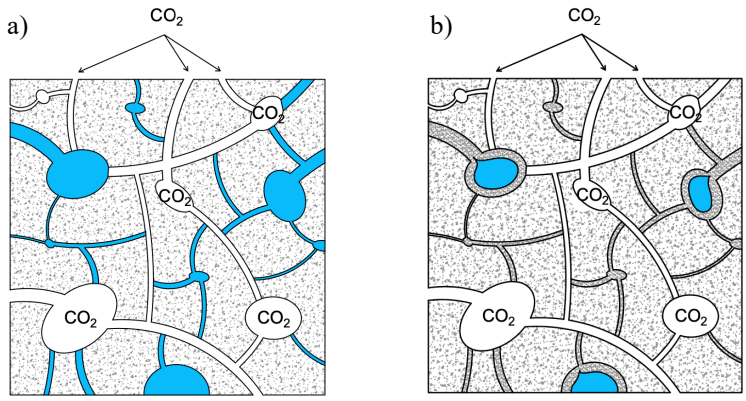

Figure 1.6: Illustration of clogging of the porous microstructure of cementitious materials after carbonation process.

There are several methods that can be used to determine the carbonation depth or to analyse the microstructure of carbonated layer. The most common one is a colorimetric method based on phenolphthalein indicator, which can identify the pH variation of the pore solution in the carbonation front. This method is simple to apply and cheap but is merely indicative as it has a poor definition and depends on the time between the application of the phenolphthalein solution and the reading of the results. The main components of cement and carbonation products can be identified by X-Ray Diffraction (XRD) or Fourier Transformation Infrared Spectroscopy (FTIR) and accurately quantified by Thermogravimetric Analysis (TGA) [67]. The internal microstructure of carbonated cementitious materials can be accessed by X-ray Computed Tomography (XCP). The carbonation depth can be determined with accuracy by optical or Scanning Electron Microscopy (SEM).
However, for application in a real case study, all these methods require the extraction of a representative sample from the structure and following a certain experimental procedure, which, in addition to damaging the structure, has a strong possibility to lead to a result deviated from reality.

1.2.6. Penetration of chlorides

Exposure to marine conditions represents a major problem in the durability of reinforced concrete structures. The presence of a certain amount of chloride ions in the pore solution interfacial to the surface of the steel reinforcement leads to a localized depassivation of the protective film, which is

formed due to the alkaline nature of cementitious materials. In cementitious materials, chlorides can be dissolved in the pore solution (free chlorides), as well as chemically and physically bound to the cement hydrates and their surfaces (bound chlorides). Only the free chlorides present in the pore solution can contribute to start the corrosion process. The chloride content necessary to initiate the localized attack on the passive layer of steel is known as the critical chloride content or chloride threshold value. The service life of concrete structures exposed to marine environment can be divided in two different stages, as proposed by Tuuti's corrosion model [68]. The initiation stage is related to the increase in the chloride content at the reinforcement level until the critical value is reached. The propagation phase is related to the evolution of the corrosion stage and the consequent degradation of the concrete cover.

Chlorides can participate in the destruction of the passive layer of steel and, subsequently, in the attack on its surface. However, there is no scientific consensus on the mechanism of destruction of the passive layer, which is probably influenced by several parameters leading to different interpretations of the process. The breakdown of the passive film in the presence of chlorides may be due to the oxidation of the inner layer of the oxide film, which origins non-protective Fe(III) oxides [69]. The onset of localized corrosion of the steel surface is due to the preferential adsorption of chloride ions in MnS inclusions giving rise to pitting corrosion sites on the steel surface [70]. The localized dissolution of MnS inclusions is accompanied by a local decrease of pH and increase in chloride content until initiate the formation of nucleating pits, which will form occluded corrosion cells with accumulation of aggressive agents, such as H^+, Cl^- or HSO_3^-.

The variation of the chloride content in the pore solution depends on the ease of penetration of chloride ions through the concrete cover and the ability of concrete to bind chlorides. The penetration of chlorides into the concrete matrix depends on the transport mechanism, and, therefore, is mainly affected by the pore structure of concrete and exposure conditions. The diffusion of chloride ions through the cement depends on the volume of water filled pores and tortuosity of the cementitious matrix [71], which defines the length of the diffusion path, as shown in Figure 1.7.

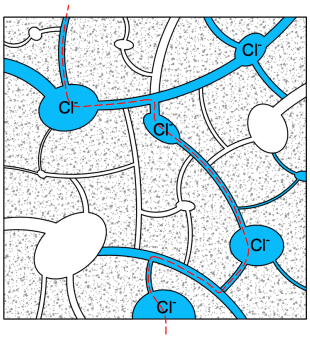

Figure 1.7: Illustration of chloride penetration tortuosity due to partial saturation of pore network.

The main factors that affect concrete porosity are water/cement ratio, concrete composition and curing conditions (temperature and aging/degree of hydration). The chloride content in the pore solution is also affected by the ability of concrete to partly immobilize chlorides [72–74]. The hydration products of cement can react with chlorides leading to the formation of calcium chloroaluminates — commonly referred as Friedel's salts. In addition, layered double hydroxides can be used as an additive due to their chloride binding capacity presented in simulated concrete pore solution [75]. However, a decrease in the pH of the pore solution can lead to the dissolution of the chloroaluminates and consequent release of bound chlorides into solution [76].

1.2.7. Acid attack

Structures based on cementitious materials are used for applications with extremely aggressive conditions, such as wastewater treatment plants and cooling towers, which promote the degradation of the cementitious matrix and, consequently, lead to a decrease in the lifetime of those structures. The aggressiveness of industrial wastewater depends on the chemical character of the acid present in solution, namely its strength, dissociation degree and the solubility of the salt formed [71,77]. In the case of strong inorganic acids (hydrochloric, sulfuric or nitric acid), the attack is very aggressive. The formed calcium salts that present very low solubility will precipitate on the concrete surface. If these salts are stable, such as calcium fluoride and oxalate, they will form a protective layer against acid attack, but if they are able to react with calcium aluminate hydrates (as calcium sulfate), it will promote concrete degradation. When exposed to sulfuric acid, the main components of Portland cement hydrates — portlandite and calcium silicate hydrates — react with the acid leading to their dissolution and to the formation of calcium sulfate dihydrate (gypsum). Then, calcium sulfates will react with the aluminates present in the cement matrix leading to the formation of ettringite. These chemical processes are represented in the following reactions, respectively:

$$H_2SO_4 + Ca(OH)_2 \rightarrow CaSO_4.2H_2O \quad (14)$$

$$3CaSO_4 + 3CaO.Al_2O_3.6H_2O + 26H_2O \rightarrow Ca_6Al_2(SO_4)_3(OH)_{12}.26H_2O \quad (15)$$

As the attack front progresses, a highly porous corroded layer, which is essentially composed by hydrated silicates [71], forms above the attacked surface, as illustrated in Figure 1.8.

The rate of corrosion of cementitious materials due to acid attack is mainly influenced by environmental factors (type of acid and its concentration, surface abrasion, fluids dynamics), fabrication factors (water/cement ratio, curing time, compactness), and chemical composition of concrete (type of cement, supplementary materials and aggregates). Solutions with a lower pH and the maintenance of a constant pH value promote faster deterioration [78]. The surface abrasion also increases the degradation rate due to the removal of the corroded layer, which is forming a protective layer that limits the acid diffusion to the cement surface [79]. For a continuous complete removal of the corrosion products, the rate of corrosion is mainly defined by the kinetics of neutralization reaction [80]. Factors related to production of concrete particularly affect its porosity and compressive strength [81]. Porosity allows the diffusion of hydroxyl ions through the concrete matrix and increases the contact area between the acid and the concrete, but as the degradation process occurs only superficially [82], its main influence is in the preventive perspective due to the higher capacity to absorb the expansion caused by the formation of gypsum [83]. Supplementary materials and aggregates also play an essential role in concrete degradation. The addition of fly ash to the concrete composition improves its resistance to acid attack [78,84]. The aggregates can be resistant or not to the acid attack. The presence of an acid resistant aggregate such as quartz, which is the main constituent of sand and is also present in bigger aggregates, increases the tortuosity of the diffusion path of ions through the corroded layer, but decreases the neutralization capacity [71].

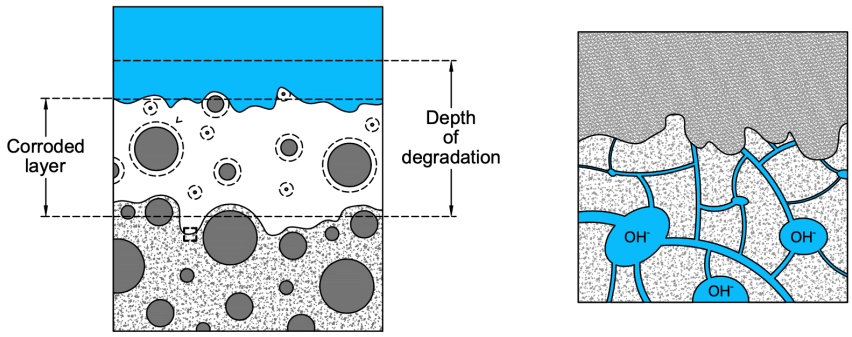

Figure 1.8: Illustration of acid attack on a cementitious surface (left) and a magnification of the attack front (right).

The evaluation of degradation rate is widely studied and is commonly achieved by mass loss and compressive strength determination under several experimental conditions. However, there is still a lack of knowledge about the mechanism of pH variation of the pore solution due to acid attack. The determination of pore solution pH can be achieved by different methods, which can be divided into destructive and non-destructive. Destructive methods are based on extracting a sample from a representative area of the structure under study and further analysis of the pore solution contained in that sample, which can be done through *ex-situ* or *in-situ* leaching method and expression method. To determine the pH non-destructively in hardened mortar samples, it is necessary to incorporate a pH sensitive device. The use of sensors, in addition to not requiring the removal of a sample, allows the determination of pH variation in real time and with good spatial resolution. The types of sensors that have been used to determine the pH in cementitious samples are fibre optic and solid-state electrochemical sensors [85]. Potentiometric sensors based on metal oxides are the most promising devices for this medium, because in addition to presenting the possibility of miniaturization and low-cost construction, they also have chemical stability and robustness. The determination of the pH variation of the pore solution of a mortar sample due to an acid attack with H_2SO_4 using embedded pH sensors is not documented in the literature, there is only one report on the assessment of the electrochemical state of the steel rod due to acid attack on reinforced concrete samples simply by measuring its open circuit potential without reaching the electrode surface [82].

1.3. Monitoring methods

The main advantages of monitoring are the early detection of the risk of corrosion condition of the reinforcement, which can allow a simpler and cheaper maintenance of the structure, and the better comprehension about the evolution of these species ingress, which will allow the optimization of the construction of these structures and the prediction of the best time for an intervention [2].
Monitoring of the aggressive agents responsible for the corrosion of steel reinforcement in concrete can be performed by analysis of pore solution, *in-situ* or in a laboratory, in order to determine the concentration of such agents. Consequently, monitoring methods are normally divided in destructive and non-destructive. Destructive methods need to extract a sample from the structure under study in order to analyse the pore solution carried by the sample through laboratory methods with established norms. However, the processes of removing a sample from the structure, its transportation to the laboratory and all sample preparation steps will change the composition of pore solution leading to a considerable associated error. Some colorimetric methods can be applied superficially on concrete

samples, avoiding the extraction of pore solution, but these methods are applied in the areas more susceptible to contamination — external surfaces of concrete samples.

1.3.1. Chloride monitoring

The monitoring of chloride ion concentration in concrete structures can be achieved by several methods that, in turn, can be divided in destructive and non-destructive methods. Figure 1.9 shows an overview of the available techniques.

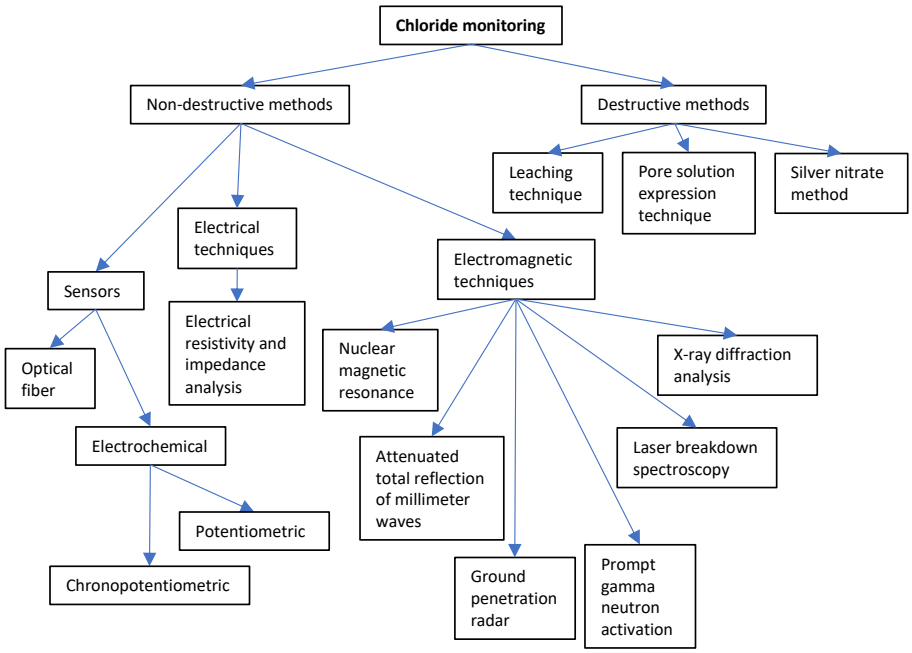

Figure 1.9: Overview of destructive and non-destructive methods to determine chloride content in concrete structures.

The most common destructive methods are the leaching technique (the most used) and pore solution expression method [86]. In order to use these methods, it is necessary to extract a sample of the structure under study, which causes its damaging and, subsequently, brings additional costs. Besides that, the heterogeneity of concrete and sample preparation leads to significant measurement errors [87]. In the case of non-destructive methods, they are mainly divided in embedded sensors, electric and electromagnetic techniques, which provide an external contactless measurement [87,88]. In the case of embedded sensors, these can be electrochemical or fiber optic and measure the content of free chlorides. Electrical resistivity (see chapter 1.2) and impedance analysis are used to determine chloride diffusion coefficients, which subsequently can be used to extrapolate chloride penetration profiles. Finally, there are several electromagnetic techniques (shown in Figure 1.9) that have been applied to the measurement of chlorides. However, these techniques require the use of heavy and expensive equipment and often present poor sensitivity to chloride ions, and therefore, these methods are sometimes used in a destructive approach through the analysis in laboratory of a sample from the in-service structure.

1.3.2. pH monitoring

pH monitoring can be carried out by several methods, which, in a similar way to chloride monitoring methods, can be classified in destructive and non-destructive methods, as shown in Figure 1.10. Non-destructive methods are limited to embedded sensors, which in turn can be divided into electrochemical and non-electrochemical. For an aggressive environment such as the concrete interior there is a need for a robust sensor capable of withstand a very alkaline environment. Among all pH sensors, metal oxide (metal/metal oxide) potentiometric electrodes and fiber optic sensors are the most used for pH monitoring in concrete structures due to the fact that they have potential to fulfill the above requirements [86,89]. The most used destructive techniques for pH measurement are the expression method that consists in the extraction of pore solution of small samples of in-service concrete structures under hydraulic pressure and its, subsequent, analysis; and leaching methods that can be performed *in-situ* and *ex-situ* by dissolving concrete powder in a solvent and further analysis of that solution pH.

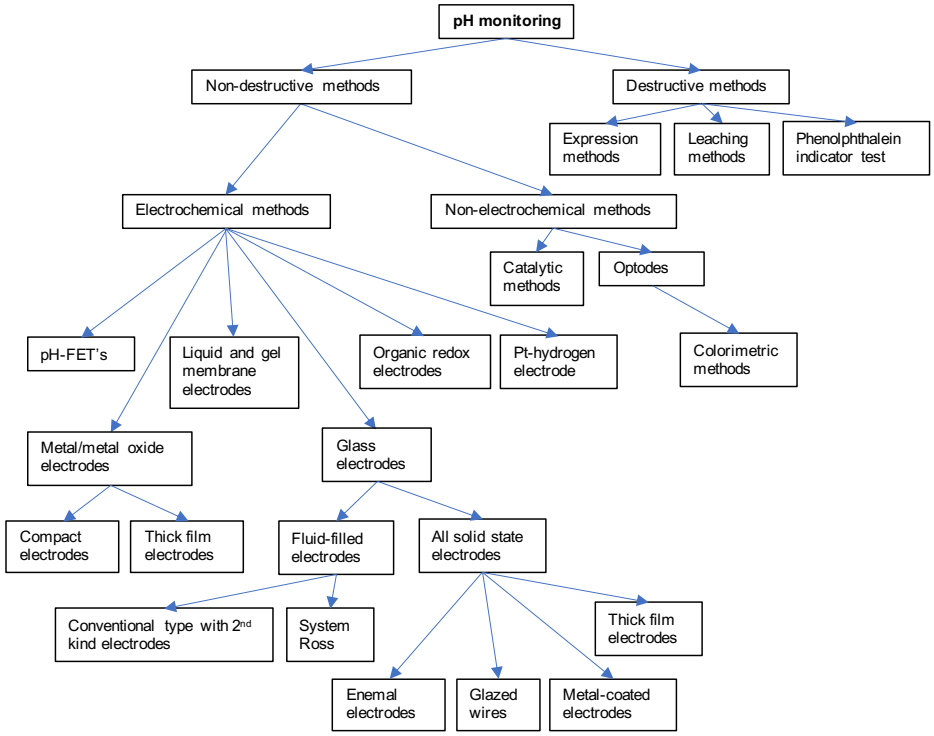

Figure 1.10: Overview of different methods to measure pH. Adapted from [86].

1.4. Electrochemical sensors

Sensors are devices, which have the ability to process physical or chemical inputs from their environment and convert it into a measurable signal. According to IUPAC a chemical sensor is defined as "a device that transforms chemical information, originating from a chemical reaction of the analyte or from a physical property of the investigated system, ranging from the concentration of a specific sample component to total composition analysis, into an analytically useful signal" [90]. A sensor is mainly composed by a receptor (sensitive material), which transforms the chemical

information into a measurable form of energy, and by a transducer (e.g., high impedance voltmeter) that converts the energy carrying the chemical information about the sample into a useful analytical output. There are different types of sensors, according to the operating principle of the transducer: electrochemical, electrical, mass-sensitive, magnetic, thermal, and optical. An electrochemical sensor is a device that transforms the effect of an electrochemical interaction between the electrode and the analyte into a measurable electric output (current or potential). Such effects may be induced electrically or simply result from a spontaneous reaction at open circuit. So, electrochemical sensors can be divided into [90,91]:

- Voltammetric sensors, which are based on the measurement of the resulting current from a redox process that occurs due to the application of a constant or swept potential (amperometric or voltammetric sensors, respectively) or to a spontaneous reaction (galvanic sensors). This type of electrochemical sensors can be based on chemically inert or active electrodes.
- Potentiometric sensors that measure the open circuit potential of the indicator electrode stablished by the electrochemical equilibrium with the species present in the surrounding environment. Several materials have been studied as indicator electrode, such as ion-selective electrodes, redox electrodes and metal/metal oxide electrode.
- Potentiometric solid electrolyte gas sensors, which work similarly to potentiometric, but require high temperature solid electrolytes and are usually used for gas detection.
- Chemically sensitized field effect transistors (CHEMFET), which are based on the variation of the source-drain current due to the effect of the interaction between the analyte and the active layer. This interaction can be considered, from the chemical point of view, similar to those occurring in the potentiometric ion-selective electrodes.

The most important parameters of an electrochemical sensor are a fast, accurate and reproducible response; sensitivity; limit of detection; stability under aggressive environments; and selectivity for the analyte to be detected (see section 3.5). For the case of embedment in concrete, sensors must also have mechanical and chemical robustness, present the least invasive design (size and shape) for the structures and have a low cost.

Several effective and mature sensors for detection of the species under study are available on the market, such as the glass membrane electrode for pH measurement. However, these commercial sensors are not functional for concrete environment and have a fragile conception that does not allow its miniaturization [89,92]. In fact, there are no commercial sensors available on the market with the necessary characteristics to be used in concrete.

Solid-state electrochemical sensors for pH [85] and chlorides [93–95] monitoring have been widely studied by the scientific community due to their fast response, remarkable stability and robustness, and possibility to be produced with a micro size, which allows a larger applicability, such as concrete monitoring [89]. Although, only a few experiments with these sensors were performed in solidified concrete samples and, therefore, there is still a lack of experimental studies on their operation under real conditions. In addition, the development of sensors allows the use of these tools for the laboratory study of the penetration mechanisms of aggressive agents in the porous network of cementitious materials, as well as the variation of the microstructure due to the reactions between the external agents and the constituents of the cementitious matrix.

1.4.1. Electrocrystallisation

The electrocrystallisation is an electrode process that involves the formation of a solid phase caused by the reduction of metallic cations in solution (metal deposition) or oxidation of electroactive species in solution (metallic oxides electrosynthesis). The process at stake is composed by several steps: diffusion of ions in solution to the electrode surface, electron transfer, formation of ad-atoms due to partial or complete loss of hydration layer, diffusion of ad-atoms through the surface, clustering of ad-atoms to form critical nuclei on the substrate surface, incorporation of ad-atoms at lattice sites, and growth of the nuclei islands until the surface of the substrate is completely covered by the deposit [96].

In the case of electrochemical nucleation, the energy involved in the incorporation of atoms depends on the lattice site. Lattice growth at step or kink sites involve surface diffusion of ad-ions due to the favoured charge transfer reactions at plane surfaces compared to steps or kinks. The diffusion of ad-ions on the surface leads to further loss of solvation layer until the atom is eventually incorporated into the lattice. The incorporation of ad-ions at active sites leads to the formation of growth centres that can further expand two- or three-dimensionally. The evolution of the density number of active sites can be described by the following equation:

$$N(t) = N_0[1 - e^{-At}] \tag{16}$$

where N_0 is the density number of nucleated particles randomly distributed over the substrate surface, and A and t are the rate and time of nucleation, respectively. The island growth kinetics is mainly influenced by the electrodeposition parameters — nucleation overpotential and electroactive species concentration. In the case of systems with a small nucleation potential, islands growth is controlled by the kinetic regime allowing the control of island shape and density. The evolution of island properties — density, shape and growth kinetics — determines the film roughness at island coalescence [97]. However, most systems of technological interest have a high nucleation overpotential and, therefore, the growth of centres is at least partially controlled by mass transport in the bulk solution [98].

For potentiostatic conditions, the applied potential controls the constant rates of steady state nucleation and of nuclei growth [99]. The type of nucleation process can be determined by the Scharifker model for instantaneous and progressive nucleation processes, whose equations are respectively [100]:

$$\left(\frac{j}{j_{max}}\right)^2 = 1.9542\frac{t_{max}}{t}\left[1 - e^{-1.2564^{t}/_{t_{max}}}\right]^2 \tag{17}$$

$$\left(\frac{j}{j_{max}}\right)^2 = 1.2254\frac{t_{max}}{t}\left[1 - e^{-2.3367\left(^{t}/_{t_{max}}\right)^2}\right]^2 \tag{18}$$

where j_{max} and t_{max} correspond to the peak current density and its corresponding time in the current-time transient, which is characteristic of a substrate completely covered by nuclei. An instantaneous process is characterized by a constant number of nuclei rapidly formed, whereas for a progressive process, the number of nuclei continues increasing with time.

1.4.2. Chloride sensors

There are not many materials available that can be used as chloride sensors. For the detection of chloride, in addition to the well-known silver/silver chloride electrodes, conducting polymers and fluorescent-based materials have been studied. In the case of conducting polymers, it was studied poly(3,4-ethylenedioxythiophene) (PEDOT) doped with chlorides and coated with different chloride-sensitive membranes [101], and polyaniline (PANI) doped with D,L-camphor sulfonic acid (CSA) [102]. In the case of fluorescence-based sensors, it was mainly investigated quinoline derivatives, such as ABQ and MEQ [103], and lucigenin [104].

1.4.2.1. Ag/AgCl sensors

Ag/AgCl has been widely studied for different applications, such as reference electrodes [105,106], photocatalysis [107,108] and chloride sensors [85,93–95,109]. The high reversibility of Ag/Ag^+ system in chloride environments provides an interesting and useful behavior of these electrodes. The equilibrium that is established at the Ag/AgCl interface is:

$$Ag + Cl^- \leftrightarrow AgCl + e^- \tag{19}$$

and the equilibrium potential is given by the Nernst equation:

$$E = E^0 - 2.3\frac{RT}{nF}\log a_{Cl^-} \tag{20}$$

Where E^0 is the standard equilibrium potential, R is the universal constant of ideal gas, T is the temperature, n is the number of electrons involved in the reaction, F is the Faraday constant and $a_{Cl^-}$is the activity of Cl^-. Since the equilibrium is established at the silver/silver chloride interface it is important that the silver chloride coating is porous and thin enough to allow a fast penetration (diffusion) of chloride ions into the boundary and to improve the response time, respectively [110,111].

The synthesis of Ag/AgCl electrodes can be done by different electrochemical or thermal methods: anodization of a silver substrate [112,113]; cathodic electrodeposition of silver on a determined substrate (stainless steel, glassy carbon, etc.) followed by anodic deposition of silver halide; thermal decomposition in a furnace of a paste of silver oxide, silver chlorate, and water to form the couple Ag/AgCl [105]; and thermal reduction of silver oxide paste followed by electrolytic formation of the silver chloride [114].

In the case of silver anodization, the electrodeposition of AgCl starts with the formation of adsorbed AgCl nuclei at the submonolayer level [112], which expand laterally until form a continuous layer [113]. At the same time, silver is electrochemically dissolved through the AgCl layer. There are several factors that can lead to different film microstructures, such as the size of alkali metal cation (H^+, Li^+, Na^+, Rb^+) used in electrodeposition, the concentration of chloride salt, the current density or potential applied — in the case of a pulse polarization — and the time of growth [106]. If the growth is done by cyclic voltammetry, the main factors related to the technique itself are the potential

window (principally, the anodic limit), the scan rate and the number of cycles. Regarding the electrolytic bath parameters, smaller alkali metal cations (H^+ or Li^+) promote a faster conversion of Ag to AgCl producing more porous microstructures and more stable electrodes [105]. The potential problem that can occur with the embedment of these sensors in concrete (high pH environment) in absence or low content of chlorides is the formation of Ag_2O, which promotes a potential shift to more negative values [115].

1.4.2.2. Lucigenin

Lucigenin (bis-N-methylacridinium nitrate) is an aromatic compound used in chemiluminescence and its structure is represented in Figure 1.11.

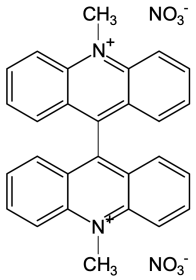

Figure 1.11: Illustration of Lucigenin structure.

This component has been widely studied as a chloride ion fluorescent indicator for fibre optic sensors [104,116]. The principle of fluorescence quenching is represented by the Stern-Volmer equation:

$$\frac{I_0}{I} = 1 + K_{SV} c_Q \tag{21}$$

where I_0 and I are the original fluorescence intensity and the fluorescence intensity after quenching, respectively, c_Q represents the concentration of quenching agent, and K_{SV} is a quenching constant that indicates the sensitivity of fluorescent indicator to quencher [117]. Although this molecule is widely applied in optical sensors, there are no documented studies on the potentiometric behaviour of this material. The electrochemical immobilization of lucigenin was already studied by scientific community. The adsorption mechanism of lucigenin is influenced by the anions added to the medium [118].

1.4.3. pH sensors

For the detection of pH, there are several materials that have been studied by the scientific community as an alternative to glass electrodes that, despite the good performance, are not suitable to miniaturization and use in aggressive environments. In the case of solid-state pH sensors, the most

promising materials are metal oxides (e.g., Sb_2O_3, IrO_x, TiO_2, MnO_2, PtO_2, SnO_2, PdO, RuO_2, ZrO_2, etc.) [119–123] and conducting polymers (Polypyrrole and Polyaniline) [124–128].

1.4.3.1. Metal/metal oxides

RuO_2 and IrO_x are the most promising metal oxide materials due to their selectivity and good stability in a wide range of pH, even at high pressure and temperature (up to 250 °C) [89]. However, its synthesis is difficult and expensive. The pH sensitivity of metal oxides can be a consequence of different mechanisms [129]: redox equilibriums, intercalation of single-phase oxygen, steady-state corrosion or ion exchange of surface hydroxyls sites. However, depending on the electrochemical equilibrium, metal oxides are commonly divided in metal/metal oxide (equation 22) and different types of oxides of the same metal (equations 23 and 24). The electrochemical equilibrium of these reactions is given by the following equations:

$$M_xO_y + 2yH^+ + 2ye^- \rightleftharpoons xM + yH_2O \quad (22)$$

$$M_2O_3 + H_2O \rightleftharpoons 2MO_2 + 2H^+ + 2e^- \quad (23)$$

$$M(OH)_3 \rightleftharpoons MO(OH)_2 + H^+ + e^- \quad (24)$$

a) Iridium oxide

Iridium is a rare precious metal that was discovered in 1803 by S. Tennant when he was working on raw platinum residues. This noble metal is extremely corrosion resistant, but it is possible to produce iridium oxides through several techniques. In the case of IrO_x, which have been tested for neural stimulation [130–132], electrocatalysis (oxygen evolution) [133–136], electrochemical degradation of pollutants [137], supercapacitors [138] and potentiometric pH sensors [121,139,140], the most used methods for its synthesis include anodic or cathodic electrodeposition on metallic surfaces (electrodeposited iridium oxide films – EIROF) [141–144], thermal decomposition of iridium salts, thermal oxidation of iridium substrates [145,146], electrophoretic deposition [147], sol-gel processes [148], pulsed-laser ablation of iridium oxide targets [149], reactive sputtering [150] and electrochemical oxidation of iridium wires (anodic iridium oxide films – AIROF) [151]. In all techniques, the resulting films predominantly contains IrO_2 [152,153], however, the hydration and density of iridium oxides vary with the growth method, leading to the formation of films with different electrochemical and structural properties [146]. In general, iridium oxides are divided in hydrous and anhydrous (poorly hydrated). The hydration of oxides leads to different properties due to its structural variation. Hydrous films present a density of 2 g/cm^3, which is about 6 times lower than anhydrous films (11.68 g/cm^3). The lower density of films leads to lower long-term stability, but the electrochemically active area is increased due to the porous matrix that allows the penetration of electrolyte into the film. The formation of compact and anhydrous films can be achieved by vacuum and high temperature methods, such as sputtering and melt oxidation, respectively.

Contrarily, electrochemical methods promote the formation of highly hydrated iridium oxides. Electrochemical depositions (EIROF) through the application of a potential or current are often performed in an alkaline iridium oxalate solution prepared according to the Yamanaka method [154], which leads to the formation of more compact, homogeneous and lustrous films. The deposition reaction for this medium is given by the following equation [154]:

$$[Ir(COO)_2(OH)_4]^{2-} \rightarrow IrO_2 + 2CO_2 + 2H_2O + 2e^- \quad (25)$$

However, there is no scientific consensus about the reaction and the species involved in this deposition. The pH response varies with the hydrate state of iridium oxides. For anhydrous films the response is close to Nernstian — approximately 60 mV/pH unit. However, for hydrated films the pH response is super-Nernstian — ranging from 62 to 90 mV/pH unit. This super-Nernstian behavior is not completely understood and was firstly discussed by Burke et al. [151] in terms of the acid base properties of the oxides involved. The model reactions for anhydrous and hydrous iridium oxides, both leading to a response of 60 mV/pH, are shown in equations 26 and 27, respectively:

$$Ir_2O_3 + H_2O \rightleftharpoons 2IrO_2 + 2H^+ + 2e^- \quad (26)$$

$$Ir(OH)_3 \rightleftharpoons IrO(OH)_2 + H^+ + e^- \quad (27)$$

Rewriting equation 27 to include the acid base equilibria, which is shown in equations 28 and 29,

$$Ir(OH)_3 \rightleftharpoons Ir(OH)_2O^- + H^+ \quad (28)$$

$$IrO(OH)_2 \rightleftharpoons IrO(OH)O^- + H^+ \quad (29)$$

results in the equation 30 where the pH response is $(1 + x - y)60$ mV/pH unit.

$$\begin{aligned}(1-x)Ir(OH)_3 + xIr(OH)_2O^- + xH^+ \\ \rightleftharpoons (1-y)IrO(OH)_2 + yIrO(OH)O^- + (1+y)H^+ + 1e^-\end{aligned} \quad (30)$$

As can be seen by equation 30, the pH response depends on the activity and pK_a value of the redox species present in the film. So, the super-Nernstian slope can be explained by a higher dissociation during oxidation due to oxidized species that present a lower pK_a than reduced species, leading to a higher number of protons than electrons.
The electrochemical equilibrium achieved by electrochemically synthetized films can be given by the following equation:

$$\begin{aligned}2[IrO_2(OH)_{2-x}(2+x)H_2O]^{(2-x)^-} + (3-2x)H^+ + 2e^- \\ \rightleftarrows [Ir_2O_3(OH)_3.3H_2O]^{3-} + 3H_2O\end{aligned} \quad (31)$$

Moreover, some authors reported a pH response with several slopes depending on the pH range.

Marzouk *et al*. [155] studied the selectivity of EIROF and found that these films are not affected by Ca^{2+}, Mg^{2+}, K^{+}, Na^{+} and Li^{+} ions. Similar experiments were performed by Fog *et al*, who showed that the pH response of anhydrous iridium oxide films is not affected by H_2O_2, Cl^{-} and K^{+} ions [129].

b) Manganese oxide

Manganese dioxide (MnO_2) is one of the most studied transition metal oxides for electrochemical capacitors [156–159], batteries (lithium ion and alkaline Zn/MnO_2) [160,161], reference electrodes [111,162] and catalysts [163], which can be explained by the several combinations existing between its crystallographic varieties and the corresponding properties. However, there are not many experimental studies testing this material as a pH sensor [122,123]. Manganese dioxide synthesis can be done by thermal decomposition of manganese powders [160], cathodic electrophoretic deposition [164] and by anodic or potentiodynamic electrodeposition [165–168]. The behavior of manganese dioxide was reported by Bodoardo *et al*. [169] and Nijjer *et al*. [170], where the overall reaction for deposition of MnO_2 is given by the following equation:

$$Mn^{2+} + 2H_2O \rightarrow MnO_2 + 4H^{+} + 2e^{-} \quad (32)$$

Paul and Cartwright [171,172] proposed a mechanism model of the electrochemical reactions in the presence of Mn (II), which is composed by three steps, corresponding to equations 33-35:

$$Mn^{2+} \rightarrow Mn^{3+} + e^{-} \quad (33)$$

$$Mn^{3+} + 2H_2O \rightarrow MnOOH + 3H^{+} \quad (34)$$

$$MnOOH \rightarrow MnO_2 + e^{-} + H^{+} \quad (35)$$

Three steps have been identified in this mechanism: the first and third are electrochemical steps and the second is a chemical step, being an *ece* reaction model. The overall reaction rate is controlled by diffusion of Mn (II) ions through the layer of MnOOH, which is a resistive layer. In the case of a low pH electrolyte, the Mn (III) ions formed on the chemical step may disproportionate to Mn (II) and Mn (IV) [173].

c) Ruthenium oxide

Ruthenium oxide has been studied for different applications, such as electrocatalysis, electrochemical sensors and supercapacitors. Together with iridium oxide, is one of the most promising metal oxides for pH sensing due to its thermal stability, good conductivity and low hysteresis. The most used methods for its synthesis are sputtering [174–178], electrodeposition [179–182], chemical vapor deposition [183] and drop casting [184]. Electrochemical methods, such as cyclic voltammetry and

potential/current pulse (anodic and cathodic) [185], have been widely studied to synthetize ruthenium oxide films.
The pH sensing mechanism of RuO_2 is a redox equilibrium between Ru(III) and Ru(IV) [186]:

$$Ru^{IV}O_2 + H^+ + e^- \rightarrow Ru^{III}O(OH) \quad (36)$$

where the Nernst equation of this electrochemical equilibrium is:

$$E = E^0 - \frac{RT}{nF}\ln\left(\frac{a_{Ru^{III}}}{a_{Ru^{IV}}a_{H^+}}\right) \quad (37)$$

At 25 ºC and assuming nearby equal activities of Ru(III) and Ru(IV), the potential of a RuO_2 electrode becomes:

$$E = E^0 - 0.059pH \quad (38)$$

1.4.3.2. Conducting polymers

Electronically conducting polymers (ECP) are a group of organic compounds that have a unique combination of properties and have aroused great interest within the scientific community due to their wide applicability. These materials exhibit the electrical and optical properties of metals or semiconductors, attractive mechanical properties, and can be synthesized easily and with the desired morphological structure.
The conductivity is due to the combination of polymer structure and its doping state. The ECP possess a conjugated backbone structure that is constituted by a chain of alternating single — σ — and double — σ and π — bonds between carbon atoms, as represented in Figure 1.12. The chemically strong σ-bonds are responsible for the mechanical strength of polymeric chains, while the weaker π-bonds allow an easier delocalization of electrons between the atoms due to their *p*-orbitals overlapping [187]. Doping consists of the insertion of charge carriers into the polymeric structure and can be carried out chemically, electrochemically and photochemically. Electrochemical doping consists of a reversible redox process, in which the insertion and expulsion of counter-ions (dopants) are carried out, accompanied by solvent, ensuring the electroneutrality and stabilization of the backbone. The electrons added by the counter-ions to the polymeric chain are relocated as polarons or bipolarons, creating charge carriers. The dopant type and its concentration affect the properties of the films, such as roughness, morphology, porosity, colour and conductivity.

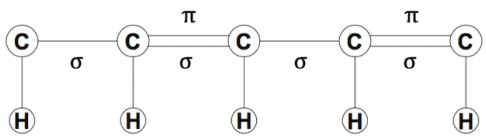

Figure 1.12: Schematic of the conjugated backbone structure of ECP

The conductivity of ECP can be explained by the band theory. The oxidation of the polymer leads to the formation of a polaron, which is a cation radical of spin=1/2, causing local distortions in the polymer chain. Thus, there is the creation of new energy levels between the conduction and valence bands. The subsequent oxidation leads to the formation of a bipolaron of spin=0, increasing the local distortion of the chain. The increasing number of polarons leads to the formation of bipolaronic bands in the optical gap, which promotes an increase in the electrical conductivity of the material.
The synthesis of ECP can be accomplished by chemical or electrochemical methods. However, the ECP synthetized by electrochemical methods presents several advantages comparing to chemical, such as higher conductivity, high purity films, control of film structure and thickness, and the possibility of using characterization techniques during the film growth. The electropolymerization can be carried out by potentiostatic, galvanostatic or potentiodynamic methods. The growth solution is constituted by the monomer of the polymer, supporting electrolyte and solvent. The requirements that a monomer must have in order to be able to carry out its electropolymerization are the following: to have an accessible redox potential, which depends on the substrate and on the electrolytic medium; the radical cation originated by the oxidation of the monomer must react more easily with another cation radical or with a neutral monomer than with the other species present in the electrolyte; and must have a higher oxidation potential than that of the formed polymer.
Due to its specific properties ECP have a wide range of possible applications, such as electrochemical supercapacitors, corrosion protection [188–190], artificial muscles [191–195], electroless precipitation [196], electrocatalysis, electrochemical sensors [197–199], electrochromic devices [200–202], smart drug delivery, and ionic transfer membranes. For electrochemical sensors, ECP can act directly as a sensor (for the case of pH sensing) or be a supporting matrix for an electroactive specie that will react with the analyte. The variation of the potentiometric response of conducting polymers for different pH values is related to protonation/deprotonation reactions of the amino groups contained in the polymer backbone [125,203]. The electrochemical equilibrium established at the interface between the polymer surface and the electrolyte is represented by the following equation:

$$PPy + H^+ + e^- \rightleftarrows (PPyH)^+ \tag{39}$$

and the equilibrium potential is given by the equation:

$$E = E^0 + 2.3\frac{RT}{nF}\log[a_{H^+}] \tag{40}$$

The potentiometric response of conducting polymers to pH is influenced by the dopant and films thickness. Electrosynthesized films with a thickness less than 2 μm present a good response with a slope of about 50 mV pH^{-1} for a higher range of pH values (2-12). The sub-Nernstian response is due to the presence of other ions in the different buffer solutions [204]. Thicker films difficult ionic diffusion through their matrix and can retain ions inside which can influence their potentiometric response [125]. Polypyrrole functionalized with a co-doping system of hydroquinone monosulfonate and oxalic acid presented a sub-Nernstian slope of about 55 mV pH^{-1} for a pH range from 2 to 12 with a response time less than 10 s. In addition, the co-doped PPy film presented selectivity to protons with respect to several cations (K^+, Na^+, Ca^{2+}, Zn^{2+} and Mg^{2+}) [205].

a) Polypyrrole

Polypyrrole (PPy) is an ECP of the aromatic heterocyclic compounds widely studied by the scientific community due to its easy synthesis, either chemically or electrochemically, that can be performed with an aqueous solvent (avoiding organic solvents that can be harmful to the environment), and to its good stability under environmental conditions [206].
The growth mechanism of polypyrrole, which is representative of others ECP, is represented in Figure 1.13. Initially, the oxidation of the monomer occurs (1), forming a radical cation, which is a highly reactive specie with other radical cations and monomers. The formation of a dimer can take place by two mechanisms. In the first, the radical cation reacts with a monomer and is subsequently oxidized and deprotonated to form a dimer (2a). In the second, the radical cation reacts directly with another radical cation, followed by deprotonation (2b). The process continues forming oligomers (3), increasing in size until reaching a critical size, in which the polymeric chains become insoluble, beginning its precipitation on the surface of the substrate.

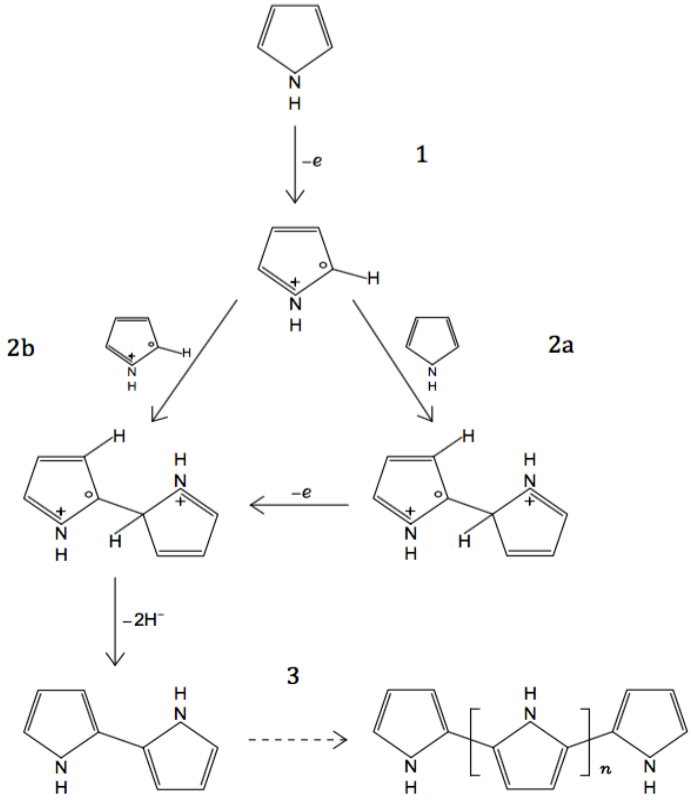

Figure 1.13: Schematic of growth mechanism of polypyrrole.

The bonds between the aromatic chains can be in positions α-α', α-β' or β-β', as shown in Figure 1.14. The most predominant and ordered structure of polypyrrole is a planar configuration of monomers joined by α-α' bonds. However, the positions α-β' and β-β' lead to a disordered growth of polymeric chains and can promote the polymer crosslinking [207].

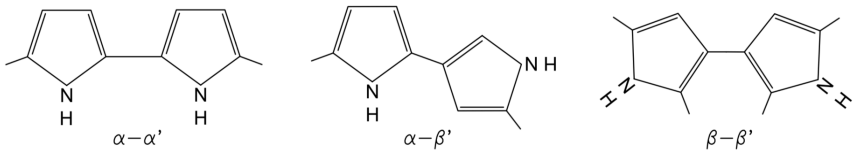

Figure 1.14: Possible configurations of aromatic chains bonding.

The electropolymerization of PPy can be carried out in several electrolytic mediums — with different solvents and supporting electrolytes — which leads to different properties of the films, such as morphology, conductivity and mechanical behavior [208–214]. The nature of dopant anion slightly affects the morphology of PPy films with thicknesses less than 1000 nm, in which the formed nuclei on the substrate have a globular shape and are oriented along the scratches. However, thicker films doped with chlorides or perchlorates have its morphologic structure with a cauli-flower shape.

The oxidation potential of the monomer varies with the nature of the substrate and the electrolytic solution — mainly, type of solvent. In the case of PPy, the application of a too high potential can over oxidize the polymer leading to the formation of carbonyl functional groups, and to an irreversible loss of mass of the polymer that causes a decrease in its electrical conductivity [215,216]. This electrochemical process (overoxidation), in aqueous medium, may be related to the oxygen evolution, since the respective potentials are coincident [217,218]. A decrease in the pH of the electrolytic solution causes an increase in the anodic potential in which the polymer is over oxidized [217,219].

PPy is used in several areas, such as biology, technology, and energy. For the biologic application, this ECP has been applied for biosensors, drug delivery systems, biomaterial in neural tissue engineering, artificial muscles, neural probes, blood conduits and nerve guidance channels. In the case of technologic area, PPy has been studied for corrosion protection, computer displays, microsurgical tools, electrochemical sensors, and electrochromic devices. Finally, the application in the energy area is mainly for electrochemical supercapacitors [220,221] and cathodic material for lithium ion batteries.

CHAPTER 2 Techniques

This chapter presents the main techniques used to carry out the experimental work. The synthesis of sensitive films was performed using the electrochemical techniques of cyclic voltammetry, chronopotentiometry and single and double pulse chronoamperometry. The characterization of the modified electrodes was carried out through potentiometry, cyclic voltammetry, electrochemical impedance spectroscopy, scanning electron microscopy, energy-dispersive x-ray spectroscopy and *in-situ* ellipsometry. Mortar samples were characterized by powder x-ray diffraction and, in the case of samples exposed to chlorides, a commercial sensor was also used to determine their chloride content.

2.1. Cyclic voltammetry

Cyclic voltammetry (CV) is a very useful electrochemical technique that, from the evolution of the voltammogram — graph of current density as a function of electrode potential — can immediately provide qualitative information on the electrochemical reactions of the working electrode under study in a given medium, and through treatment of voltammetric data it is possible to determine quantitatively certain electrochemical parameters.

This technique consists in the application of a potential to the working electrode (WE), which is immersed in a solution, and in the measurement of the resulting current density. The WE potential, which is measured in relation to a reference electrode (RE), is swept linearly with a certain scanning speed — ν — that determines the time scale of the experiment, being comprised in a previously established potential window. If the scanning starts in the potential (E_i) in the positive direction, it continues until it reaches the potential value of anodic limit (E_1). Then the direction of the potential scan is reversed and goes in the negative direction until it reaches the cathodic limit (E_2), and so on for n cycles, as represented in Figure 2.1 (left). Figure 2.1 (right) presents a typical cyclic voltammogram of a reversible process.

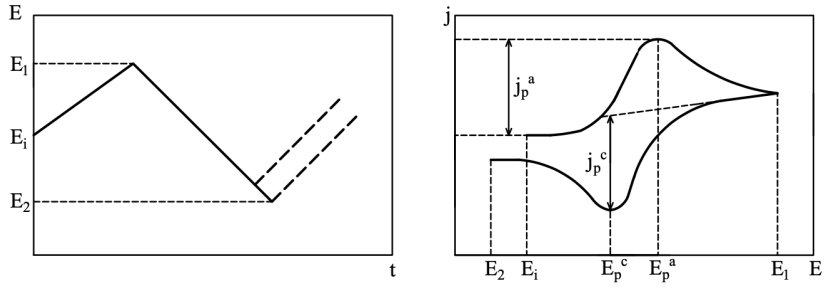

Figure 2.1: Potential-time profile for cyclic voltammetry and typical cyclic voltammogram of a reversible process.

The resulting current is constituted by faradaic current, which is based on the heterogeneous charge transfer at the electrode-solution interface, i.e., the electron flow corresponding to the reduction or oxidation of electroactive species present in the solution; and capacitive current, which results from

the separation of charges in the double layer between the electrode and the solution. The heterogeneous charge transfer reaction is described by the current-overpotential equation given below:

$$j = j_0 \left[\frac{c_0(0,t)}{c_0^*} e^{-\alpha n f \eta} - \frac{c_R(0,t)}{c_R^*} e^{(1-\alpha) n f \eta} \right] \quad (41)$$

where j_0 is the exchange current density, α is the transfer coefficient, n is the number of electrons involved, f is equal to F/RT, η is the overpotential, $c_x(0,t)$ and $c_x{}^*$ represent the concentration of oxidized (x=O) or reduced (x=R) species on the surface of the electrode over time, and within the solution, respectively. Mass transfer is described by Fick's equations:

$$j = nFD_i \frac{\delta c_i}{\delta x} \quad (42)$$

$$\frac{\delta c_i}{\delta t} = D_i \left(\frac{\delta^2 c_i}{\delta x^2} \right) \quad (43)$$

where D_i is the diffusion coefficient of species *i*.
Equation 41 considers the mass transport occurring exclusively by diffusion, which is a process caused by a concentration gradient between the surface of the electrode and within the solution. This happens because the experiment is designed so that solution is quiescent and has a support electrolyte present, which eliminates the convection and migration of the present species, respectively.
The position and shape of the voltammograms reflect the properties and structure of the films, and therefore, depend on several experimental factors, such as the type of substrate, the composition of the working solution, the potentials window and the scan speed. In the case of electrochemical synthesis by CV, the increase in the distance between the oxidation and reduction peaks reflects an increase in the internal resistance of the grown film, and the increase of the current density in the redox peaks with the successive cycles is due to the increase of active centers, which could mean an increase in the film thickness.
The most important parameters in a voltammogram are the current densities of the anodic and cathodic peaks, j_{pa} e j_{pc}, respectively, and the respective potentials of anodic peak, E_{pa}, and of cathodic peak, E_{pc} [96,222].

2.2. Chronoamperometry

Chronoamperometry is a very efficient potentiostatic electrochemical technique for the quantitative analysis of the nucleation processes. In this technique the WE potential is changed from an initial potential value, for which no electrode reactions occur, to a final potential, in which the oxidation/reduction of the electroactive species present in solution takes place, as illustrated in Figure 2.2. This process is controlled by the diffusion mechanism of ionic species from the solution to the surface of the working electrode. At the instant when the final potential is applied, the concentration gradient in the diffusion layer is maximum, which causes a maximum at time *t=0*. Then, the current begins to decrease exponentially due to the formation of the double layer, a process in which the

capacitive current is dominant until reaching a minimum. Finally, the resulting current is faradaic, being the process controlled by diffusion.
A chronoamperogram represents the curve resulting from the current as a function of time, and the shape thereof depends on several factors such as the substrate, the composition of the electrolytic solution, the applied potential and the time at which it is applied. These experimental parameters influence the structure and properties of the modified electrodes. The faradaic current, for a flat electrode, is expressed by the Cottrell equation:

$$j = \frac{nFD^{1/2}c_O^*}{\pi^{1/2}t^{1/2}} \tag{44}$$

where j is the current density, n is the number of electrons involved in the reaction, F is the Faraday constant, D is the diffusion coefficient, c_O^* is the concentration of the oxidized or reduced species in solution, and t is the time (step width). For processes controlled exclusively by diffusion the current is proportional to $t^{-1/2}$ and, therefore, the graphical representation of j as a function of $t^{-1/2}$, often used as a test for diffusion control, is linear and passes at the origin, and the diffusion coefficient of the electroactive species can be determined from the gradient of the line. This technique is widely used for the synthesis of films. On the one hand, it allows to carry out the electrosynthesis very fast with the obtaining of denser films; on the other hand, it can be used for the investigation of phase formation and adsorption processes.

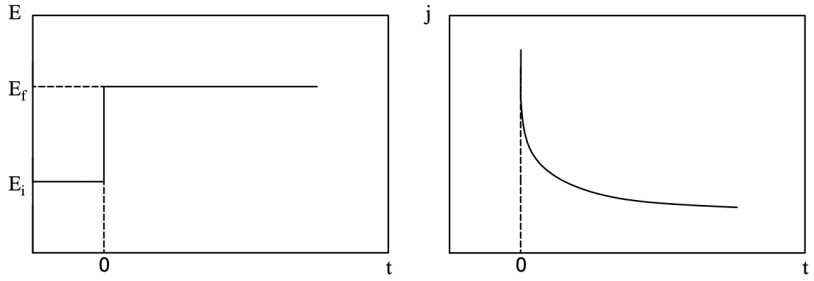

Figure 2.2: Potential-time profile for potentiostatic experiment and theoretical current-time transient.

2.3. Double pulse chronoamperometry

Double pulse or step potential chronoamperometry is an electrochemical potentiostatic technique that is specially used to study *ec* reactions (electron transfer step with a following chemical reaction) and to determine diffusion coefficients of electroactive species [223–225]. When applied to electrodeposition, this technique is commonly expressed in a more generic way as pulse or pulse-reverse electrodeposition, depending on the mode of the second potential pulse. Firstly, from the instant *t=0*, a certain potential is applied, to which the desired electrochemical reactions occur, during a given step width — τ. Then, the potential pulse is changed to a value under which complementary electrochemical reactions occur, also during a given time step, as shown in Figure 2.3. If the second pulse is the open circuit potential, this step is usually called as off-time pulse. These pulses can be repeated many times. In the case of electrodeposition, the main advantages of this technique comparing to single pulse one is the ionic replenishment of substrate diffusion layer and the selective

dissolution of film protrusions, during the second potential step. In addition, the higher number of experimental parameters allows a larger manipulation of films morphology and composition [226,227].

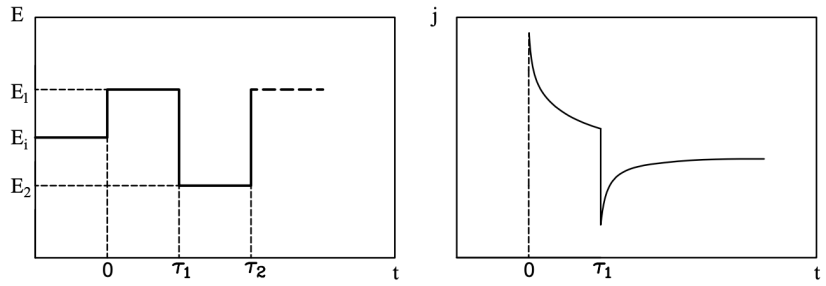

Figure 2.3: Potential-time profile of double pulse experiment and theoretical current-time data for a double potential regime.

For a flat electrode, the current density is given by the Cottrell equations that are expressed below:

$$0 < t < \tau_1 : \quad j = \frac{nFD^{1/2}c_O^*}{\pi^{1/2}t^{1/2}} \tag{45}$$

$$\tau_1 < t < \tau_2 : \quad j = nFD^{1/2}c_O^*[\pi^{-1/2}(t-\tau)^{-1/2} - (\pi\tau)^{-1/2}] \tag{46}$$

For the case of electrodeposition, this technique is commonly expressed in a more generic way as pulse or pulse-reverse electrodeposition, depending on the mode of the second potential pulse.

2.4. Chronopotentiometry

Chronopotentiometry is a galvanostatic electrochemical technique that is analogous to chronoamperometry [96]. In this method, the current is instantaneously changed from zero to a finite and constant value in which the redox processes of the electroactive species present in solution take place and, therefore, the overall reaction rate is fixed, as represented in Figure 2.4.

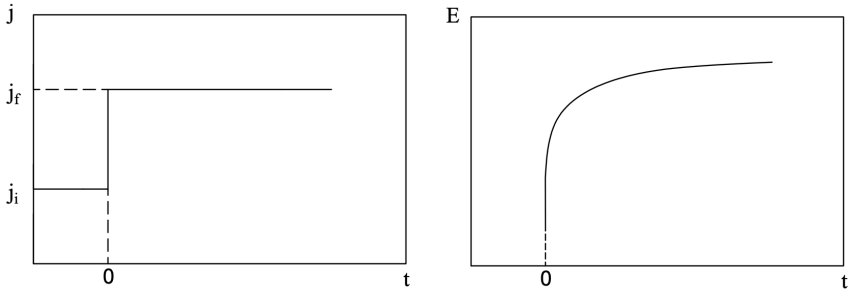

Figure 2.4: Current-time profile of galvanostatic experiment and theoretical potential-time transient.

A chronopotentiogram is the graphical representation of the working electrode potential as a function of time. For an anodic process, when the current pulse is applied, the potential increases sharply due

to the formation of the double layer until a potential value is reached at which occurs the oxidation of the electroactive species present in solution. Then, the process is determined by the Nernst equation until the surface concentration of the species being oxidized reach nearly zero. The solution of these systems is given by Sand's equation [96]:

$$\left|j\tau^{1/2}\right| = \frac{nFD_O^{1/2}\pi^{1/2}c_O^*}{2} \quad (47)$$

Where τ is the transition time [96,222]. The main advantage of this galvanostatic technique is the correction of the ohmic effect, which is unavoidable in the electrochemical processes [228].

2.5. Potentiometry

The first electrochemical sensors were based on potentiometric measurement that can be used to determine several chemical species not allowed by voltammetric methods. Cremer developed the first selective potentiometric electrode [229] (hydrogen-responsive glass electrode) that enabled the production of different analytical transducers to determine the activity of specific species in a solution. In a potentiometric test the potential is established by the system thermodynamic properties. The main advantage of potentiometric electrodes is the maintenance of the composition of the analyte in the sample due to an electrochemical equilibrium process that, in contrast to amperometric sensors, does not involve faradaic processes, does not alter the redox state of electroactive species, does not consume or produce new species, and does not promote analyte mass transport in the solution [230]. In addition, the necessary equipment is cheaper and simpler. Ion-selective electrodes (ISE) are commonly divided according to the nature of the ion-selective membrane or the shape and size of the electrode. The main types of membrane electrodes are the glass membrane electrodes, liquid or polymeric ion-selective membrane electrodes and solid-state electrodes. The potentiometric response of ISE probes is linearly dependent on the logarithm of the analyte activity and is described by the Nernst equation.

2.5.1. Properties of potentiometric electrodes

The limit of detection (LOD) is, according to IUPAC, the lowest (LLOD) or highest (HLOD) ion activity that can be detected with confidence, but ISEs usually present a linear response in a concentration range between 1 and 10^{-7} M, in practice, LOD rarely reaches 10^{-6} M. The LOD of a specie A is usually determined by the interception between the linear range curve and the parallel curve to the x-axis with the mean potential values of limiting extremes of activity, as shown in Figure 2.5. The reliability of the extrapolated LOD depends on the number of acquired data points, especially in the range near the limits, and the concentration range used to determine the linear section [231].
The response time is the time that an ISE needs to reach the equilibrium potential since is brought into contact with a certain solution. According to IUPAC, the limiting value is 1 mV/minute [231].

Some authors consider the response time as the time necessary to reach 95% of the total OCP of the system measured, as shown in Figure 2.6.

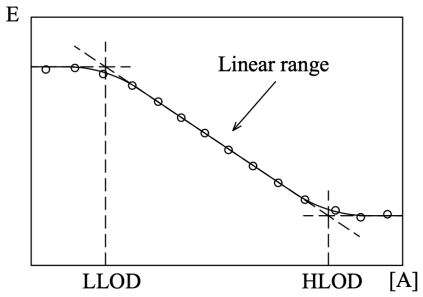

Figure 2.5: Representation of potentiometric response of an ion-selective electrode to a specie A and its limits of detection (lower and higher).

This important parameter of potentiometric responses is affected by thickness of outer layer (in the case of inner/outer layer equilibrium), facility of releasing/adsorbing the analyte, convection at the sensor surface, and the impedance of the measuring equipment.

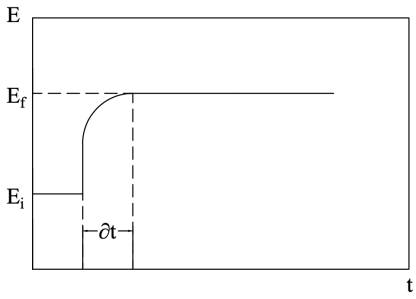

Figure 2.6: Representation of potentiometric time of response.

Figure 2.7 shows an ideal potentiometric response for different pH solutions that presents an immediate response, maximum limit of detection on both extremes and a Nernstian slope — 59 mV/pH unit.

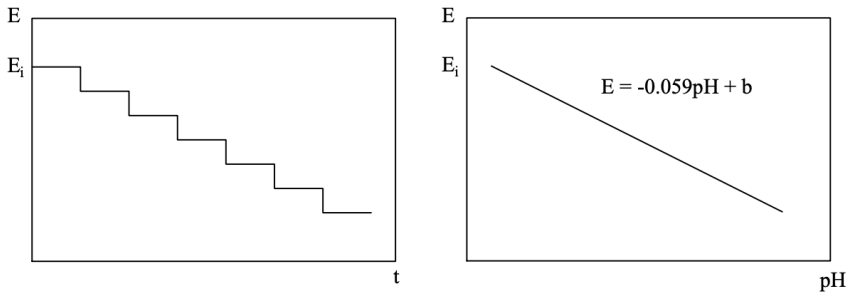

Figure 2.7: Potential-time profile steps for different pH solutions (left) and respective calibration curve of potential as a function of pH (right).

The presence of other ions in solution can change the performance of the potentiometric sensors, since there are not electrodes completely selective to the ions to be detected. The selectivity coefficient — $K_{A,B}^{pot}$ — of an ISE defines its ability to interact selectively to a target ion — *A* —, in the presence of other (interfering) ions — *B* — and can be determined by two different procedures: fixed

interference method and separate solution method [231]. In the fixed interference method, the potential of the probe is measured in several solutions with the same activity of the interfering ion and different activities of the target ion. The potential values are plotted as a function of activity and the selectivity coefficient is calculated by the Nicolsky-Eisenman equation [230,232]:

$$K_{A,B}^{pot} = \frac{a_A^*}{a_B^{z_A/z_B}} \tag{48}$$

where a_A^* is the intersection of the extrapolated linear portions of the potential-activity graphic. In the case of separate solution method, the potential is measured in two separate solutions with the same activity containing only one type of the ions in each. Therefore, the selectivity coefficient can be determined by following equation:

$$log\, K_{A,B}^{pot} = \frac{E_B - E_A}{2.303(RT/z_A F)} + \left(1 - \frac{z_A}{z_B}\right) log\, a_A \tag{49}$$

This second approach is less desirable because it does not reflect the real conditions under which the probes are usually used and, besides that, this method is only recommended for electrodes that present a Nernstian response [233]. Selectivity coefficients depend on the experimental conditions and, therefore, can't be considered as physical constants.

2.6. Electrochemical impedance spectroscopy

Electrochemical impedance spectroscopy (EIS) is a useful characterization technique to study electrode processes through the individual contribution of mass transfer, process kinetics and formation of the double layer [234]. Impedance is defined as the ability of a circuit to resist the flow of electrical current. This technique applies a sinusoidal excitation over a wide range of frequencies to the system and measures the values of Z_{real} and Z_{imag} (resistive and reactive parts of impedance, respectively) in response to the disturbance to equilibrium. The graphical representation is usually carried out using two types of plots: the Nyquist diagram with Z_{imag} as a function of Z_{real} at different frequencies, and the Bode diagram that has independent graphical representations for the variation of the log of impedance magnitude and phase angle with the log of frequency, as shown in Figure 2.8.

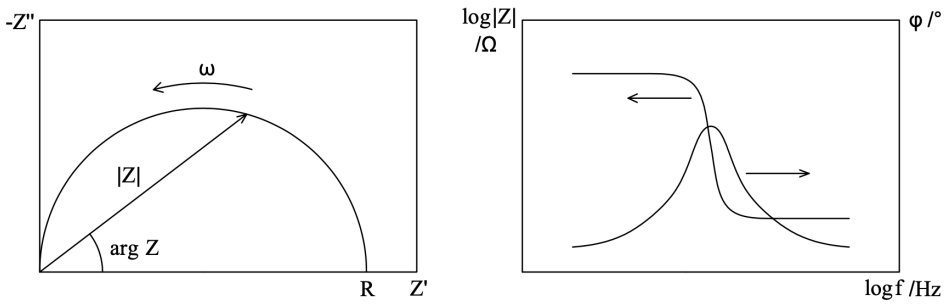

Figure 2.8: Graphical representation of experimental data through Nyquist and Bode diagrams, respectively.

The graphical representation of impedance spectrum provides a qualitative overview of the system impedance and its components. The Bode representation shows more clearly the variation of the impedance with the excitation frequency, which facilitates the understanding of single components contribution. In addition, if the system is composed by high and low impedance components, the Nyquist representation does not allow to distinguish the low impedance semicircle.
The fitting of the results is carried out through the application of an appropriate equivalent circuit and with real physical significance, which should include a combination of resistors and capacitances in order to represent the different components of the electrode process, such as the ohmic resistance between working and reference electrodes (R_S), double layer capacity (C_{dl}) and charge transfer resistance (R_{ct}). The simple representation of an electrochemical system is known as Randles circuit [234]; however, it is necessary to consider the Warburg impedance due to the increase of impedance at low frequencies that is caused by the depletion of electroactive species in the diffusion layer, as shown in Figure 2.9 (left). The impedance of Warburg element can be calculated by the equation [96]:

$$Z_W = \frac{\sigma}{\sqrt{2\pi f}} - j\frac{\sigma}{\sqrt{2\pi f}} \tag{50}$$

where σ is the Warburg coefficient ($\Omega\ s^{-1/2}$) and can be extrapolated from experimental data or calculated according to the equation:

$$\sigma = \frac{RT}{n^2F^2A\sqrt{2}}\left(\frac{1}{c_O D_O^{1/2}} + \frac{1}{c_R D_R^{1/2}}\right) \tag{51}$$

where A is the electrode area, D_O and D_R are the diffusion coefficients for species O and R in solution, and c_O and c_R are those species bulk concentration. The relative size of the charge transfer resistance and the Warburg impedance at any given frequency is a measure of the balance between kinetic and diffusion control [96]. The charge transfer impedance is very small for an electrochemical reaction with a large exchange current (i_0), and, consequently, the Warburg impedance will be the dominant term. For a sluggish reaction, the high charge transfer resistance is primarily responsible for the impedance of the electrochemical process.
Figure 2.9 (right) presents a Nyquist plot from a simple electrochemical system. At high frequencies, the Warburg impedance is negligible relatively to the charge transfer resistance, and at low frequencies the process is controlled by mass transfer.

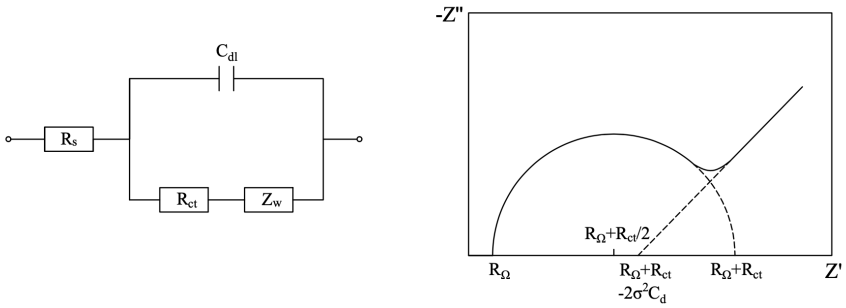

Figure 2.9: Representation of Randles equivalent circuit (left) and Nyquist diagram (right) from a simple electrochemical system.

For the case of the study of reinforced cementitious samples, EIS can be used to determine the electrochemical state of the reinforcement surface [235–237] and the microstructure and interfacial properties of bulk concrete [238]. The Bode representation allows a preliminary qualitative analysis of the mortar/steel system through the values of the impedance magnitude at low and high frequencies.
This technique has some drawbacks. The counter electrode must have an area higher than the working electrode (measurement target), which in the case of steel reinforcement of a concrete structure, is difficult to achieve [236]. In addition, an adequate definition of the experimental conditions, as well as the choice of an appropriate mathematical model, are needed for an accurate description of the system [239,240].

2.7. Ellipsometry

Ellipsometry is a non-destructive optical technique, which is based on the determination of the polarization state variation of a monochromatic light beam after specular reflection. This technique is very sensitive to the structure and thickness of thin films and, therefore, is used to characterize surfaces, interfaces and thin films *in-situ* and *ex-situ*.
The interaction between an incident light beam and a certain surface will cause an alteration of the polarization state of the specularly reflected light. The electric field vector is composed by two orthogonal components: one with parallel direction — p — and other with perpendicular direction to incidence plane — s — as can be seen in the Figure 2.10. In the case of the components p and s being in phase, the radiation will be linearly polarized. If these components have a phase difference of 90°, so the radiation will be circularly polarized. Finally, the radiation will be elliptically polarized if its difference of phase is higher than 0° and less than 90°.

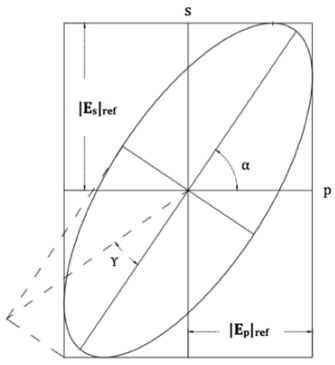

Figure 2.10: Illustration of the ellipse and its parameters: ellipticity, γ, and azimuth, α.

The Fresnel reflection coefficients — $\hat{r}_p$ and $\hat{r}_s$ — are the ratios between the electric field vectors of reflected beam — E_p^{ref} e E_s^{ref} — and of incident beam — E_p^{inc} and E_s^{inc} — as are presented by the following equations:

$$\hat{r}_p = \frac{E_p^{ref}}{E_p^{inc}} \qquad \hat{r}_s = \frac{E_s^{ref}}{E_s^{inc}} \tag{52}$$

Considering a two semi-infinite phases system, as can be observed in Figure 2.11, the Fresnel reflection coefficients for parallel and perpendicular components are given by the following equations, respectively:

$$\hat{r}_p^{02} = \frac{\hat{n}_2 cos\phi_0 - \hat{n}_0 cos\phi_2}{\hat{n}_2 cos\phi_0 + \hat{n}_0 cos\phi_2} \qquad \hat{r}_s^{02} = \frac{\hat{n}_0 cos\phi_0 - \hat{n}_2 cos\phi_2}{\hat{n}_0 cos\phi_0 + \hat{n}_2 cos\phi_2} \tag{53}$$

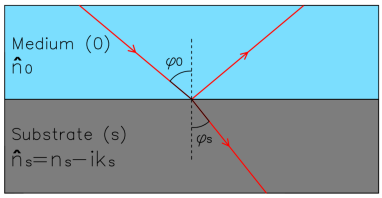

Figure 2.11: Schematic representation of specular reflection of light in a system constituted by 2 semi-infinite phases (electrolyte and substrate).

where, $\hat{n}_0$ and $\hat{n}_2$ are the complex refraction indexes of phases 0 and 2; ϕ_0 and ϕ_2 are the angles of incidence in medium 0 and of refraction in medium 2, respectively. These angles are related by Snell's Law:

$$\hat{n}_0 sin\phi_0 = \hat{n}_2 sin\phi_2 \tag{54}$$

For a determined phase, the refractive index is a complex number, $\hat{n} = n - jk$, where k is the extinction coefficient and n is the refractive index of that phase. The refractive index can be used as an indicator of relative porosity of a film or substrate. For example, in the case of a very porous material, which will have its pores filled by the environment fluid (electrolytic solution or air), its refractive index will be near of the medium index.
Considering a three-phase system (medium, film and substrate), as it is illustrated in Figure 2.12, the Fresnel reflection coefficients are given by Drude equations:

$$R_p = \frac{\hat{r}_p^{01} + \hat{r}_p^{12} e^{-2i\beta}}{1 + \hat{r}_p^{01} \hat{r}_p^{12} e^{-2i\beta}} \qquad R_s = \frac{\hat{r}_s^{01} + \hat{r}_s^{12} e^{-2i\beta}}{1 + \hat{r}_s^{01} \hat{r}_s^{12} e^{-2i\beta}} \tag{55}$$

where β is the phase change due to propagation of the light wave through the film and is given by the following equation:

$$\beta = 2\pi \frac{d}{\lambda} \hat{n}_1 cos\phi_1 \tag{56}$$

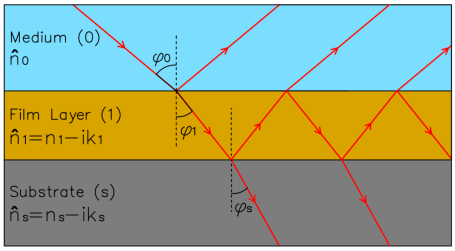

Figure 2.12: Schematic representation of specular reflection of light in a system constituted by 3 phases (electrolyte, film and substrate).

where d is the film thickness. In an ellipsometric study it is only possible to determine the parameters Δ and Ψ. Delta is the variation in phase difference that occurs by the interaction between the light beam and the material in study and its value can be from 0 to 360°. Psi is the ratio between the magnitudes of the total reflection coefficients and its value can be between 0 and 90°. The complex quantity — ρ — on one hand represents the ratio between total reflection coefficients for parallel and perpendicular components, relatively to incidence plane, and on the other hand, relates the ellipsometric parameters, through the following equations, respectively:

$$\rho = \frac{R_p}{R_s} \qquad \rho = tan\Psi e^{i\Delta} \tag{57}$$

Through the relation between the last two equations, we obtain the fundamental equation of ellipsometry, which relates the ellipsometric parameters — Δ and Ψ — with Fresnel reflection coefficients — R_p and R_s:

$$tan\Psi e^{i\Delta} = \frac{R_p}{R_s} \tag{58}$$

The main elements that constitute an ellipsometer are a light beam emitter, a support base for the sample under study, and a receptor for the reflected light beam, as shown in Figure 2.13. The emitter is constituted by a monochromatic non-polarized light source (e.g., He-Ne laser) and an optical element to convert unpolarised light into elliptically polarized light. The support base can be adjusted three-dimensional in order to the reflected beam reaches the receptor unerringly. Finally, the receptor is constituted by an optical element to determine the polarization state of the reflected light beam, and by a detector to measure light intensity [241–243].

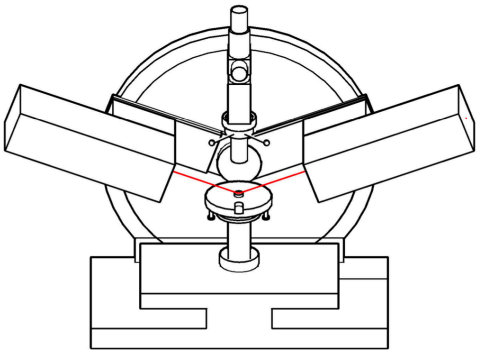

Figure 2.13: Illustration of a monochromatic ellipsometer.

The evolution of ellipsometric parameters collected *in-situ* during the growth of thin films depends on the substrate, which stablishes the first values corresponding to time zero, the material being synthesized and its light absorption, as well as the kinetics of the growth process that depends mainly on the electrolyte nature and concentration, and on the pulse growth applied. The growth of a transparent film produces a Psi-Delta loop that closes when the product of film thickness and the cosine of the angle of refraction is equal to half the wavelength of light in the film [244].
The most used and well succeeded procedure to determine the optical properties and film thickness variation during the electrodeposition consists in fitting the experimental data with a generated curve

from a theoretical three-phase model [245–248], which is based on the equations previously described. The procedure consists in simulating the optical parameters that leads to the best fitting between the experimental data and the simulated ellipsometric parameters. The fitting is initiated considering the formation of a single homogeneous film on the substrate surface. However, if it is not possible to obtain a complete reasonable fitting, it can be considered the growth of different and homogeneous layers.

2.8. Scanning electron microscopy

Scanning electron microscopy (SEM) is a multifunction and very useful tool for morphologic characterization of materials through the interaction between the incident electron beam and the sample. A SEM is mainly constituted by an electron column, a specimen chamber, a vacuum system, and a computer control system [249], as is illustrated in Figure 2.14.

The electron column is the most important component being responsible for the electron beam power and quality. This component is a long cylindrical body, which is located above the specimen chamber, and is constituted by a monochromatic source of high energy electrons, two or more electron lenses, scan coils, and condenser and objective apertures [249,250].

The specimen chamber is composed by a specimen stage and holder, couple-charged device camera, and several detectors to collect and analyze the electrons and x-rays emanating from within the sample. The resultant signal due to the interaction between incident electrons and sample atoms is composed by secondary and backscattered electrons that are used to form images, and x-rays that can be used to determine elemental composition of the sample. The backscattered electrons result from the elastic collision between incident electrons and the atoms of the sample, which leads to incident electrons scattering, allows to determine the phase discrimination based on atomic number; the secondary electrons result from the ionization of less energetic electrons of sample atoms due to its interaction with incident electrons and allow to obtain high resolution images from sample surface; and the x-rays result from the transition of electrons from higher-energy shells to holes in the inner shells, which were caused by the incident beam excitation.

The samples under study must be solid and stable under high vacuum conditions and be electrically conductive in order to avoid charge accumulation that leads to image artifacts [251].

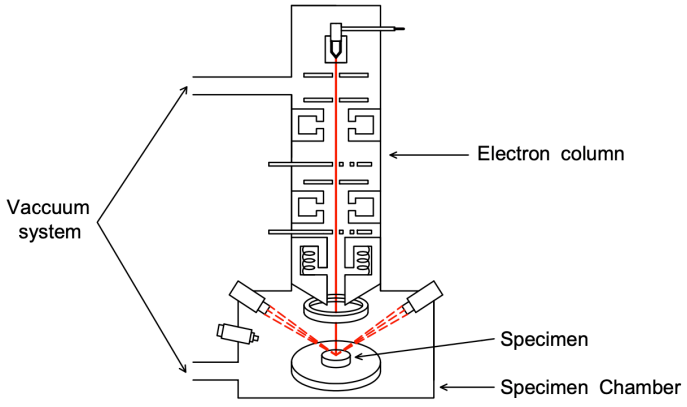

Figure 2.14: Illustration of SEM and its main components.

2.9. X-ray diffraction

X-ray diffraction (XRD) is a non-destructive analytic technique used to characterize crystalline materials through the determination of their structure, phase, preferential crystal orientations and other structural parameters — grain size, crystallinity, and crystal defects. XRD is based on constructive interference of monochromatic x-ray incident beam and a set of parallel planes of atoms with interlayer spacing of d_{hkl}, as shown in Figure 2.15.

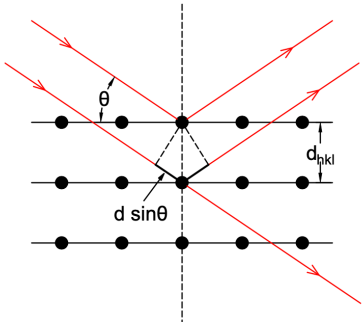

Figure 2.15: Schematic representation of diffraction of an incident beam by a set of parallel planes of atoms.

The condition for diffraction is given by Bragg's law, which is represented in the following equation:

$$n\lambda = 2d_{hkl}\sin\theta \tag{59}$$

Where n is an integer, λ is the x-ray wavelength, θ is the angle of incidence and d_{hkl} is the spacing between planes of atoms.

The main parameters of a diffractogram — intensity, width at half height and peak shapes — allow to obtain information about the composition and structure of the material under study.

The main constituents of an x-ray diffractometer are an x-ray tube, which is the source of x-rays, a goniometer, which is the platform that holds and moves the system, a sample holder, and a detector to count the scattered x-rays by the sample [252].

CHAPTER 3 Experimental procedure

This chapter presents the reagents and substrates used to carry out the experimental work. It also describes the methodology carried out for assembling the electrodes and arrays of sensors, synthesis and characterization of the modified electrodes, and their application in mortar samples. Finally, it is described the monitoring apparatus and destructive analysis of mortar samples after experiments.

3.1. Reagents and electrodes

Tables 3.1 and 3.2 summarize all reagents and substrates, respectively, used in the experimental work.

Table 3.1: Reagents used in the experimental work and their chemical formulas and suppliers.

Reagent type	Name	Chemical Formula	Supplier
Solvent	Water[1]	H_2O	Millipore
	Acetonitrile	C_2H_3N	Alfa Aesar
Supporting electrolyte	Lithium perchlorate	$LiClO_4$	Sigma Aldrich
For chloride sensors	Hydrochloric acid	HCl	Fluka
	N,N′-Dimethyl-9,9′-biacridinium dinitrate (Lucigenin)	$C_{28}H_{22}N_4O_6$	Sigma Aldrich
	3,4-ethylenedioxythiophene (EDOT)	$C_6H_6O_2S$	Sigma Aldrich
	Potassium chloride	KCl	Fluka
	Sodium chloride	NaCl	Fluka
For pH sensors	Manganese sulphate monohydrated	$MnSO_4.H_2O$	Alfa Aesar
	Nickel (II) chloride	$NiCl_2$	Alfa Aesar
	Sulfuric acid	H_2SO_4	Sigma Aldrich
	Iridium tetrachloride	$IrCl_4$	Alfa Aesar
	Hydrogen peroxide	H_2O_2	Alfa Aesar
	Potassium carbonate	K_2CO_3	Fluka
	Oxalic acid	$C_2H_2O_4$	Sigma Aldrich
	Ruthenium (III) chloride	$RuCl_3$	Sigma Aldrich
	Pyrrole (Py)[2]	C_4H_5N	Sigma Aldrich
Other reagents	Sodium hydroxide	NaOH	Riedel-de Haen
	pH buffer solutions	-	Fluka

[1] Millipore water presents a resistivity of 18 MΩ cm at room temperature.
[2] This monomer was used as received, without further distillation.

Table 3.2: Substrates used in experimental work.

Substrates	Diameter /mm	Purity /%	Supplier
Glassy Carbon	3.0	-	GoodFellow
SS 316L	0.8	-	GoodFellow
SS 316L	3.175	-	GoodFellow
Platinum	1.0	99.99	Mateck
Silver	0.8	99.99	GoodFellow
Iron	1.0	99.90	GoodFellow

To perform this experimental work, different geometries — cylindrical, helicoidal, wire and circular with different areas — were used for the working electrode, as shown in Figure 3.1.

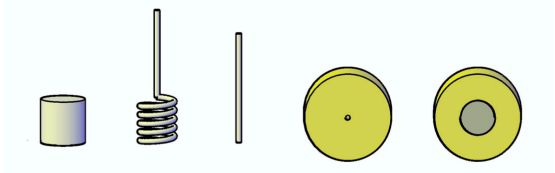

Figure 3.1: Illustration of different geometries used for working electrodes.

3.2. Preparation of solutions

The preparation of the electrodeposition solution of iridium was based on Yamanaka method [154]. First, 0.15 g of $IrCl_4$ was dissolved in 100 mL of deionised water, with magnetic stirring for 30 minutes. Then, 0.5 g of oxalic acid was added as a complexing agent to prevent precipitation of IrO_x in alkaline media [130], followed by 10 minutes of stirring before adding 1 mL of H_2O_2 (30%). After more 10 minutes of stirring, the pH was raised to 10.5 by the slowly addiction of sodium or potassium carbonate [130]. The carbonate addiction is needed to prevent the passivation of the stainless steel surface due to spontaneous oxide formation [121]. The solution was finally stored avoiding contact with light and is ready to be used when presents a blueish colour after few days.
All the other growth solutions were prepared before each synthesis with Millipore water and the calibration solutions for chlorides were prepared by dilution of a mother solution of 10^{-3} M NaCl.

3.3. Preparation of electrodes

The preparation of working electrodes (assembly and surface treatment) depended on their final geometry, which was different for the study of the optimization of sensitive materials and for the application in mortar samples.
In the case of synthesis and characterization, the electrodes were connected to a conductive copper wire through colloidal silver suspension (Ted Pella Inc, USA), with the connection reinforced and isolated with Araldite. Then, electrodes were encased in epoxy resin (EpoKwick™ FC, Buehler, USA) forming a disk with a circular exposed area depending on the diameter of each substrate. The polishing of electrodes was initiated with sandpapers with successively smaller grain size up to grit 4000 using a metallographic polisher. Then, the electrodes were polished manually on a polishing cloth using alumina suspensions with grain size of 1 μm. Finally, the electrodes were cleaned with

acetone and distilled water to remove alumina and other impurities that could be present in the surface of substrates due to the polishing process.
For mortar application, the assembly of sensors was similar to the process mentioned above, but without the epoxy encasing in order to obtain a wire-shaped substrate with an exposed circular (only the tip of the electrode) or cylindrical area (the tip plus an extension in length of the wire). The polishing was carried out exclusively to the edge of electrodes due to their non-flat geometry. The electrodes were designed to obtain an accurate measurement, maintaining the robustness required to withstand an environment as aggressive as cementitious materials, but without becoming excessively invasive to the cement matrix in which they will be embedded.
The cleaning of secondary electrode — platinum rod — was done frequently by applying a potential pulse of 2 V *vs*. RRE in an aqueous solution of H_2SO_4 0.5M for 120 seconds and then rinsed with distilled water. Besides that, before each synthesis this electrode was annealed until it became incandescent in order to remove possible organic matter that could be adsorbed on its surface and to ensure the same physical properties of the counter surface.

3.4. Experimental design

Some experiments were designed according to Taguchi method in order to verify the correlation between the experimental parameters of film synthesis and the quality factors of the sensors. This statistical method uses orthogonal arrays to study all the design parameters with minimum of experiments [253,254]. The correlation coefficient can be positive or negative depending on whether the experimental factor is directly or inversely proportional to the quality factor. A coefficient between 0.4 and 0.8 is considered acceptable, and greater than 0.8 is indicative of a strong correlation between the parameters.

3.5. Embedding of the set of sensors in mortar samples

The assembly of the sensors combs was carried out after the synthesis and potentiometric characterization of each modified electrode. 8 electrodes spaced 5 mm apart were grouped in each set. Afterwards, the combs were embedded in mortar samples with the following dimensions: 5 cm^2 of base area and 6.5 cm of height. For this purpose, maritime plywood molds were used for the hardening of the mortar samples allowing the passage of the electrical cables of the set of electrodes and keeping the comb perpendicular to the top face and with the desired distance. The composition of the mortar, which is described in Table 3.3, was chosen in order to obtain a very porous cementitious matrix to accelerate the penetration process of aggressive agents. In addition, it was decided to avoid large aggregates in order to decrease the tortuosity and to increase the homogeneity of distribution of the different phases in the sample and, consequently, increase the reproducibility of the system. The mortar paste hardened inside the molds for 1 week and, after removing the molds, the solidified samples were immersed in distilled water for 2 weeks for curing process. The first hardening period was determined by the samples with LDH, which took about 1 week to complete the hardening.

Table 3.3: Mortar composition in mass percentage.

Mortar composition	Mass %
Cement I 42.5N	20.83
LDH (>125 um)	0 or 2
Sand 0-2 mm	62.50
Water	16.67
water/cement	0.8
sand/cement	3

Finally, all the faces of the mortar samples, with exception of the top (perpendicular face to the set of sensors at a distance of 5 mm from the first sensor and 40 mm from the last), were isolated with Araldite, as shown in Figure 3.2. In the case of carbonation study, an additional hole was made in the mortar samples to fit the sponges that will retain the electrolytic solution between the mortar and the reference electrode.

Several samples of mortar without embedded sensors were prepared according to the procedure described above in order to perform a destructive analysis of the chloride content through a commercial sensor for different immersion times in 3.5% NaCl. For this purpose, a central core was extracted from the samples with a dry cut, to avoid changing the pore solution, and transversely sliced into 5 mm pieces with the help of a plier, as can be seen in Figure 3.2. Then, 0.4 g of each ground fragment was added to 16 mL of distilled water with ultrasonic stirring for 2 minutes. Finally, the chloride content in each aliquot was determined using a commercial chloride selective sensor (Mettler Toledo). The powder of each fragment was also analysed by XRD, between Bragg angles of 5º and 25º using a step size of 0.02°, in order to identify the formation of Friedel salts.

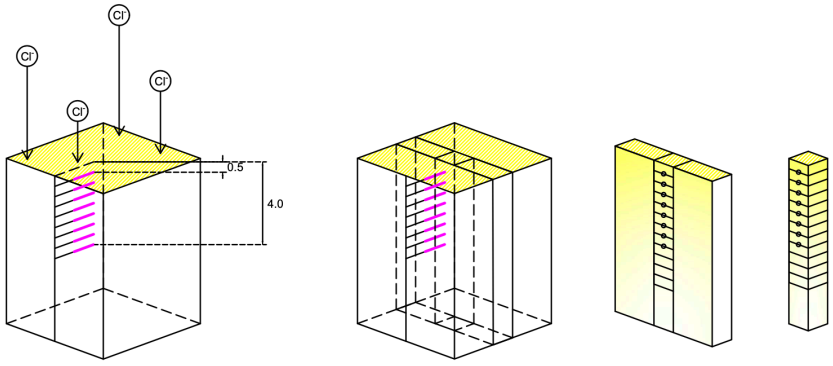

Figure 3.2: Illustration of the spacing of the set of sensors embedded in a mortar sample (left) and illustration of core extraction from a mortar sample for destructive analysis (right).

3.6. Equipment and experimental conditions

The synthesis of pH and chloride sensors were performed in an electrochemical cell consisting of one-compartment plastic container with a platinum wire as counter electrode and a Red Rod electrode (199 mV *vs*. SHE, T= 25 °C, Radiometer analytical, France) as reference (RRE), which is represented in Figure 3.3. In the case of potentiometric characterization, it was used a saturated calomel electrode (SCE) as reference. These electrochemical experiments were performed at room temperature and without removal of the dissolved oxygen that could be present in the solution.

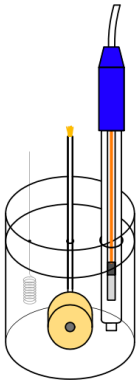

Figure 3.3: Electrochemical cells with one compartment used for sensors synthesis and characterization.

The potentiostat used for the synthesis and potentiometric characterization of modified electrodes was an Autolab PGSTAT 302N (METHROM, Netherlands). The electrochemical experiments were done inside a Faraday cage in order to avoid electromagnetic noise.
For *in-situ* ellipsometric experiments, an electrochemical cell constituted by 2 compartments was used, which is represented in Figure 3.4. The main compartment was built to work with a light beam angle of 70° having two quartz windows with 20° for incidence and reflection of the light beam to avoid refraction in the glasses. The working electrode was a stand-alone disk of stainless steel with a geometrical area of 0.785 cm^2, which was mounted in the centre of the electrochemical cell base. The counter electrode was a platinum mesh that was secured to the inside of the cell cover so as to be immersed in the solution without interfering with the light beam, and the reference electrode was a Saturated Calomel Electrode (SCE) mounted in the second compartment, which has a Luggin capillary near the working electrode in order to decrease solution resistance between the reference and working electrodes. The equipment used for the electrochemical growth was a Princeton Applied Research model 273A and the ellipsometric data was measured by an ellipsometer SENTECH 400 with rotative analyser and a He-Ne laser (λ=6328 Å). The refractive indexes of electrolytic solutions were determined by a refractometer Atago NAR-1T liquid.

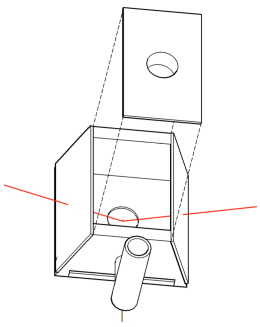

Figure 3.4: Electrochemical cell used for in-situ ellipsometry experiments.

The system used to acquire the response of the sensors and iron electrodes embedded in the mortar samples was constituted by a CompactStat potentiostat (Ivium Technologies, Netherlands) coupled to a peripheral differential amplifier (PDA) with several channels for simultaneous measurements, as shown in Figure 3.5. In the case of acid attack study, a reservoir for the solution was attached to the top (non-isolated face) of the mortar sample, while in the chloride penetration study, the mortar

sample itself was immersed in the chloride solution, as can be seen by Figure 3.5 b) and a), respectively.

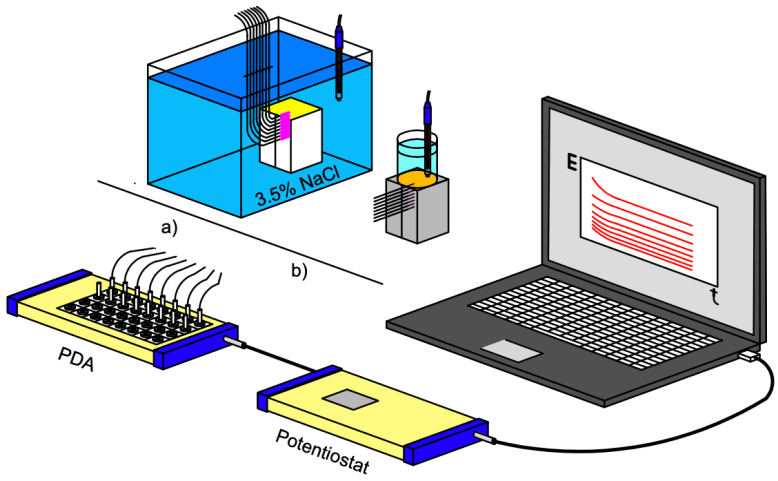

Figure 3.5: Illustration of the system used to acquire the response of the sensors set embedded in mortar sample.

EIS measurements on iron electrodes were performed using a Gamry Reference 600 equipment, with a 10 mV *rms* potential perturbance, at OCP, in frequency range from 10^5 to 10^{-3} Hz, with 7 points per decade with logarithmic distribution. A saturated calomel electrode was used as reference and a platinum wire was the counter electrode.
The modified electrodes were analysed by scanning electron microscopy (Hitachi SU-70) and EDS (Bruker Nano GmbH Berlin, Germany with a primary energy of 15 keV).
The powders of the mortar samples and the debris from the acid attack study were analysed by XRD using a diffractometer Panalytical (Almelo, Netherlands), model X'Pert PRO with a copper tube.

CHAPTER 4 Chloride sensors

In this chapter sensors for the detection of chloride ions based on Ag/AgCl and lucigenin were developed. In the case of Ag/AgCl electrodes, the influence of electrodeposition parameters on the potentiometric response for the detection of chlorides was studied. The films growth was accomplished through chronoamperometry, chronopotentiometry and cyclic voltammetry. In addition to electrochemical characterization, the modified electrodes were also analysed by SEM. Finally, the potentiometric response of lucigenin immobilized directly on a stainless steel substrate through cyclic voltammetry was studied.

4.1. Silver/Silver chloride

The synthesis of Ag/AgCl electrodes was performed using electrochemical techniques such as cyclic voltammetry, chronoamperometry and chronopotentiometry and optimized according to their potentiometric response for the detection of chlorides.
Before starting the electrodeposition, it was necessary to investigate the electrochemical system — substrate and electrolyte — through cyclic voltammetry in order to determine the working potential window, the redox potentials and current densities. The voltammogram of the electrochemical response of silver in an aqueous solution of HCl 0.1 M with a scan rate of 50 mV/s is represented in Figure 4.1. The scan started in the cathodic limit and evolved in the anodic direction.

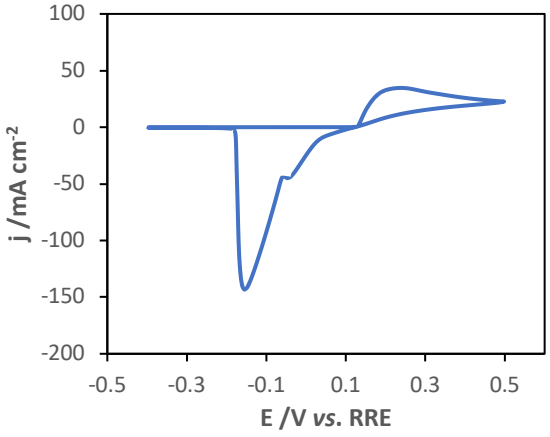

Figure 4.1: Voltammogram of the electrochemical response of silver in an aqueous solution of 0.1 M HCl with a scan rate of 50 mV s^{-1}.

The potentiodynamic response of the modified electrode presents well-defined redox peaks, as shown in Figure 4.1. The anodic peak at 238 mV *vs*. RRE is related to the electro-oxidation of silver, which will lead to the formation of silver chloride. The cathodic peak at -154 mV *vs.* RRE corresponds to the electro-reduction of silver chloride [112].

4.1.1. Galvanostatic synthesis

The potentiodynamic and galvanostatic synthesis of Ag/AgCl films were performed applying a set of experiments according to the Taguchi method in order to verify the correlation between parameters that can influence films growth and the quality factors of the sensors. For the galvanostatic growth, a Taguchi L_9 orthogonal array was applied in order to study the effects of current density, time of growth and concentration of electrolyte on the response of the samples as potentiometric chloride sensors. These factors were studied at three levels. The values for the selected levels for each factor were determined based on the literature review and previous experiments. Table 4.1 shows the chosen combination of the factors and levels. It also presents the growth charge for each experiment.

Table 4.1: L_9 orthogonal array of experiments with the parameters of current density, time of growth and concentration of HCl.

Sample	j /mA cm^{-2}	t_{growth} /hours	[HCl] /M	Q_{growth} /mC
1	0.5	0.25	1.00	2.2608
2	0.5	1.00	0.10	9.0432
3	0.5	2.25	0.01	20.3472
4	1.0	0.25	0.10	4.5225
5	1.0	1.00	0.01	18.0900
6	1.0	2.25	1.00	40.7025
7	2.0	0.25	0.01	9.0450
8	2.0	1.00	1.00	36.1800
9	2.0	2.25	0.10	81.4050

Figure 4.2 shows the potential-time transients of Ag/AgCl growths with the different experimental parameters (current density, electrolyte concentration and time of growth), for the first 200 seconds. The kind of line represents the different concentrations of HCl (dashed line is 1 M, pointed line is 0.1 M, and full line is 0.01 M) and the colour represents the current density applied for electrodeposition (black is 0.5 mA cm^{-2}, red is 1 mA cm^{-2}, and blue is 2 mA cm^{-2}).

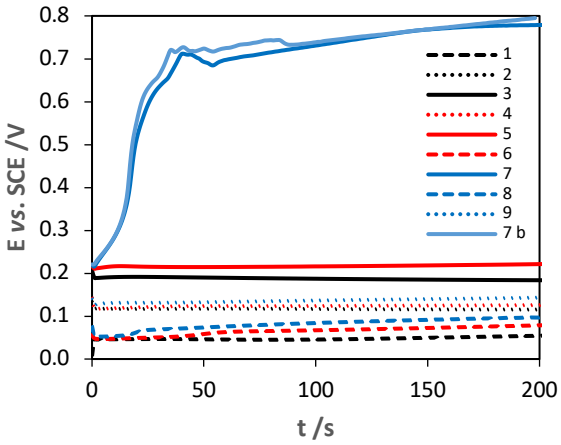

Figure 4.2: Potential-time transients for the different growth parameters. The kind of line represents the different concentrations of HCl (dashed line is 1 M, pointed line is 0.1 M, and full line is 0.01 M) and the colour represents the current density applied for electrodeposition (black is 0.5 mA/cm^2, red is 1 mA/cm^2, and blue is 2 mA/cm^2).

As it can be seen in Figure 4.2, for each level of concentration, as the applied current density gets higher, the measured potential increases and the beginning of nucleation and subsequent formation of the first monolayer become faster. The different levels of HCl concentration show a near Nernstian

increase of potential (59 mV). The growth transient of sample 7 presents a behaviour completely different from all of the other samples. Considering the possibility of error within this experiment, the growth was repeated (sample 7 b) using another silver electrode but in the same conditions. A similar transient was obtained, suggesting a completely different growth mechanism in these particular conditions. The sudden increase in potential may have been caused by the lower ionic conductivity combined with the higher current pulse applied, which required a greater deviation from the equilibrium potential in order to enable the reaction rate associated with the applied pulse.

Figure 4.3 a) that presents the open circuit potentials for different chloride concentration of sample 7, shows a typical potential response of an Ag/AgCl electrode to step variation of chloride concentration of an order of magnitude between 1 M and 10^{-6} M. As can be seen, the response time is almost immediate (a few seconds). The calibration curves of each electrode are represented in Figure 4.3 b).

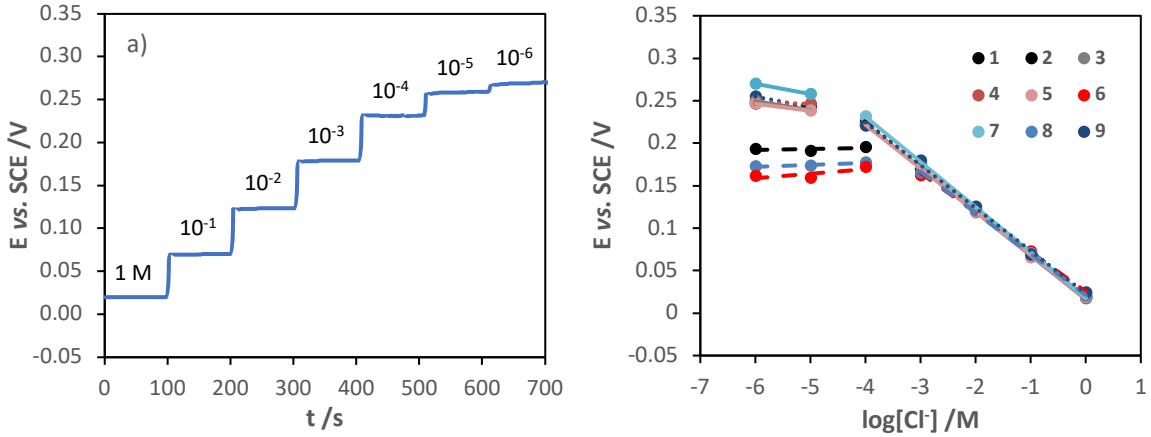

Figure 4.3: Open circuit potentials of sample 7 for different chloride concentrations (a) and calibration curves of different modified electrodes (b).

Clearly, it is possible to identify two different linear regions: one for samples 1, 6 and 8 and another for the other samples. The three films grown in 1 M HCl (1, 6 and 8) presented a linear region from 1 to 10^{-3} M. In the case of the other electrodes (2, 3, 4, 5, 7 and 9), the calibration curve was extended to 10^{-4} M and for lower values it presented a less inclined curve. This can be related to a secondary reaction that is only felt for very low concentrations of chlorides. However, to prove this behaviour it would be necessary to test more points of concentration, such as between 10^{-5} and 10^{-4} M and below 10^{-6} M.

The results of the quality parameters of each sample (slope, detection limit and correlation coefficient) are summarized in Table 4.2.

Table 4.2: Quality parameters (slope, lower limit of detection and correlation coefficient) of each sample.

Sample	Slope /mV	LLOD /10^{-5} M	R^2
1	-50.404	38.1	0.99980
2	-51.924	4.83	0.99970
3	-51.468	4.76	0.99917
4	-51.468	3.48	0.99951
5	-51.012	4.77	0.99892
6	-46.527	134	0.99740
7	-53.141	3.14	0.99980
8	-48.503	75.5	0.99908
9	-50.328	4.34	0.99711

The sensors that were grown in 1 M HCl (1, 6 and 8) present the worst quality parameters, with lower slope and higher limit of chloride detection. In the case of the films grown in lower HCl concentrations, it can be seen that for 0.1 M the best result is for the lowest current applied (sample 4) and for 0.01 M the best result is for the highest pulse applied (sample 7). This suggests a compromise between the concentration of HCl and the density of current used in the electrodeposition. Clearly, the sensor 7 presents the best quality parameters among all the electrodes. Figures 4.4 shows the morphology of the different modified electrodes. SEM images can be associated to the final stages of AgCl growth as described in literature [112,113]. The growth begins with the formation of rounded nuclei until the first layer is complete. For initial growth stage, the ionic transport between the dissolving silver electrode and the electrolyte is realized through the spaces between AgCl particles. As the film grows and the spaces between the first nuclei get covered, micro-channels (as shown in Figure 4.5) are formed through AgCl to allow ionic transport. Posteriorly, small segments are formed interconnecting the clusters of nuclei, as can be seen in the image of sample 1 in Figure 4.4. Finally, for longer times of growth, these segments will lead to the formation of a matrix of plates (as evidenced in the images of samples 6, 8 and 9).

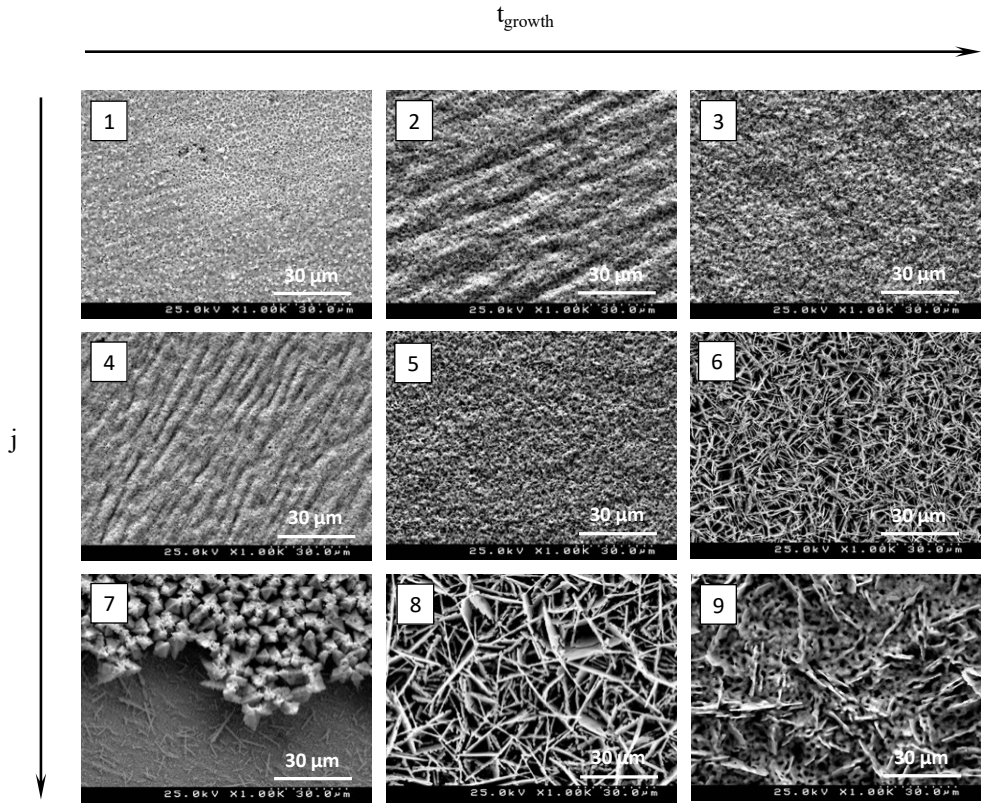

Figure 4.4: SEM images of galvanostatically grown films of Ag/AgCl. Numbers correspond to samples in Table 4.1.

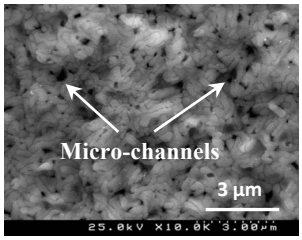

Figure 4.5: SEM image of sample 3 showing the micro-channels formed during synthesis to allow ionic transport.

The sample 7 has a completely different structure comparing to the other samples. It presents a pyramidal crystal shape structure that appears to be growing from the periphery of the electrode — where more defects exist — to the centre. However, it would be required more experiments in order to understand this mechanism of nucleation, such as, SEM images at the different stages of growth in these conditions and XRD analysis for determination of atomic and molecular structure of the film.

The relative porosity of each sample, for the two ampliations used (1000 and 5000 times), is presented in Table 4.3. The samples 6, 8 and 9, which had the highest electrodeposition charges (40.7, 36.18 and 81.41 mC, respectively), present the highest relative porosity.

Table 4.3: Porosity of each sample for different magnifications (1000 and 5000 times)

Sample	Porosity /%	Porosity /%
1	2.2430	2.6930
2	5.7790	6.6920
3	6.5370	5.3180
4	1.7720	2.5280
5	11.971	12.403
6	23.706	31.434
7	13.806	12.801
8	33.512	42.131
9	13.790	14.137

Table 4.4 presents the correlation coefficients between growth parameters (current density, time of growth and HCl concentration) and quality factors (detection limit, slope and porosity). In the case of detection limit, it has a strong correlation factor (> 0.8) with the HCl concentration. The decrease of HCl concentration leads to a lower chloride detection limit. The slope is mainly affected by the electrolyte concentration and less by the time of growth. The increase of electrodeposition time and HCl concentration leads to sub-Nernstian slopes (smaller than 59 mV). The correlation coefficients between growth factors and slope are negative because Ag/AgCl electrodes present a sub-Nernstian response, and this quality factor is better (higher and closer to Nernstian slope) for smaller values of HCl concentration and time of growth.

Lastly, the porosity presents a similar correlation coefficient with the current density and the electrolyte concentration. As expected, the increase of current density and HCl concentration promotes the formation of more porous surfaces. As the current applied increases, the rate of reaction also increases and consequently the ad-ions will not have enough time to diffuse on the surface until finding the site thermodynamically more stable and, therefore, the electrodeposition will evolve in a more disordered way [255].

Table 4.4: Correlation coefficients between the growth parameters (current density, time of growth and HCl concentration) and quality factors (lower limit of detection, calibration curve slope, and porosity of film surfaces).

	j	t_{growth}	[HCl]
LLOD	0.056	0.310	0.848
Slope	-0.069	-0.483	-0.792
Porosity	0.555	0.298	0.595

The high correlation with HCl concentration is caused by the highest value of concentration (1 M) that leads to the worst results for quality parameters — less Nernstian slope and higher limit of chloride detection — and, therefore, this value should be discarded in future works.

4.1.2. Potentiodynamic synthesis

For the potentiodynamic synthesis, a Taguchi L_9 orthogonal array was also applied in order to study the effect of number of cycles, scan rate and concentration of electrolyte on the response of the modified electrodes as potentiometric chloride sensors. These factors were studied at three levels. Table 4.5 shows the chosen combination of the factors and levels. The electrolyte concentration of 1 M that led to the worst potentiometric response of the galvanostatically grown films was discarded for this synthesis.

Table 4.5: L9 orthogonal array of experiments. The studied experimental parameters were number of cycles, scan rate and electrolyte concentration).

Sample	N° cycles	ν /mV s^{-1}	[HCl] /M
1	10	25	0.10
2	10	50	0.05
3	10	75	0.01
4	20	25	0.05
5	20	50	0.01
6	20	75	0.10
7	30	25	0.01
8	30	50	0.10
9	30	75	0.05

Cyclic voltammograms of Ag/AgCl film synthesis, for different experimental conditions, are represented in Figure 4.6. The synthesis started from the cathodic limit in anodic direction.

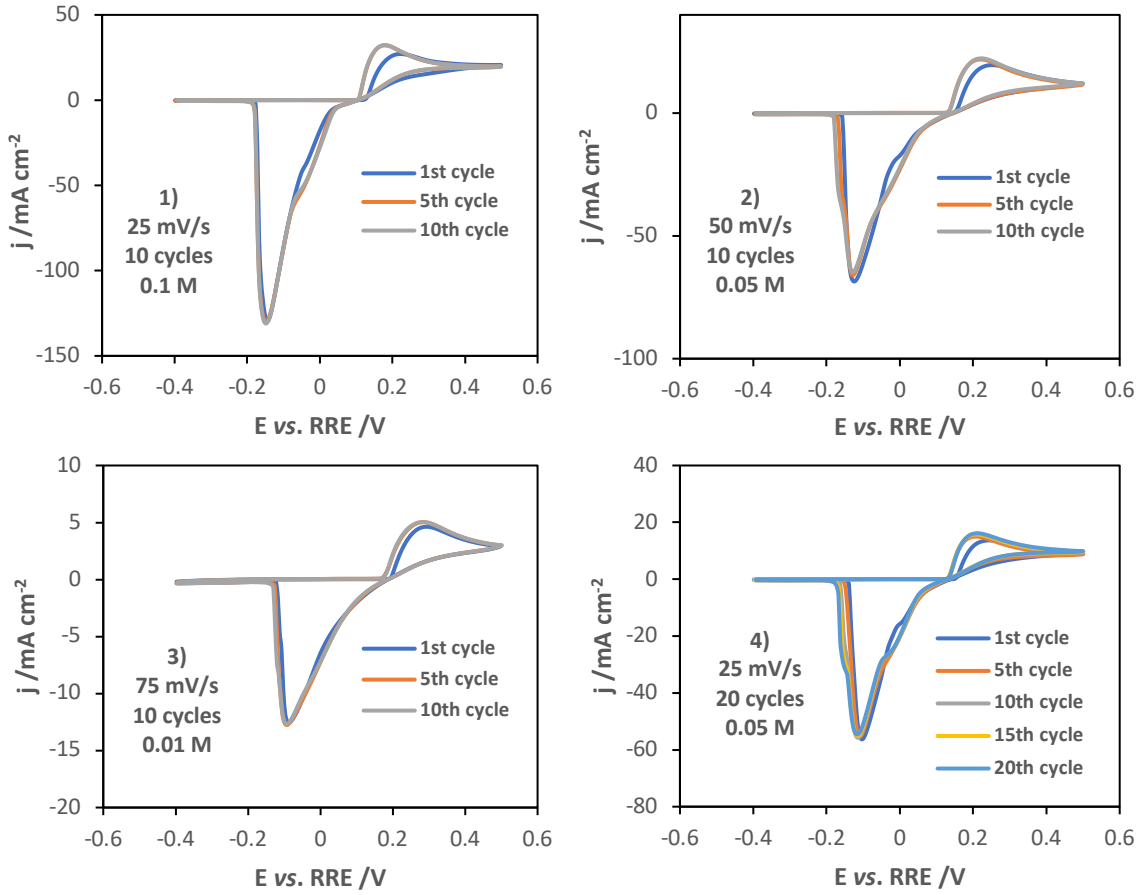

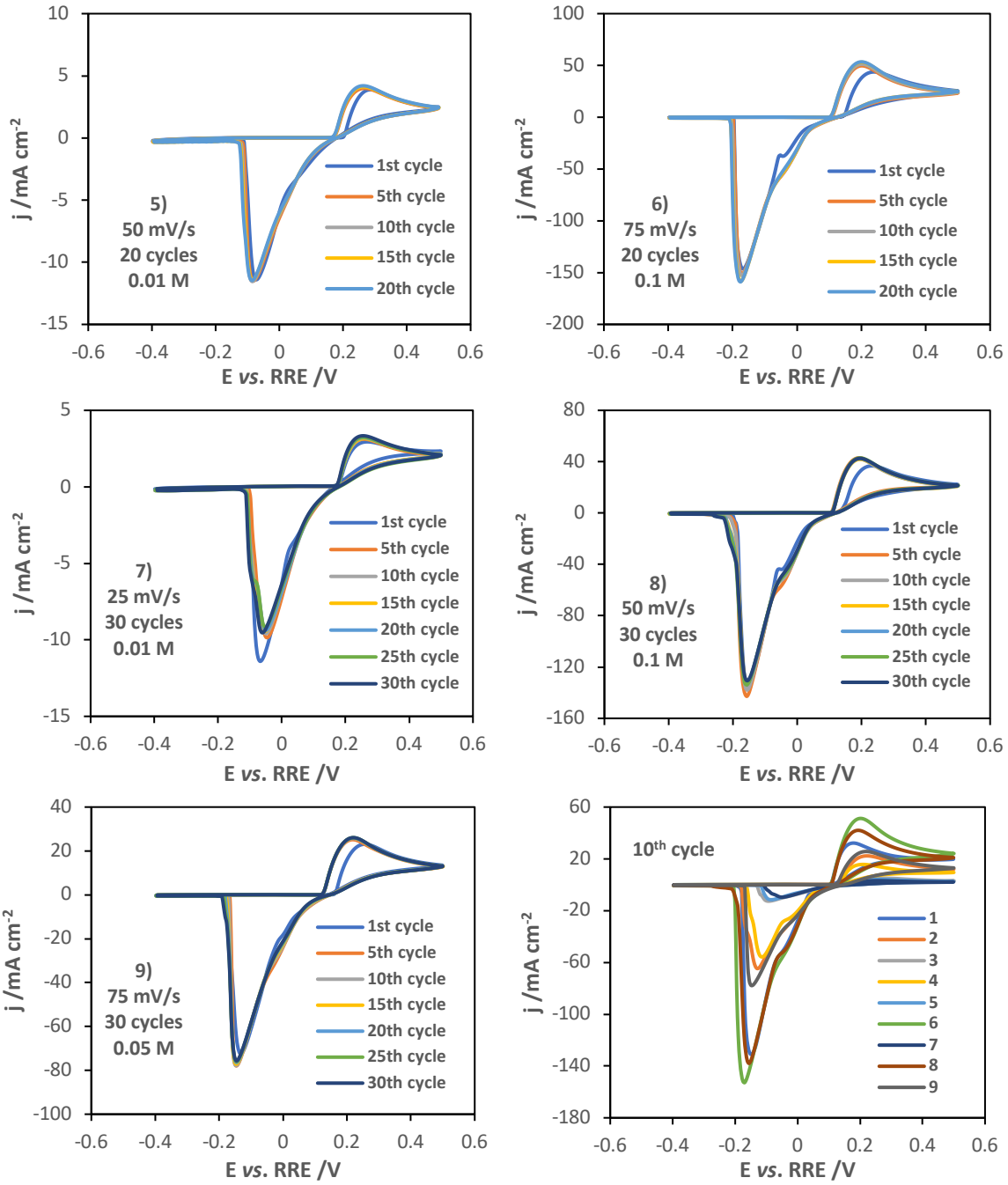

Figure 4.6: Cyclic voltammograms of each growth and the 10th cycle voltammograms of all synthesis.

As can be seen from the growth voltammograms, the anodic peak of the first cycle occurs at more anodic potentials with a smaller current density, which is due to the absence of silver ions in the first cycle needing higher potential values to oxidize the substrate and form a new phase of AgCl above it. As the number of cycles increase, the current density of the anodic peak also increases due to the continuous growth of the film, and its potential peak deviated slightly to more anodic values as a result of the highest number of AgCl nuclei on the substrate, which hinders the oxidation of silver due to its smaller exposed area. The cathodic peak current density decreases, and its potential moves to more negative values with successive cycles, showing a more resistive phase being formed and an increased difficulty to electro-reduce silver chloride. Table 4.6 presents the redox values — potentials

and current densities peaks — for all the potentiodynamic growths performed, for the different parameters under study.

Table 4.6: Redox values of the 2nd cycle for different potentiodynamic growths of Ag/AgCl.

Sample	$E_{p,a}$ /V_{RRE}	$j_{p,a}$ /mA cm^{-2}	$E_{p,c}$ /V_{RRE}	$j_{p,c}$ /mA cm^{-2}	$E_{p,a}+\|E_{p,c}\|$ /V_{RRE}
1	0.178	31.413	-0.144	-129.075	0.322
2	0.222	21.644	-0.131	-67.500	0.353
3	0.284	4.9950	-0.089	-12.646	0.373
4	0.206	14.984	-0.111	-56.014	0.317
5	0.268	3.8530	-0.077	-11.074	0.345
6	0.207	49.159	-0.172	-150.203	0.379
7	0.259	3.0330	-0.051	-10.242	0.310
8	0.194	41.825	-0.158	-139.518	0.352
9	0.228	23.963	-0.144	-76.109	0.372

As displayed in table 4.6, the increase of electrolyte concentration leads to higher anodic and cathodic current densities and promotes a shift of the redox peak potentials to lower values. The increase of current densities is explained by the higher conductivity of the medium and by the higher production of electroactive species leading to a faster formation and subsequent precipitation of AgCl nuclei. The shift of redox potentials is due to higher electrolyte concentration, which promotes an oxidation at lower potentials. The higher deposition during anodic process leads to a more resistive film, which requires more energy to be reduced, and consequently the cathodic peak shifts to lower potentials. The increase of scan rate promotes an increase of the separation between the anodic and cathodic peaks, which is characteristic of an irreversible system where the rate of electron transfer is not sufficient to maintain the Nernstian equilibrium at the electrode surface. The correlation between growth parameters under study and the redox parameters from growth voltammograms were analysed by the Taguchi method, and the obtained correlation coefficients are shown in Table 4.7.

Table 4.7: Correlation coefficients between the growth parameters (sweep rate and electrolyte concentration) and redox parameters.

	Scan rate	[HCl]
$E_{p,a}$	0.306	-0.919
$j_{p,a}$	0.247	0.953
$E_{p,c}$	0.353	-0.905
$j_{p,c}$	0.112	0.991
$E_{p,a}+\|E_{p,c}\|$	0.983	0.139

The characterization of the modified electrodes as potentiometric sensors for chloride detection was done in the same way as for galvanostatically grown films. Figure 4.7 a) presents the potentiometric characterization of sample 1, for different chloride concentrations, which is representative of all modified electrodes. It is possible to see that for the chloride concentrations of 10^{-4} and 10^{-5} the potential starts to decrease, which is possibly due to the dissolution of AgCl. This hypothetic conclusion should be confirmed by an analytical method in order to determine if there is appearance of silver oxide in the electrode after its immersion.

The calibration curves of each modified electrode are represented in Figure 4.7 b). The samples 3, 5 and 7, which were grown in 0.01 M HCl, presented an open circuit potential shift to lower values and lower slopes. The other samples presented a very similar behaviour with coincident and slightly sub-Nernstian slopes. All the modified electrodes had a small decrease of OCP for the 10^{-4} M NaCl solution (as observed in Figure 4.7 a) and, therefore, this point was not included in the calibration

curve. For the less concentrated solution of 10^{-5} M, the OCP decreased abruptly tending to the value obtained in solution of 10^{-4} M NaCl. This behaviour can be related to the film dissolution in low concentrated solutions, which will increase the chloride concentration in medium and consequently shifts the electrochemical equilibrium to lower potential values.

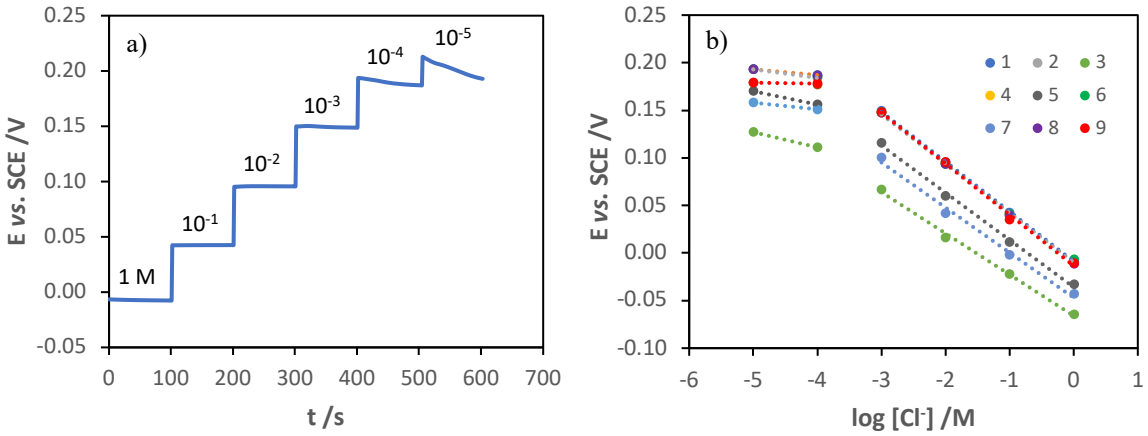

Figure 4.7: Open circuit potentials of sample 1 for different chloride concentrations (left) and calibration curves of different modified electrodes.

The results of the quality parameters of each sample (slope, detection limit and correlation coefficient) are grouped in Table 4.8. The modified electrodes 3, 5 and 7, which were synthetized in 0.01 M HCl, had the worst quality parameters in terms of slope — below 50 mV/pH unit —, chloride detection limit and correlation coefficients. As happened for the galvanostatic growths, the concentration of electrolyte was the most significant parameter for the quality parameters of the sensors, but contrasting with the galvanostatic synthesis, here the films grown in the less concentrated solutions presented the worst results, which is also due to the fact that the concentration of 1 M was not considered for potentiodynamic synthesis.

Table 4.8: Quality parameters (slope, lower limit of detection and correlation coefficient) of each sample.

Sample	Slope /mV	LLOD /10^{-4} M	R^2
1	52.4	3.74	0.9998
2	51.8	3.74	0.9989
3	43.3	4.09	0.9968
4	52.4	3.58	0.9998
5	49.6	3.87	0.9972
6	51.8	3.74	0.9991
7	47.4	4.18	0.9929
8	52.9	3.75	0.9998
9	53.6	3.57	0.9975

The morphology of these films was analysed by SEM, which is shown in Figure 4.8. Clearly, the HCl concentration affects the surface coverage of the substrate. The higher HCl concentration (0.1 M) promoted the formation of more compact films, as evidenced by the images of the modified electrodes 1, 6 and 8. Thus, the potentiometric response of potentiodynamically synthesized Ag/AgCl electrodes seems to be correlated with the porosity of the films. The number of AgCl nuclei affects the interfacial area between silver and silver chloride, which in turn influences the electrochemical equilibrium — the films synthetized with higher and lower HCl concentrations presented, respectively, the best and the worst potentiometric response for chloride detection. The higher

number of silver chloride nuclei present in the films grown with higher electrolyte concentration is also evidenced by the higher redox peaks during their synthesis (Figure 4.6).

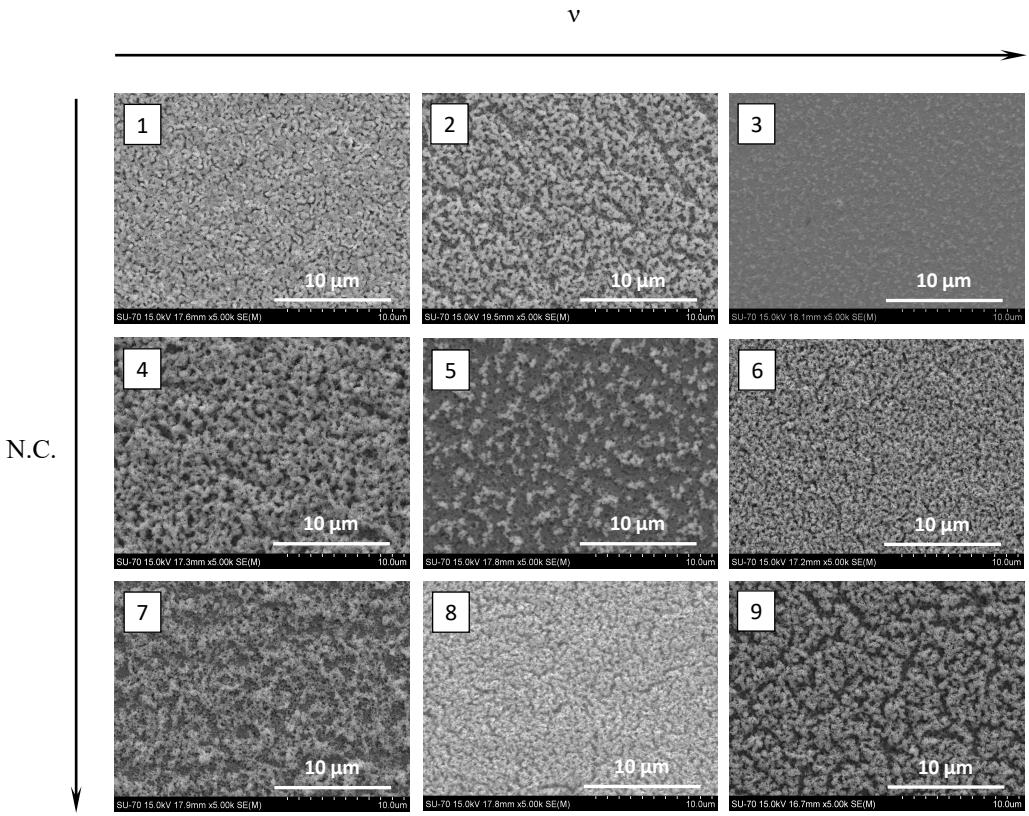

Figure 4.8: SEM images of different potentiodynamically grown films of Ag/AgCl. Numbers correspond to samples in Table 4.5.

Table 4.9 summarizes the correlation coefficients between growth parameters (number of cycles, sweep rate and HCl concentration) and quality factors (detection limit, slope and correlation coefficients). As previously concluded, the electrolyte concentration was the most important growth parameter affecting the potentiometric response of the Ag/AgCl sensors.

Table 4.9: Correlation coefficients between the growth parameters (number of cycles, sweep rate and HCl concentration) and quality parameters (lower limit of detection, slope and correlation coefficient).

	Nº of cycles	**Scan rate**	**[HCl]**
LLOD	0.048	0.069	0.588
Slope	0.278	0.152	0.700
R^2	0.342	0.058	0.743

4.1.3. Potentiostatic synthesis

Finally, a preliminary study of the growth of Ag/AgCl films by chronoamperometry was performed for different applied potentials based on the value of the anodic peak of the initial voltammogram (Figure 4.1). The synthesis was done in aqueous 0.1 M HCl applying a pulse of 150, 200 or 250 mV (*vs*. RRE), for 3600 seconds. The current-time transients are shown in Figure 4.9 a). Initially the

current density decreased abruptly with time due to the formation of the double layer and the formation of the first AgCl nuclei. Then, the current continued decreasing at a slower pace, which was due to the formation of a resistive AgCl film that hampered the penetration of electrolyte through the film leading to a slower conversion rate [105]. The calibration curves of potentiostatically modified electrodes for the different applied potential pulses are represented in Figure 4.9 b).

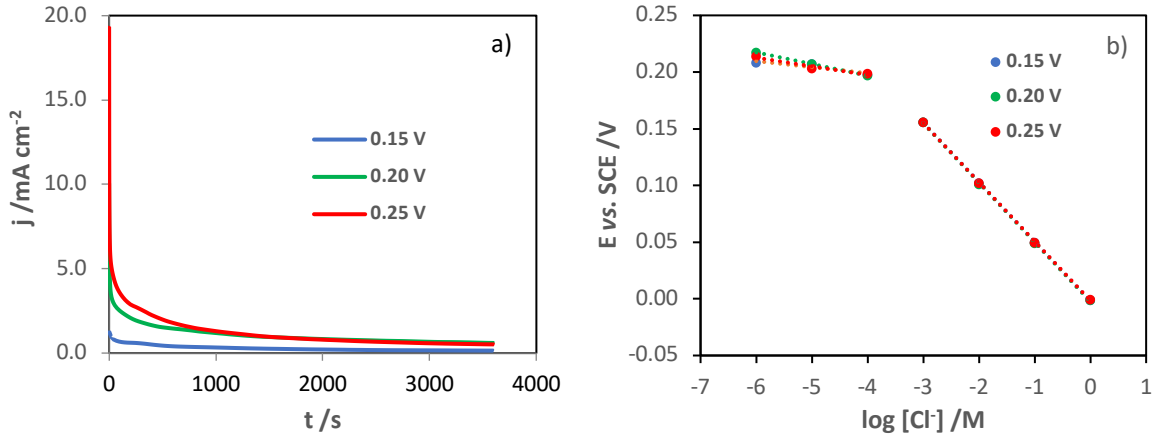

Figure 4.9: Current density-time transient of Ag/AgCl growths with different potential pulses applied for 3600 seconds (a) and calibration curves of the modified electrodes (b).

The calibration curves of the films grown potentiostatically shown in Figure 4.9 b) are almost coincident, and it can be concluded that the different oxidation potentials did not affect the potentiometric response of Ag/AgCl sensors for chloride detection. These results are very similar to the best results of the modified electrodes obtained by cyclic voltammetry.
Table 4.10 summarizes the quality parameters of these sensors, where it is possible to observe the similarity of values, corroborating the conclusion that the applied potential does not affect neither the slope nor the detection limit of the Ag/AgCl films.

Table 4.10: Quality parameters (slope, lower limit of detection and correlation coefficient) of each sensor of Ag/AgCl grown potentiostatically.

V_g /V *vs.* RRE	Slope /mV pH^{-1}	LLOD /10^{-4} M	R^2
0.15	-52.46	3.81	0.9998
0.20	-52.46	3.80	0.9996
0.25	-52.23	3.83	0.9997

4.1.4. Stability study

The aging of galvanostatically grown Ag/AgCl sensors due to contact with different environments for a long period, namely saturated $Ca(OH)_2$, buffer solutions with pH 13 and pH 2, distilled water and air, was studied through the evolution of their potentiometric response, which is represented in Figure 4.10. The media with high pH were intended to simulate the pore solution of cementitious materials, while air and distilled water are two possible environments to store these sensors.
After 75 days, only the potentiometric response of the sensor in contact with the buffer solution of pH 13 was clearly affected, which, from the 30th day, showed a decrease in the slope and a shift in the calibration curve to more negative potentials. The degradation of the Ag/AgCl electrodes can be

explained by the conversion of AgCl into Ag_2O or by its dissolution, when in contact with an environment with high pH and low chloride content, which decreases the available interfacial area for the electrochemical equilibrium.

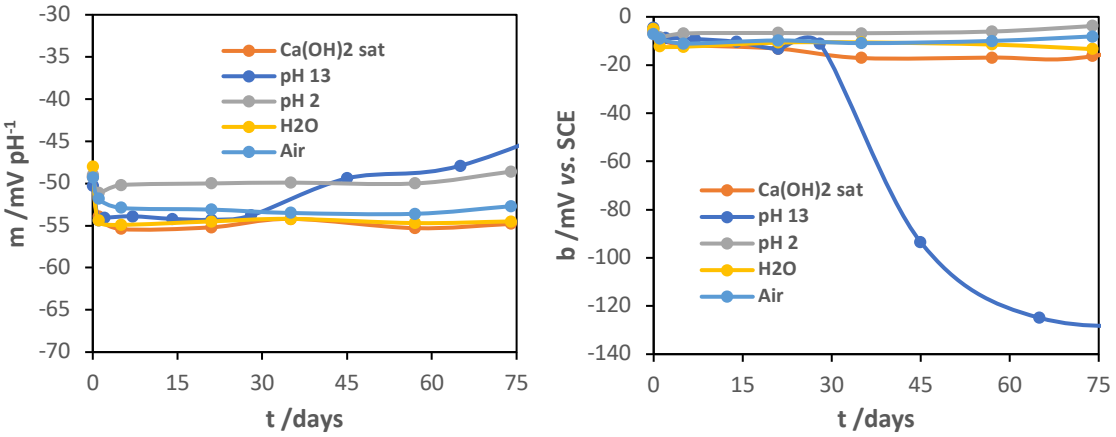

Figure 4.10: Evolution of calibration curve parameters (slope and E-axis intersection) with time in contact with different environments ($Ca(OH)_2$ saturated, pH 13 and 2, distilled water and air).

The Ag/AgCl sensor in contact with $Ca(OH)_2$ saturated was also analyzed by SEM and EDS after 75 days of immersion. Figure 4.11 (left) shows the morphology of the modified electrode immediately after its synthesis (a) and after immersion in the simulated pore solution (b). The immersion in $Ca(OH)_2$ saturated media led to the dissolution of the silver chloride plates and the formation of cracks on the AgCl inner layer. The cracks may have been caused to maintain ionic transport to the silver. The formation of Ag_2O may have blocked the micro-channels of the AgCl layer. A grey-black deposit was formed around the electrode and the immersion solution assumed a different colour (from transparent to brownish). The elemental analysis by EDS, shown in Figure 4.11 (right), shows a decrease in the chloride content and the appearance of oxygen in the electrode after immersion, which is in accordance with the partial dissolution of the silver chloride film and the formation of silver oxides, respectively.

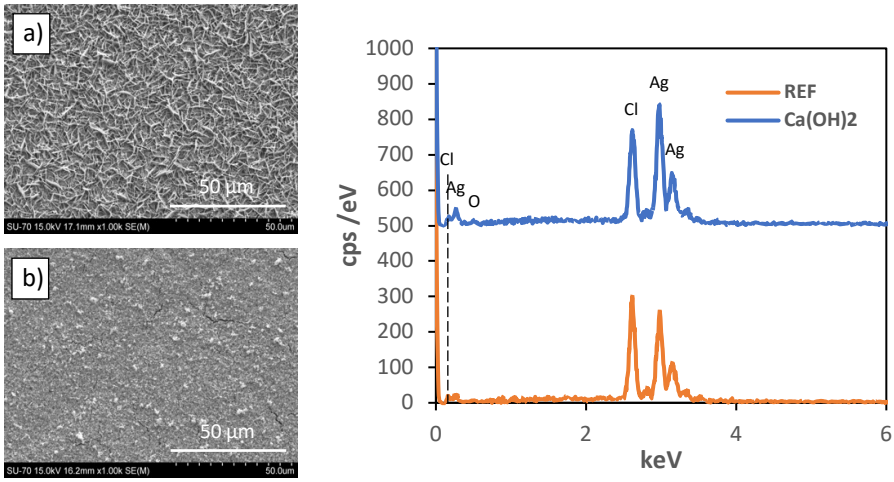

Figure 4.11: SEM images and EDS analysis of Ag/AgCl electrode before (a) and after 75 days of immersion in $Ca(OH)_2$ saturated solution (b).

4.2. Other chloride sensors

Besides Ag/AgCl, other materials were tested for chloride sensor. Firstly, an electronically conducting polymer — Poly(3,4-ethylenedioxythiophene), PEDOT — doped with chloride [101]. The synthesis was done by a galvanostatic pulse of 0.2 mA/cm^2, for a synthesis charge of 10 mC, in an aqueous solution containing 0.01 M EDOT and 0.1 M KCl as the supporting electrolyte. The potential-time transient is represented in Figure 4.12.

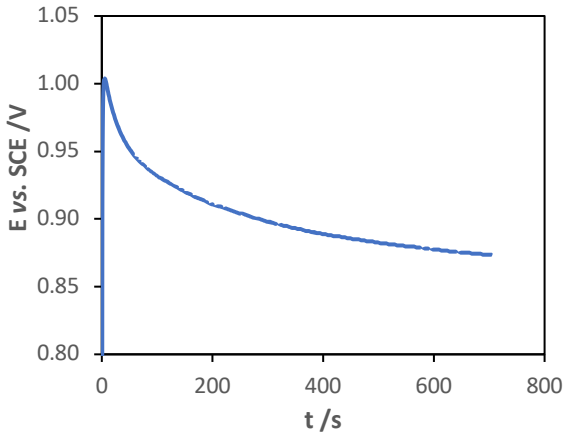

Figure 4.12: Chronoamperogram of PEDOT growth with a pulse of 0.2 mA cm^{-2} and maximum charge of 10 mC.

However, this modified electrode presented a bad behaviour as a chloride sensor. The synthesis, which was replicated from the literature, was not a good approach knowing that the monomer used — EDOT — is insoluble in an aqueous solvent. Thus, it was necessary to agitate the solution in order to create a kind of emulsion with small droplets of monomer.

Finally, a new material was also tested as an electrochemical sensor for chloride detection — Lucigenin. This molecule has been widely studied as an active molecule for optical sensors for chloride detection. The electrode modification was done through direct immobilization of this molecule onto a stainless steel substrate by cyclic voltammetry. The potentiodynamic growth of Lucigenin (0.1 mM) in an aqueous solution with 0.1 M $LiClO_4$ as supporting electrolyte with a scan rate of 50 mV/s, for 60 cycles, is shown in Figure 4.13.

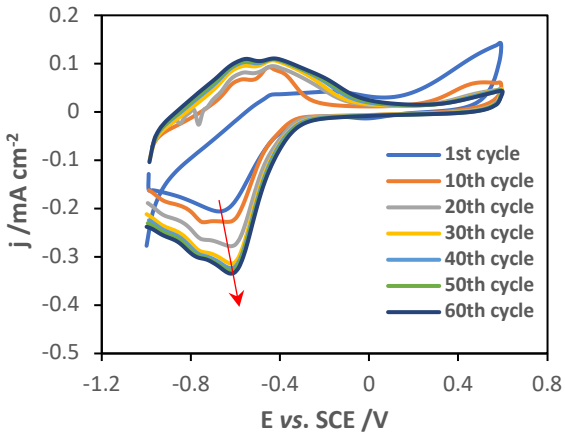

Figure 4.13: Cyclic voltammograms of Lucigenin direct immobilization on a stainless steel electrode with a scan rate of 50 mV/s for 60 cycles.

Figure 4.14 presents the potentiometric characterization of the modified electrode, for different chloride concentrations (1 to 10^{-4} M), through open circuit potential measurements.

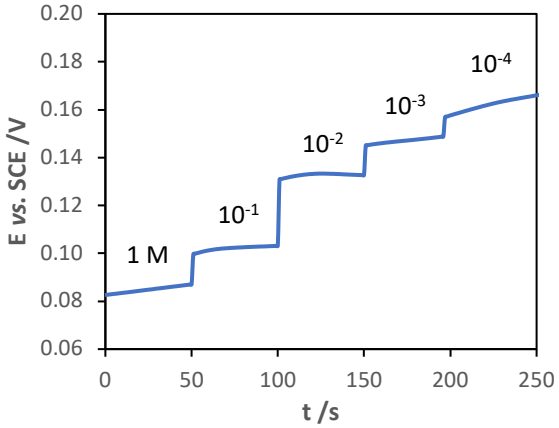

Figure 4.14: Potentiometric characterization of the modified electrode for different chloride concentrations.

As evidenced by the characterization, this sensor presented a sub-Nernstian slope — about 20 mV— showing poor sensibility and slow time of response. Besides that, the modified electrode did not present reversibility when the concentration of chlorides was reversed to higher values.

4.3. Conclusions

Electrodes sensitive to chloride ion were based on two materials: Ag/AgCl and lucigenin. In the case of Ag/AgCl electrodes, the electrochemical synthesis was made by galvanostatic, potentiostatic and cyclic voltammetry. For each regime, the influence of experimental parameters on the electrode response was analysed.

It became clear that the potentiometric response — slope and limit of detection — is strongly influenced by the concentration of HCl, independently of the electrochemical method used to produce the sensor. In galvanostatic synthesis, HCl concentrations equal or greater than 1 M must be avoided. For both electrochemical synthesis regimes, the 0.1 M HCl concentration appears to be the most suitable value to obtain the best potentiometric response.

In the case of galvanostatic synthesis, the increase in the anodic polarization time and in the concentration of HCl promotes the formation of thicker films, which hinder the ionic transport to the silver/silver chloride interfacial zone — where the electrochemical equilibrium takes place — and, as such, leads to a sub-Nernstian slope. The porosity of modified electrodes is increased by the increasing current pulse applied and electrolyte concentration.

For the case of potentiodynamic growth, HCl concentration was the only experimental parameter that affected the potentiometric response, in terms of slope and limit of detection, of the modified electrodes. Decreasing electrolyte concentration leads to the formation of more porous films.

In the case of potentiostatic synthesis, the applied potential pulse (within the range of silver oxidation peak) does not affect the potentiometric response of the sensors.

The storage of galvanostatic Ag/AgCl films in air, distilled water, and pH 2 or 13 was studied. After 75 days, all sensors presented still a good potentiometric behaviour, except for the sensor immersed

in the pH 13 buffer solution, which showed signs of degradation, evidenced by the shift of the calibration curve to more negative potentials.

The development of sensors to determine the chloride content was completed with the potentiodynamic growth of lucigenin on stainless steel and the potentiometric response of the resulting electrode. Direct mobilization of lucigenin was successfully achieved, but the modified electrode presented a bad potentiometric response, with poor sensibility and slow time of response.

CHAPTER 5 pH sensors

This chapter presents the study of electrochemical synthesis and characterization of several materials sensitive to pH: MnO_2, IrO_x, RuO_2/IrO_x and PPy. The synthesis of MnO_2 sensors was performed using cyclic voltammetry and chronoamperometry. Potentiostatic growths were further characterized by *in-situ* ellipsometry. For the IrO_x sensors, an extensive study of their electrochemical growth was carried out using cyclic voltammetry and double pulse chronoamperometry. In addition, the effect of adding $RuCl_3$ to the growth solution on the potentiometric response of modified electrodes was studied, for the case of potentiodynamic synthesis. Finally, the growth of PPy films was performed through a potentiostatic regime. The modified electrodes were characterized electrochemically (potentiometric response and cyclic voltammogram) and by SEM.

5.1. Manganese dioxide

The initial synthesis of MnO_2 electrodes was based on literature, and the composition of growth electrolyte was an aqueous solution of 0.3 M $MnSO_4.H_2O$ with pH adjusted to 1.8 using concentrated sulfuric acid [122]. Figures 5.1 a) and b) present, respectively, the first cycle of the potentiodynamic behaviour of a stainless steel 316 L substrate in a 0.3 M $MnSO_4$ solution, for different scan rates (5, 10, 20, 50 or 100 mV/s), with normalized currents to the respective sweep rate, and for different anodic limits (1.1, 1.2 and 1.3 V *vs*. RRE) with a scan rate of 10 mV/s. Cyclic voltammograms with this substrate did not present the cross-over on the cathodic branch reported for other working electrodes, such as gold [165]. The anodic segments present two well-defined oxidation peaks related to the initial formation of MnOOH that subsequently is oxidized to MnO_2, as the electrode potential gets higher. The first reduction peak at 0.95 V *vs*. RRE is related to MnO_2 reduction to MnOOH and the reduction peak at 0.0 V *vs*. RRE is related to the reduction of Mn(III) species.

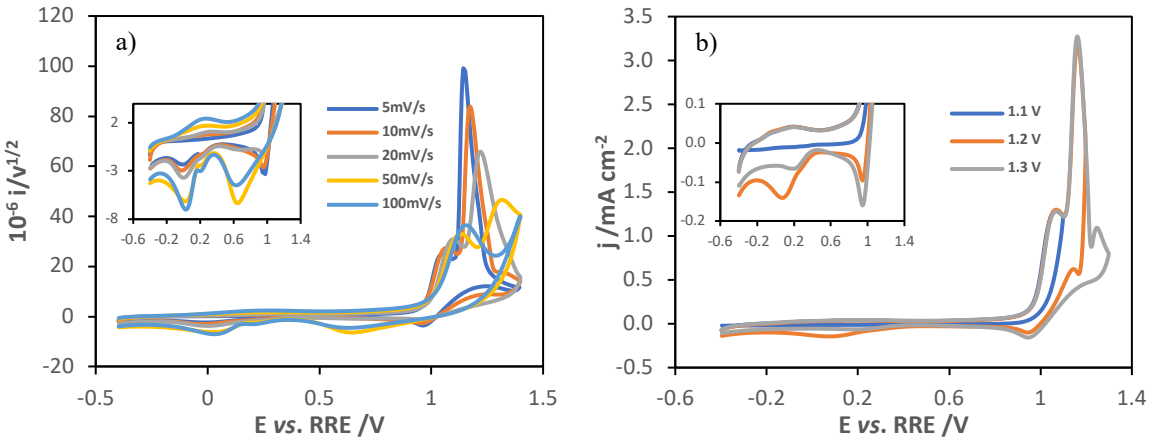

Figure 5.1: 1st cycle of potentiodynamic growth of MnO_2 on stainless steel for different scan rates (5,10,20,50 and 100 mV/s with the current normalized to the square root of the sweep rate) (a), and for different anodic limits with a scan rate of 10 mV/s (b).

However, all the films grown potentiodynamically, for different growth parameters — scan rate, anodic limit and cycle number —, presented poor adhesion to the substrate (stainless steel 316 L), evidenced by its delamination during the washing after characterization. To solve this problem, a pre-treatment based on Wood's Nickel Strike (WNS) was adopted to improve the film adhesion to substrate. This method is an intermediate strike, which is typically used on nickel based alloys and stainless steels, to produce a thin and adherent film of nickel that serves as a base for subsequent depositions [256]. The synthesis of this intermediate film was done by applying a current pulse of -0.855 mA, in an aqueous solution containing 1.85 M $NiCl_2$ and 3.9 M HCl, for 2 minutes. The potential-time transient of WNS is shown in Figure 5.2 (a). Initially, the potential increases rapidly, as the first Ni nuclei grow on the stainless steel substrate. Then, the potential stabilizes at -0.44 V *vs*. RRE in the metal deposition region [257]. After this pre-treatment, a film of MnO_2 was grown potentiodynamically with a scan rate of 50 mV/s, for 20 cycles, in the potential window between -0.4 and 1.4 *vs*. RRE. The voltammogram of the MnO_2 synthesis is displayed in the Figure 5.2 (b).

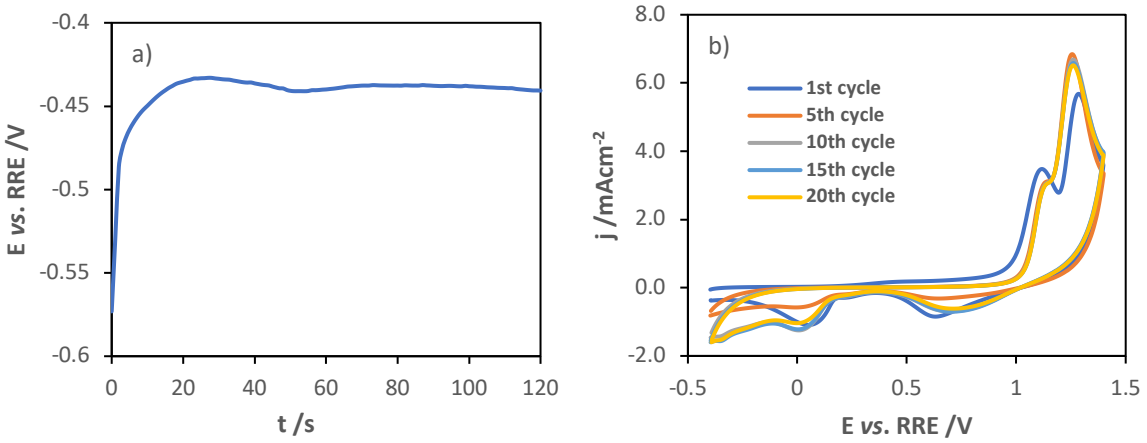

Figure 5.2: Potential-time transient of WNS pre-treatment on stainless steel substrate (a) and cyclic voltammograms of MnO_2 synthesis with a scan rate of 50 mV/s, for 20 cycles, after WNS pre-treatment (b).

The potentiometric characterization of the MnO_2 modified electrode is presented in Figure 5.3 a), and was performed by measuring its open circuit potential in different buffer solutions in the pH range between 12 and 4. The respective calibration curve is shown in Figure 5.3 b).

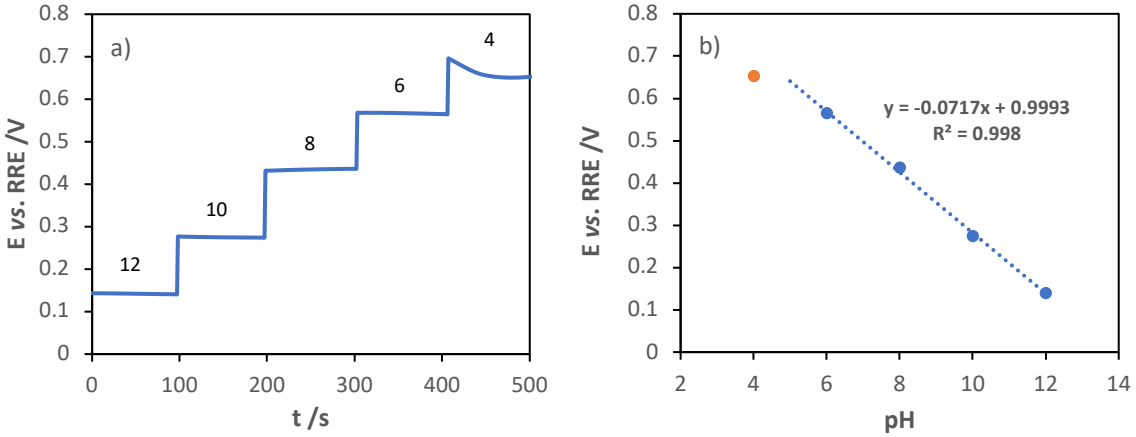

Figure 5.3: Potentiometric characterization of MnO_2 electrode grown on Ni base, for different pH buffer solutions (a) and the respective calibration curve (b).

The MnO_2 sensor exhibits a super-Nernstian slope of 71.7 mV/pH and an immediate response. The potentiometric response is stable in the pH range between 12 and 6. Media with pH<6 led to dissolution of the MnO_2 films, which was previously evidenced by the potential decrease in the pH 4 buffer solution. Figure 5.4 shows the aspect of two MnO_2 films synthetized in the same electrochemical conditions, with and without WNS pre-treatment. Clearly, the pre-treatment led to a different morphological structure of the grown film, which was more homogeneous and does not present defects. However, this method to improve stainless steel adhesion represents a large increase in the cost and time of MnO_2 sensors synthesis due to the high price of $NiCl_2$ and to an additional production step, respectively.

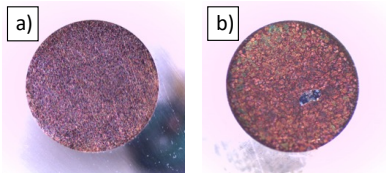

Figure 5.4: Visual inspection of MnO_2 films grown potentiodynamically with a scan rate of 50 mV/s for 20 cycles with (a) and without (b) WNS pre-treatment. Diameter of 3.175 mm.

Instead of applying an intermediate layer, the growth solution was changed for a neutral pH removing the sulfuric acid and adding $LiClO_4$ as the supporting electrolyte. Firstly, the potentiodynamic growth of MnO_2 was studied in this new medium. Figure 5.5 presents the first 5 cycles of the cyclic voltammogram of film synthesis in an aqueous solution containing 0.3 M $MnSO_4.H_2O$ and 0.1 M $LiClO_4$ within the potential window of -0.1 to 0.9 V *vs*. RRE, with a scan rate of 5 mV/s.

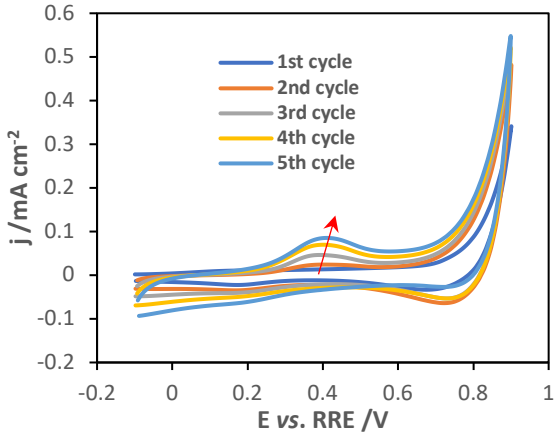

Figure 5.5: Cyclic voltammograms of MnO_2 growth with a scan rate of 5 mV/s for 5 cycles on stainless steel.

The voltammogram presents an anodic peak at 0.4 V *vs.* RRE that increased its current density and deviated in anodic direction with successive cycles, suggesting the growth of a film with increased resistivity. The adhesion of the film to the substrate was tested by mechanical exfoliation through the use of an adhesive tape, and it was observed a substantial improvement of its adhesion. The characterization of the modified electrode as a pH sensor was done by measuring the open circuit potential in different buffer solutions in the pH range between 13 and 8, which is represented in Figure 5.6. a). It started from pH 13 to 8 and then reversed until again pH 13. The respective calibration curve is shown in Figure 5.6 b). As revealed by the characterization graphs, the sensor response was fast and reversible. The slope is super-Nernstian — about 66 mV/pH unit — being characteristic of hydrated metal oxides. This new growth solution provided the synthesis of a MnO_2

film with a promising potentiometric response for pH determination in the alkaline region. In order to optimize the potentiometric response of this metal oxide, the influence of growth parameters, such as the scan rate, number of cycles and anodic limit was investigated.

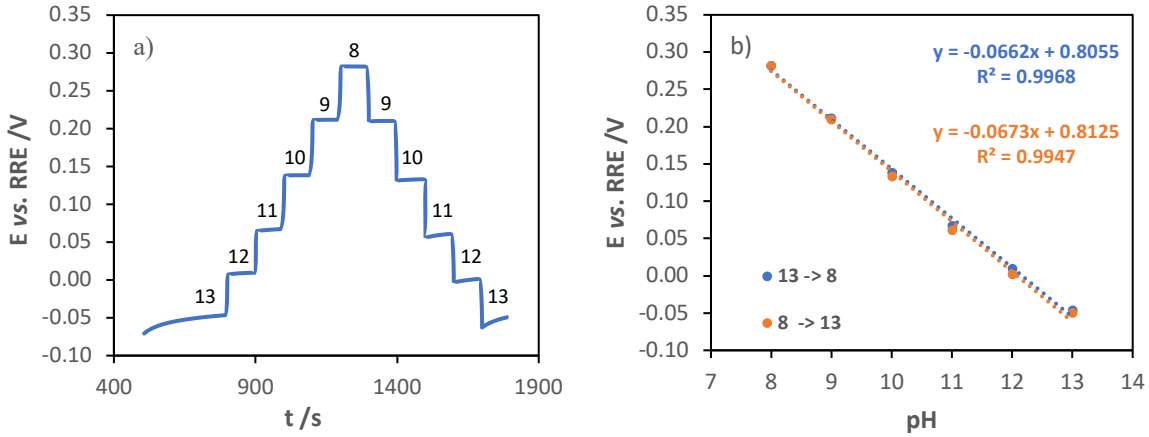

Figure 5.6: Potentiometric characterization (a) and calibration curve (b) of the potentiodynamically grown MnO_2 electrode with a scan rate of 5 mV/s for 5 cycles.

Increasing the anodic limit from 0.9 to 1.4 V *vs*. RRE led to a slow and irreversible response. On the other hand, increasing the number of cycles from 5 to 10, no differences were observed. Lastly, increasing the scan rate to 50 mV/s, for different number of cycles (5, 10 and 20), showed the best response for 20 cycles. Its potentiodynamic synthesis is shown in Figure 5.7.

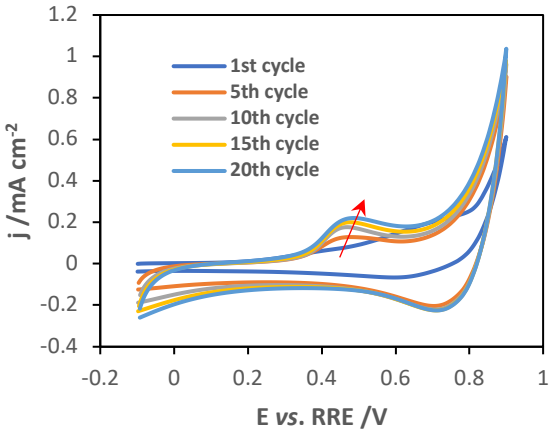

Figure 5.7: Cyclic voltammograms of MnO_2 growth with a scan rate of 50 mV/s for 20 cycles on stainless steel.

The characterization of the potentiometric response of the MnO_2 film grown potentiodynamically with a scan rate of 50 mV/s, for 20 cycles, is represented in Figure 5.8 a). It started from pH 13 to 9 and then reversed until again pH 13. The respective calibration curve, which is shown in Figure 5.8 b), presents a slope of about 61 mV/pH. The obtained results showed that the potentiometric response of the potentiodynamically grown MnO_2 sensors is mainly affected by the anodic limit and time of oxidation, which was possibly caused by the formation of different oxidation states with the successive cycles and subsequent oxidation time. The increasing scan rate may not allow the formed MnOOH to be completely oxidized to MnO_2 requiring more cycles. As such, it is pertinent to study the potentiostatic growth of MnO_2 films for different anodic potentials and charges of synthesis.

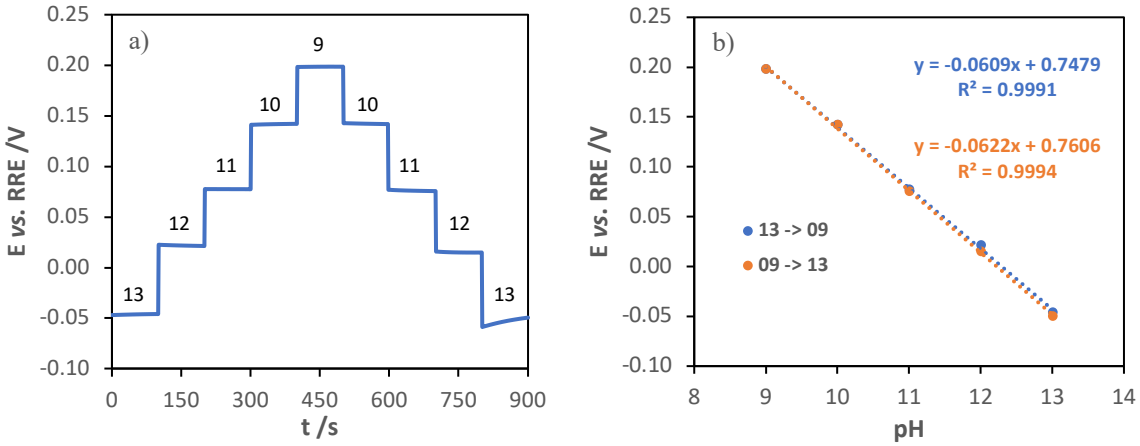

Figure 5.8: Potentiometric characterization (a) and calibration curve (b) of the potentiodynamically grown MnO_2 electrode with a scan rate of 50 mV/s, for 20 cycles.

The potential pulses to be studied for potentiostatic growth were based on the anodic peak of potentiodynamic synthesis of MnO_2. So, the potentiostatic synthesis for different applied potentials — 0.8, 0.9 and 1.0 V *vs*. RRE — and growth density charges — 36, 9 and 4 mC/cm^2 — were studied. Figure 5.9 presents the current density-time transient of the electrodeposition of MnO_2 with an applied potential of 0.8 V and a total charge density of 9 mC/cm^2. The obtained chronoamperogram is characteristic of the growth of a resistive phase. Initially, the current drops sharply due to the formation of double layer and oxidation of electroactive species in solution, and then stabilizes at a value in the metal oxide deposition region.

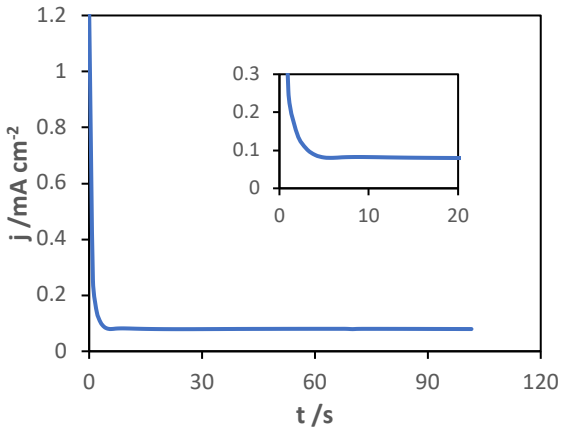

Figure 5.9: Chronoamperogram of MnO_2 synthesis for an applied potential pulse of 0.8 V vs. RRE with a total charge density of 9 mC/cm^2.

The potentiometric characterization of the modified electrode as a pH sensor and its calibration curve are represented in Figure 5.10. It started from pH 13 to 8 and then reversed until again pH 13.
As shown from the characterization graphs, the sensor response was relatively fast and reversible, presenting a super-Nernstian slope of about 72 mV/pH unit. However, the potential shift to lower values during OCP measurement highlights an eventual need to reduce the films to obtain a more stable potentiometric response, as achieved by the potentiodynamically grown films. As reported, the reduction process of MnO_2 films decreases the refractive index and the extinction coefficient, which is attributed to the increase of film porosity [258].

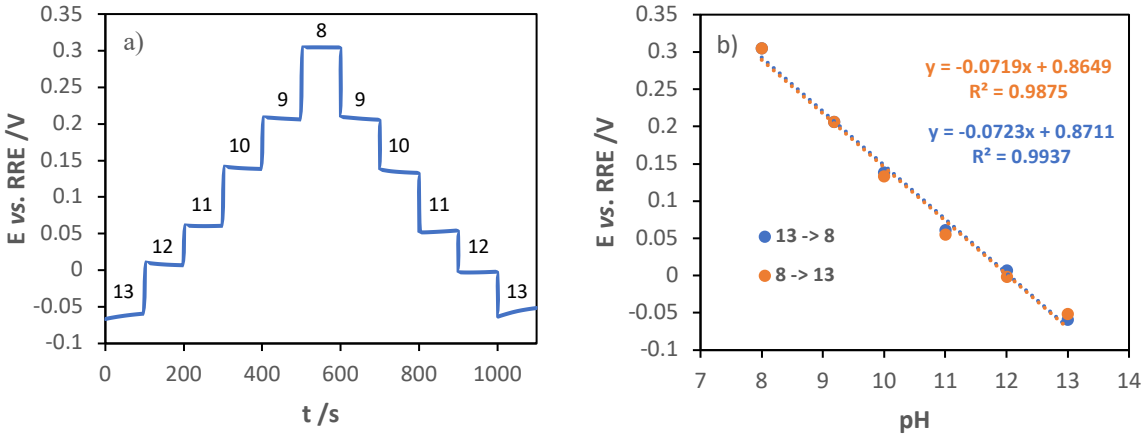

Figure 5.10: Potentiometric characterization (a) and calibration curve (b) of MnO_2 electrode for different pH buffer solutions (from 13 to 8 and from 8 to 13).

The characterization parameters for all potentiostatic growths are summarized in Table 5.1.

Table 5.1: Characterization parameters (slope, E-intercept, R^2 and slope shift) for each modified electrode.

Q /mC cm^{-2}	E *vs.* RRE /V	pH 13 → 8			pH 8 → 13			Slope shift /mV$_{RRE}$
		m /mV pH^{-1}	b /mV$_{RRE}$	R^2	m /mV pH^{-1}	b /mV$_{RRE}$	R^2	
36	**1**	76	975.9	0.9989	78.2	990.7	0.9907	-2.2
	0.9	74.4	961.3	0.9986	76.6	977.4	0.999	-2.2
	0.8	69.2	920.1	0.9984	73.2	952.0	0.9984	-4
9	**0.8**	72.3	871.1	0.9937	71.9	864.9	0.9875	0.4
4	**0.8**	77.5	843.2	0.9947	-	-	-	-

As reflected in Table 5.1, for the same deposition charge of 36 mC/cm^2, the decrease in the applied potential leads to a decrease of the slope, which approaches the Nernstian value, and to a potential shift to lower values. The decrease of synthesis charge, for the same potential pulse of 0.8 V *vs*. RRE, leads to an increase of the slope.

Previously, an ellipsometric study determined that the deposition conditions affect the optical properties of MnO_2 films [244]. As a consequence, it was decided to use ellipsometry to study the effect of the applied potential on the optical parameters of the MnO_2 films and correlate it with its potentiometric response as pH sensors. Figure 5.11 a) shows the ellipsometric parameters — Psi and Delta — collected during the potentiostatic deposition of MnO_2 onto a stainless steel substrate at a potential pulse of 0.9 V *vs*. RRE, for 25 minutes, in an aqueous solution with 0.3 M $MnSO_4$ and 0.1 M $LiClO_4$ and Figure 5.11 b) shows the experimental ellipsometric parameters obtained for different applied potentials — 0.7, 0.8, 0.9 and 1.0 V *vs.* RRE. The evolution of ellipsometric parameters presents a similar behaviour for different potential pulses, with exception for 700 mV *vs*. RRE.

The measurement started from the ellipsometric parameters characteristic of bare substrate, which depend on its nature and on the state of its surface (polishing degree and presence of contaminants). Then, the ellipsometric parameters formed an almost closed loop that is characteristic of a slightly light absorbing film. The growth of a transparent film produces a Psi-Delta loop that closes when the product of film thickness and the cosine of the angle of refraction is equal to half the wavelength of light in the film [244]. Finally, it continued spiralling rapidly inward toward a point as the film become thicker, which is due to the small effect of the interference on the polarization of the reflected light.

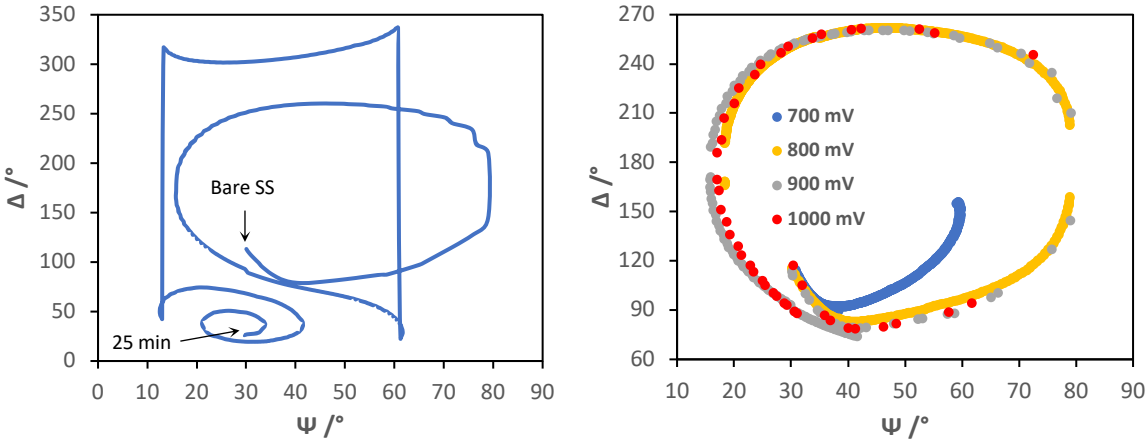

Figure 5.11: Evolution of ellipsometric parameters during the potentiostatic synthesis of MnO_2 onto a stainless steel substrate, with a potential pulse of 0.9 V vs. RRE for 25 minutes, in an aqueous solution of 0.3 M $MnSO_4$ and 0.1 M $LiClO_4$ (a) and ellipsometric parameters obtained for different applied potentials — 0.7, 0.8, 0.9 and 1.0 V vs. RRE.

Figure 5.12 presents the experimental values of Delta as a function of Psi and the computationally simulated curves for the potentiostatic growths of MnO_2, for the different applied potentials, showing the optical parameters and the respective thickness.

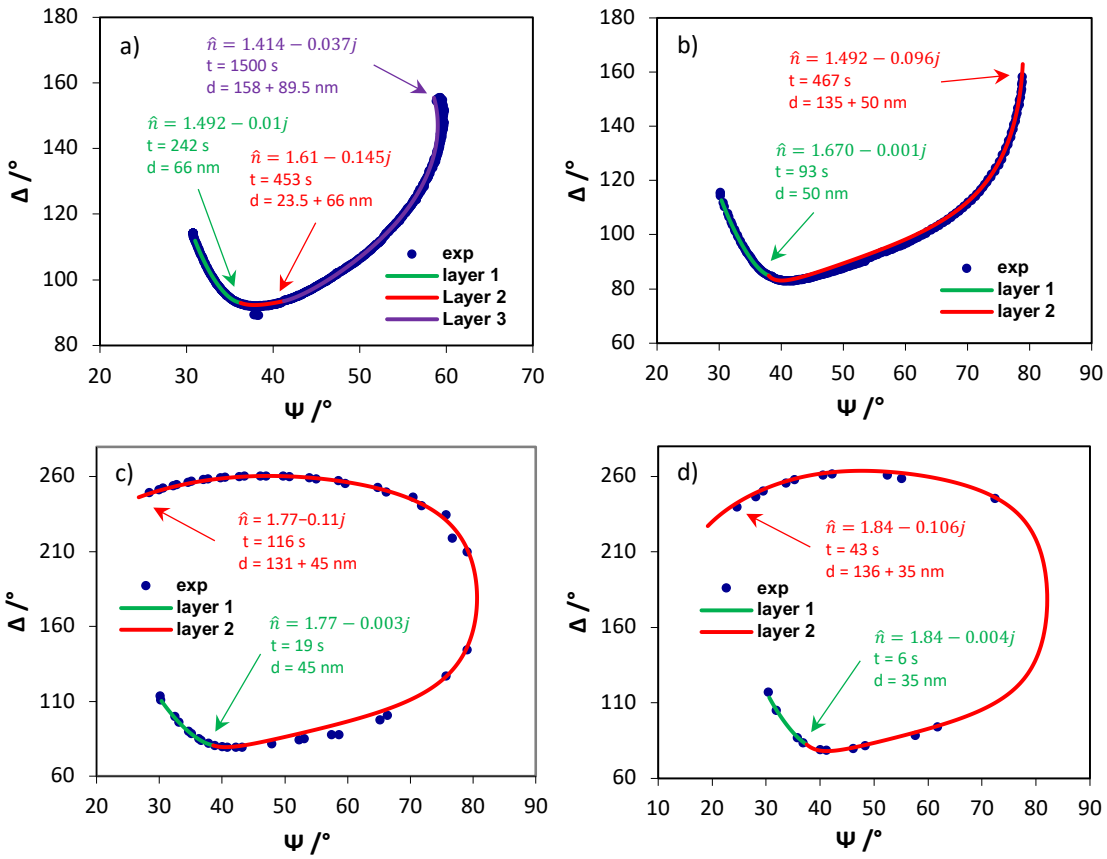

Figure 5.12: Experimental values of Ψ and Δ recorded during the potentiostatic growth of MnO_2 for the applied potentials of 0.7 (a), 0.8 (b), 0.9 (c) and 1.0 (d) V vs. RRE and the respective simulated trajectory assuming the formation of two distinct homogeneous layers: inner layer with green solid line, and outer layer with red solid line. Note that for the film modified with 0.7 V vs. RRE it was necessary to consider a third one, with purple solid line, to obtain a good fitting.

A three-phase model (solution, film and substrate) was used to simulate the growth of a single homogeneous layer on the electrode surface. The procedure consists in determining the complex refractive index of the film that produces the best adjustment between theoretical and experimental ellipsometric curves — Delta *vs*. Psi. However, it was necessary to consider the formation of different homogeneous layers to achieve a reasonable complete fitting of experimental data. Table 5.2 summarizes the simulated ellipsometric values of the MnO_2 films, for different growth potentials.

Table 5.2: Simulated ellipsometric parameters for different potentiostatic growths of MnO_2.

		0.7 V_{RRE}	**0.8 V_{RRE}**	**0.9 V_{RRE}**	**1.0 V_{RRE}**
Inner layer	**d /nm**	66	50	45	35
	$\hat{n}$	1.492-0.010j	1.670-0.001j	1.770-0.003j	1.840-0.004j
	Rate of growth /nm s^{-1}	0.27	0.54	2.37	5.83
Outer layer	$\hat{n}$	1.410-0.037j	1.492-0.096j	1.770-0.110j	1.840-0.106j
	Rate of growth /nm s^{-1}	0.11	0.36	1.35	3.68

As illustrated in the previous table, the increase of the applied potential leads to an increase of the thickness, rate of growth and refraction index of the inner and outer layer. The increase of *n* can be related to the increase of film density or to the change in the composition. The porosity is explained by a more disorderly nucleation process for a greater deviation from the equilibrium potential, while the composition may be related to the content of different manganese oxides. The second layer presents a decrease in rate of growth and an increase of *k* comparing to inner layer. The slopes of the calibration curves of the MnO_2 sensors are affected by the applied potential, which promotes the formation of films with different porosity and thickness. The ellipsometric study confirmed the formation of an inner more resistive MnOOH layer between the electrode surface and the manganese compounds film, as reported by several authors [165,170,172].
The morphology of MnO_2 films grown potentiostatically for the applied potentials of 0.9 and 1.0 V with a total charge of growth of 36 mC/cm^2 was analysed by SEM and its images are shown in Figure 5.13. The increasing potential pulse leads to the formation of more compact films, which is in agreement with ellipsometric results.

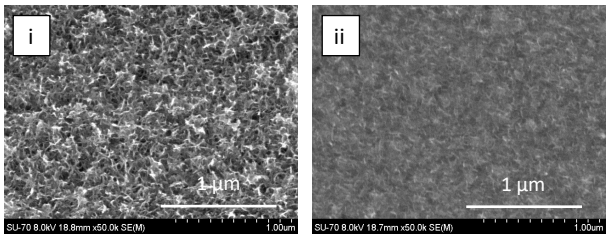

Figure 5.13: SEM images of MnO_2 films synthetized potentiostatically with an applied potential of 0.9 V (i) and 1.0 V (ii).

5.2. Iridium oxide

Electrochemically synthetized iridium oxide films are commonly divided according to the method used for the growth. Anodic iridium oxide films (AIROF) are based on the anodizing of an iridium substrate in an acid media, and can be carried out through cyclic voltammetry or a galvanostatic/potentiostatic pulse. Electrodeposited iridium oxide films (EIROF) are grown from an iridium compound solution by cyclic voltammetry and can be done on several substrates.

In this work, the synthesis of IrO_x was first done through the anodization of an iridium substrate by cyclic voltammetry. The influence of some electrochemical growth parameters — scan rate and number of cycles — in the potentiometric response as a pH sensor was studied. Based on literature data, a scan rate of 50 mV/s was tested for 250 and 1500 cycles, and a scan rate of 3 V/s for 15000 and 60000 cycles. The response time of these sensors was too slow, which, together with the high price of iridium substrate, led to the decision of finding a different approach. The alternative was a film deposited from an iridium solution onto a stainless steel substrate. The iridium solution was prepared according to Yamanaka method, as described in the experimental procedure. A first experiment was conducted to determine the potential window and redox parameters of the electroactive species present in the growth solution. The minimum anodic potential that allowed the film growth, which can be seen by the continuous increase of redox peaks for successive cycles, was around 700 mV *vs*. RRE. The potentiodynamic synthesis of IrO_x with a scan rate of 50 mV/s, for 50 cycles, in the potential window of -0.3 to 0.7 V (*vs*. RRE) is represented in Figure 5.14 from the first cycle, and then every 5th cycle, until the 50th.

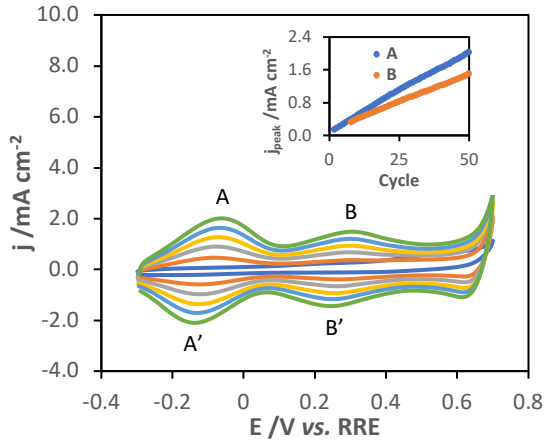

Figure 5.14: Cyclic voltammograms of potentiodynamic growth of IrO_x with a scan rate of 50 mV/s for cycles, from the first cycle, every 5 cycles, to the 50th and evolution of anodic peaks current density with number of cycles (inset).

The first cycle shows the capacitive response of the stainless steel substrate. Upon cycling, the cyclic voltammogram starts displaying well-defined redox peaks of IrO_x with increasing peak current and a shift between cathodic and anodic peaks as the film gets thicker and more resistive. The peaks — A/A' and B/B' — are commonly assigned to the redox couples Ir(III)/Ir(IV) and Ir(IV)/Ir(V), respectively [142]. The film has a metallic bluish colour and presents good adhesion to the stainless steel. The characterization of this modified electrode as a pH sensor is presented in Figure 5.15 a). The potentiometric characterization started from pH 6 to 2, with unit change, and then reversed until pH 13. Finally, an extreme variation in the pH value between 13 and 2 was tested. The respective calibration curve is shown in Figure 5.15 b). Clearly, the IrO_x sensor presents a fast and reversible response, even for large pH variations between 13 and 2. It has a super-Nernstian slope of 72.9 mV/ pH unit. This IrO_x sensor presented a promising potentiometric response for pH determination.
Having carried out this preliminary study on the electrochemical growth of IrO_x on stainless steel, the next step was to study in detail the electrosynthesis of this pH sensitive material through different electrochemical techniques and understand the influence of the main experimental parameters on the potentiometric response of the modified electrodes.

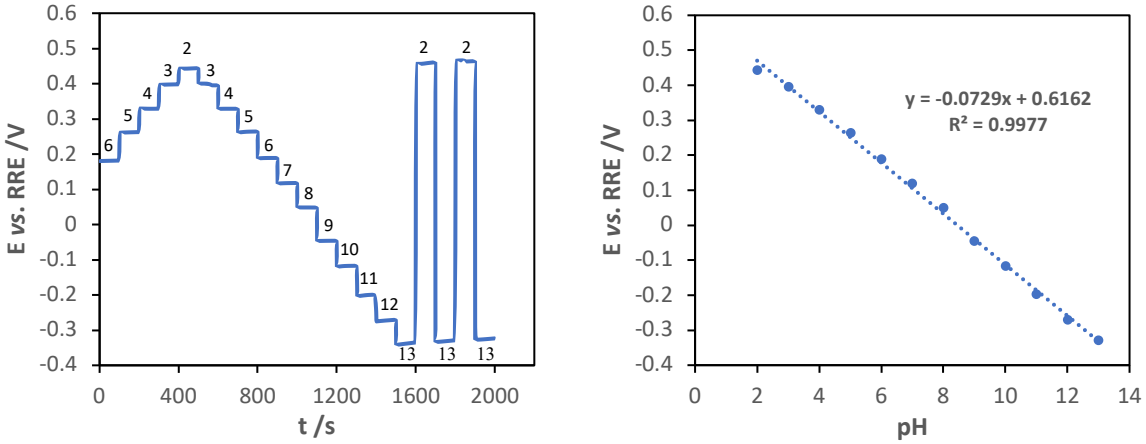

Figure 5.15: Potentiometric characterization of modified electrode for pH detection (left) and corresponding calibration curve (right).

5.2.1. Potentiodynamic synthesis

It was important to understand the influence of cyclic voltammetry growth parameters on the electrochemical response of iridium oxide films, with special attention to their potentiometric response as pH sensors. The most important experimental parameters of this electrochemical technique that could affect the morphology and composition of such films are the anodic and cathodic limits of the working potential window, the scan rate and the number of cycles. The growth solution could also be changed in terms of its reagents concentration or even using a different source of iridium ions. However, this growth solution was already object of several studies to understand the purpose of each reagent and its optimum concentration in order to optimize the deposition. So, the growth solution was not changed in this experimental study. As the peak current density is dependent on the square root of the potential sweep rate, scan rate values were chosen in order to obtain an integer value of their square root. The number of cycles was based on previous experiments, which shown that growths with more than 100 cycles presented an iridium deposit on the resin surface around the electrode, and with less than 20 cycles, the films were optically transparent. A Taguchi L_9 orthogonal array was applied in order to study the effect of the experimental parameters on the potentiometric response of the IrO_x films. Table 5.3 summarizes the experimental values under study — scan rate, number of cycles and anodic potential limit — for each sample.

Table 5.3: Summary of growth parameters — scan rate, number of cycles and anodic limit — of each sample.

Sample	v /mV s^{-1}	Nº cycles	E_{anodic} /V
1	16	20	0.75
2	16	50	0.80
3	16	80	0.85
4	49	20	0.80
5	49	50	0.85
6	49	80	0.75
7	100	20	0.85
8	100	50	0.75
9	100	80	0.80

Figures 5.16 a)-i) present the cyclic voltammograms of each sample, and Figure 5.16 j) presents the anodic peaks from 20th cycle as a function of anodic limit and scan rate, in which it is possible to observe that redox peaks A (at *ca*. -0.1 V *vs.* RRE) and B (at *ca*. 0.3 V *vs*. RRE) are related with the growth experimental parameters. The ratio between the peaks intensities appears to be dependent on the scan rate and on the anodic potential limit, as shown in Figure 5.16 j). The increase of the sweep rate as well as the decrease of the anodic potential limit leads to a decrease in the ratio between peaks B and A that is possibly due to the lower conversion of Ir(IV) to Ir(V). So, these experimental conditions influence the quantity of different iridium oxides that constitute the modified electrodes. The ratios between peaks A and B for each growth present a good reproducibility for several repetitions with the same conditions.

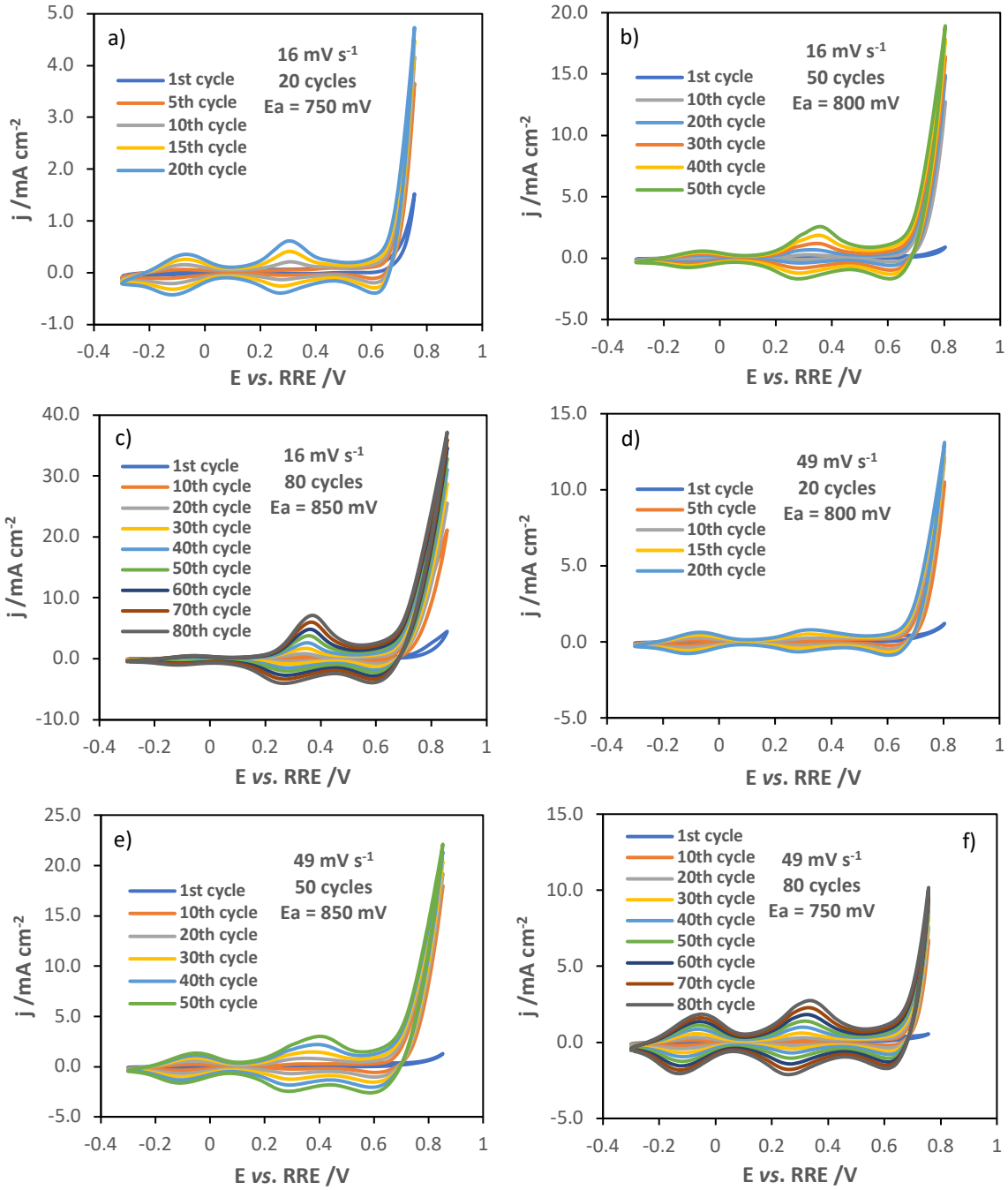

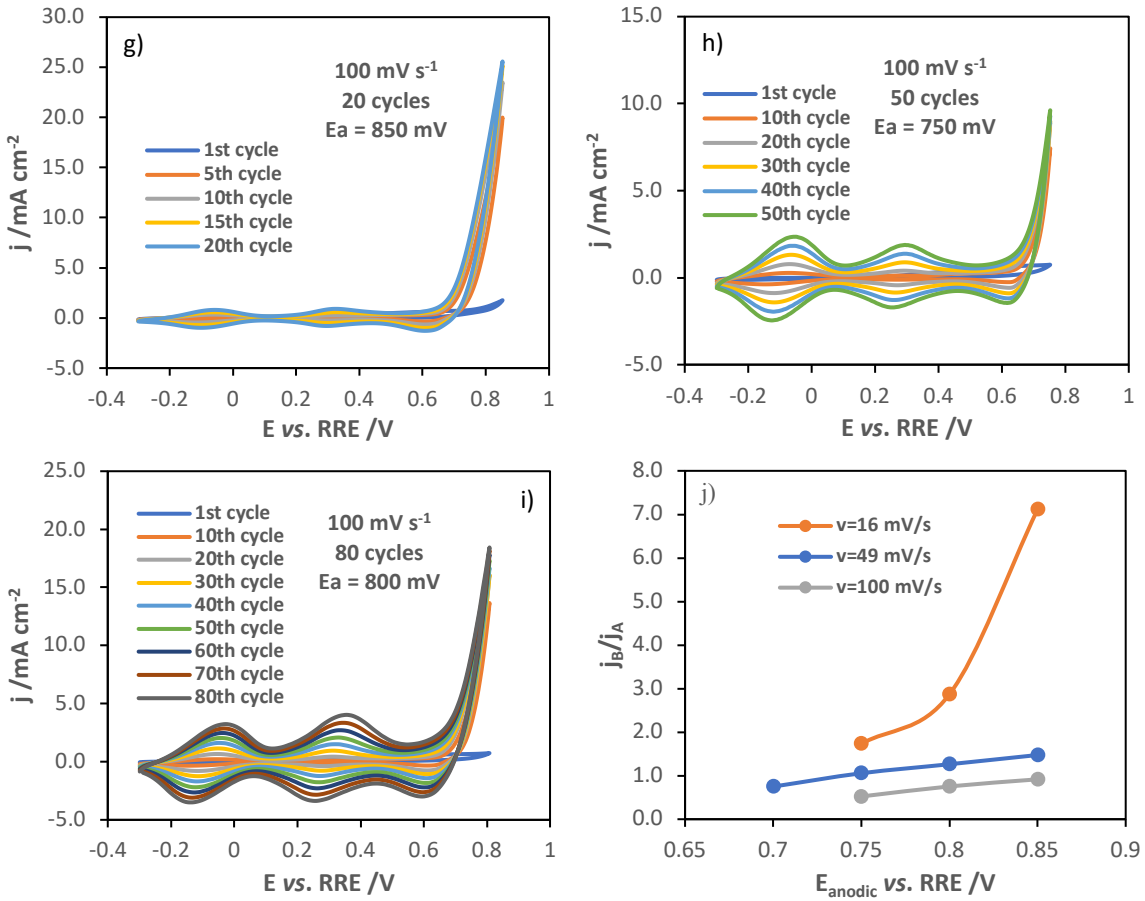

Figure 5.16: Cyclic voltammograms of each sample (a) to i)) and anodic peaks ratio from 20th cycle as a function of anodic limit and scan rate (j).

The potentiometric characterization of sample 3, which is representative of all samples in terms of response time and reversibility, and its calibration curve are represented in Figures 5.17 a) and b), respectively.

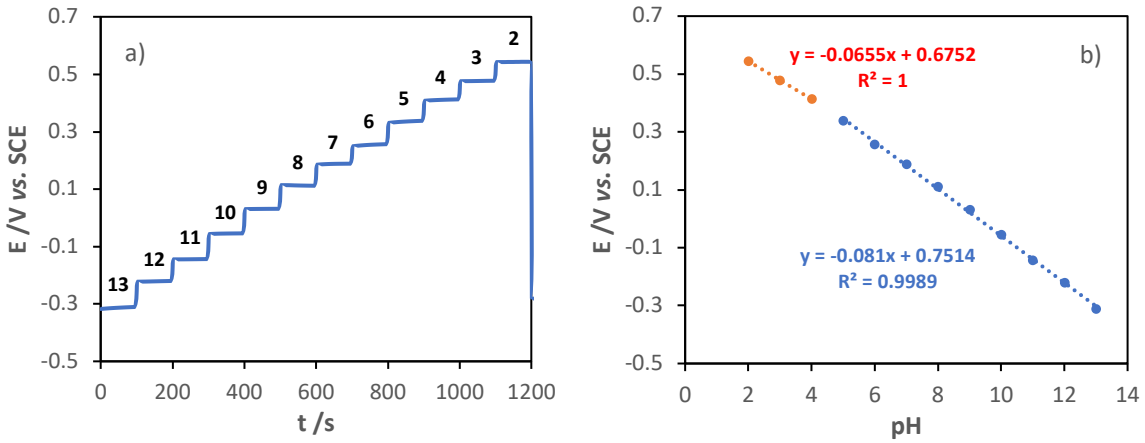

Figure 5.17: Potentiometric characterization of sample 3 (scan rate of 16 mV/s for 80 cycles with an anodic limit of 0.85 V vs. RRE) from pH 13 to 2 (a), and the corresponding calibration curve with two pH regions (b).

The potentiometric response presents two regions in agreement with a previous study [259], in which it was demonstrated through probe beam deflection that the potentiometric response of

electrochemically grown iridium oxide films is divided in two regions: one below and another above pH 4, which are dominated by the exchange of H^+ and OH^-, respectively. The acid region (pH<4) has a near Nernstian slope compared to the second one (pH>4), which presents a super-Nernstian one. The time of response of these sensors is considered immediate taking into account that in the first second of the potentiometric measurement the open circuit potential already represented more than 98% of the final value.

The potentiometric parameters —slope and E_{SCE}-axis intercept — of all samples are summarized in Table 5.4. Region 1 presents a near-Nernstian slope between -59.0 and -65.5 mV pH^{-1}, while the slope of region 2 is super-Nernstian (-79.0 to 81.0 mV pH^{-1}).

Table 5.4: Summary of potentiometric parameters —slope, E-intercept and coefficient of correlation of all potentiodynamically grown samples for each pH region (1 and 2).

Sample	Region 1			Region 2		
	Slope /mV pH^{-1}	b /mV_{SCE}	R^2	Slope /mV pH^{-1}	b /mV_{SCE}	R^2
1	-61.1	583.2	0.9999	-79.7	673.6	0.9995
2	-62.7	627.9	1	-80.4	713.6	0.9994
3	-65.5	675.2	1	-81.0	751.4	0.9989
4	-60.7	601.4	1	-79.5	690.7	0.9995
5	-61.3	628.9	1	-80.7	720.5	0.9996
6	-62.1	599.0	1	-79.4	683.3	0.9994
7	-65.5	675.2	1	-81.0	751.4	0.9995
8	-59.0	565.8	0.9999	-79.0	661.4	0.9994
9	-61.8	611.0	0.9997	-79.3	697.0	0.9995

Calibration curve parameters of both regions present a strong correlation with the anodic limit of film synthesis. Figure 5.18 a) and b) presents, respectively, slope and E-intercept of potentiodynamically grown films with a scan rate of 16 mV/s, for both regions of pH, as a function of the respective anodic limit of synthesis. The decrease of anodic limit leads to a decrease of slope and a shift of E-intercept to lower potential values, for both regions. The anodic limit of potentiodynamic depositions was already reported to influence the slope of the potentiometric response due to a variation of the ratio between iridium oxides with different valance states [120].

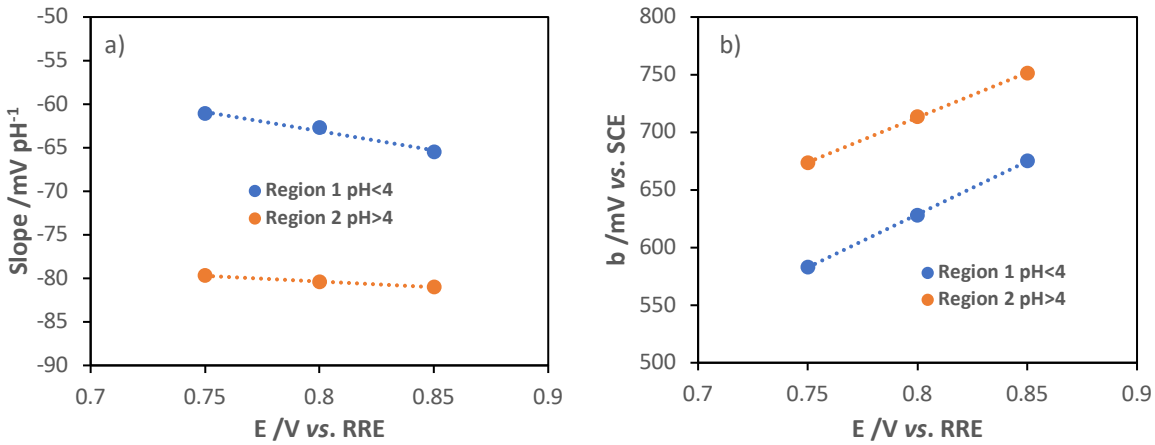

Figure 5.18: Potentiometric parameters — slope and E-intercept — of potentiodynamically grown films with a scan rate of 16 mV/s, as a function of anodic limits of synthesis, for both pH regions

The electrochemical behavior of the potentiodynamically grown iridium oxide films was also accessed through cyclic voltammetry. Figure 5.19 presents the potentiodynamic response of the modified electrodes with different number of cycles (a) and different scan rates (b), with a scan rate

of 50 mV/s in an aqueous solution of 0.1 M $LiCLO_4$. The scans started from the cathodic limit with anodic direction. The well-defined anodic peak between 0.55 and 0.6 V *vs*. SCE is related to the Ir(III)/Ir/IV) reaction [260].

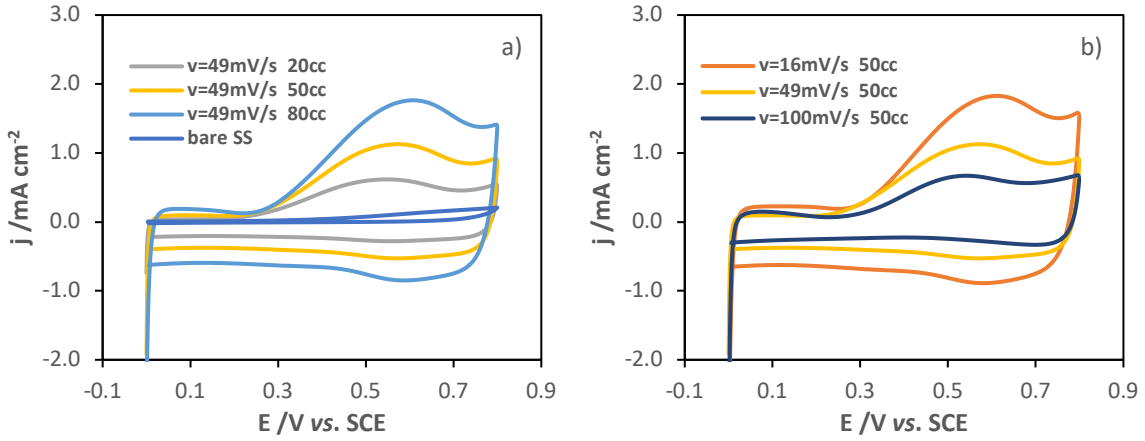

Figure 5.19:Cyclic voltammograms of modified electrodes with different number of cycles (a) and different scan rates (b).

The morphology of these films was studied by scanning electron microscopy. Figure 5.20 presents SEM images of the different modified electrodes, where the number of cycles increases from left to right (20, 50 and 100 cycles) and the scan rate increases from top to bottom (16, 49 and 100 mV s^{-1}).

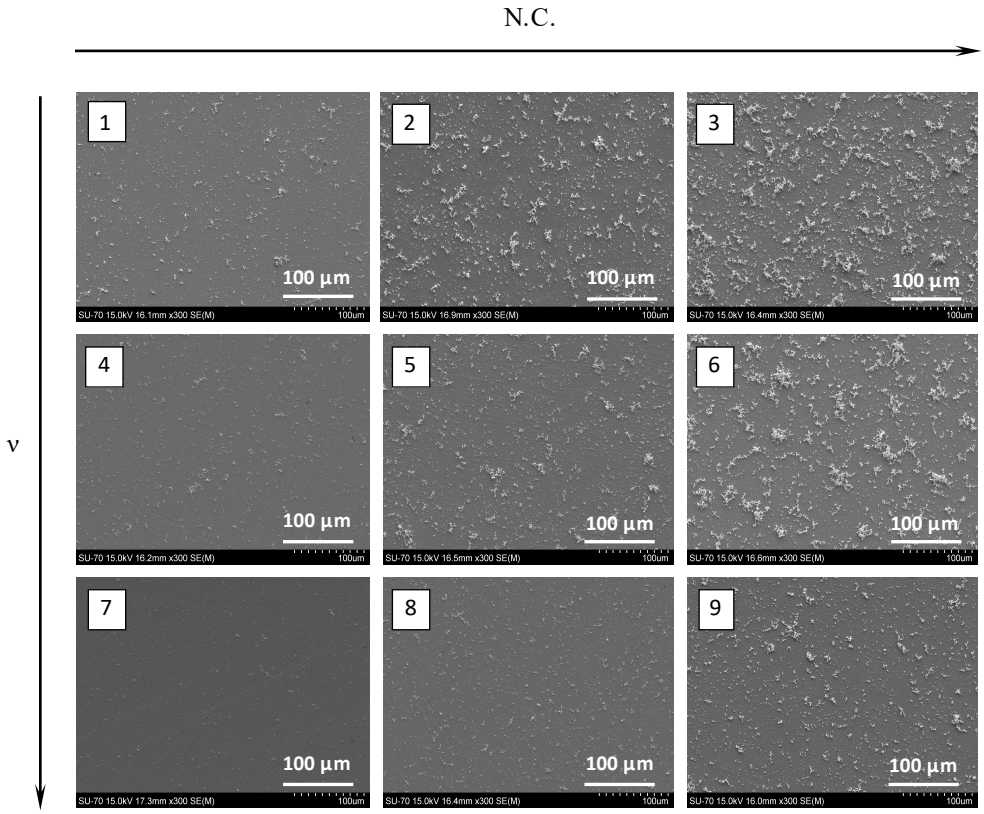

Figure 5.20: SEM images of the different modified electrodes potentiodynamically with increasing number of cycles in each line and increasing scan rate in each row.

Clearly, it is possible to visualize that the number of iridium oxide nuclei increases with increasing number of cycles and lower scan rate. The nucleation process seems to be constituted by two stages. First, there is the formation of a homogeneous layer on the substrate constituted by small nuclei of iridium oxide with globular shape. This first dense layer presents some cracks that occur due to its dehydration [179]. Then, there is the formation of big porous islands made up of globular iridium nuclei, as can be seen by Figure 5.20. The formation of these aggregate structures was already reported [144].

The EDS analysis identified the main elements present in the iridium oxide films. Figure 5.21 shows a qualitative analysis of the sample 1 to the presence of iridium and oxygen and Table 5.5 presents the mass percent analysis of each modified electrode.

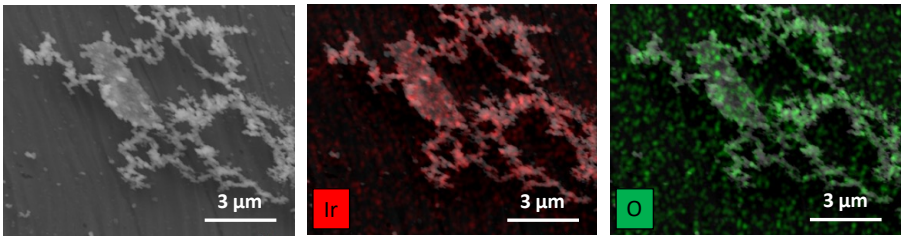

Figure 5.21: EDS analysis to IrO_x modified electrode to the presence of iridium and oxygen.

Table 5.5: Mass percent analysis of each sample.

Sample	Mass percent /%						
	O	Ir	Fe	Ni	Cr	Si	S
1	10.71	1.5	61.31	9.25	15.54	0.57	1.12
2	18.46	3.89	54.08	8.27	13.76	0.75	0.79
3	25.68	4.65	48.51	7.48	12.59	0.45	0.64
4	7.09	0.93	64.37	9.52	15.96	0.73	1.42
5	12.25	2.12	59.98	8.81	15.21	0.56	1.07
6	20.48	4.15	51.19	8.59	13.94	0.68	0.97
7	1.55	2.09	64.99	10.45	15.62	0.34	0.79
8	3.05	4.54	60.98	9.88	14.76	0.35	0.7
9	4.85	8.6	59.01	9.71	14.35	0.41	0.47

The oxygen and iridium content increases as the nucleation process progresses. The increase of growth potential sweep rate promotes the formation of films with higher content of iridium and lower presence of oxygen. It would be expected a higher content of oxygen as well, due to the presence of a higher number of iridium oxide nuclei. This can be result of a lower hydration state of iridium oxides or to a lower oxidation state due to a higher content of Ir(III) than Ir(IV).

Table 5.6 presents the correlation coefficients between the growth parameters — scan rate, number of cycles and anodic limit — and characterization parameters — slope and E-intercept for both regions, charge density and relative amount of oxygen and iridium. The correlation was obtained using the Taguchi method and the high correlation coefficients are represented in green. The calibration curve is only affected by the synthesis potential window. The decrease in the anodic limit leads to a decrease of the slope and a shift of the calibration curve to lower potential values. The other growth parameters do not change the potentiometric response of the modified electrodes because they only affect the film morphology (thickness and porosity) and the electrochemical equilibrium for pH determination is a surface process between oxides with different valence states. The anodic peak current densities of the modified electrodes decrease with higher synthesis scan rate

and increase with the number of cycles. The electrochemical response depends on the number of electroactive nuclei, which, in turn, increase with the number of deposition cycles and with a slower sweep rate [143,261].

Table 5.6: Correlation coefficients between the growth parameters — scan rate, number of cycles and anodic limit — and characterization parameters — slope and E-intercept for both regions, charge density and relative amount of oxygen and iridium.

	Scan rate	N° of cycles	Anodic limit
Slope 1	0.165	-0.142	-0.681
b 1	-0.109	0.097	0.885
Slope 2	0.316	0.093	-0.854
b 2	-0.110	0.072	0.922
Q	-0.626	0.746	0.010
O /%	-0.479	0.854	0.033
Ir /%	0.367	0.798	-0.082

To complete the study of potentiodynamic growth of IrO_x films, ruthenium chloride was added to the growth solution with the aim of obtain a slope closer to the Nernstian value, which is characteristic of RuO_2 sensors [184,262]. Mixed iridium-ruthenium oxide films have been tested as electrocatalyst for the oxygen evolution reaction [263] and as electrochemical capacitors [181]. Initially, the electrochemical growth of ruthenium oxide on stainless steel electrode, through cyclic voltammetry, was studied to determine the redox peaks and the anodic potential value that allows the electrodeposition of this oxide. The ruthenium oxide synthesis was done potentiodynamically in an aqueous solution of 5 mM $RuCl_3$ and 0.1 M $LiClO_4$ with a scan rate of 50 mV/s for 65 cycles. The potential window used was from -0.25 to 1.4 V (*vs*. RRE), with the scan starting from the cathodic limit in anodic direction. Figure 5.22 presents the voltammograms of the first and last cycles (65^{th}). The anodic segment presents two well-defined peaks: one at about 1.1 V *vs*. RRE and a latter at about 1.3 V *vs*. RRE, which establishes the minimum potential value that allows the film to grow under these conditions. In the case of the cathodic segment, the voltammogram presents two well-defined peaks at about 0.6 and 0.1 V *vs*. RRE. The peak B_1/A_1 is attributed to deposition/conversion from $RuCl_3.xH_2O$ to $RuCl_y.nH_2O$, and the peak B_2/A_2 is related to the conversion of $Ru(OH)_\delta Cl_{a-\delta}.nH_2O$ into the oxy-hydroxyl-ruthenium structure ($RuO_\omega(OH)_{a-2\omega}.nH_2O$) and, therefore, is the essential process for the hydrous ruthenium oxide deposition [264].

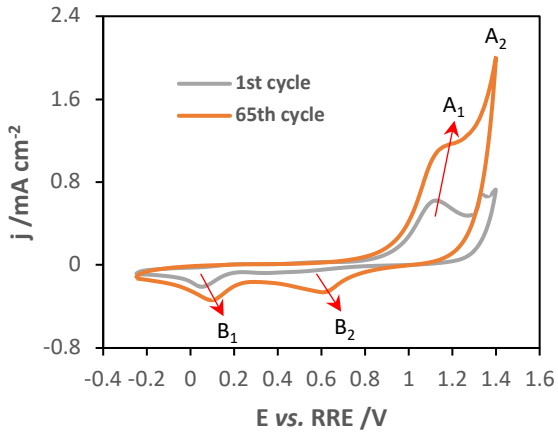

Figure 5.22: Cyclic voltammograms of RuO_2 synthesis with a scan rate of 50 mV/s, for 65 cycles, in an aqueous solution of 5 mM $RuCl_3$ and 0.1 M $LiClO_4$.

Then, the effect of adding different concentrations of $RuCl_3$ — 1, 5 and 10 mM — to the iridium growth solution and the variation of the anodic limit of synthesis — 850, 900 and 950 mV *vs*. RRE — on the potentiometric response of the potentiodynamically synthesized films was studied. Figures 5.23 a), b) and c) present the cyclic voltammograms of the growths with 1, 5 and 10 mM $RuCl_3$, respectively, with a scan rate of 50 mV/s, for 50 cycles. The presence of 1 mM $RuCl_3$ did not affect the growth of the iridium film, which presents a potentiodynamic evolution similar to that of the synthesis under the same conditions, but without ruthenium compound. The concentrations of 5 and 10 mM $RuCl_3$ inhibited the film growth rate, as given by the decrease of the peak currents in Figure 5.23 d). Redox peaks related to ruthenium oxide were not observed in any voltammogram. The increasing concentration of ruthenium in the growth solution also increased the resistivity of the films, as evidenced by the increasing potential difference between the redox peaks. The modified electrode in the presence of 5 and 10 mM $RuCl_3$ were optically transparent, possibly due to the small thickness of the obtained films. Regarding the films grown in the presence of 1 mM $RuCl_3$, they showed the characteristic colour (metallic blue) of previously synthesized IrO_x films.

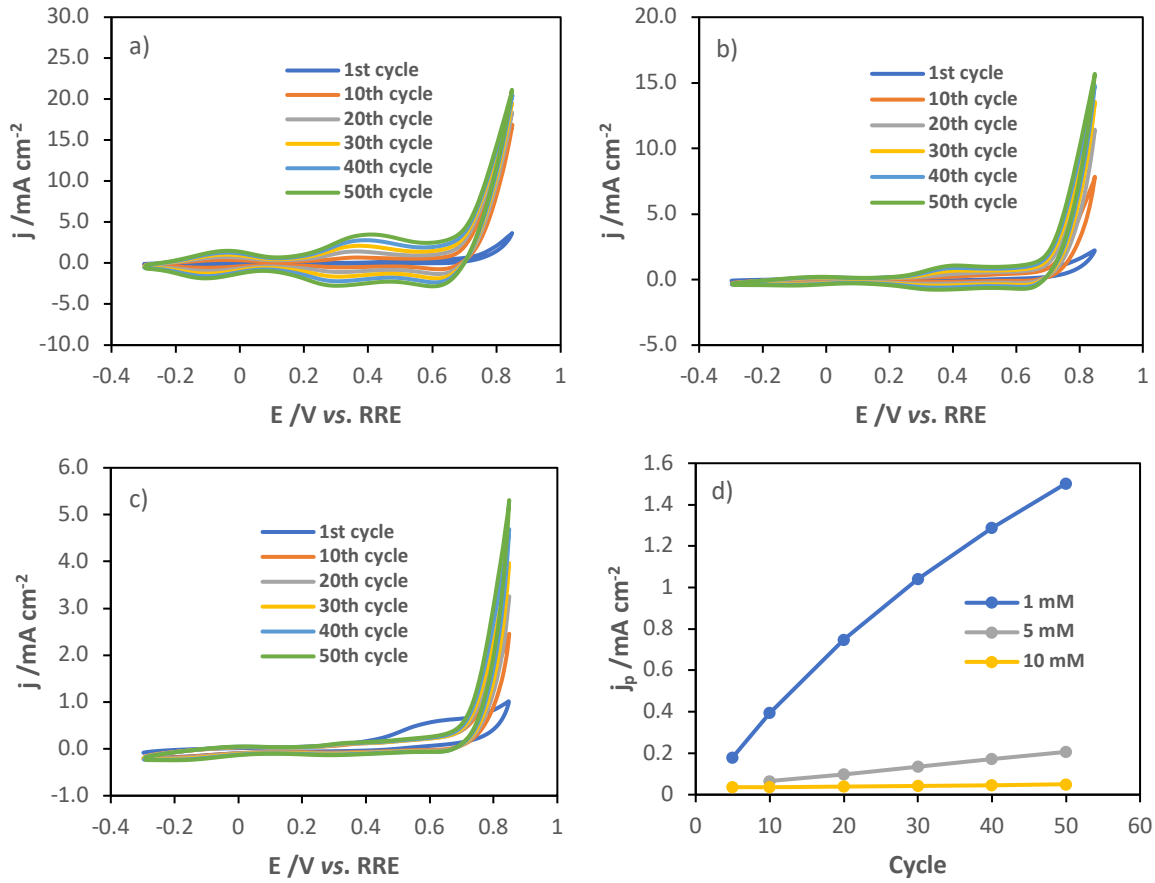

Figure 5.23: Cyclic voltammograms of potentiodynamic synthesis of IrO_x with a scan rate of 50 mV/s for 50 cycles in the presence of a) 1, b) 5 and c) 10 mM $RuCl_3$, respectively, and d) the evolution with number of cycles of current density of first anodic peak of each synthesis.

Then, the modified electrodes were characterized potentiometrically for the determination of pH. Figure 5.24 shows the potentiometric characterization and its respective calibration curve of the modified electrode in the presence of 5 mM $RuCl_3$ with an anodic limit of 850 mV *vs*. RRE. The modified electrode presents a potentiometric response with two different pH regions, as happened

with the IrO_x films presented before. The main pH region (13<pH<4) has an almost Nernstian slope — 63.2 mV/pH — with a instantaneous time of response. However, the sensibility of the sensor decreases in the acid zone (pH<4), which is possibly due to the oxidation of the modified electrode. This region presents a sub-Nernstian slope of 40.7 mV/pH.

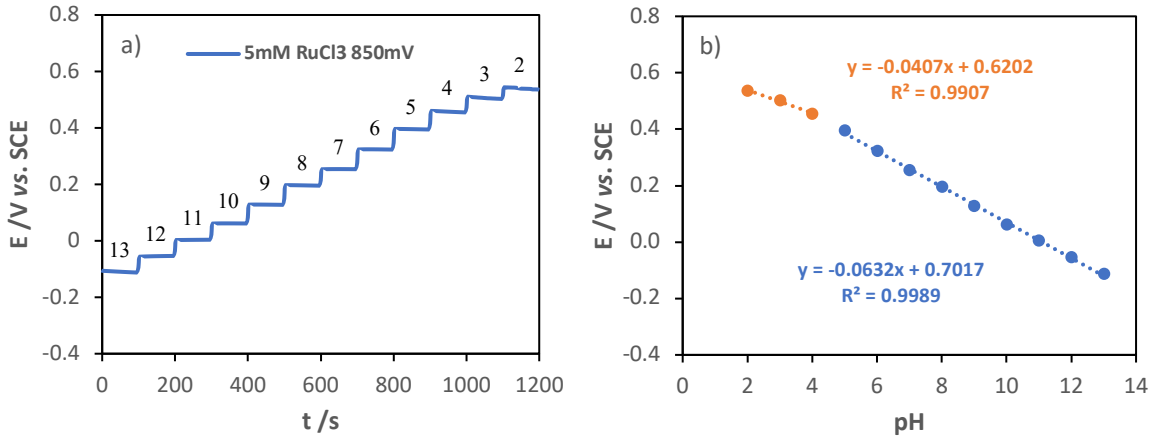

Figure 5.24: Potentiometric characterization of modified electrode with a scan rate of 50 mV/s for 50 cycles for 5 mM $RuCl_3$ (a), and the respective calibration curve (b).

The potentiometric parameters — slope, E-intercept and correlation coefficient — of the modified electrodes in the presence of ruthenium chloride are summarized in Table 5.7. The synthesis with a content of 1 mM $RuCl_3$, in addition to not affecting the cyclic voltammograms of growth, does not change the potentiometric response of the modified electrodes, which remains similar to that of films synthesized without the presence of ruthenium chloride. In the case of electrodes modified in the presence of 5 and 10 mM $RuCl_3$, their potentiometric response presents a near-Nernstian slope that decreases with the increase of the ruthenium content and with the increase of the anodic limit of growth. The decrease in the slope of the calibration curve may be explained by the eventual co-deposition of ruthenium oxide or with the decrease in the degree of hydration of the iridium oxides. In addition, all the modified electrodes with the higher concentrations of ruthenium chloride presented a worse potentiometric response in the acid region with a sub-Nernstian slope and an unstable response in pH 2 buffer solution. The correlation coefficients of calibration curves decrease with higher anodic potentials of synthesis.

Table 5.7: Summary of potentiometric parameters — slope, E-intercept and correlation coefficient — of modified electrodes potentiodynamically in the presence of different ruthenium chloride concentrations.

[$RuCl_3$] /mM	E_a /V *vs.* RRE	m /mV pH^{-1}	b /mV *vs.* SCE	R^2
1	850	82.3	685.4	0.9995
	900	82.5	856	0.999
	950	82.4	857	0.9988
5	850	63.2	701.7	0.9989
	900	56.6	656.2	0.9957
10	850	59.5	696.2	0.9977
	900	57.3	738.1	0.9963

Finally, the electrochemical behaviour of the potentiodynamically modified electrodes in the presence of ruthenium chloride was accessed by cyclic voltammetry in 0.1 M $LiClO_4$ with a scan rate of 50 mV/s, as represented in Figure 5.25. The scans started at the cathodic limit in anodic direction. The capacitive response of the modified electrodes decreased with the increase in

ruthenium chloride present in the growth solution, being coherent with the cyclic voltammograms of the synthesis of these films, which showed a decrease in the current density for these conditions. The anodic limit of synthesis has no influence on the electrochemical response of the modified electrodes.

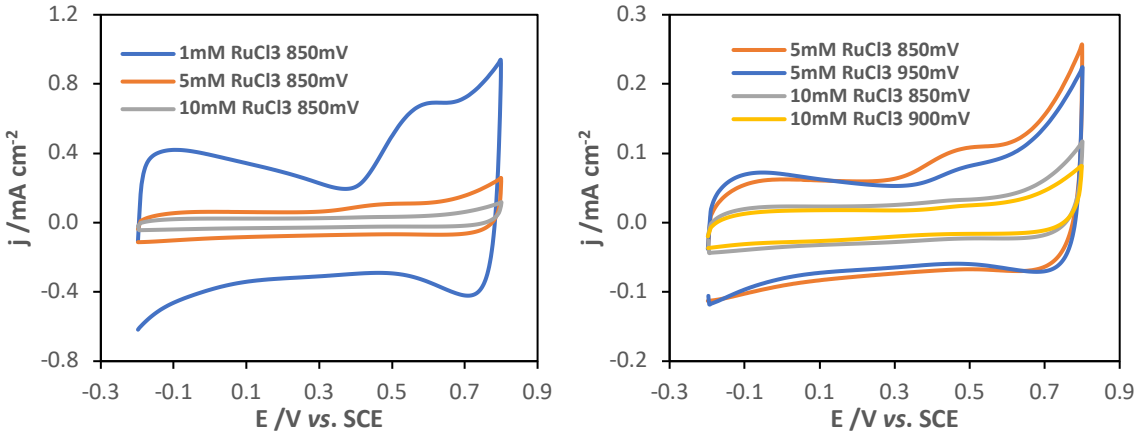

Figure 5.25: Cyclic voltammograms of the IrO_x films grown potentiodynamically in the presence of different ruthenium chloride contents.

5.2.2. Potentiostatic synthesis

Moving on to the case of electrochemical synthesis through the application of a constant potential pulse, the experimental parameters inherent to this technique are the magnitude of the applied potential and the pulse time. The pulse can be singular or repeated several times. The potentiostatic growth of IrO_x films was studied through the application of a single anodic pulse and a double pulse — anodic and cathodic. In the case of a synthesis with double pulse, in addition to the parameters listed above, the number of pulses, the applied cathodic potential and the respective pulse time are added.

5.2.2.1. Single pulse deposition

The study of the potentiostatic synthesis began with the analysis of a single anodic pulse for depositing the iridium oxide film. The growth potentials were based on preliminary tests by cyclic voltammetry, which showed that an anodic limit below 0.7 V (*vs*. RRE) did not allow the film growth and films grown with an anodic limit higher than 0.9 V_{RRE} presented a slow potentiometric response. Figure 5.26 a) presents the current-time transients for different anodic growth potentials — 0.7, 0.75, 0.80, 0.85 and 0.90 V *vs*. RRE — for 60 seconds. Time-current transients show a characteristic growth of a conductive film, as shown in Figure 5.26 b). Initially there is a sharp drop in current due to double layer formation and to oxidation of electroactive species in solution (i) until a minimum of current is achieved (ii), which indicates the beginning of the formation of the first nuclei onto substrate surface. The nucleation process continues until substrate is completely covered (iii). Then, the current falls slowly as the film thickness increases, indicating a diffusion-controlled process [265]. As can be seen from Figure 5.26 a), the increase of the applied potential leads to faster

nucleation processes due to the increase of rate of reaction, meaning that the ad-ions did not have enough time to diffuse on the surface until finding the site thermodynamically more stable. Consequently, it promotes the formation of more disordered and porous deposits [255].

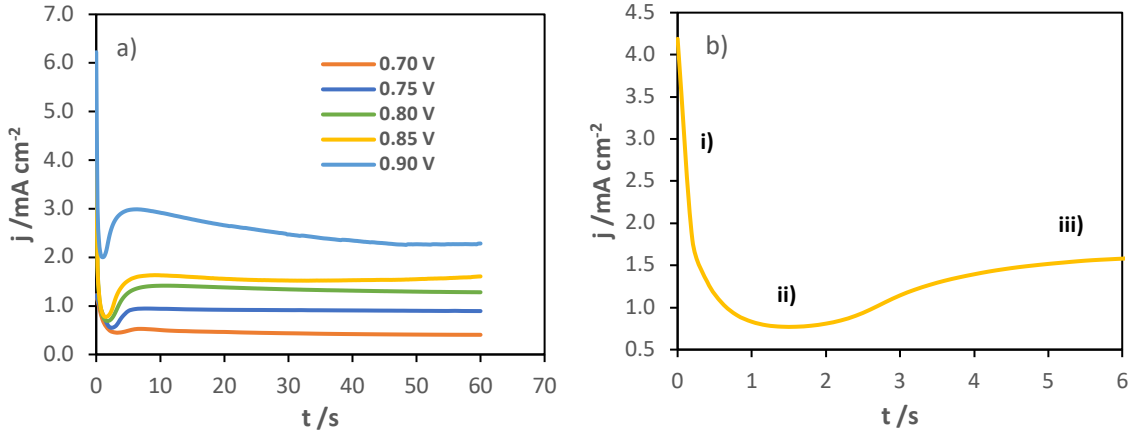

Figure 5.26: Chronoamperograms of IrO_x growth for different applied potentials — 0.70, 0.75, 0.80, 0.85 and 0.90 V vs. RRE — for 60 seconds (a), and initial instant of growth with the pulse of 0.85 V enumerating the different stages of nucleation process (b).

For potentiostatic conditions, the applied potential controls the constant rates of steady state nucleation and of nuclei growth [99]. The nucleation process of this growth was checked through the application of Scharifker model for instantaneous and progressive nucleation processes. An instantaneous process is characterized by a constant number of nuclei rapidly formed, whereas for a progressive process, the number of nuclei continues increasing with time. Figure 5.27 presents a non-dimensional plot of $(j/j_{max})^2$ as a function of t/t_{max} for the experimental and theoretical values of the potentiostatic growth of iridium oxide at 0.9 V *vs*. RRE, which presents a maximum peak current of 2.99 mA cm^{-2} that occured at 6.4 seconds.

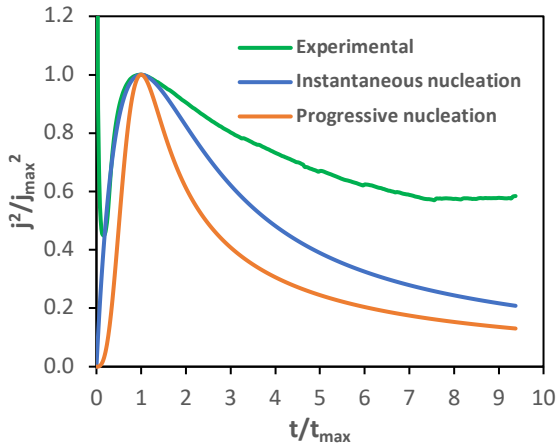

Figure 5.27: Non-dimensional representation of $(j/j_{max})^2$ as a function of t/t_{max} for the experimental and theoretical values of the potentiostatic growth of IrO_x for an applied pulse of 0.9 V vs. RRE.

From Figure 5.27 it is possible to visualize that until the growth stage iii), where the maximum peak of current is reached, the nucleation process follows an instantaneous mechanism, which means that the first nuclei grown above the substrate will evolve tri-dimensionally until the surface is completely covered. The diffusion coefficient for the potentiostatic electrodeposition of iridium oxide at 0.9 V

vs. RRE is 2.82 x 10^{-5} cm^2 s^{-1} and was determined by applying Cottrell equation considering c_0=4 mM, A=0.0792 cm^2 and n=2.

The potentiometric characterization of the potentiostatically grown film at 0.9 V *vs.* RRE, which is represented in Figure 5.28 a), was initiated at pH 13 decreasing unitarily until pH 2 — each level represents a pH value. As can be seen from Figure 5.28, the modified electrodes are unstable in pH below 4 — during characterization in pH 3 and 2, a sharp drop of open circuit potential occurred. The potentiometric response showed a non-linear variation in the alkaline pH range above 10 and a linear curve in the pH range 4 to 8-9. Sensors behaviour in alkaline media can be related to an eventual gradual hydrolysis of iridium oxide to its hydroxides [266], which will promote a sluggish response, and the time used in the potentiometric characterization was not enough to achieve electrochemical equilibrium.

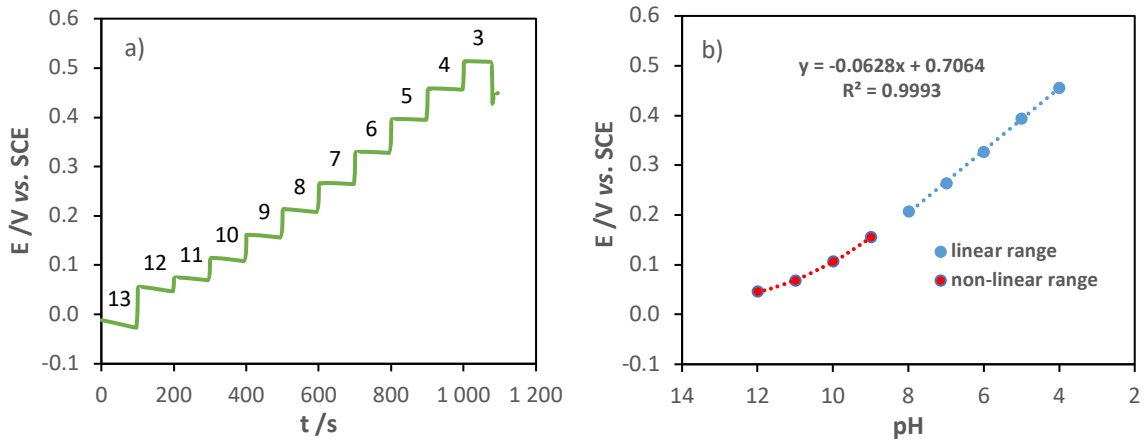

Figure 5.28: Potentiometric characterization for pH detection of the IrO_x film grown potentiostically at 0.9 V vs. RRE (a) and its corresponding calibration curve (b).

The main potentiometric parameters for each potentiostatic growth are presented in Table 5.8. All modified electrodes present a slope close to the Nernstian value, between 60.3 and 62.8 mV/pH unit, which is characteristic of anhydrous or low hydrated iridium oxide films [151]. The increase of applied potential leads to higher slope (super-Nernstian) and to a potential shift of calibration curve to more negative values. The pH range achieved by potentiostatically synthetized iridium oxide electrodes is within positive values of potential and limited between pH 9 and 4.

Another interesting observation is that iridium oxide films grown by single pulse chronoamperometry were optically transparent, contrarily to potentiodynamically grown films that presented a metallic bluish colour. This optical characteristic of electrochemically synthetized iridium oxide films was already reported, which can vary from several shades of blue to colourless transparent, depending on its oxidation state [141,267,268].

Table 5.8: Summary of potentiometric parameters — slope, E-axis intercept and correlation coefficient — of the IrO_x films grown potentiostatically for different applied potentials.

E_a /V *vs.* RRE	Slope /mV pH^{-1}	b /mV_{RRE}	R^2
0.70	-60.9	731.3	0.9975
0.75	-61.0	724.6	0.9973
0.80	-61.7	687.1	0.9976
0.85	-60.3	715.0	0.9969
0.90	-62.8	706.4	0.9993

During the potentiometric characterization for very high pH, a spontaneous reduction of films was evidenced by the potential shift to more cathodic values, revealing a hypothetical need to reduce the films during the synthesis. In fact, the difference between potentiostatic and potentiodynamic synthesis is the scanning at cathodic potentials.
For this reason, it was decided to study the application of a reduction potential pulse during synthesis and its effect on the potentiometric response of such sensors.

5.2.2.1. Double pulse deposition

The most important experimental parameters of double pulse chronoamperometry are the anodic and cathodic potentials — E_a, E_c — and their steps — t_a, t_c —, which can influence films composition (different valence oxides ratio or hydrogen content) and morphology (structure and porosity) [269,270]. Besides pulse parameters, growths through this technique can also be controlled with the time of synthesis that is determined by the number of cycles. Among all growth parameters, it was considered that pulse parameters have higher relevance, since the sensitivity of electrochemical sensors based on an equilibrium between metal oxides with different oxidation states depends on the ratio between those metal oxides and surface area of sensitive material [120]. Therefore, different anodic and cathodic steps — 1, 4 and 9 seconds — and different anodic potentials — 0.75, 0.8 and 0.85 V *vs*. RRE— were studied for a constant cathodic potential — -0.3 V *vs*. RRE — and constant total time of oxidation — 180 seconds — adjusted through the number of cycles. Table 5.9 summarizes the growth parameters for each sample.

Table 5.9: Experimental parameters of IrO_x synthesis (E_a, τ_a, τ_c and number of cycles) for each sample. The cathodic potential (E_c=-0.3 V_{RRE}) and total time of oxidation (180 s) were kept constant.

Sample	E_a /V_{RRE}	t_a /s	t_c /s	Nº of cycles
1	0.75	1	1	180
2	0.75	4	4	45
3	0.75	9	9	20
4	0.80	1	4	180
5	0.80	4	9	45
6	0.80	9	1	20
7	0.85	1	9	180
8	0.85	4	1	45
9	0.85	9	4	20
10	0.80	1	1	180
11	0.80	4	4	45
12	0.80	9	9	20
13	0.80	1	9	180
14	0.80	4	1	45
15	0.80	9	4	20
16	0.85	1	1	180
17	0.85	4	4	45
18	0.85	9	9	20

Figure 5.29 shows the double pulse chronoamperogram with an anodic potential and step of 800 mV (*vs*. RRE) and 1 second, respectively, and a cathodic potential of -300 mV (*vs*. RRE) with a step of 4 seconds. Time-current transients of iridium oxide synthesis by double pulsed potential method are presented through the overlapping of successive cycles in order to easily visualize the evolution of

current density in anodic and cathodic pulses. Anodic and cathodic transients present a peak of current density at 0.2 and 0.1 seconds, respectively, which increases with successive cycles, suggesting an increase of the number of iridium oxide nuclei.

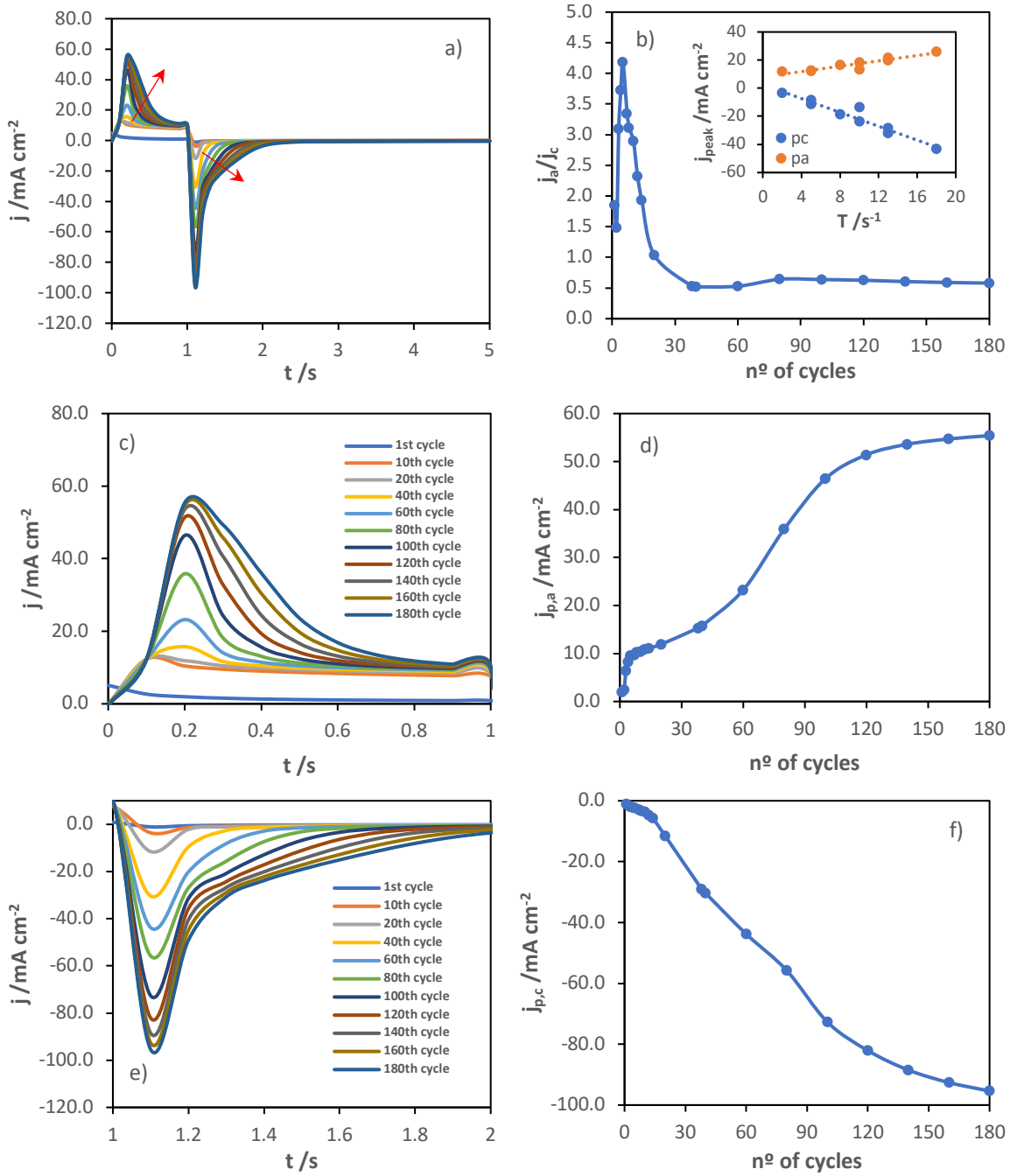

Figure 5.29: a) Current-time transients of double pulse growth with an anodic step of 0.8 V_{RRE} for 1 second, and a cathodic pulse of -0.3 V_{RRE} for 4 seconds (180 cycles); b) evolution of the rate between redox peaks with the number of cycles and redox peaks of the 20th cycle as a function of cycle time (sum of anodic and cathodic steps) as inset; c) detail of anodic steps; d) evolution of anodic peak; e) detail of cathodic steps; and g) evolution of cathodic peak.

The evolution of anodic and cathodic peaks of sample 4 (Figure 5.29 b) suggests that the growth presents three main stages. Until 5th cycle, the oxidation peak increases with a higher rate than the cathodic one, reaching a ratio j_a/j_c of about 4. This behavior is attributed to the initial substrate

coverage by the first iridium oxide nuclei until it gets a complete layer of deposit. Then, the magnitude of the reduction rate increases until reaching the double of the magnitude of the oxidation peak from the 40th cycle until the end of electrodeposition. Redox peaks are mainly affected by the pulse period (as shown in the inset of Figure 5.29 b) increasing linearly with the increase of the sum of anodic and cathodic steps. The increase of cathodic peaks was 2.5 higher than the increase of anodic peaks.

The electrochemical behavior of these modified electrodes was studied by cyclic voltammetry with a scan rate of 50 mV/s in an aqueous solution of 0.1 M lithium perchlorate (supporting electrolyte) and is shown in Figure 5.30. The scans started at the cathodic limit in the anodic direction. Iridium oxide films presented a considerable capacitive response, as already reported [260].

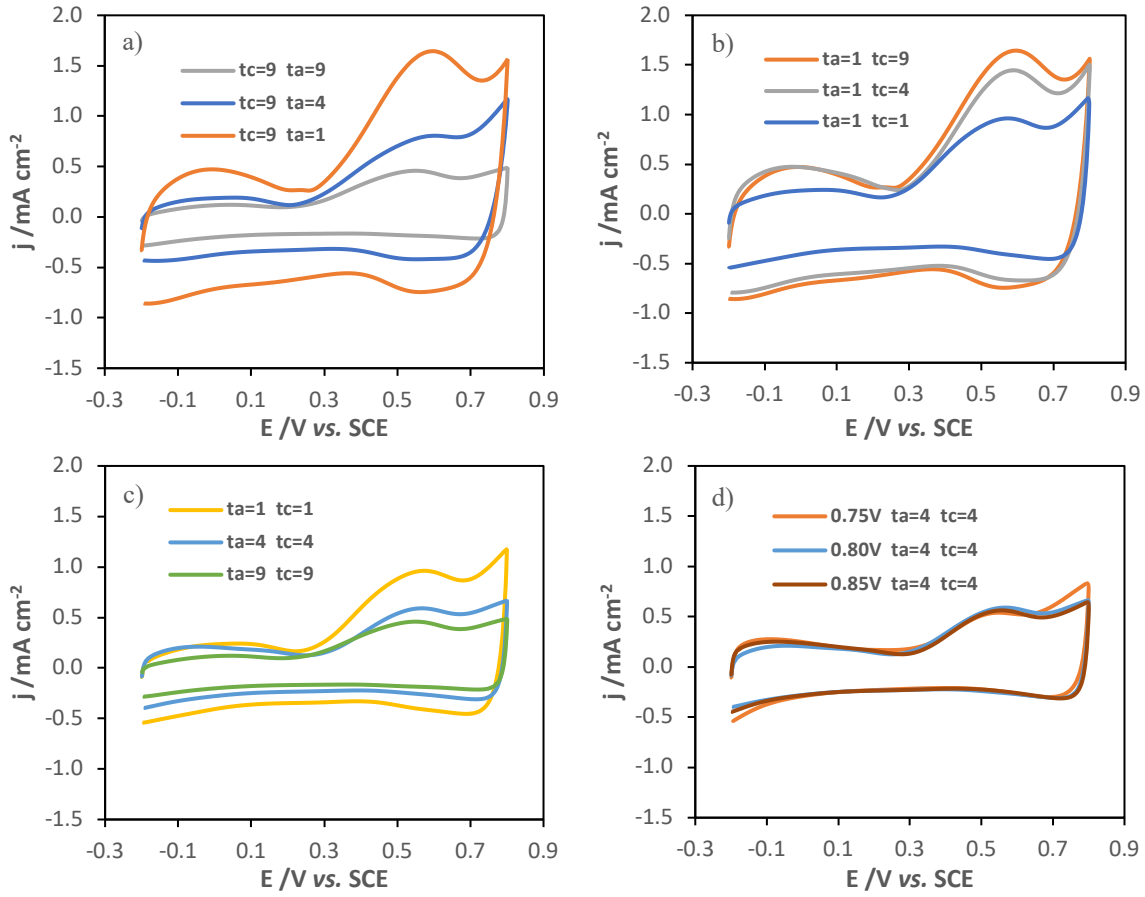

Figure 5.30: Cyclic voltammograms of electrochemical behaviour of double pulse modified electrodes, in an aqueous solution of 0.1 M $LiClO_4$ with a scan rate of 50 mV s^{-1}.

Cyclic voltammograms present a well-defined anodic peak at around 600 mV *vs.* SCE associated with the Ir(III)/Ir/IV) reaction [260]. The decrease of anodic step for the same cathodic step leads to a higher redox and capacitive response of iridium oxide films (Figure 5.30 a). The pulse frequency also influences the electrochemical behavior of modified electrodes. The increase of pulse discretization leads to higher anodic peak and capacitive response. From other side, the anodic potential does not influence the electrochemical behavior of such films (Figure 5.30 b and d, respectively). The dependence of the anodic peak at 600 mV *vs*. SCE on anodic and cathodic steps of electrodeposition is shown in Figure 5.31. This peak increases exponentially with the increase of the square route of cathodic step and with the decrease of anodic step used in the double pulse

synthesis of iridium oxide films. The high correlation between the anodic peak of the electrochemical response and the square root of the reduction time reveals the reduction is a fundamental process in the growth of these films.

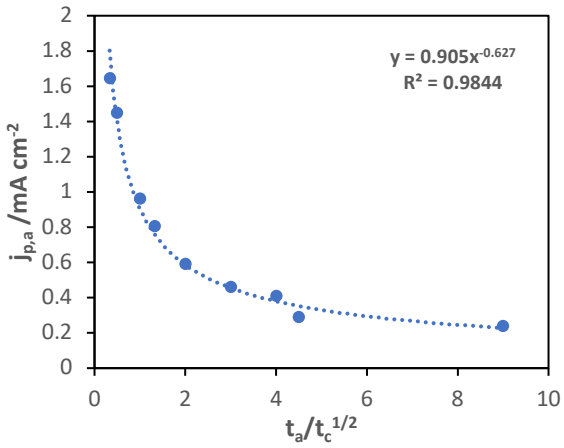

Figure 5.31: Relation between the anodic peak of voltammetric characterization and the rate of anodic and cathodic steps of electrodeposition.

Figure 5.32 a) and b) shows the potentiometric response of two representative samples grown with step ratios of 1/9 and 4, and the calibration curve of the sample with t_a/t_c=1/9, respectively. Only the sensors synthetized with a ratio t_a/t_c<0.5 presented a stable potentiometric response for pH 2, as shown in Figure 5.32 (a), which can be seen by the continuous open circuit potential with time, for pH 2 buffer solution.

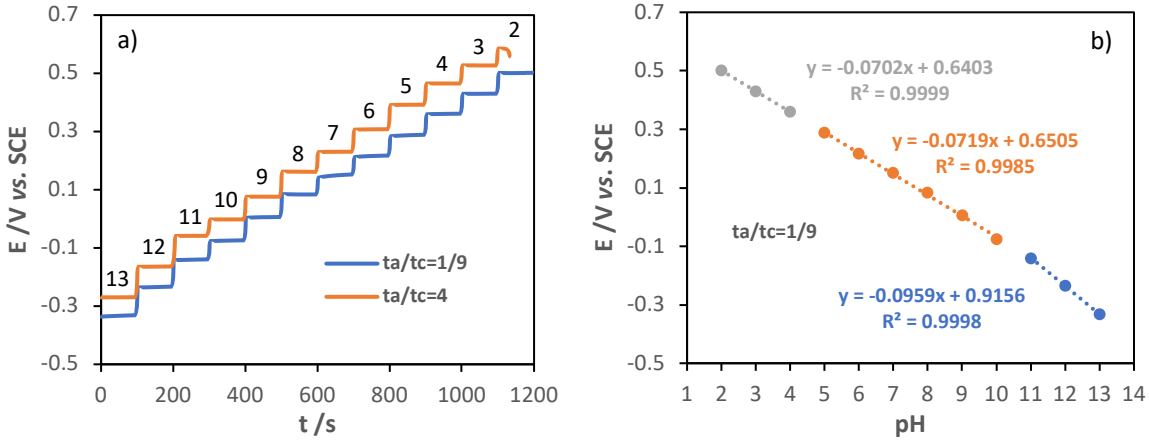

Figure 5.32: Potentiometric response of IrO_x films grown by double pulse chronoamperometry with τ_a/τ_c of 4 and 1/9 (a) and calibration curve of sample grown with τ_a/τ_c of 1/9 (b).

The potentiometric response of these films presents 3 different pH regions. Several authors have reported this behavior of electrochemically synthetized iridium oxide sensors [271]. The potentiometric response of AIROF prepared by cyclic voltammetry in 1 M $HClO_4$ was studied through probe beam deflection presenting two regions: a pH<4 region dominated by H^+ exchange, and a pH>4 region dominated by OH^- exchange [259]. These modified electrodes also present a pH>11 region that present a super-Nernstian slope between 92.5 and 105.2 mV_{SCE} pH^{-1} unit. Region 1 (pH<4) presents near Nernstian slopes that vary between 49.7 and 70.2 mV_{SCE} pH^{-1} unit and region 2 (11>pH>4) has a super-Nernstian slope between 69.6 and 78.7 mV_{SCE} pH^{-1} unit. Table 5.10

summarizes the potentiometric parameters of each pH region for all samples. The existence of different pH regions in the potentiometric response of the IrO_x electrodes may be related to the different content of oxides with different valence states.

Table 5.10: Summary of potentiometric parameters —slope, E-intercept, and correlation coefficient — for each pH region (1, 2 and 3) of all samples.

	Region 1			Region 2			Region 3		
Sample	**slope /mV pH^{-1}**	**b /mV$_{SCE}$**	**R^2**	**slope /mV pH^{-1}**	**b /mV$_{SCE}$**	**R^2**	**slope /mV pH^{-1}**	**b /mV$_{SCE}$**	**R^2**
1	-62.5	589.1	1	-74.1	641.7	0.9991	-92.5	847.8	0.9997
2	-58.3	599.7	0.9993	-75.5	673.8	0.9994	-94.5	888.1	0.9998
3	-60.4	605.2	1	-75.8	674.0	0.9992	-94.1	877.9	0.9999
4	-68.2	600.9	0.9999	-71.9	621.8	0.9981	-93.2	856.4	0.9999
5	-63.7	624.9	1	-74.8	675.4	0.9991	-95.4	906.0	1
6	-56.3	761.8	0.9999	-72.6	824.2	0.9989	-94.1	1069.2	0.9996
7	-70.2	640.3	0.9999	-71.9	650.5	0.9985	-95.9	915.6	0.9998
8	-49.7	687.2	0.9897	-76.7	797.7	0.9996	-99.3	1055.2	0.9997
9	-56.8	664.9	0.9985	-78.7	755.4	0.9998	-100.3	1004.8	1
10	-60.7	616.1	1	-75.3	678.4	0.9996	-100.8	975.6	0.9996
11	-60.0	622.9	1	-75.9	691.1	0.9996	-101.9	993.5	0.9998
12	-57.0	599.1	1	-75.5	677.0	0.9997	-101.9	983.2	0.9997
13	-69.5	584.2	0.9999	-69.6	588.3	0.9982	-98.4	913.1	0.9998
14	-60.1	704.4	0.9998	-78.0	778.7	0.9994	-105.2	1098.7	1
15	-62.0	669.4	0.9993	-77.4	738.3	0.9996	-104.2	1053.7	1
16	-60.8	649.4	1	-77.0	717.6	0.9995	-103.3	1027.8	1
17	-57.1	632.7	0.9984	-76.4	712.0	0.9996	-102.6	1021.7	1
18	-59.3	631.9	0.9999	-76.0	702.0	0.9994	-104.1	1031.1	1

As only sensors synthetized with a ratio t_a/t_c<0.5 presented a stable potentiometric response for pH 2, more points were studied within this ratio with different anodic and cathodic time pulses — 0.5 and 16 seconds, respectively.

In order to obtain the individual contribution of anodic and cathodic steps, experiments were conducted maintaining constant the total time of oxidation and also the anodic and cathodic potentials at 800 and -300 mV *vs*. RRE, respectively. Figures 5.33 a) and b) show the dependence of slope and E-intercept, of region 2, on anodic and cathodic steps.

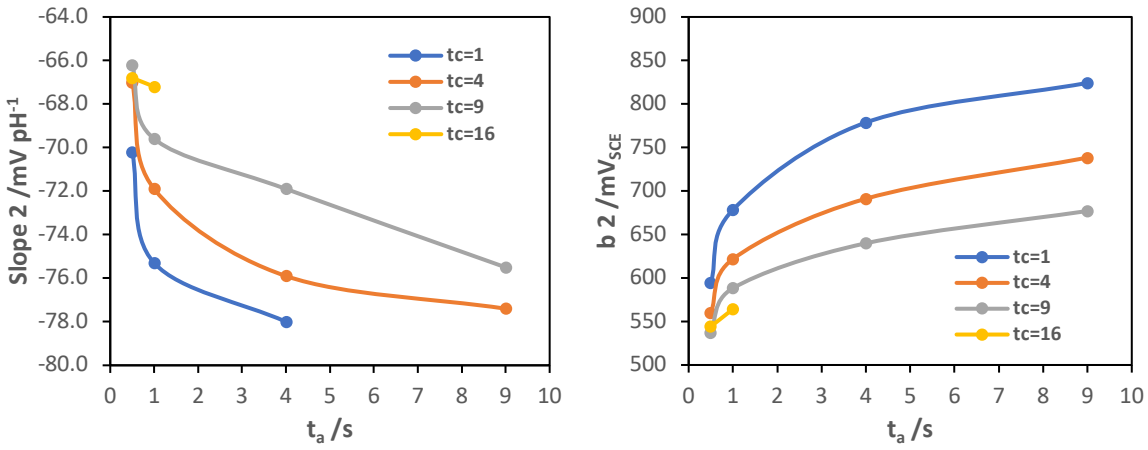

Figure 5.33: Potentiometric parameters — slope and E-intercept — for region 2 as a function of anodic and cathodic steps.

The decrease of the anodic step leads to near-Nernstian slope and a shift of the calibration curve to more negative potentials. The decrease was verified either by keeping constant the cathodic step and decreasing the anodic step or by fixing the anodic step and increasing the cathodic step (time of cathodic polarization). Similarly, the anodic step constant, higher cathodic steps have the same effect as with a decrease of anodic time. Therefore, the potentiometric response of iridium oxide films depends on a compromise between anodic and cathodic steps.

Figure 5.34 presents the potentiometric parameters of region 2 as a function of the ratio between anodic and cathodic steps (a and b) and as a function of the total time of reduction (c and d). The slope and E-intercept for the medium pH level present a logarithmic correlation with the ratio t_a/t_c in which an increase of the ratio, due to anodic step increase or to cathodic step decrease, leads to more super-Nernstian slope (Figure 5.34 a) and to a potential shift of the calibration curve to more positive values (Figure 5.34 b). This correlation is even stronger for t_a/t_c <1. Since the total oxidation time is fixed for all the samples (180 seconds), it is natural to have a considerable correlation between E-intercept and the total reduction time.

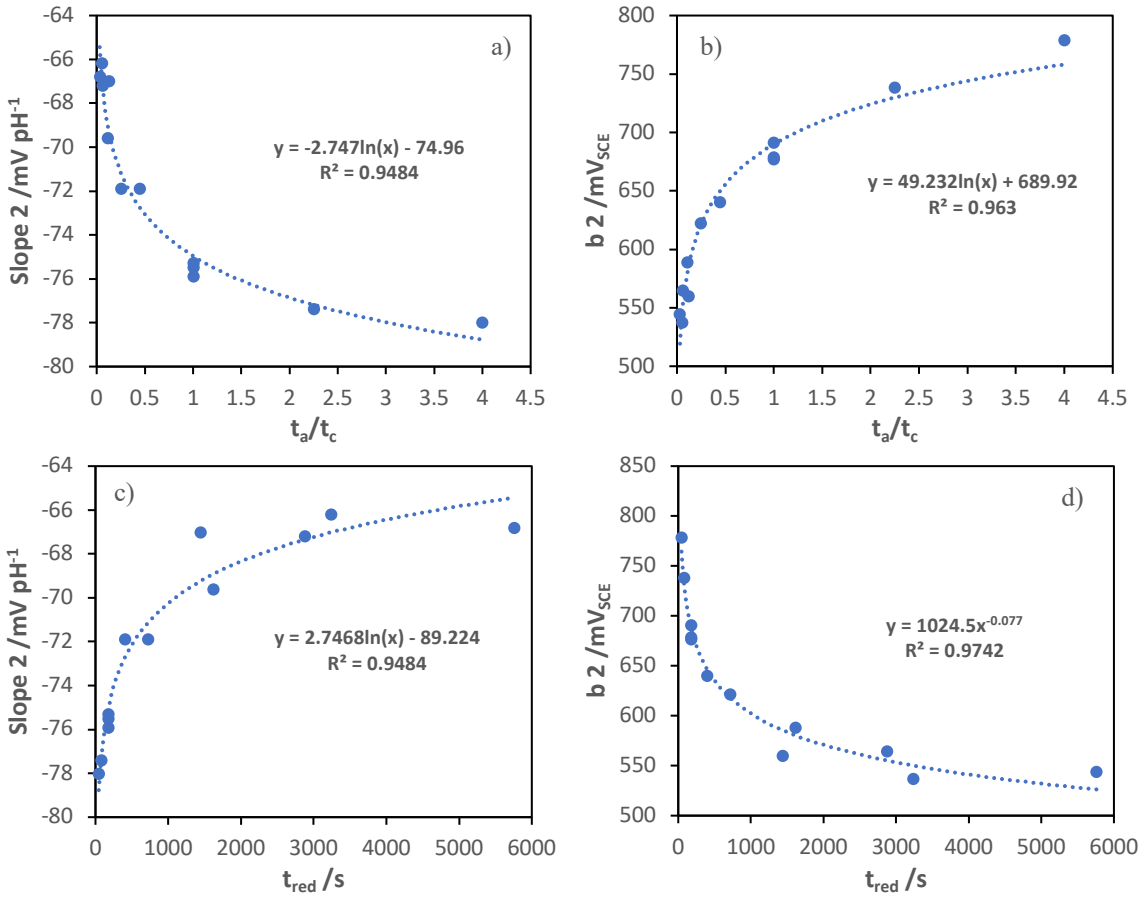

Figure 5.34:Potentiometric parameters — slope and E-intercept — for pH region as a function of the rate of anodic and cathodic steps (a and b, respectively) and total reduction time (c and d, respectively).

In line with previous results from the first sensors, new modified electrodes with a ratio t_a/t_c equal or less than 0.5 continue showing a stable response for pH values lower than 4, as shown in Figure 5.32 a). Besides the higher stability in the acid range, modified electrodes within this ratio also present a homogeneous bluish colour. Figure 3.35 a) and b) presents the slope and E-intercept, respectively, of all samples for each pH level as a function of t_a/t_c. Potentiometric parameters of levels 1 and 2

intercepts at values of t_a/t_c equal to 0.1 and, therefore, modified electrodes with these particular growth conditions present a calibration curve with only 2 levels: a pH>11 region with a slope of about 100 mV/pH unit, and a pH<11 level with a slope between 66 and 70 mV/pH. The increase of frequency pulse with higher cathodic and lower anodic steps leads to an improve of potentiometric response of double potential pulse synthetized iridium oxide films.

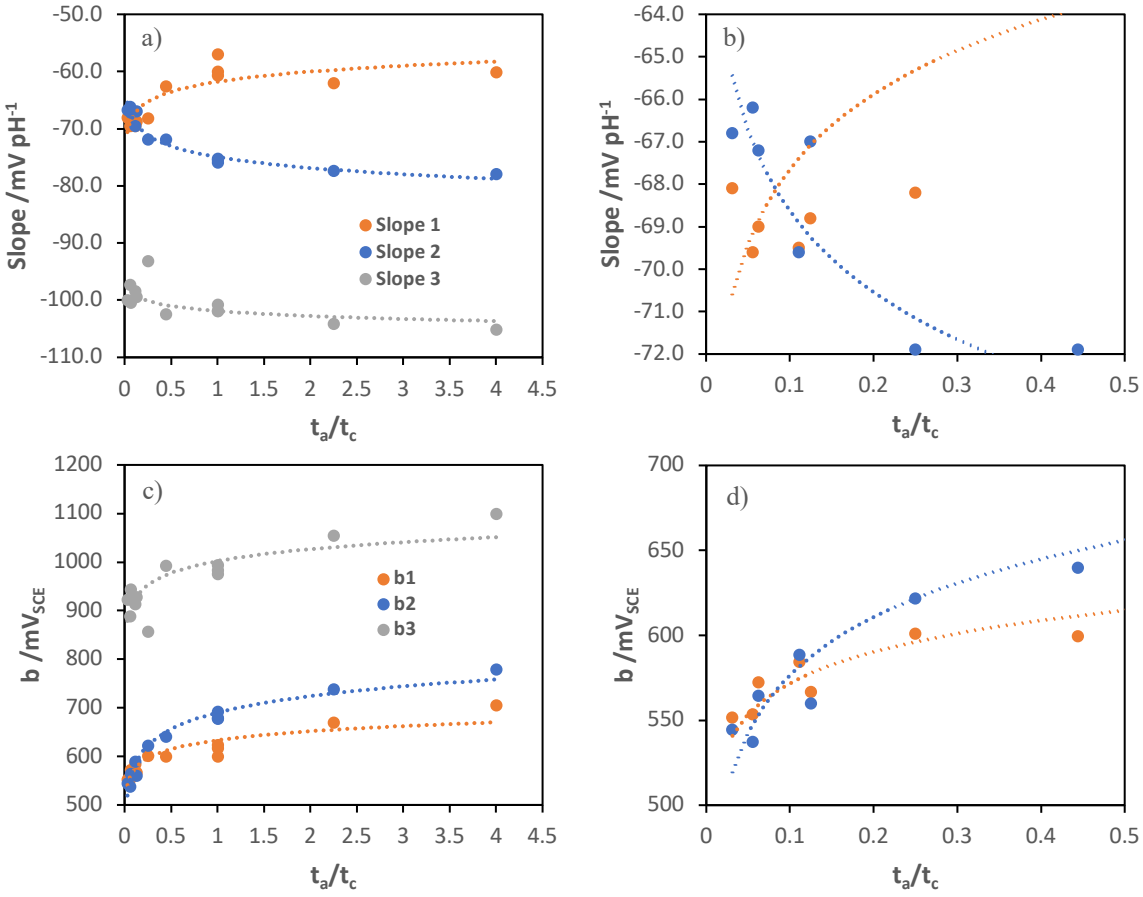

Figure 5.35: Potentiometric parameters — slope and E-intercept — of each pH region as a function of τ_a/τ_c (a and c, respectively) and detail of interception of slope and E-intercept of region 1 and 2 (c and d, respectively).

The effect of different anodic potentials of synthesis —0.75, 0.80 and 0.85 V_{RRE} — on the potentiometric response of iridium oxide films for pH detection was also studied for different pulse period (sum of anodic and cathodic steps) — 2, 8, and 18 —, as shown in Figure 5.36.

The influence of anodic potential on the potentiometric response of iridium oxide films increases for higher pulse frequency growths. Just as was the case with the single pulse potentiostatic growths, the increase of oxidation potential leads to the formation of more hydrated iridium oxide films presenting a potentiometric response with a higher slope (super-Nernstian) and a shift to more positive open circuit potentials.

The IrO_x films synthesized in a double pulse potentiostatic regime showed a linear response in the pH region between 10 and 2, while potentiodynamically grown sensors exhibit a linear response in the pH region between 13 and 5. Consequently, IrO_x sensors synthesized by cyclic voltammetry are more suitable for application in an environment such as the pore solution of a cementitious material.

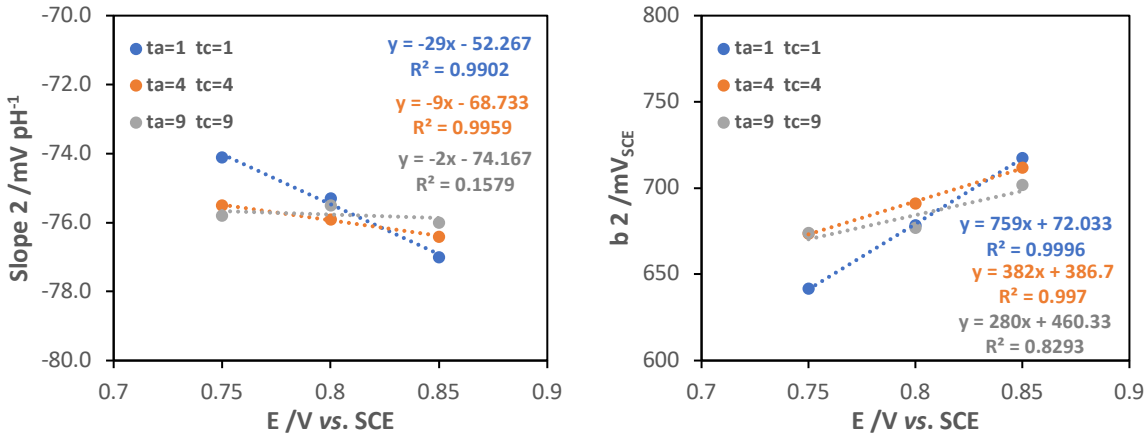

Figure 5.36: Potentiometric parameters — slope and E-intercept — for pH region 2 as a function of anodic potential — 750, 800 and 850 mV vs. RRE — for synthesis with different pulse frequencies — 1/2, 1/8 and 1/18.

5.2.3. Stability study

With the aim of studying the influence of electrodes aging on their potentiometric response, 4 sensors were prepared by cyclic voltammetry with a scan rate of 50 mV s^{-1} for 50 cycles in the potential window of -0.3 to 0.8 V (*vs.* RRE). After the growth, modified electrodes were immediately characterized potentiometrically (day 0) and then they were stored in different environments — air, buffer solutions with pH 4, 7 and 11. Figure 5.37 a) and b) shows, respectively, the potentiometric response of the sensors stored in pH 4 buffer solution and in air immediately after their synthesis (day 0) and after 262 days of storage. The response time of the sensor immersed in buffer solution with pH 4 was slightly affected as the film degraded. In the measurement carried out on day 262, it was evident that most of this IrO_x film was removed from the substrate and, consequently, the potentiometric response of the electrode was dominated by the stainless steel. In the case of the electrode stored in air, after 262 days, the potentiometric response showed a shift towards more negative potentials but remained fast and reversible for the pH range between 13 and 2.

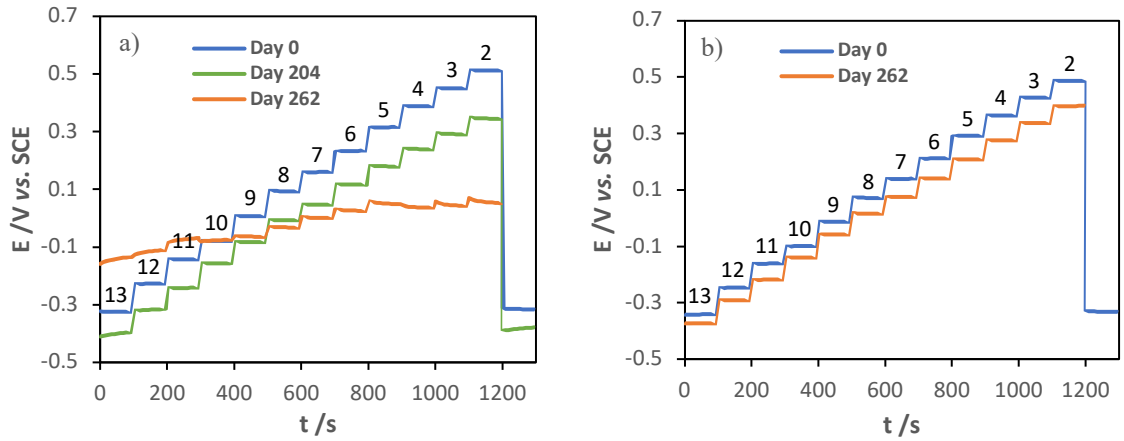

Figure 5.37: Evolution of the potentiometric response of the IrO_x electrodes after 204 and 262 days of immersion in pH 4 buffer solution (a) and after 262 days stored in air (b).

Figure 5.38 shows the evolution of calibration curve parameters with time of storage in the different media. The storage environment influences the potentiometric response of iridium oxide films. The slope of region 1 is slightly affected by different storage media, which present a maximum variation of 3 mV_{SCE} for 85 days of storage in buffer solution with pH 4. The media — air, pH 7 and 4 — promote a shift of both regions of the calibration curve to more negative values and decreases its slope, while an alkaline media — pH 11 — leads to a shift in the opposite direction and to a higher slope. The variation due to the storage in an alkaline environment was already reported, but without suggesting an explanation for this behavior [120]. The potentiometric response in the acid region (pH<4) of the electrode stored in pH 4 buffer solution began to degrade between the 50th and 100th days of immersion, which was evidenced by the decrease of the slope in region 1. The variation of calibration curve parameters is higher in the first 50 days of storage and then start to stabilize with time.

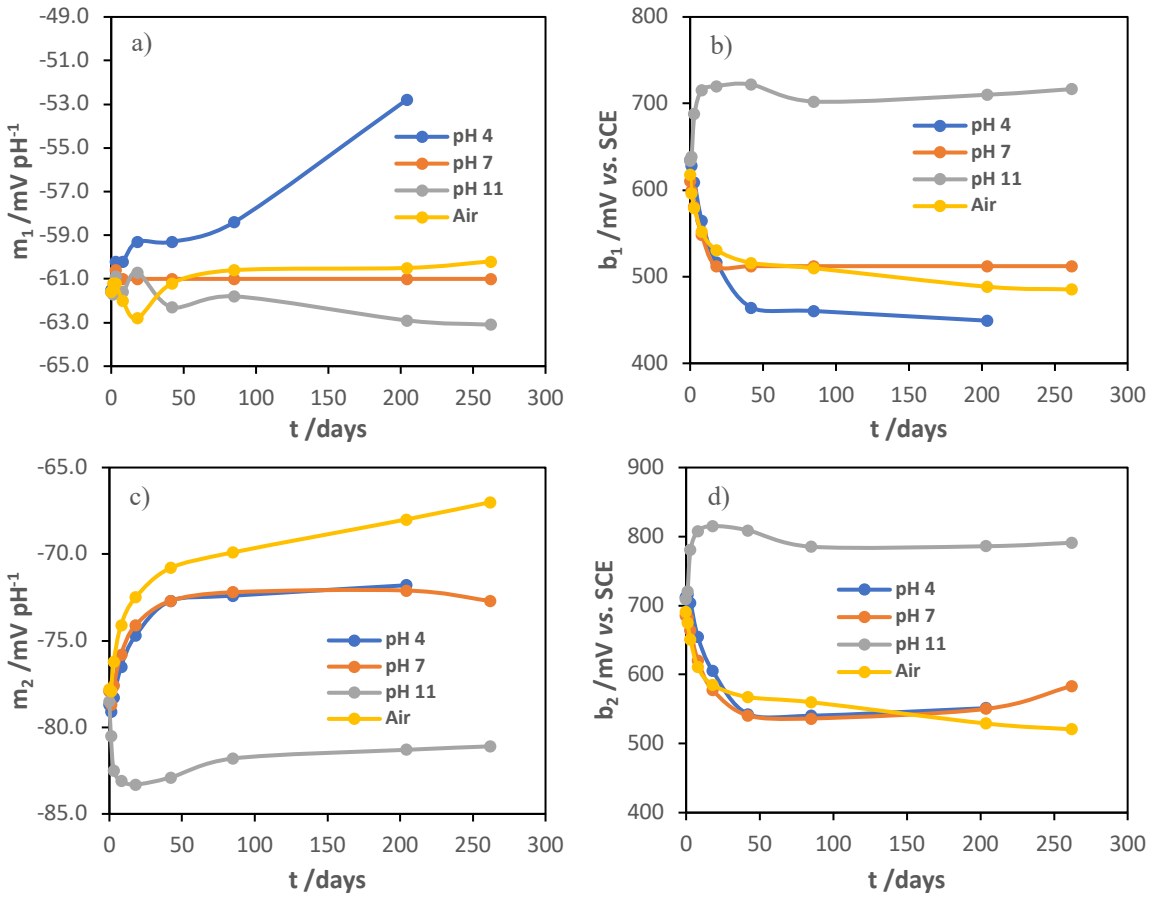

Figure 5.38: Evolution of potentiometric parameters — slope and E-intercept — for pH regions 1 and 2, with aging in different environments — air, pH 4, 7 and 11.

Even after about 37 weeks, all modified electrodes, with the exception of the one stored in buffer solution with pH 4, continued to show an immediate and reversible potentiometric response. The electrode stored in buffer solution with neutral pH exhibited the smallest variation of potentiometric parameters with aging.

5.3. Polypyrrole

The last material that was tested as a pH sensor was polypyrrole. Initially, a potentiodynamic growth was performed in order to determine the potentials range at which there is oxidation of the monomer in solution, without reaching a potential that could lead to an over-oxidation of the conducting polymer. The potentiodynamic growth of the polypyrrole film on a platinum electrode in a solution of 0.1 M Py and 0.1 M $LiClO_4$ with a scan rate of 50 mV/s, for 10 cycles, is represented in Figure 5.39. The current density corresponding to the oxidation of the monomer increases with successive cycles, due to the easier nucleation on the polymer itself than on the substrate. The current densities corresponding to the reduction (undoping) and oxidation (doping) of the polymer increase as the number of cycles increases due to the increase of the number of active nuclei adsorbed on the working electrode. In addition, the distance between the redox peaks increases as well due to the increase of film resistivity, which is mainly related with the ionic mobility within the polymeric matrix.
The synthesis of the films was carried out through a potentiostatic regime in an aqueous solution of 0.1 M Py and 0.1 M $LiClO_4$, for different applied potential pulses — 0.70, 0.65 and 0.60 V *vs*. SCE —, with a total synthesis charge of 1 mC. After synthesis, the conducting polymers were discharged in an aqueous solution of 0.1 M $LiClO_4$ for 10 s with an applied cathodic potential of -0.4 V *vs*. SCE. Figure 5.39 b) presents the current-time transients of film growth.

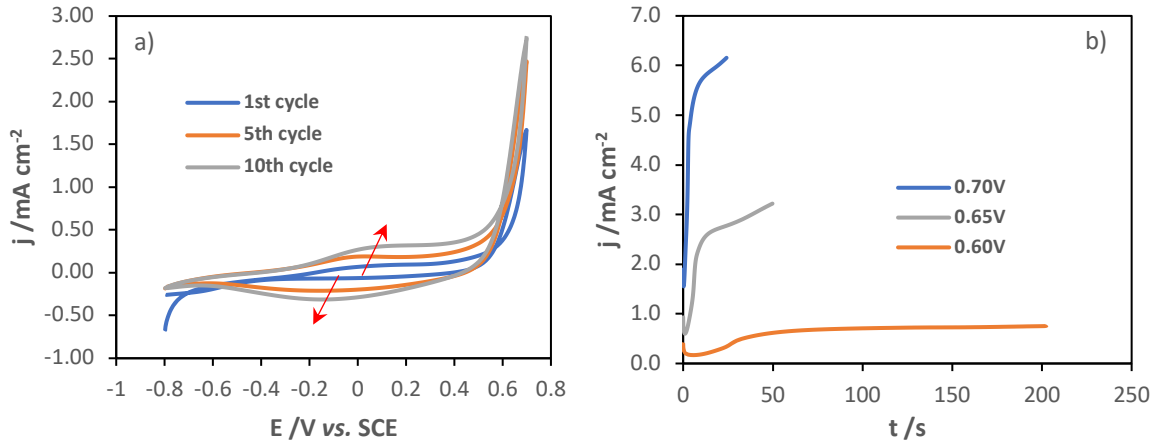

Figure 5.39: Cyclic voltammogram of the potentiodynamic synthesis of polypyrrole on platinum in an aqueous solution of 0.1 M Py and 0.1 M $LiClO_4$ with a scan rate of 50 mV/s for 10 cycles (a) and potentiostatic synthesis of polypyrrole for different applied potentials — 0.60, 0.65 and 0.70 V vs. SCE — for a synthesis charge of 1 mC (b).

From the growth transients it is possible to identify the different stages of the electropolymerization process. Initially, there is an abrupt decrease in the current density caused by the formation of the double layer and the oxidation of monomers and consequent formation of oligomers. When the oligomer chains become insoluble in solution, they start to precipitate on the substrate surface, the current density reaches a minimum value. At this point, the growth of polymeric nuclei starts, causing a gradual increase in the current density, as the nucleation process progresses. Finally, the current density reaches a *plateau* varying slightly due to the fact that the inner layer is more compact and the increasing thickness difficult the doping ions diffusion within the polymeric matrix. From the chronoamperograms of PPy synthesis for different oxidation potentials, it is observed that the increase of the applied potential leads to a faster growth of the film. Both the process of double layer formation and nucleation occur faster. Polypyrrole films grown on platinum present a greenish

colour. In addition to the oxidation potential, the effect of different synthesis charges on the potentiometric response of modified electrodes was also studied.

The potentiometric characterization for pH determination of the modified electrode for an applied potential of 0.65 V *vs*. SCE with a total synthesis charge of 1mC, and its calibration curve, which are representative of all samples, are shown in Figure 5.40 a) and b), respectively.

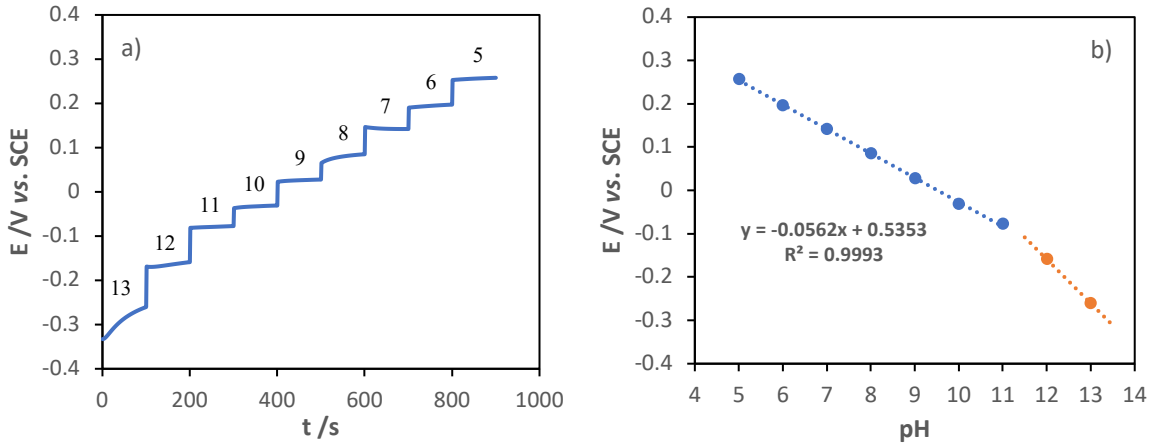

Figure 5.40: Potentiometric characterization of potentiostatically grown polypyrrole film with an applied potential pulse of 0.65 V vs. SCE for a total synthesis charge of 1 mC, and its calibration curve.

The modified electrodes show a slow response in the region of pH above 11 and have a detection limit below pH 5. However, these films present a fast and stable response in the pH region between 11 and 5 with a sub-Nernstian slope between 53.7 and 56.9 mV/pH. Table 5.11 presents the calibration curve parameters — slope and E-intercept — for the potentiostatically grown polypyrrole films.

Table 5.11: Summary of calibration curve parameters — slope, E-intercept and correlation coefficient — for the different potentiostatic synthesis of polypyrrole.

E /V *vs*. SCE	Q /mC	m /mV pH^{-1}	b /mV *vs*. SCE	R^2
0.6	1	56.9	503.6	0.9994
0.65	0.5	56.5	534.4	0.999
	1	56.2	535.3	0.9993
	2	53.7	493.4	0.9991
0.7	1	53.7	522.3	0.9994

The increase of the applied potential pulse, as well as the total charge of synthesis, decreases the slope of the calibration curve.

Finally, the modified electrodes were characterized electrochemically through cyclic voltammetry in an aqueous solution with the same supporting electrolyte used for the synthesis of the films (0.1 M $LiClO_4$) with a scan rate of 50 mV/s. The cyclic voltammograms of polypyrrole films grown for different oxidation potentials, which are represented in Figure 5.4, present well-defined anodic and cathodic peaks at 0.22 and. -0.12 V *vs*. SCE. The oxidation potential does not affect the electrochemical behaviour of the modified electrodes. On the other hand, the increase in the total synthesis charge leads to an increase in the irreversibility of the electrochemical response of the modified electrodes, which is evidenced by the increase in the distance between the redox peaks. The increase in the current density is due to the greater thickness of the film and, consequently, to the higher number of active nuclei.

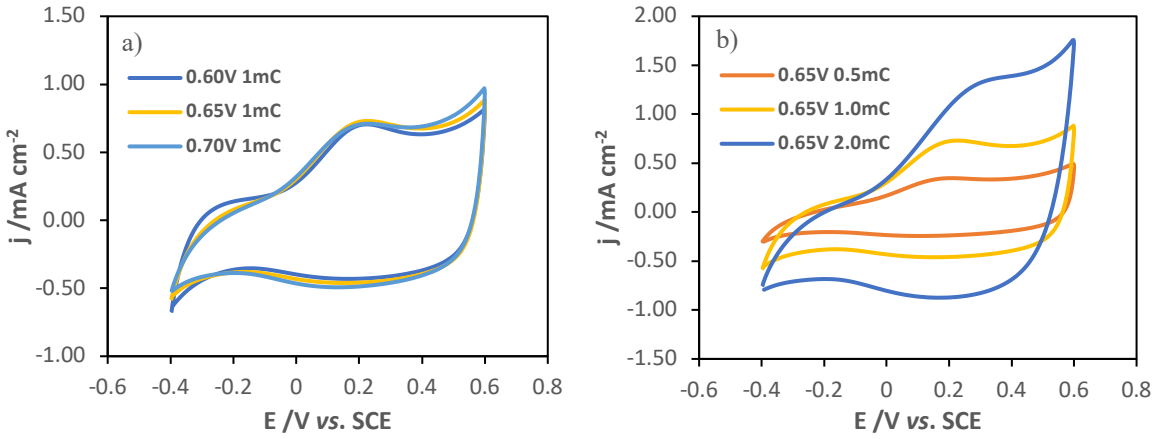

Figure 5.41: Electrochemical characterization of potentiostatically grown polypyrrole films for different applied potentials (a) and for different total charge of synthesis (b).

Polypyrrole films presented an acceptable potentiometric response for the pH region between 11 and 5, but as the response for the alkaline region is too slow, these modified electrodes are not suitable for application in cementitious materials.

5.4. Conclusions

For the determination of pH, metallic oxides and a conducting polymer (PPy) were tested. Regarding metallic oxides, several materials were studied: MnO_2, IrO_x and $IrO_x + RuO_2$.

MnO_2 films potentiodynamically synthesized on stainless steel 316L with a growth solution based on the literature showed poor adhesion to the substrate, regardless of the experimental parameters used (scan rate, number of cycles and anodic limit).

The adhesion was successfully achieved through the growth of an intermediate Ni layer. The MnO_2 film grown on the Ni layer by cyclic voltammetry presented a stable and immediate potentiometric response in the pH region between 6 and 12, with a super-Nernstian slope of 71.7 mV/pH.

A new growth solution with 0.1 M $LiClO_4$ as supporting electrolyte was tested to avoid the time-consuming and costly pre-treatment. The adhesion of the MnO_2 films presented a substantial improvement. The MnO_2 sensors were synthesized potentiodynamically and presented a stable and reversible potentiometric response with a slope of 61 mV/pH.

The results of the different experimental conditions of potentiodynamic synthesis of MnO_2 films suggested a relation between the oxidation time and the potentiometric response (reversibility and time of response). Consequently, the potentiostatic growth of MnO_2 films was studied for different applied potentials and pulse times. The decrease in the applied potential and the increase in the pulse time leads to a decrease in the slope of the calibration curve of the modified electrodes to values closer to the Nernstian.

The synthesis of MnO_2 films for different applied potentials was followed by *in-situ* ellipsometry. The evolution of ellipsometric parameters was similar for the different potential pulses, with exception of 0.7 V *vs*. RRE, suggesting that the nucleation mechanism is not affected by the applied potential. The Psi-Delta values formed an almost closed loop, which is characteristic of a slightly light absorbing film. The formation of two homogeneous layers was considered to achieve a reasonable complete fitting of the experimental data. Initially, an inner more resistive MnOOH layer

between the electrode surface and the manganese compounds film was formed. The increase of the applied potential leads to an increase of the thickness, rate of growth and refraction index of both layers (inner and outer). The increase of refractive index is related to the increase of film density. The outer layer presented a slower rate of growth and a higher conductivity compared to the inner. The film conductivity is related to its extinction coefficient.

MnO_2, despite not having been widely explored by the scientific community as a pH sensor, showed a relevant potentiometric response. In addition, this material represents a low-cost and simple synthesis alternative for pH determination.

IrO_x films produced with the Yamanaka solution were studied in detail. The electrochemical synthesis was performed by cyclic voltammetry, potentiodynamic and potentiostatic methods.

The cyclic voltammogram of IrO_x presented two well-defined redox peaks, A and B, related respectively to the redox couples of Ir(III)/Ir(IV) and Ir(IV)/Ir(V). The increase of the scan rate as well as the decrease of the anodic limit led to a decrease in the ratio between peaks B and A. The potentiometric response of the IrO_x films presented two pH regions: one below pH<4 with near-Nernstian slopes, between 59.0 and 65.5 mV/pH unit, and another for pH>4 with super-Nernstian slopes (between 79.0 and 81.0 mV/pH unit). The response was fast and stable over the entire tested pH range (13-2).

Decreasing the anodic limit of the potentiodynamic synthesis led to a decrease of the slope and a shift of the calibration curve to lower potential values, in both pH regions. The scan rate and number of cycles did not affect the potentiometric response.

The capacitive response of IrO_x films is correlated with the number of iridium oxide nuclei. Both increased with lower scan rate of deposition and higher number of cycles.

The nucleation presents two stages. First, there is the deposition of a homogeneous layer composed by small IrO_x nuclei, followed by the formation of large porous islands made up of round nuclei formed above the first layer.

The study of potentiodynamic synthesis of IrO_x films included the influence of $RuCl_3$ in the growth solution. A concentration of 1 mM $RuCl_3$ showed no effect. Concentrations of 5 and 10 mM $RuCl_3$ decreased the rate of film growth and increased the film resistivity. Their potentiometric response presented a near-Nernstian slope between 56.6 and 63.2 mV/pH that decreased with higher ruthenium content and with higher anodic limit of growth. The capacitive response of the modified electrodes decreased with the increase in ruthenium in solution.

The potentiostatic growth of IrO_x films with a single anodic pulse followed an instantaneous mechanism of nucleation, increasing for higher applied potentials. The increase of the applied pulse intensity led to higher slopes and to a shift of the calibration curve to lower potentials. The potentiometric response was slow and unstable, with an almost Nernstian slope between 60.3 and 62.8 mV/pH.

In the potentiostatic growth with double potential pulse (anodic and cathodic), the anodic and cathodic peaks were mainly affected by the pulse period, presenting a linear increase with increasing growth period (sum of anodic and cathodic steps).

The capacitive response increased with lower anodic pulse time (for the same cathodic pulse time and total time of oxidation) and with higher cathodic pulse time (for the same anodic pulse time). The anodic potential did not affect the capacitive response.

The well-defined peak at 0.6 V *vs*. SCE in the characterization voltammogram increases exponentially with the increase of the square route of cathodic step and with the decrease of anodic step that were used in the double pulse synthesis of IrO_x films.

The potentiometric response of films grown by double pulse chronoamperometry presented 3 different linear pH regions with different slopes: one below pH<4, another between pH 4 and 11 and a third above pH 11.
Finally, potentiostatically grown polypyrrole films were tested for pH determination. The increasing applied potential pulse, as well as the total charge of synthesis, leads to slope decrease to more sub-Nernstian values. PPy sensors present a linear pH region between 11 and 5.
The IrO_x films synthesized by double pulse chronoamperometry showed a linear response in the pH region between 10 and 2, while potentiodynamically grown sensors exhibit a linear response in the pH region between 13 and 5 being, therefore, more suitable for application in concrete.
To finalize the experimental work of IrO_x sensors, the effect of storage of potentiodynamically produced sensors was investigated in air and in buffer solutions with pH 4, 7 and 11. The variation of potentiometric parameters was higher in the first 50 days and then started stabilizing with time. The buffer solution with pH 4 led to the dissolution of IrO_x film after 200 days of immersion. The other electrodes continued showing a fast and stable response after 262 days of test. The electrode stored in buffer solution with neutral pH showed the smallest variation of slope and E-intercept.

CHAPTER 6 Mortar monitoring

The present chapter describes the application of the sensors developed in the previous chapters to monitor the chloride penetration and the pH variation of the pore solution in mortar samples. The pH variation was studied in cases of carbonation and acid attack of cementitious materials. To complement the investigation, iron electrodes were also embedded in mortar samples with the same arrangement as the sensors to simulate steel reinforcement, and their electrochemical state was monitored. Initially, the sensors and the iron electrodes were tested in solution to understand their behaviour in simulated conditions. At the end of the experiments, the mortar samples were sectioned and ground to be analysed by XRD and, in the case of samples subjected to chlorides, to determine the chloride content through a commercial sensor.

6.1. Passivation of iron rebar

The growth of the passive film on the surface of the iron reinforcement is studied through EIS and *in-situ* ellipsometry to understand the electrochemical state of the iron electrodes at the beginning of the tests with the mortar samples.

Before starting the experiments with the electrodes embedded in the hardened mortar, it was important to understand their behavior in simulated solution conditions, both for the initial conditioning of the iron electrodes during the period from the mortar samples casting until the beginning of the acid attack, as well as for the exposure of the electrode to sulfuric acid. An iron electrode was immersed in in an aqueous solution of NaOH 0.1 M with a pH of 12.9 until its OCP reaches a *plateau*, as shown in Figure 6.1.

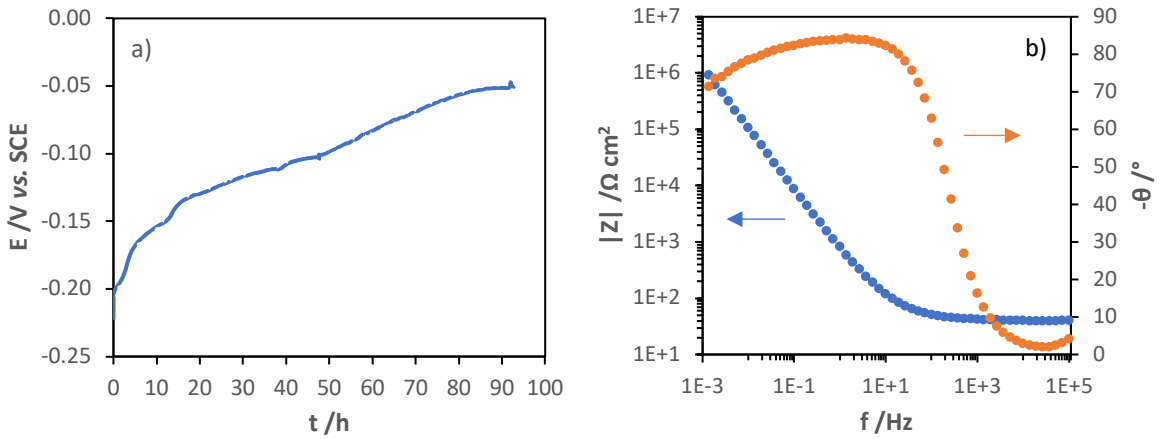

Figure 6.1: Evolution of open circuit potential of the iron electrode immersed in 0.1 M NaOH (a) and Bode diagram of electrode impedance after 92 hours of immersion (b).

The immersion in a very alkaline medium promotes the formation of a passive layer, which is a slow process that takes almost 4 days until its OCP starts to evolve slowly. The most significant variation occurs in the first 3 hours and then the passivation process proceeds more slowly as the film gets

thicker. Figure 6.1 b) shows the impedance of the iron wire in the passive state, after 90 hours of immersion in NaOH 0.1 M, which presents a capacitive response at lower frequencies due to the passive layer formed during immersion in the alkaline solution.

The initial stage of the passive layer growth on a steel electrode was also followed by *in-situ* ellipsometry. The ellipsometric measurements with a frequency of a point per minute were immediately started after the immersion of the electrode. The variation of ellipsometric parameters, which is presented in Figure 6.2 a), was very small suggesting a very low change of the electrode. The Psi and Delta presented a variation of 0.2° and 2°, respectively, for about 16 hours of immersion. Due to this small variation, it is necessary to fit simultaneously the time evolution of the ellipsometric parameters and the delta as a function of psi in order to achieve reliable results. The initial decrease of Psi until reaching a minimum has been reported to be a typical behaviour of most metal and semiconductor surfaces during the initial stages of oxidation due to oxygen incorporation [272]. The decrease of Psi may be related to the initiation of metal oxide islands formation due to adsorbed OH^- until reaching a minimum, which can be related to the full coverage of substrate surface [273].

Figure 6.2 b) presents the ellipsometric values of delta as a function of psi and the computationally simulated curves for the growth of the passive layer on steel. As can be seen in Figure 6.2 b), to achieve a reasonable and complete fitting of the experimental data it was necessary to consider the formation of three distinct and homogeneous layers. The process of island formation began immediately after immersion and the first oxide layer was formed in about 15.5 minutes, showing a higher porosity (space between nuclei) than the substrate that is expressed on the low refractive index (n_f=1.43), which is close to the solution refractive index (n_s=1.335). The extinction coefficient (k_f=0.108) still has a strong influence of the substrate — k_f is higher than the subsequent layers but lower than the substrate (k_{steel}=3.856).

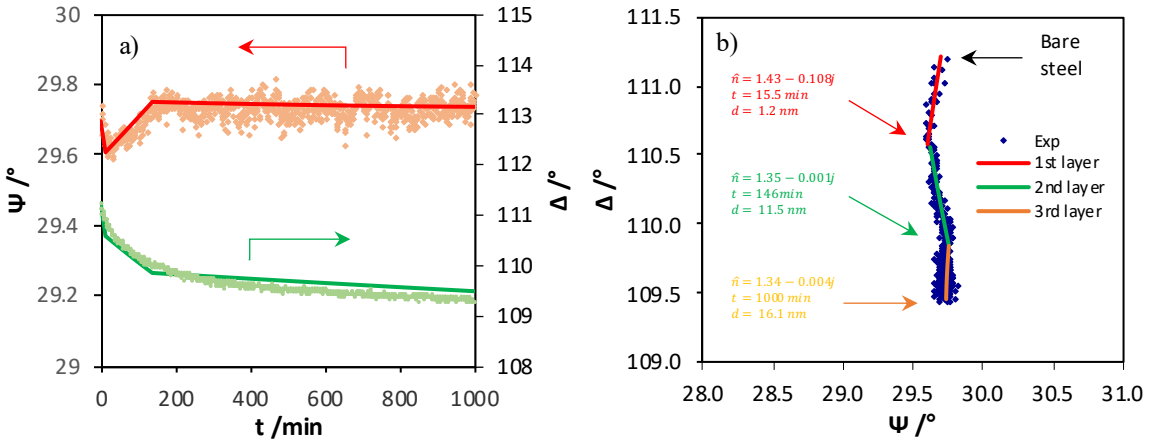

Figure 6.2: Evolution of the ellipsometric parameters — Ψ and Δ — during 1000 minutes of immersion of the steel electrode in 0.1 M NaOH (left) and experimental values of Δ as a function of Ψ collected during the natural growth of a passive layer on the steel surface and simulated trajectory generated by assuming the formation of two distinct layers after the initial molecular adsorption on steel surface.

The subsequent layers (intermediate and outer) are more porous (lower n) and very resistive (low k) reaching a thickness of 11.5 and 16.1 nm, respectively. The outer layer is more porous than the intermediate (lower n) and slightly less resistive (high k). The total thickness that the film reaches in 16 hours of immersion is about 28.8 (1.2+11.5+16.1) nm. The determined optical parameters are in agreement with other studies [273,274]. The refractive index of the inner layer — 1.43 — is attributed to $Fe(OH)_2$ formation [273]. The intermediate and outer layer was suggested to be composed by a

porous film of iron hydroxides filled with sodium hydroxide. The lower refractive index of outer layers was explained by the formation of colloidal particles of iron hydroxide with electrolyte incorporated, which leads to slightly different optical properties of the film [274]. The schematic representation of the different layers that make up the grown film is shown in Figure 6.3.

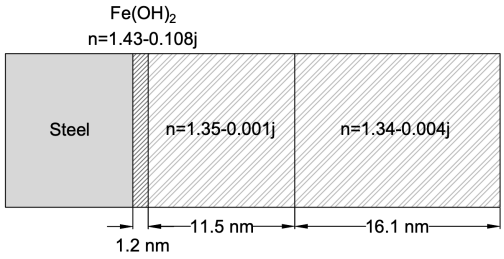

Figure 6.3: Schematic of simulated formation of three distinct and homogeneous layers during steel passivation.

6.2. Chloride penetration

In this section, the process of penetration of chlorides in cementitious materials was studied, with and without an additive (LDH) with the hypothetical ability to capture chloride ions [75], using sensors embedded in the samples at different depths (Fig. 3.2). In parallel, mortar samples exposed to chlorides, with different immersion times, were analysed by XRD and their total chloride content was determined by a commercial sensor. In addition, the electrochemical state of embedded Fe electrodes simulating the steel rebar was also studied during the exposure to the chloride medium.

6.2.1. Synthesis and characterization of sensors

The growth of Ag/AgCl films was performed galvanostatically according to the range of values of the best conditions previously established, with a pulse of 2 mA/cm^2 for 30 minutes in a 0.1 M HCl solution. The *E-t* transient and the calibration curve are presented in Figures 6.4 a) and b).

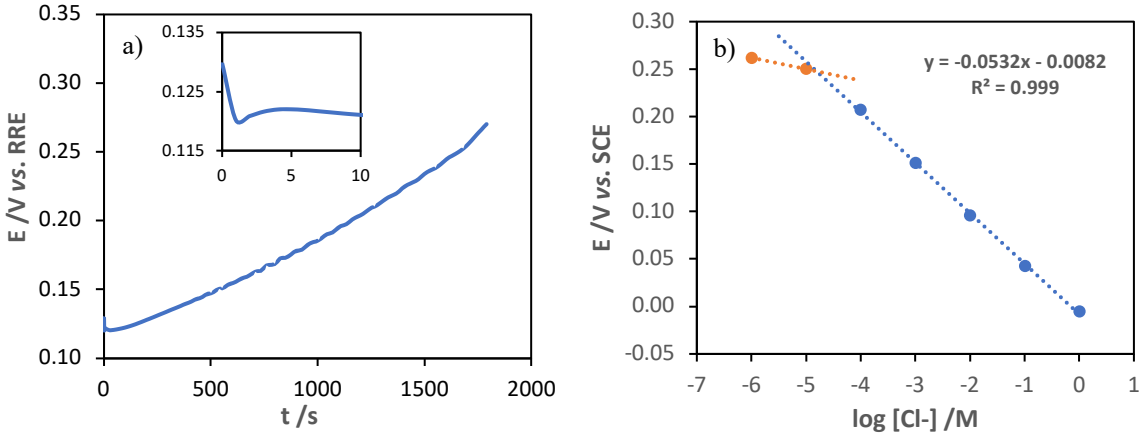

Figure 6.4: a) Potential-time transient of Ag/AgCl electrode synthesis with a current density pulse of 2 mA cm^{-2} for 30 minutes in a 0.1 M HCl solution and b) the calibration curve of the modified electrode.

The calibration curve presents a sub-Nernstian slope of 53.2 mV/pH, which is possibly due to the number of micro-channels formed in the film of silver chloride and to film thickness, which limit the ionic transport until the interfacial region between silver and silver chloride.
Finally, the sensors were grouped on 8-electrode combs with a spacing of 5 mm between each wire. The combs were positioned in the centre of the mortar sample with the outer sensor at 5 mm from the mortar surface, as shown in Figure 3.2.

6.2.2. Response of the sensors

The signal acquisition of each chloride sensor was started immediately after the total immersion of the mortar samples in 3.5% NaCl solution and the open circuit potentials were converted to pH from the calibration curve of each sensor, as shown in Figure 6.5. Two mortar samples with different compositions were tested: one with LDH-NO_2 (which has the hypothetical ability to capture chlorides [75]) and another without this additive (referred as reference sample).
The sample with LDH showed an evolution of the concentration of chlorides as a function of depth much slower than the reference — after 20 days of immersion, only the sensor at 5 mm detected the arrival of chlorides, while in the case of the reference, chloride was already being detected at a depth of 20 mm. The slower ingress of chlorides into the sample with LDH may be due to the capture of chlorides through ionic exchange by the LDH. Recent work has shown that extremely alkaline environments lead to partial dissolution of LDH and preferential ionic exchange of hydroxide ions [275]. An alternative reason for the lower ingress of chlorides in LDH containing samples is a decrease of porosity induced by the presence of LDH particles, or if LDH is partially dissolved, by the formation of Friedel's salts with aluminium ions from the dissolved LDH and chloride from the pore solution, with the consequent decrease of free chloride ions.
The evolution of the chloride content in the reference sample presented two main stages. Initially, chloride penetration was governed by the diffusion process, with a gradual increase in chloride content as a function of depth. On the 40th day, there was the formation of a crack parallel to the sensors, which caused the permeation of solution leading to a rapid increase in the chloride content and reaching a greater depth of chloride arrival. The crack may be caused by the arrangement of the embedded wires.

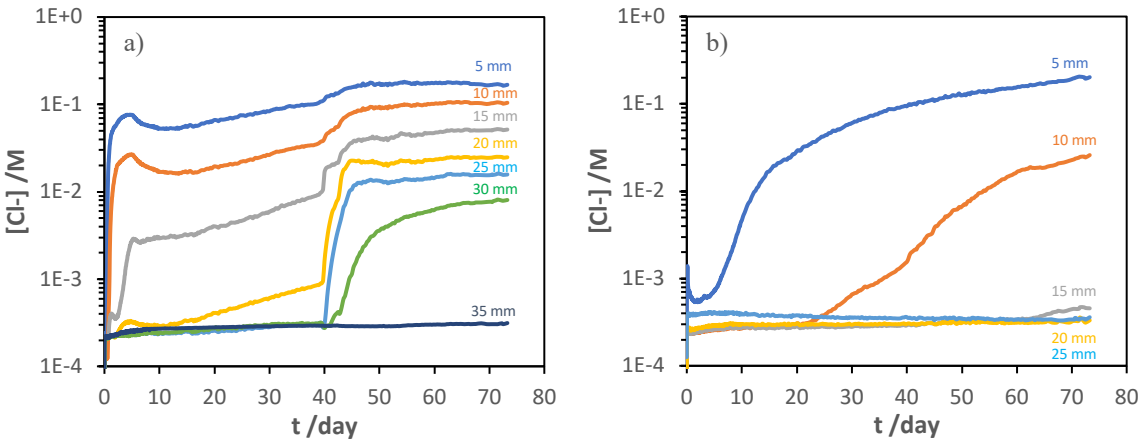

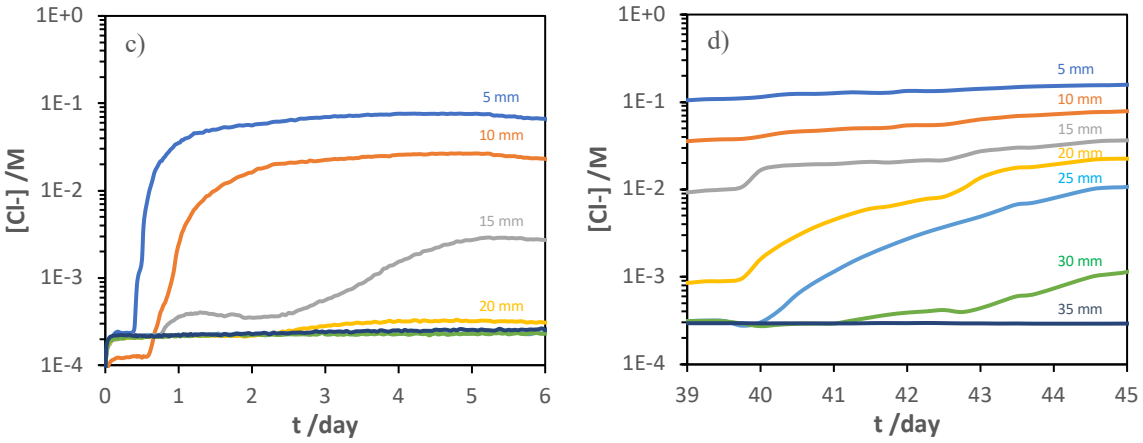

Figure 6.5: Response of embedded Ag/AgCl sensors at different depths — 5, 10, 15, 20, 25, 30 and 35 mm — in mortar samples without (a) and with LDH (b) and detail of the main moments of penetration of chlorides in the sample without LDH (c and d).

6.2.3. Destructive analysis of mortar samples

In parallel with the monitoring with Ag/AgCl sensors, chemical analysis was also conducted on mortars samples, from the same batch, after 0, 6, 16 and 65 days of immersion. After removing the samples from solution, a core was extracted through a dry cut (see Fig. 3.2). Afterwards, this core was sliced into 5 mm sections, which were ground and then diluted in distilled water. The chloride content present in each solution was measured potentiometrically with a chloride ion selective electrode (Mettler Toledo). Figure 6.6 presents the evolution of chloride content per kg of mortar as a function of depth of samples with (b) and without LDH (a). The chloride content is presented in relation to the mortar mass.

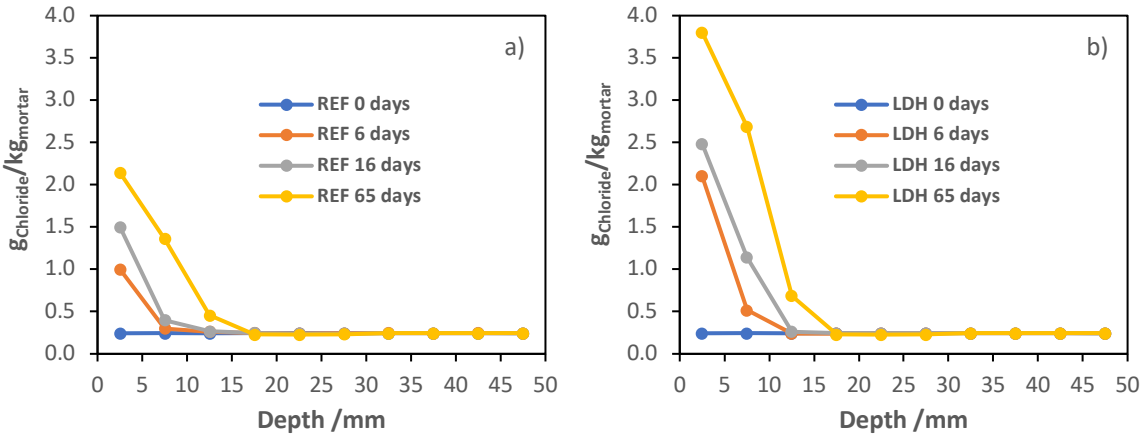

Figure 6.6: Depth profile evolution of chloride content in mortar samples without (a) and with LDH (b) obtained by destructive analysis.

After 65 days of immersion, the samples with LDH presented 3.8, 2.7 and 0.7 g of chloride per kg of mortar, at depths of 2.5, 7.5 and 12.5 mm, respectively. The reference samples only contained 2.1, 1.4 and 0.4 g of chloride per kg of mortar, for the same depths. Contrary to what one would expect, the sample with LDH presented higher chloride content than reference, which can be explained by

the removal of chloride ions from the pore solution through capture by LDH or through the formation of Friedel salts. The removal of chlorides from solution leads to an increase in the bound chlorides content, which in turn will lead to an increase in the total amount of chlorides (free and bound chlorides). Interestingly, the samples have a similar maximum penetration depth — about 15 mm — after 65 days of immersion, which suggests a similar progression of liquid through the pore network in both samples (with and without LDH).
Posteriorly, the samples used for the determination of chlorides content through the destructive method were also analysed by XRD in order to identify the eventual formation of Friedel salts. Figure 6.7 presents the diffractograms of mortar samples with and without LDH for 16 days of immersion at 5 and 10 mm of depth.

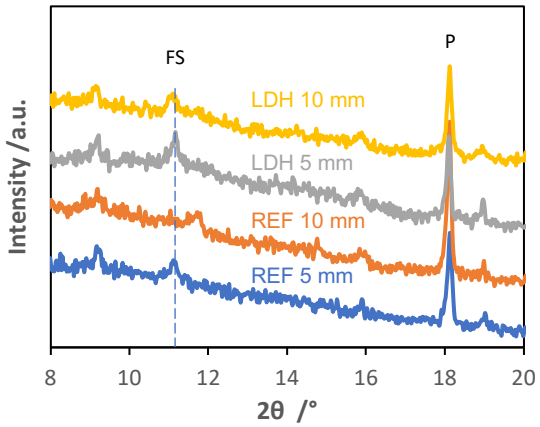

Figure 6.7: Diffractograms of mortar samples with and without LDH, at 5 and 10 mm of depth, after 16 days of immersion in 3.5% NaCl solution. The identified phases were portlandite (P) and Friedel's salts (FS).

The diffractograms were inconclusive. Although it is possible to identify the peak related to Friedel's salts, there is no significant difference between the samples. The big amount of non-crystalline phases present in the sample may have masked the diffractograms.

6.2.4. Response of the iron rebars

In order to confirm the results obtained by the chloride sensors, a set of tests was performed with iron electrodes embedded in the mortar samples to simulate the steel reinforcement. Apart the reference (without LDH) and LDH-NO_2, a third mortar sample with a LDH loaded with an anion without inhibition ability — NO_3^-— was also tested, to show the singular effect of the eventual chloride capture by LDH on the evolution of the electrochemical state of the electrodes. The evolution of the open circuit potentials of the iron electrodes, with the immersion time, is shown in Figure 6.8. It should be noted that the results of the 5 mm electrodes were discarded due to the big heterogeneity of the samples outer surface.
The OCP was initially between 0 and -0.1 V *vs*. SCE, which is typical of passive steel inside mortar. Then, the OCP of the electrodes at 10 and 15 mm of the reference sample (without LDH) dropped and attained values of the active corrosion of iron after, respectively, 5 and 10 days. After 30 days of immersion, the OCP of all electrodes of the LDH samples were still at the potential level characteristic of iron. The results are in agreement with those from the sensors, which showed a rapid

ingress of chlorides up to the first 15 mm of the reference sample during the first month of immersion, while in the sample with LDH, the chlorides only reached the first 5 mm for the same period. The fact that both samples with LDH (LDH-NO_2 and LDH-NO_3) show high OCP indicates lower chloride content and a positive effect from the presence of LDH.

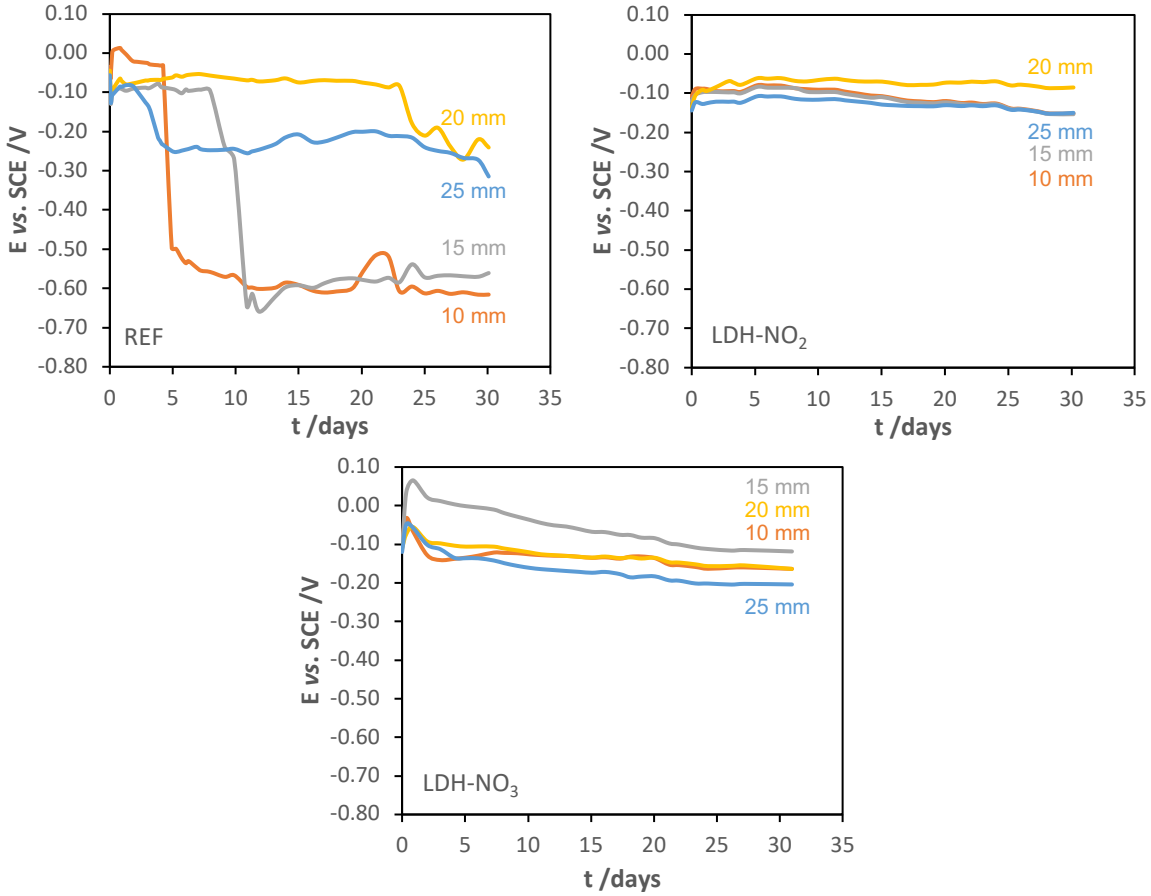

Figure 6.8: OCP evolution of iron electrodes, at different depths — 10, 15, 20 and 25 mm — embedded in mortar samples without additives (REF) and with LDH-NO_2 and LDH-NO_3, for 30 days of immersion in 3.5% NaCl solution.

In addition to monitoring the OCP of the electrodes, the electrochemical state of the iron wire was also accessed by performing EIS. Figure 6.9 presents the Bode diagrams of the EIS carried out to the electrodes at 10, 15, 20 and 25 mm in depth on the 28th day of immersion. In the case of reference sample, the impedance spectra show that the electrodes at 10 and 15 mm present low impedance and are in an advanced stage of corrosion. The electrodes positioned at greater depth are still in a passive state, but already showing signs of corrosion. The spectra show an increase of the resistance at lower frequency with the depth of the electrodes, which is initially associated with the passive state of the electrodes and later, as the corrosion process progresses, with the charge transfer resistance. This result is in agreement with the stratification of chloride content with distance to the surface obtained by the Ag/AgCl sensors.

In the case of samples with LDH, after about 1 month of immersion, all electrodes were still passivated, only showing very slight signs of processes related to the beginning of the destruction of their passive layer. The iron electrodes of the sample with LDH-NO_3 also presents high impedances after 28 days of immersion, which seems to be a result of less chlorides in the pore solution due to

removal of chlorides from the pore solution of the mortar samples. The passive state of the electrodes is evidenced by the capacitive response at lower frequencies.

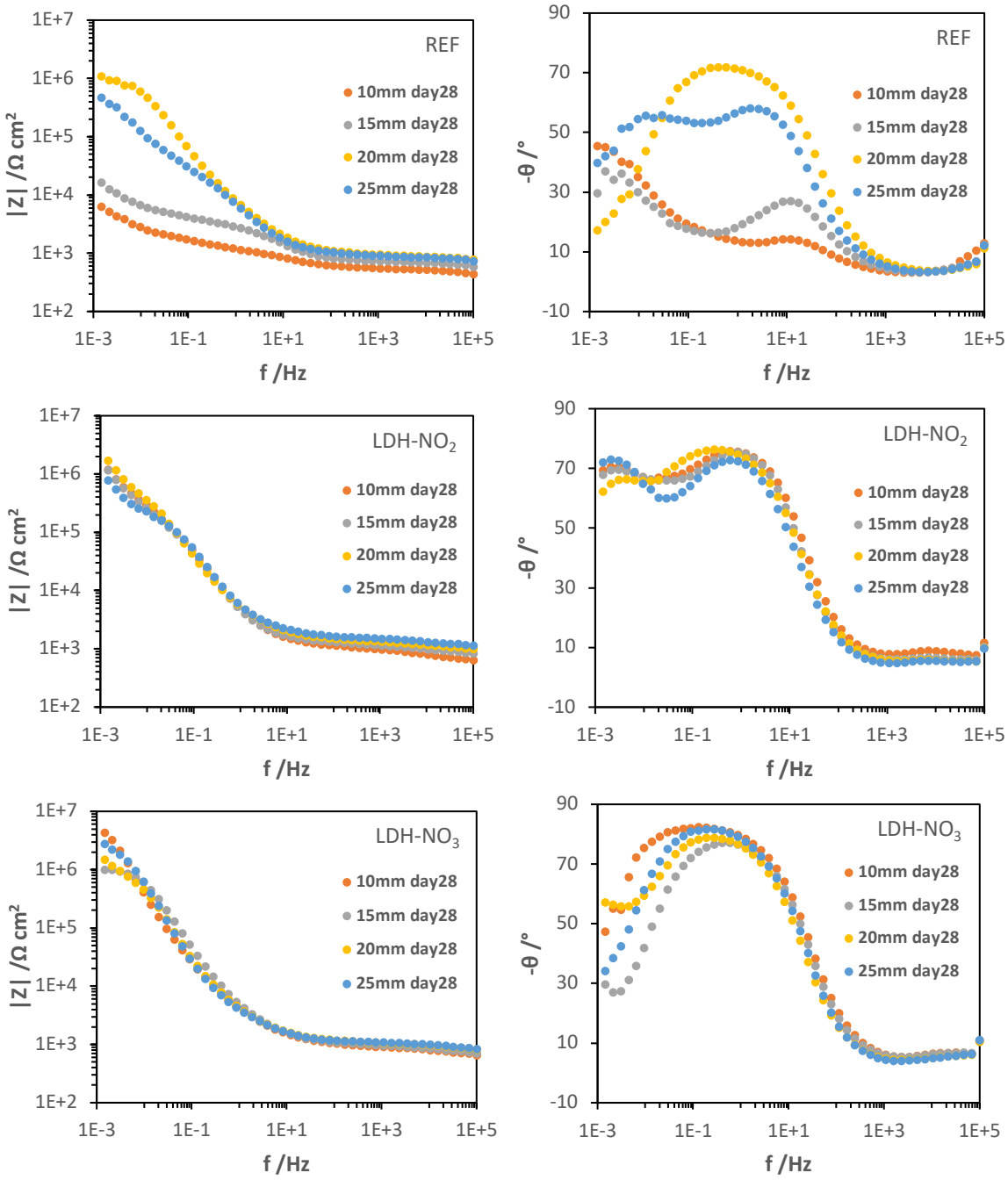

Figure 6.9: Bode diagrams of iron electrodes at 10, 15, 20 and 25 mm of mortar samples without (REF) and with LDH (LDH-NO_2 and LDH-NO_3) at 28th day of immersion.

All samples presented an increase in the resistance at high frequencies as a function of electrode depth, which is due to the increased ionic path, through the interconnected porous network, and increasing distance between the reference and working electrodes.

Chloride capture can be harmful in long term for the reinforced cementitious samples due to the contribution to the increase in the total chloride content, although a large part is bonded. In the case of cementitious structures that are subject to carbon dioxide penetration, the consequent decrease in

the pH of pore solution will lead to the release of bound chlorides to the internal solution [75], which, in turn, will promote the localized attack of the steel reinforcement.

6.3. pH sensors inside mortar samples

This section presents the application of IrO_x sensors to determine the pH variation of the pore solution of mortar samples due to exposure to sulfuric acid and carbon dioxide. In the case of the study of acid attack, a series of complementary experiments was carried out.

6.3.1. Synthesis and characterization of sensors

In this part, the growth conditions adopted for the synthesis of the sensors to be implemented in the mortar samples are described, as well as the potentiometric response of the modified electrodes.
The growth of IrO_x films was done potentiodynamically with a scan rate of 50 mV/s for 50 cycles in the potential window of -0.3 to 0.8 V *vs*. RRE. Figure 6.10 a) presents the growth voltammogram from the first cycle, every 10 cycles, to the 50th, which presents well defined redox peaks —A/A' and B/B' — that are commonly assigned to redox couples Ir(III)/Ir(IV) and Ir(IV)/Ir(V), respectively [142].

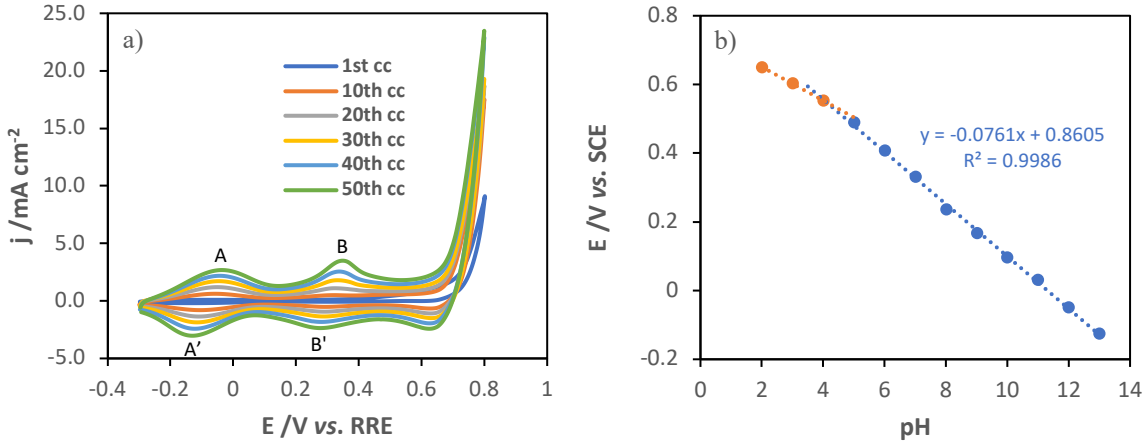

Figure 6.10: Cyclic voltammograms of IrO_x synthesis on stainless steel wires with 50 mV/s for 50 cycles (a) and calibration curve of modified electrode (b).

The potentiometric characterization of IrO_x films, which is represented in Figure 6.10 b), was initiated at pH 13 decreasing unitarily until pH 2. The sensors showed a fast and stable response to the unitary pH variation, with a super-Nernstian slope of 76.1 mV/pH in the pH range between 13 and 4. This super-Nernstian response is attributed to the hydration state of iridium oxides, which is characteristic of electrochemically synthetized films [152].

6.3.2. Carbonation of cementitious materials

The next experimental work consisted of applying the IrO_x sensors in order to study the pH variation of the pore solution of a cementitious matrix due to the carbonation process. The samples were exposed to carbon dioxide, which was produced in an external container from the reaction between hydrochloric acid and calcium carbonate. Two samples were tested: one reference and one with an additive capable of capturing carbonate ions — LDH-NO_2. Carbonates present a high affinity for LDH intercalation [75]. Figure 6.11 shows the pH evolution of pore solution at different depths in the mortar samples during the first 28 hours. Initially, the OCP values of each electrode were recorded before starting the carbon dioxide production. After 4 hours of monitoring, the release of carbon dioxide in the chamber that contains the mortar samples was initiated. The gas release instant is identified by the arrows. The OCP was converted to pH from the calibration curve of the respective sensor. The sensor at 5 mm in the LDH sample began to record a decrease in the pH of the pore solution immediately after the release of carbon dioxide into the atmosphere surrounding the mortar samples. This local pH variation was higher in the instant of new gas release, as shown in Figure 6.11 (LDH-NO_2), which decreased whenever more gas was released, but about 5 hours after the last CO_2 release there was a re-alkalinization of the medium due to the imminent arrival of hydroxyl ions. In the case of the reference sample, only the sensor at 10 mm started to register a pH variation, about 8 hours after the beginning of the gas release. The fact that the 10 mm sensor starts to respond before the sensor closer to the surface may be due to a higher air-filled network in the outer layer, which prevents the 5 mm sensor from detecting carbon dioxide as it can penetrate deeper until it dissolves in the pore solution.

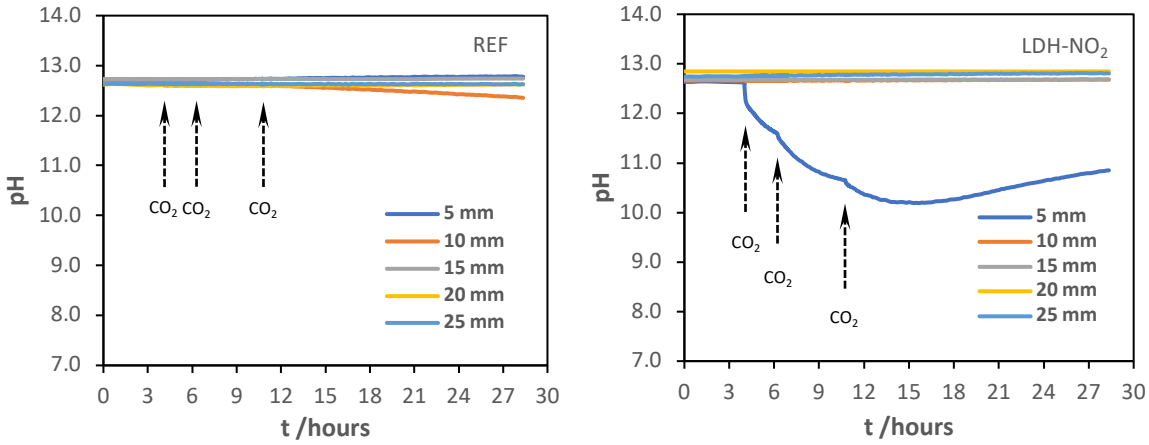

Figure 6.11: Response of embedded IrO_x sensors at different depths (5, 10, 15, 20 and 25 mm) in mortar samples without (REF) and with LDH-NO_2, exposed to CO_2 ingress for 28 hours.

After a few days of carbon dioxide production, the pH of the pore solution of the outer layer of the samples (between 5 and 10 mm of depth) decreased to a value close to pH 9 and, since then, the pH no longer varied independently of the numerous gas releases. The pure carbon dioxide release regime possibly caused a strong carbonation process of the outer layer of the samples, which led to the clogging of the porous network, thus preventing the entry of more gases.

Finally, the samples were cut along the gas penetration direction and analysed by applying a phenolphthalein solution on the surface of the mortar, as shown in Figure 6.12. The colour variation shows an outer zone, between 0.5 and 1 cm from the surface, with a pH below 8, while the rest of the sample remains at a high pH, which is in agreement with the results obtained by the sensors.

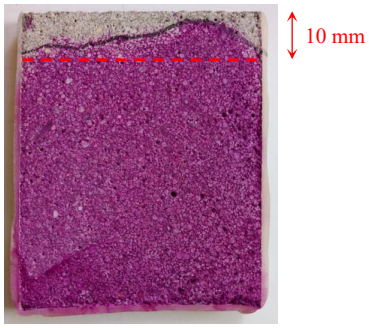

Figure 6.12: Photo of the profile of the sample wetted with phenolphthalein solution, after the carbonation test.

This experimental test showed that the carbon dioxide release regime influences the evolution of the carbonation process of cementitious samples. To obtain a more gradual carbonation process and reach greater depths, it is necessary to reduce the content of carbon dioxide released and increase the humidity of the surrounding atmosphere.

6.3.3. Acid attack

This work studies the pH change of pore solution of cementitious materials due to a high concentrated sulfuric acid solution and characterizes the electrochemical state of iron electrodes as the acid front reaches them. The objective was to simulate the attack of reinforced concrete occurring in some harsh environments like industrial wastewater, sewage treatment plants, and mining. The pH of the pore solution was monitored by potentiodynamically synthesised IrO_x sensors and the corrosion state of the iron electrodes was followed by reading their OCP and performing EIS over time. In addition, the reaction products resulting from the acid attack on the mortar samples were analysed by XRD and the surface of the sensors that were exposed to the acid was analysed by SEM and EDS.

6.3.3.1. Response of the sensors to H_2SO_4 in simulated conditions

The response of the IrO_x sensor to the sulfuric acid attack was studied in simulated conditions. Firstly, the modified electrode was placed in saturated $Ca(OH)_2$ solution during 2 months to simulate the period between the casting of the mortar samples and the acid exposure. Then, the sensor was moved to the solution under study — 1 M H_2SO_4 —, and its OCP was immediately measured again. The potentiometric response of the IrO_x electrode is represented in Figure 6.13. Initially, the OCP was stable at around -0.08 V *vs*. SCE, which from the calibration curve corresponds to a pH 12.4. As soon as the electrode was immersed in the acid solution, it immediately responded shifting to a potential that, according to the sensor calibration curve, corresponds to a pH close to 0. However, the strong acidic environment promotes a subsequent progressive removal of the IrO_x film creating a mixed potential due to the partial exposure of the stainless steel substrate which leads to a decrease in the OCP until the signal is dominated by the corrosion potential of stainless steel 316L.

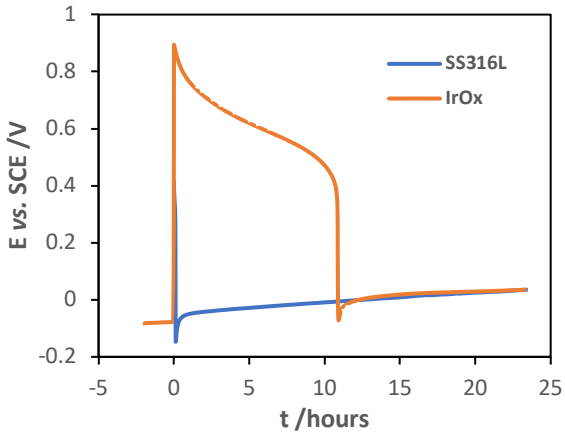

Figure 6.13: OCP evolution of IrO_x sensor initially immersed in $Ca(OH)_2$ saturated solution for about 60 days (t<0) and then changed to 1M H_2SO_4 solution (t>0), compared to the substrate (316L wire) response in 1M H_2SO_4.

After the acid attack, the IrO_x surface was inspected by SEM and EDS analysis. Figure 6.14 a) and b) show the sensor surface before and after the attack, respectively, and the corresponding spectra are presented in Figure 6.14 c). A magnification of the sensor after the acid attack is shown in Figure 6.14 b) inset.

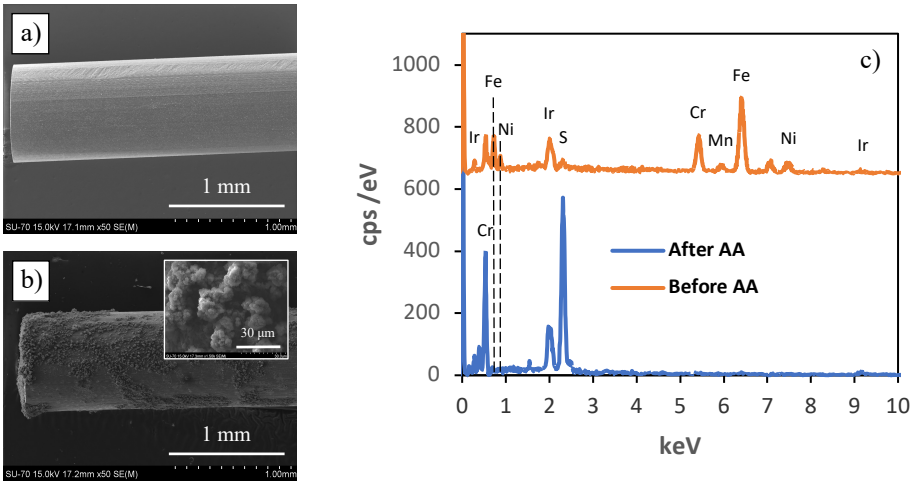

Figure 6.14: SEM images of IrO_x sensor before (a) and after immersion in 1M H_2SO_4 (b) and respective EDS analysis (c).

The acid caused the dissolution of a large part of the iridium oxide film and attacked the partial exposed surface of the stainless steel. The EDS analysis shown in Figure 6.14 d) presents the formation of corrosion products (sulfates and oxides), which can be confirmed by the peaks of S and O. The decrease in Ir and Fe peaks is related to the IrO_x removal and to the attack on the substrate.

6.3.3.2. Measurement of pH inside mortar with the sensors

Figure 6.15 presents the evolution of pH sensors response, at 5, 10, 15 and 20 mm of depth, which was obtained by converting the OCP signals to pH values from the calibration curve of each sensor.

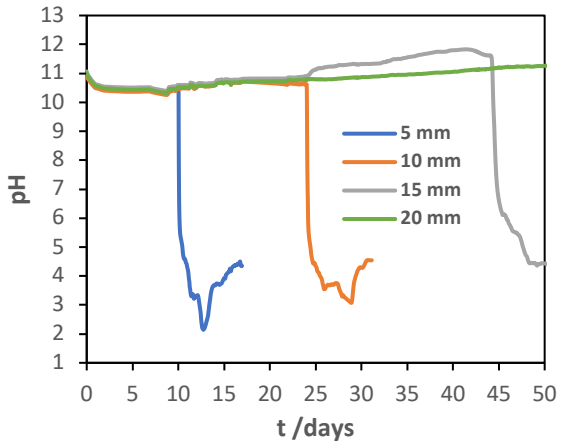

Figure 6.15: Sensors response to acid attack at different depths — 5, 10, 15 and 20 mm — for 50 days.

The first sensor responded 10 days after the beginning of the acid attack, the second responded after 24 days and, finally, the third one took 44 days to respond. The first sensor, at 5 mm, only became visible on the attacked surface of the mortar sample one day after its potentiometric response began to vary due to the corroded layer above the attack front. The response of the sensors located at greater depths (20, 25, 30, 35 and 40 mm) remained constant in the alkaline region, which shows that the pH inside the sample was not affected, possibly due to the immediate neutralization of the H^+ ions at the region between the solution and the mortar. The cement matrix acts as an infinite reservoir of hydroxyl ions. The slower response of the sensors in mortar compared to their response in solution can be due to a pH gradient region above the attack front surface. Figure 6.16 a) shows the variation of the sensor response at 5 mm in detail, and Figure 6.16 b) compares the pH variation relative to the initial pH value of the sensors at 5, 10 and 15 mm. As can be seen, sensors at different depths presented a very similar pH evolution, which initially had an abrupt drop in pH of 5 units, in about 4.5 hours in sensors positioned at 5 and 10 mm and about 20 hours in the case of the 15 mm sensor, as shown in Figure 6.16 b). The slower sensor response at 15 mm is possibly due to the growing corroded layer as the attack front moves.

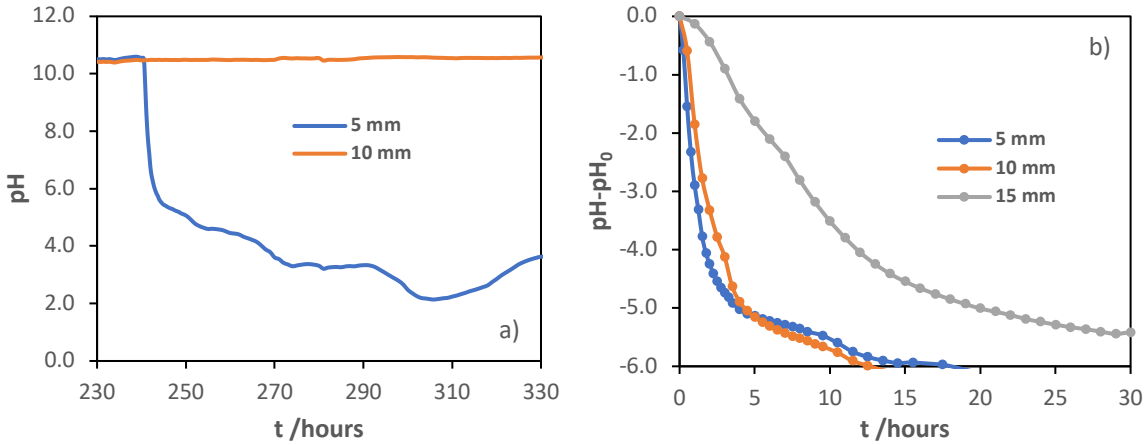

Figure 6.16: Detail of pH evolution at 5 mm (a) and pH variation relative to initial pH value at 5, 10 and 15 mm (b).

After 50 days of acid attack, the sample was cut parallel to the comb of sensors and the surface of the mortar was titrated with a solution of phenolphthalein in order to visually check the internal pH of the sample, as shown in Figure 6.17 a).

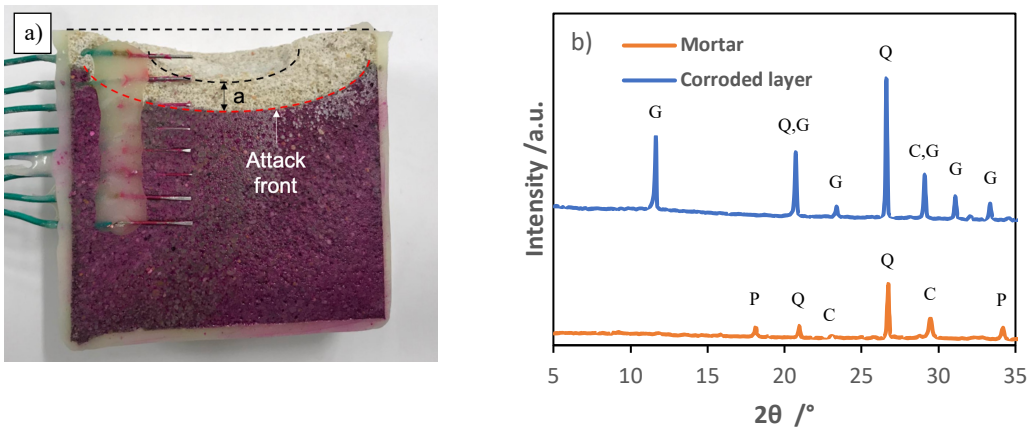

Figure 6.17: (a) Photo of the mortar sample profile after the acid attack for 50 days with detail of the attack front and the thickness of corroded layer — a — and (b) diffractograms of mortar samples before (Mortar) and after the acid attack (Corroded layer). The identified phases were portlandite (P), calcite (C), quartz (Q) and gypsum (G).

The visual inspection is in accordance with the results obtained by the sensors showing that the pH of the bulk of the sample was not affected by the acid attack, except for a very narrow region below the attack front, which is reasonably consistent with the results obtained by the IrO_x sensors. The corroded layer from the attacked zone, after 50 days of immersion, and the mortar sample before attack (Mortar) were analyzed by XRD and the resulting diffractograms are represented in Figure 6.17 b). The main components of mortar — calcite, portlandite and quartz — were detected in the XRD analysis of the mortar sample before attack. As expected, the acid attack leads to a change in the chemical composition of the cementitious material, as shown in the diffractogram from the attacked sample, with the formation of gypsum and consumption of calcite and portlandite.

The surface of the electrode placed at 5 mm was analyzed by SEM and EDS after the end of the potentiometric test, as shown in Figure 6.18 a) and b), respectively. The acid attack led to the total destruction of the IrO_x film, which was removed from substrate surface, and to the formation of corrosion products from the mortar attack.

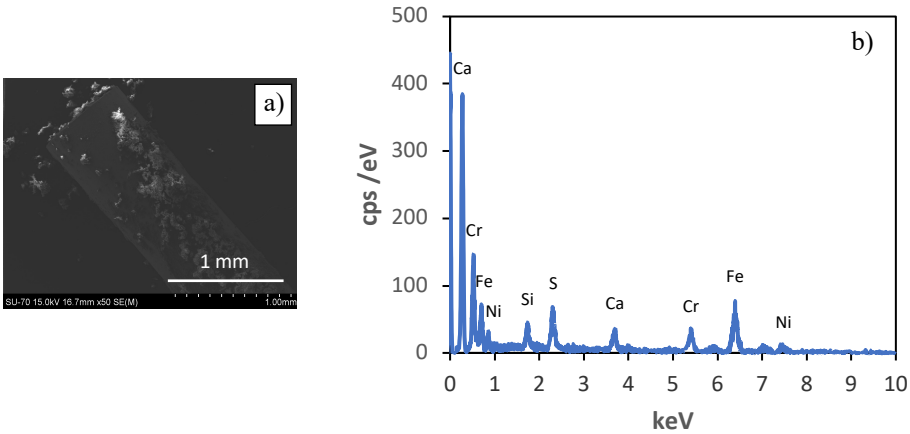

Figure 6.18: SEM (a) and EDS (b) analysis to IrO_x sensor after embedment in mortar sample and further acid attack).

6.3.3.3. Corrosion of iron rebars in simulated conditions

Before starting the experiments with the electrodes embedded in the hardened mortar, it was important to understand their behavior in simulated solution conditions, both for the initial conditioning of the iron electrodes during the period from the mortar samples casting until the beginning of the acid attack, as well as for the exposure of the electrode to sulfuric acid. An iron electrode was immersed in an aqueous solution of NaOH 0.1 M with a pH of 12.9 until its OCP reaches equilibrium and then, the immersion solution was changed to H_2SO_4 1 M (for t=0), as shown in Figure 6.19 a).

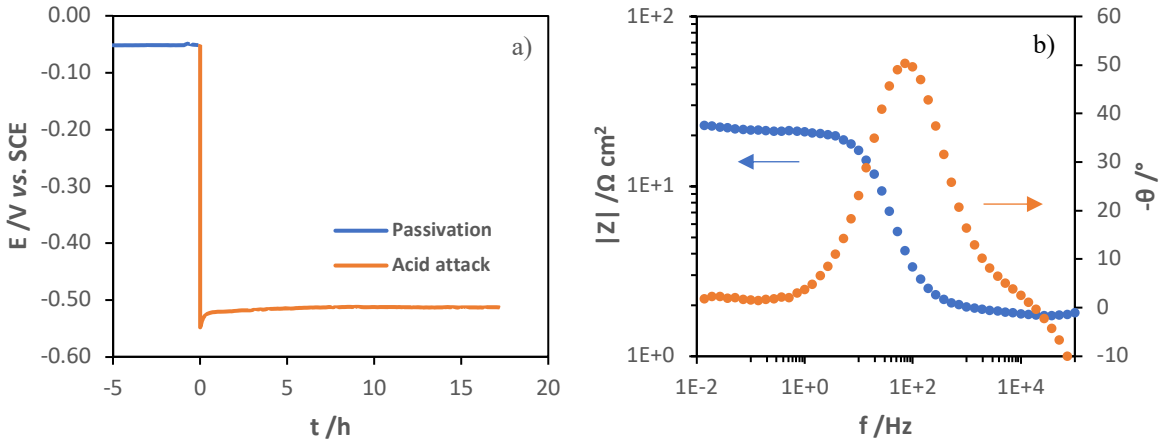

Figure 6.19: OCP evolution of an iron electrode initially immersed in $Ca(OH)_2$ saturated solution for about 90 hours (t<0) and then changed to 1 M H_2SO_4 solution (t>0) (a); and Bode diagram of the iron electrode impedance after 5 hours of acid attack (b).

Initially, the iron electrode was in a passivated state. Then, when exposed to a very acidic solution (t>0), the passive layer was destroyed immediately and its OCP dropped instantly to a characteristic value of a corrosion stage tending to -0.55 V *vs*. SCE. Figure 6.19 b) presents the impedance of the iron wire under acid attack, after 5 hours of immersion in H_2SO_4 solution, which, clearly, shows the electrode in an advanced state of corrosion (evidenced by the low impedance at lower frequencies).

6.3.3.4. Corrosion of iron rebars in mortar samples

The effect of acid attack on the iron embedded in mortar at different depths was studied by measuring the evolution of the electrodes open circuit potential as the acid dissolves the mortar and approaches the surface of the iron wires, as shown in Figure 6.20. Initially, the iron wires were protected by a strong passive layer and present a typical and constant OCP near 10 mV *vs.* SCE. The acid does not affect the iron electrodes until it reaches its surface. In contrast with the tests in solution, the drop in the open circuit potential of the iron electrodes is slower and presents two stages: an abrupt initial decrease up to -0.358 V *vs*. SCE in the first 2 hours after the start of the response; then it presents a slower drop down to -0.55 V *vs*. SCE in about 35 hours. These two steps were also evidenced in the potentiometric response of the IrO_x sensors (Figure 6.16 b). The initial drop can happen when the electrode is covered only by a corroded layer, and the second part due to the neutralization of that layer by the acid front.

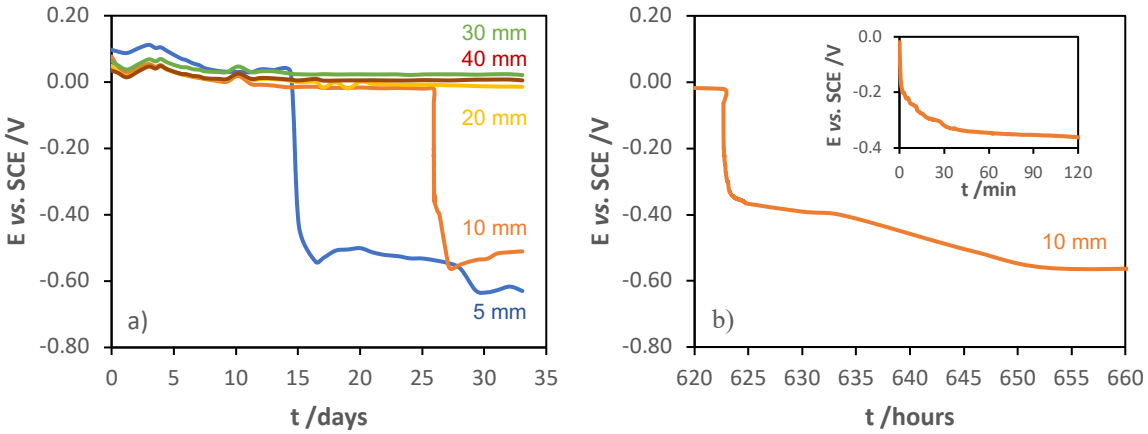

Figure 6.20: OCP evolution of iron electrodes at different depths — 5, 10, 20, 30 and 40 mm — during acid attack (a) and detail of response of the iron electrode at 10 mm (b).

EIS was also used to monitor the evolution of the electrochemical state of the system — pore solution and electrode — before, during and after varying the open circuit potential of the electrodes due to arrival of the acid front. Figure 6.21 a) presents the electrochemical impedance of electrodes at 5, 10, 10, 30 and 40 mm of depth for different days of acid attack, before the acid reaches none of them. The response was very similar, with essentially two regions, a resistive one at high frequencies and a mainly capacitive one at lower frequencies. The response at higher frequencies is due to the resistance of the H_2SO_4 solution (with just a small contribution because of its high conductivity) in series with the resistance of the pore solution in the mortar. The response at lower frequencies comes from the capacitance of the passive film, or the double layer capacitance for longer times. For the sake of comparison and to avoid an inconclusive discussion based on just a few measurements, it was decided to use a simple $R_{HF}(CPE_{LF}R_{LF})$ circuit to numerical fit the experimental data, where R_{HF} represents the resistance at higher frequencies, CPE_{LF} is a constant phase element used to express the capacitive behavior and R_{LF} is the resistance at lower frequencies, either the passive film resistance or charge transfer resistance, depending on the evolution stage. The fitting was performed with the ZView program (Scribner Associates, USA) and the results are presented in Table 6.1. R_{HF} is in the same order of magnitude for the different iron specimens and is expected to be higher in first days of testing and for wires positioned deeper in the mortar.

It is very informative to follow the impedance evolution of the same wires as the acid attack progresses. This is shown in Figure 6.21 b) for the wire located 10 mm deep inside the mortar. The impedance for low frequencies was very similar during the first 25 days, whereas the resistance at high frequencies decreased due to the thickness reduction of the mortar cover as it was dissolved and the solution front approached the wire. Then, a fast decrease in impedance was observed between days 26 to 28, easily observed in the resistances R_{HF} and R_{LF} (Table 6.2), the first, at higher frequencies, related to the mortar cover and the second, at low frequencies, associated initially with the passive film and progressively with the charge transfer resistance, therefore, related to the corrosion rate of the iron wire. The decrease of R_{HF} illustrates the fast dissolution of the mortar cover until the wire became totally exposed in day 28. The values of R_{LF} reflect the condition of the wire, from the passive state with high resistance, followed by a noticeable decrease as the acid dissolved the passive layer and finally very low resistance corresponding to the iron corrosion in acid solution. The corrosion rate was so intense in this last stage that in a single day the exposed volume of the electrode was dissolved. Hydrogen gas bubbling was easily seen being formed from day 28.

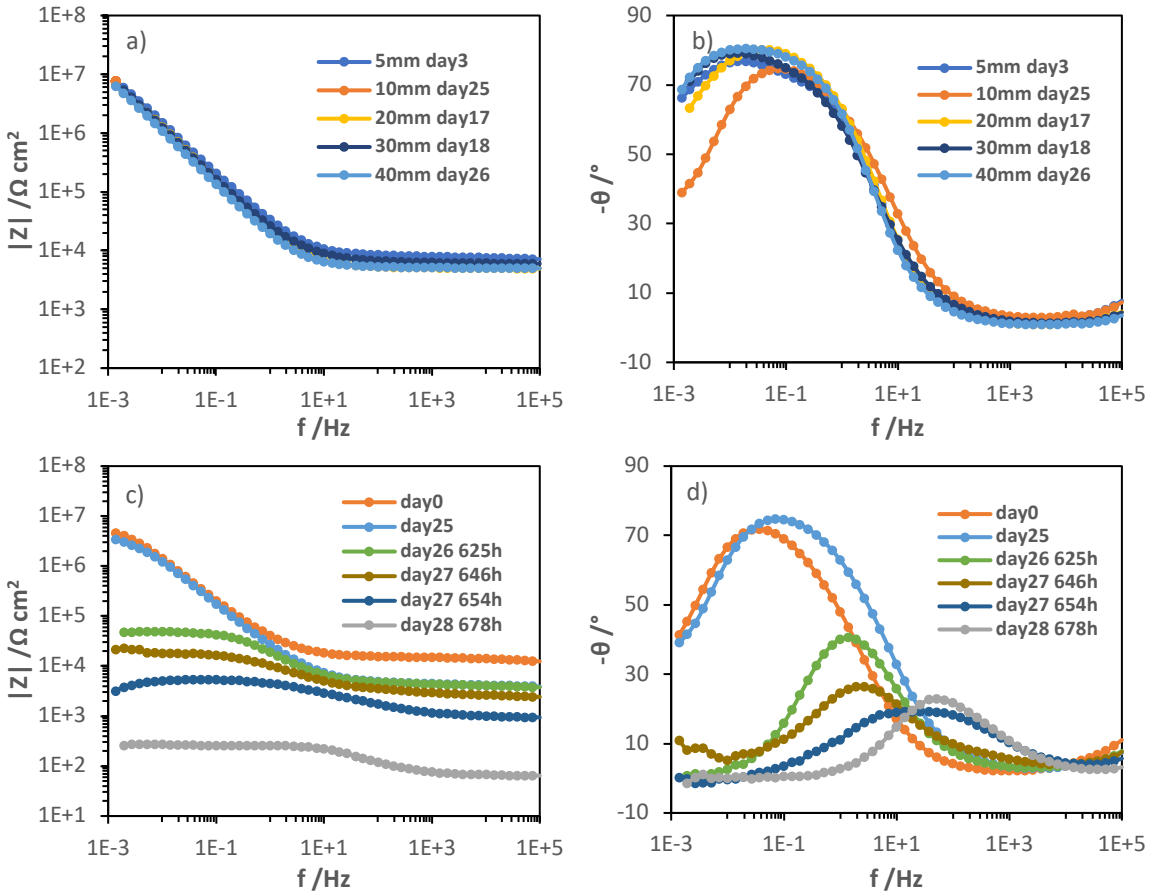

Figure 6.21: Bode diagrams of the impedances of the iron electrodes embedded in mortar samples before the arrival of the attack front (a and b) and impedances of electrodes at 10 mm for different times of the acid attack (c and d).

The electrochemical characterization of iron electrodes showed a rapid transition between the passive state of steel and its active state with high corrosion rate.

Table 6.1: Summary of electrical parameters obtained by fitting of impedance spectra in Figure 6.21 a) and b).

Depth /mm	R_{hf} /Ω cm²	Y_{lf} /10^{-5} $Ω^{-1}$ s^n cm^{-2}	n_{lf}	R_{lf} /10^6 Ω cm²	10^4 $χ^2$
5	1315	4.16	0.840	11.6	19
10	731	4.92	0.829	0.907	9
20	860.7	5.66	0.886	3.18	14
30	1061	5.21	0.850	1.01	29
40	865.7	6.62	0.891	7.31	11

Table 6.2: Summary of electrical parameters obtained by fitting of impedance spectra in Figure 6.21 c) and d).

t /days	R_{hf} /Ω cm²	Y_{lf} /10^{-5} $Ω^{-1}$ s^n cm^{-2}	n_{lf}	R_{lf} /Ω cm²
0	2451	4.11	0.81	1.5 x 10^6
25	731	4.92	0.829	9.07 x 10^5
26 (625h)	725	8.28	0.733	2950
27 (646h)	425	7.33	0.737	2497
27 (654h)	156	23.3	0.841	231
28 (678h)	10.84	48.8	0.829	21.5

6.4. Conclusions

To complete this scientific work, the sensors developed in the previous chapters were used to monitor the ingress of chlorides and the pH variation of the pore solution in mortar samples. To complement the sensors results, iron electrodes with the same arrangement and experimental conditions were also tested.

The *in-situ* ellipsometric study showed the formation of three distinct and homogeneous layers during iron passivation. The nucleation process started with the formation of metal oxide islands. Then, it continued until a first layer of $Fe(OH)_2$ with 1.2 nm of thickness was formed, after about 15 minutes. Finally, two outer layers, with lower electrical conductivity (lower k) and higher porosity (lower n), were formed reaching, respectively, 11.5 and 16.1 nm of thickness, for about 15 hours. The passive layer reached a total thickness of 28.8 nm, after 16 hours of immersion in 0.1 M NaOH solution.

First, the ingress of chlorides into mortar samples with and without LDH was studied through the use of Ag/AgCl sensors positioned at different depths in the samples. The sample with LDH-NO_2 presented a much slower evolution of chloride content as a function of depth that the reference. In the sample containing LDH-NO_2, after 20 days of immersion, the ingress of chlorides was only detected by the sensor at 5 mm, while in the reference sample, for the same time, chloride was already being detected at 20 mm of depth.

The destructive analysis of the mortar samples immersed for different periods showed the presence of a higher total chlorides content in the sample with LDH.

The lowest concentration of free chloride in the pore solution and, at the same time, the higher content of total chlorides in the mortar sample containing LDH, can be explained by the removal of chloride ions from the pore solution and its sequestration in the solid phase. The sequestration can be due to ionic exchange with LDH or due to the formation of Friedel salts due the Al ions released by the dissolution of LDH.

However, the analysis by XRD to identify peaks related to the formed hypothetical Friedel salts were inconclusive.

To confirm the results obtained by the sensors, iron electrodes were also embedded in mortars in a similar arrangement as the sensors. This time, together with the reference mortar and the LDH-NO_2, LDH-NO_3 was also used to eliminate the passivating effect of the nitrite ion on iron. The only possible effect of LDH-NO_3 is the decrease of chloride ions content in the pore solution by ionic exchange. Initially, the corrosion potential of all iron electrodes in all mortar samples was similar and presented values typical of the passive state. After immersing the mortars in NaCl solution the electrodes of the reference sample were the first to drop the potentials to the active region. These results are in line with those obtained with the sensors and are a clear indication of the action of the LDH in lowering the chloride in the pore solution.

Another study used IrO_x sensors to study the pH variation of the pore solution of a mortar sample due to carbon dioxide ingress. The sensors at 5 mm showed an almost immediate local pH variation, after the initial release of carbon dioxide. However, there was a subsequent re-alkalinization of the medium due to the imminent arrival of OH^- ions. The pure carbon dioxide regime promoted the clogging of the porous network in the outer layer of the mortar samples, which made it impossible to continue testing.

A last application of IrO_x sensors was the monitoring of pH variation of the pore solution of cementitious samples due to sulfuric acid attack. The sensors only responded as the attack front reached their surface, while for greater depths than the acid front, the pH is not affected due to the immediate neutralization of protons at the solution/mortar interface. After the acid front reached the

sensors there was a fast pH drop of 5 units, in about 4.5 hours for sensors at 5 and 10 mm depth, and about 20 hours for the sensor at 15 mm. Then, the pH decreased in a slower way until it reached a minimum value, in which the electrode film started to degrade. The XRD analysis of the layer formed due to acid attack, showed the formation of gypsum and the consumption of calcite and portlandite. Tests with iron electrodes validated the results obtained by the sensors. The variation of the OCP of the electrodes due to the acid front also presents two stages: an abrupt initial decrease up to around -0.35 V *vs*. SCE in the first 2 hours and then a lower drop down to -0.55 V *vs*. SCE in about 35 hours. The EIS spectra showed that the electrodes are in the passive state until the arrival of the attack front and then, the transition to the active state is fast with high corrosion rate.

The developed sensors were successfully used in mortar. IrO_x sensors showed great potential for monitoring the internal pH of cementitious structures, as they presented an enormous resistance to the extremely alkaline environment of cement pore solution and continued working even after more than one year embedded in mortar samples.

The Ag/AgCl sensors also allowed to study the evolution of the chloride content in different cementitious samples exposed to chlorides. However, these sensors do not last very long in an environment as alkaline as cement due to the silver oxidation. One way to overcome this limitation would be through the use of a selective membrane to chlorides that would prevent the contact of silver with hydroxyl ions and its consequent oxidation.

CHAPTER 7 Global conclusions and future work

In order to finish the present scientific work, it holds great significance to analyse the main conclusions reached with the investigation carried out to fully explain the results obtained, which will also serve as basis for drawing up the next paths to be followed.

This experimental work can be divided into two main parts: the production of electrochemical sensors for the determination of pH and chloride content; and the application of the modified electrodes for monitoring the processes of pH variation and chloride arrival in the pore solution of cementitious materials.

Two sensitive materials to chlorides were studied: Ag/AgCl and lucigenin. The synthesis of Ag/AgCl electrodes was carried out electrochemically through cyclic voltammetry, potentiostatic and galvanostatic regimes. The galvanostatically modified electrodes showed the best potentiometric response with lower limit of detection and a slope closer to the Nernstian value. The best growth conditions turned out to be with an electrolyte concentration (HCl) equal or less than 0.1 M, a growth time up to 30 minutes, and a range of current pulses between 0.5 and 2 mA/cm^2.

The potentiometric response — slope and limit of detection — of electrochemically synthetized Ag/AgCl electrodes is mainly influenced by the concentration of HCl, independently of the used technique. In galvanostatic synthesis, HCl concentrations equal or greater than 1 M must be avoided. For both electrochemical synthesis regimes, the 0.1 M HCl concentration appears to be the most suitable for obtaining the best potentiometric response.

High pH environments lead to early degradation of Ag/AgCl electrodes. A solution to extend the lifetime of these sensors would be using an outer membrane selective to chlorides.

Direct mobilization of lucigenin on stainless steel through cyclic voltammetry was successfully achieved, but the modified electrode presented a bad potentiometric response, with poor sensibility and slow time of response.

For the determination of pH, several materials were tested: MnO_2, IrO_x, $IrO_x + RuO_2$ and PPy. The material that presented the best potentiometric response, in terms of reversibility, response time and linearity in the widest pH range, was iridium oxide.

The pH sensors chapter started with the study of MnO_2 electrodes. The MnO_2 sensor synthesized potentiodynamically in an aqueous solution of 0.3 M $MnSO_4$ and 0.1 M $LiClO_4$, with a scan rate of 50 mV/s, for 20 cycles presented a stable and reversible potentiometric response with a slope of 61 mV/pH in the pH range between 13 and 8. The results of the different experimental conditions of potentiodynamic synthesis of MnO_2 films suggested a relation between the oxidation time and its potentiometric response quality (reversibility and time of response). Consequently, the potentiostatic growth of MnO_2 films was studied for different applied potentials and times of pulse, using the same growth solution. The decrease in the applied potential and the increase in the pulse time leads to a decrease in the slope of the calibration curve of the modified electrodes. Then, the synthesis of MnO_2 films, for different applied potentials — 0.7, 0.8, 0.9 and 1.0 V *vs*. RRE —, was followed by *in-situ* ellipsometry. The evolution of ellipsometric parameters present a similar behaviour for the different potential pulses, with exception for 0.7 V, suggesting that the nucleation mechanism is not affected by the applied potential. The Psi-Delta values formed an almost closed loop, which is characteristic of a slightly light absorbing film. The formation of two homogeneous layers was considered to

achieve a reasonable complete fitting of the experimental data. The ellipsometric study confirmed the formation of an inner more resistive MnOOH layer between the electrode surface and the manganese compounds film. The increase of the applied potential leads to an increase of the thickness, rate of growth and density (higher n) of both layers (inner and outer). The outer layer presented a slower rate of growth and a higher conductivity (higher k) compared to the inner one. MnO_2, despite not having been widely explored by the scientific community as a pH sensor, showed an acceptable potentiometric response. In addition, this material represents a low-cost and simple synthesis alternative for pH determination.

Posteriorly, the effect of experimental parameters of the electrochemical synthesis of IrO_x films, based on Yamanaka growth solution [154], on their potentiometric response for pH determination was studied in detail.

The synthesis of IrO_x films was performed using cyclic voltammetry and a potentiostatic regime. In the case of potentiodynamic growth, IrO_x sensors presented a linear potentiometric response with two pH regions: one in the pH range between 13 and 5, with a super-Nernstian slope between 79.0 and 81.0 mV/pH, and another for pH<4, with a slope closer to the Nernstian one between 59.0 and 65.5 mV/pH. The best potentiometric response was achieved with the lowest anodic limit of the cycles that allows film deposition — 0.7 to 0.75 V *vs*. RRE —, a scan rate of about 50 mV/s, and for a range of cycles between 20 and 80. The decrease in the anodic limit of synthesis led to a decrease of the slope and a shift of the calibration curve to lower potential values, for both pH regions. The other growth parameters (scan rate and number of cycles) did not affect the potentiometric response of the modified electrodes.

To conclude the study of potentiodynamic synthesis of IrO_x films, the influence of the presence of $RuCl_3$ in the growth solution on the potentiometric response of modified electrodes was studied. The film grown in the presence of 10 mM $RuCl_3$, with an anodic limit of 0.85 V *vs*. RRE and a scan rate of 50 mV/s, for 50 cycles presented the best potentiometric response, with a Nernstian slope of 59.5 mV/pH in the linear pH range between 13 and 5. The slope decreases with higher ruthenium content and with higher anodic limit of growth. The presence of 1 mM $RuCl_3$ does not affect the film growth and its potentiometric response.

The potentiostatic synthesis of IrO_x films was carried out through the application of a single anodic pulse and a double pulse (anodic and cathodic). This experimental investigation began by studying the effect of applying an anodic potential pulse on the IrO_x nucleation process and on the potentiometric response of the modified electrodes. The nucleation process, which follows an instantaneous mechanism, increases with higher applied potentials. However, the modified electrodes presented a slow and unstable potentiometric response, with an almost Nernstian slope between 60.3 and 62.8 mV/pH. The increase of the applied pulse led to higher slopes and to a shift of the calibration curve to lower potential values.

Then, the growth of IrO_x films was investigated through the application of a double pulse potential. The best potentiometric response was achieved by applying a 0.75 V *vs*. RRE anodic pulse with a step of 1 second, followed by a -0.3 V *vs*. RRE cathodic pulse with a 9 second step, for 180 cycles. IrO_x sensors exhibited a linear response in the pH range between 10 and 2, being more suitable for applications that reach low pH values.

The potentiometric response of films grown by double pulse chronoamperometry presented 3 different linear pH regions: a region 1 (pH<4) with a slope between 49.7 and 70.2 mV/pH; a region 2 (4<pH<11) with a slope between 69.6 and 78.7 mV/pH; and a region 3 (pH>11) with an over-Nernstian slope between 92.5 and 105.2 mV/pH. The decrease of the anodic step and the increase of the cathodic step led to near-Nernstian slopes and to a shift of the calibration curve to lower values,

for region 2. The calibration curve parameters — slope and E-intercept — are logarithmically correlated with the ratio between the duration of the anodic and cathodic steps — t_a/t_c. The decrease of the anodic potential pulse led to a decrease in the slope and to a shift of the calibration curve to more negative values.

To finalize the experimental investigation of IrO_x sensors, the effect of aging, in different environments — air and buffer solutions with pH 4, 7 and 11 —, of potentiodynamically modified electrodes on their potentiometric response was studied. The variation of potentiometric parameters was higher in the first 50 days, after film synthesis, and then start to stabilize with time. The buffer solution with pH 4 led to the total dissolution of IrO_x film after about 200 days of immersion. The other modified electrodes continued to present a fast and stable potentiometric response after 262 days of test. The electrode stored in buffer solution with neutral pH showed the smallest variation of slope and E-intercept with aging.

Finally, potentiostatically grown polypyrrole films presented a linear pH region between 11 and 5. The best potentiometric response was achieved by a film grown with a 0.6 V *vs*. SCE pulse, for a growth charge of 1 mC. The increase of the applied potential pulse, as well as the total charge of synthesis, leads to slope decrease to more sub-Nernstian values.

In-situ ellipsometric study of the passive film formed on steel at the open circuit potential showed the formation of three main distinct and homogeneous layers: an inner layer composed by $Fe(OH)_2$ and two outer porous layers of iron hydroxides filled with sodium hydroxide. The passive layer reached a thickness of 28.8 nm in 16 hours of immersion in 0.1 M NaOH solution.

The chlorides ingress study presented a much slower evolution of the chloride content as a function of depth for the sample with LDH-NO_2 than the reference (without LDH). After 20 days of immersion, the ingress of chlorides was only detected by the sensor at 5 mm in the LDH containing sample, while in the reference, for the same time, chlorides were already detected at 20 mm of depth.

The destructive analysis to the mortar samples immersed for different periods showed the presence of a higher total chlorides content in the sample with LDH. The lower concentration of free chlorides in the pore solution and the higher content of total chlorides in the mortar sample with LDH-NO_2 can be explained by the removal of chloride ions from the pore solution, which leads to an increase in the bound chlorides content. The removal of chloride ions can be due to ionic exchange with LDH or to the formation of Friedel salts.

The passive state of the iron electrodes in the LDH samples (LDH-NO_2 and LDH-NO_3), which was evidenced by the OCP value and high impedance after 30 days of immersion, was indicative of a chloride removal by LDH, being in agreement with the results obtained with the sensors . The LDH promoted a decrease in the evolution of the chloride content in the pore solution of mortar samples. However, chloride capture can be harmful in long term for the reinforced cementitious structures that are susceptible to carbon dioxide penetration due to the contribution to the increase in the total chloride content, although most of it is bonded. The decrease in the pH of the pore solution will lead to the release of bound chlorides to the pore solution, which will promote a strong localized attack to the steel rebar.

The carbonation study showed an almost immediate local pH variation near the surface, after the initial release of gas, followed by a subsequent re-alkalinization of the medium due to the imminent arrival of OH^- ions. However, the pure carbon dioxide regime promoted the clogging of the porous network in the outer layer of mortar samples, which led to the early termination of the experiment. The experimental conditions influence the carbonation process and, therefore, in future works it

should be used a lower carbon dioxide content and higher moisture to obtain a more gradual carbonation process and reach greater depths.

Finally, IrO_x sensors were used to monitor the pH variation of the pore solution of cementitious samples due to sulfuric acid attack. The sensors showed that the pH variation was limited to just a small layer in the order of 1-2 mm due to the immediate neutralization of protons at the region between the solution and the mortar. The potentiometric response presents two regions: an initial 5 units pH drop, in about 4.5 hours for sensors at 5 and 10 mm, and about 20 hours for sensor at 15 mm, followed by a slower pH decrease until a minimum is reached, in which the film starts to be oxidized and removed from the substrate. The XRD analysis to the corroded layer showed the formation of gypsum and the consumption of calcite and portlandite. Tests with iron electrodes validated the results obtained by the sensors. The variation of the OCP of the electrodes due to the arrival of the acid front also presents two stages: an abrupt initial decrease up to around -0.35 V *vs*. SCE in the first 2 hours after the starting of the response; followed by a lower drop down to -0.55 V *vs*. SCE in about 35 hours. The EIS spectra showed that the electrodes are in the passive state until the arrival of the attack front and then, the transition to the active state is fast with high corrosion rate.

The developed sensors were successfully applied to mortar samples. IrO_x sensors showed great potential for monitoring the internal pH of cementitious structures, as they presented an enormous resistance to extremely alkaline environments, such as cement pore solution, continuing to work even after more than one year embedded in mortar samples. In addition, stainless steel, used as the substrate, also provides greater mechanical strength at a relatively affordable cost. The Ag/AgCl sensors allowed to study the evolution of the chloride content in different cementitious samples exposed to chlorides. However, these sensors do not last long in an environment as alkaline as cement due to the silver oxidation. One way to overcome this limitation would be through the use of a selective membrane to chlorides that would prevent the contact of silver with hydroxyl ions and its consequent oxidation.

Future Work

To close this experimental work, the next paths to be explored are listed below:

- Study the degradation of Ag/AgCl electrodes in simulated pore solution.
- Produce Ag/AgCl electrodes with an outer chloride selective membrane in order to avoid its degradation in high pH media.
- Achieve an IrO_x synthesis capable to produce electrodes with a linear potentiometric response in the pH range between 13 and 2.
- Develop sensors for the detection of dissolved oxygen.
- Perform carbonation tests in conditions where the process evolves more gradually and can be monitored by pH sensors.
- Identify the mechanism responsible for removing chloride ions from solution in the mortar sample containing LDH.

References

[1] J.K. Wight, J.G. MacGregor, Reinforced Concrete: Mechanics and Design, 5th ed., Pearson Education, Inc, 2009.

[2] P. Pedeferri, L. Bertolini, B. Elsener, E. Redaelli, R.B. Polder, Corrosion of Steel in Concrete - Prevention, Diagnosis, Repair, Wiley-VCH, 2013.

[3] E. Bowman, G. Jacobson, G. Koch, J. Varney, N. Thopson, O. Moghissi, M. Gould, J. Payer, International Measures of Prevention, Application, and Economics of Corrosion Technologies Study, 2016.

[4] G. Habert, S.A. Miller, V.M. John, J.L. Provis, A. Favier, A. Horvath, Environmental impacts and decarbonization strategies in the cement and concrete industries, Nat. Rev. (2020).

[5] S.A. Miller, F.C. Moore, Climate and health damages from global concrete production, Nat. Clim. Chang. 10 (2020) 439–443. doi:10.1038/s41558-020-0733-0.

[6] P.R. Roberge, R. Pierre, Handbook of Corrosion Engineering, MacGraw-Hill, 1999.

[7] K. De Weerdt, G. Plusquellec, A. Belda Revert, M.R. Geiker, B. Lothenbach, Effect of carbonation on the pore solution of mortar, Cem. Concr. Res. 118 (2019) 38–56. doi:10.1016/j.cemconres.2019.02.004.

[8] L. Freire, X.R. Nóvoa, M.F. Montemor, M.J. Carmezim, Study of passive films formed on mild steel in alkaline media by the application of anodic potentials, Mater. Chem. Phys. 114 (2009) 962–972. doi:10.1016/j.matchemphys.2008.11.012.

[9] H. Zheng, C.S. Poon, W. Li, Mechanistic study on initial passivation and surface chemistry of steel bars in nano-silica cement pastes, Cem. Concr. Compos. 112 (2020) 103661. doi:10.1016/j.cemconcomp.2020.103661.

[10] A. Alhozaimy, R. Rizwan, A. Al-negheimish, Significance of oxygen concentration on the quality of passive film formation for steel reinforced concrete structures during the initial curing of concrete, Cem. Concr. Compos. 65 (2016) 171–176. doi:10.1016/j.cemconcomp.2015.10.022.

[11] P. Ghods, O.B. Isgor, G. McRae, T. Miller, The effect of concrete pore solution composition on the quality of passive oxide films on black steel reinforcement, Cem. Concr. Compos. 31 (2009) 2–11. doi:10.1016/j.cemconcomp.2008.10.003.

[12] E. Volpi, A. Olietti, M. Stefanoni, S.P. Trasatti, Electrochemical characterization of mild steel in alkaline solutions simulating concrete environment, J. Electroanal. Chem. 736 (2015) 38–46. doi:10.1016/j.jelechem.2014.10.023.

[13] Z. Chen, Y. Nong, Y. Chen, J. Chen, B. Yu, Study on the adsorption of OH^- and $CaOH^+$ on Fe (100) surface and their effect on passivation of steel bar: Experiments and DFT modelling, Corros. Sci. 174 (2020). doi:10.1016/j.corsci.2020.108804.

[14] J.R. Vilche, A.J. Arvia, O.A. Albani, J.O. Zerbino, A comparative electrochemical and ellipsometric study of iron electrodes in different alkaline electrolytes, Electrochim. Acta. 31 (1986) 1403–1411.

[15] M. Sánchez, J. Gregori, C. Alonso, J.J. García-Jareño, H. Takenouti, F. Vicente, Electrochemical impedance spectroscopy for studying passive layers on steel rebars immersed in alkaline solutions simulating concrete pores, Electrochim. Acta. 52 (2007) 7634–7641. doi:10.1016/j.electacta.2007.02.012.

[16] L. Jiang, B. Lin, Y. Cai, A model for predicting carbonation of high-volume fly ash concrete, Cem. Concr. Res. 30 (2000) 699–702. doi:10.1016/S0008-8846(00)00227-1.

[17] J.B. Aguiar, C. Júnior, Carbonation of surface protected concrete, Constr. Build. Mater. 49 (2013) 478–483. doi:10.1016/j.conbuildmat.2013.08.058.

[18] A.B. Ribeiro, T. Santos, A. Gonçalves, Performance of concrete exposed to natural carbonation: Use of the k-value concept, Constr. Build. Mater. 175 (2018) 360–370. doi:10.1016/j.conbuildmat.2018.04.206.

[19] M. Dąbrowski, M.A. Glinicki, K. Gibas, D. Jóźwiak-Niedźwiedzka, Effects of calcareous fly ash in blended cements on chloride ions migration and strength of air entrained concrete, Constr. Build. Mater. 126 (2016) 1044–1053. doi:10.1016/j.conbuildmat.2016.08.115.

[20] W. Prince, R. Gagné, The effects of types of solutions used in accelerated chloride migration tests for concrete, Cem. Concr. Res. 31 (2001) 775–780. doi:10.1016/S0008-8846(01)00473-2.

[21] B. Šavija, M. Luković, E. Schlangen, Lattice modeling of rapid chloride migration in concrete, Cem. Concr. Res. 61–62 (2014) 49–63. doi:10.1016/j.cemconres.2014.04.004.

[22] Y. Liu, X. Shi, Ionic transport in cementitious materials under an externally applied electric field: Finite element modeling, Constr. Build. Mater. 27 (2012) 450–460. doi:10.1016/j.conbuildmat.2011.07.019.

[23] M.T. Hasholt, O.M. Jensen, Chloride migration in concrete with superabsorbent polymers, Cem. Concr. Compos. 55 (2015) 290–297. doi:10.1016/j.cemconcomp.2014.09.023.

[24] A. Akhavan, S.M.H. Shafaatian, F. Rajabipour, Quantifying the effects of crack width, tortuosity, and roughness on water permeability of cracked mortars, Cem. Concr. Res. 42 (2012) 313–320. doi:10.1016/j.cemconres.2011.10.002.

[25] J. Zhang, P. Zhang, J. Wu, X. Feng, F. Bian, Y. Zhang, Time-dependent correlation between micro-structural parameters and gas permeability of concrete in a natural tidal environment, Constr. Build. Mater. 205 (2019) 475–485. doi:10.1016/j.conbuildmat.2019.01.200.

[26] Y. Zhang, H. Li, A. Abdelhady, J. Yang, H. Wang, Effects of specimen shape and size on the permeability and mechanical properties of porous concrete, Constr. Build. Mater. 266 (2021) 121074. doi:10.1016/j.conbuildmat.2020.121074.

[27] S. Dehghanpoor Abyaneh, H.S. Wong, N.R. Buenfeld, Computational investigation of capillary absorption in concrete using a three-dimensional mesoscale approach, Comput. Mater. Sci. 87 (2014) 54–64. doi:10.1016/j.commatsci.2014.01.058.

[28] S. Hong, W. Yao, B. Guo, C. Lin, B. Dong, W. Li, D. Hou, F. Xing, Water distribution characteristics in cement paste with capillary absorption, Constr. Build. Mater. 240 (2020) 117767. doi:10.1016/j.conbuildmat.2019.117767.

[29] P. Zhang, F.H. Wittmann, M. Vogel, H.S. Müller, T. Zhao, Influence of freeze-thaw cycles on capillary absorption and chloride penetration into concrete, Cem. Concr. Res. 100 (2017) 60–67. doi:10.1016/j.cemconres.2017.05.018.

[30] W.P.S. Dias, Reduction of concrete sorptivity with age through carbonation, Cem. Concr. Res. 30 (2000) 1255–1261. doi:10.1016/S0008-8846(00)00311-2.

[31] S. Ahmad, Reinforcement corrosion in concrete structures, its monitoring and service life prediction - A review, Cem. Concr. Compos. 25 (2003) 459–471. doi:10.1016/S0958-9465(02)00086-0.

[32] Y. Zhao, Y. Wu, W. Jin, Distribution of millscale on corroded steel bars and penetration of steel corrosion products in concrete, Corros. Sci. 66 (2013) 160–168. doi:10.1016/j.corsci.2012.09.014.

[33] E. Sola, J. Ožbolt, G. Balabanić, Z.M. Mir, Experimental and numerical study of accelerated

corrosion of steel reinforcement in concrete: Transport of corrosion products, Cem. Concr. Res. 120 (2019) 119–131. doi:10.1016/j.cemconres.2019.03.018.

[34] R. Rodrigues, S. Gaboreau, J. Gance, I. Ignatiadis, S. Betelu, Reinforced concrete structures: A review of corrosion mechanisms and advances in electrical methods for corrosion monitoring, Constr. Build. Mater. 269 (2021) 121240. doi:10.1016/j.conbuildmat.2020.121240.

[35] K. Suda, S. Misra, K. Motohashi, Corrosion products of reinforcing bars embedded in concrete, Corros. Sci. 35 (1993) 1543–1549. doi:10.1016/0010-938X(93)90382-Q.

[36] A. Köliö, M. Honkanen, J. Lahdensivu, M. Vippola, M. Pentti, Corrosion products of carbonation induced corrosion in existing reinforced concrete facades, Cem. Concr. Res. 78 (2015) 200–207. doi:10.1016/j.cemconres.2015.07.009.

[37] F. Chen, C.Q. Li, H. Baji, B. Ma, Quantification of non-uniform distribution and growth of corrosion products at steel-concrete interface, Constr. Build. Mater. 237 (2020) 117610. doi:10.1016/j.conbuildmat.2019.117610.

[38] J. Hou, D.D.L. Chung, Effect of admixtures in concrete on the corrosion resistance of steel reinforced concrete, Corros. Sci. 42 (2000) 1489–1507. doi:10.1016/S0010-938X(99)00134-1.

[39] P. Garcés, P. Saura, E. Zornoza, C. Andrade, Influence of pH on the nitrite corrosion inhibition of reinforcing steel in simulated concrete pore solution, Corros. Sci. 53 (2011) 3991–4000. doi:10.1016/j.corsci.2011.08.002.

[40] R.B. Figueira, A. Sadovski, A.P. Melo, E. V. Pereira, Chloride threshold value to initiate reinforcement corrosion in simulated concrete pore solutions: The influence of surface finishing and pH, Constr. Build. Mater. 141 (2017) 183–200. doi:10.1016/j.conbuildmat.2017.03.004.

[41] H. Bensabra, N. Azzouz, Study of rust effect on the corrosion behavior of reinforcement steel using impedance spectroscopy, Metall. Mater. Trans. A Phys. Metall. Mater. Sci. 44 (2013) 5703–5710. doi:10.1007/s11661-013-1915-4.

[42] J. Ming, J. Shi, Distribution of corrosion products at the steel-concrete interface: Influence of mill scale properties, reinforcing steel type and corrosion inducing method, Constr. Build. Mater. 229 (2019) 116854. doi:10.1016/j.conbuildmat.2019.116854.

[43] M. Pour-Ghaz, O.B. Isgor, P. Ghods, The effect of temperature on the corrosion of steel in concrete. Part 1: Simulated polarization resistance tests and model development, Corros. Sci. 51 (2009) 415–425. doi:10.1016/j.corsci.2008.10.034.

[44] M. Pour-Ghaz, O. Burkan Isgor, P. Ghods, The effect of temperature on the corrosion of steel in concrete. Part 2: Model verification and parametric study, Corros. Sci. 51 (2009) 426–433. doi:10.1016/j.corsci.2008.10.036.

[45] J.M. Deus, B. Díaz, L. Freire, X.R. Nóvoa, The electrochemical behaviour of steel rebars in concrete: An Electrochemical Impedance Spectroscopy study of the effect of temperature, Electrochim. Acta. 131 (2014) 106–115. doi:10.1016/j.electacta.2013.12.012.

[46] M. Stefanoni, U. Angst, B. Elsener, The mechanism controlling corrosion of steel in carbonated cementitious materials in wetting and drying exposure, Cem. Concr. Compos. 113 (2020) 103717. doi:10.1016/j.cemconcomp.2020.103717.

[47] R. Rizwan, T. Ishida, Influence of connectivity of concrete pores and associated diffusion of oxygen on corrosion of steel under high humidity, Constr. Build. Mater. 24 (2010) 1014–1019. doi:10.1016/j.conbuildmat.2009.11.017.

[48] S. Real, J.A. Bogas, Oxygen permeability of structural lightweight aggregate concrete, Constr. Build. Mater. 137 (2017) 21–34. doi:10.1016/j.conbuildmat.2017.01.075.

[49] C. Andrade, D. Baza, Porosity and electrical resistivity-based empirical calculation of the oxygen diffusion coefficient in concrete, Constr. Build. Mater. 198 (2019) 710–717. doi:10.1016/j.conbuildmat.2018.11.269.

[50] Y.S. Ji, M. Wu, Z. Tan, F. Gao, F. Liu, Process control of reinforcement corrosion in concrete. Part 2: Time-dependent dominating factors under different environmental conditions, Constr. Build. Mater. 73 (2014) 214–221. doi:10.1016/j.conbuildmat.2014.09.103.

[51] Y.S. Ji, G. Zhan, Z. Tan, Y. Hu, F. Gao, Process control of reinforcement corrosion in concrete. Part 1: Effect of corrosion products, Constr. Build. Mater. 79 (2015) 214–222. doi:10.1016/j.conbuildmat.2014.12.083.

[52] M. Stefanoni, U. Angst, B. Elsener, Local electrochemistry of reinforcement steel - Distribution of open circuit and pitting potentials on steels with different surface condition, Corros. Sci. 98 (2015) 610–618. doi:10.1016/j.corsci.2015.06.004.

[53] U. Angst, Ø. Vennesland, R. Myrdal, Diffusion potentials as source of error in electrochemical measurements in concrete, Mater. Struct. Constr. 42 (2009) 365–375. doi:10.1617/s11527-008-9387-5.

[54] K. Hornbostel, C.K. Larsen, M.R. Geiker, Relationship between concrete resistivity and corrosion rate - A literature review, Cem. Concr. Compos. 39 (2013) 60–72. doi:10.1016/j.cemconcomp.2013.03.019.

[55] F. Presuel-Moreno, Y. Liu, Y.Y. Wu, Numerical modeling of the effects of rebar presence and/or multilayered concrete resistivity on the apparent resistivity measured via the Wenner method, Constr. Build. Mater. 48 (2013) 16–25. doi:10.1016/j.conbuildmat.2013.06.053.

[56] R.B. Polder, Test methods for on site measurement of resistivity of concrete - a RILEM TC-154 technical recommendation, Constr. Build. Mater. 15 (2001) 125–131. doi:10.1016/S0950-0618(00)00061-1.

[57] M. Stern, A.L. Geary, Electrochemical Polarization, 1. A Theoretical Analysis of the Shape of Polarization Curves, J. Electrochem. Soc. 104 (1957) 56–63. doi:10.1149/1.2428473.

[58] M.A. Peter, A. Muntean, S.A. Meier, M. Böhm, Competition of several carbonation reactions in concrete: A parametric study, Cem. Concr. Res. 38 (2008) 1385–1393. doi:10.1016/j.cemconres.2008.09.003.

[59] B. Šavija, M. Luković, Carbonation of cement paste: Understanding, challenges, and opportunities, Constr. Build. Mater. 117 (2016) 285–301. doi:10.1016/j.conbuildmat.2016.04.138.

[60] V.G. Papadakis, Effect of supplementary cementing materials on concrete resistance against carbonation and chloride ingress, Cem. Concr. Res. 30 (2000) 291–299. doi:10.1016/S0008-8846(99)00249-5.

[61] E. Gruyaert, P. Van Den Heede, N. De Belie, Carbonation of slag concrete: Effect of the cement replacement level and curing on the carbonation coefficient - Effect of carbonation on the pore structure, Cem. Concr. Compos. 35 (2013) 39–48. doi:10.1016/j.cemconcomp.2012.08.024.

[62] P. Duan, C. Yan, W. Zhou, Effects of calcined layered double hydroxides on carbonation of concrete containing fly ash, Constr. Build. Mater. 160 (2018) 725–732. doi:10.1016/j.conbuildmat.2017.11.099.

[63] Z.H. Shui, R. Yu, Y.X. Chen, P. Duan, J.T. Ma, X.P. Wang, Improvement of concrete

carbonation resistance based on a structure modified Layered Double Hydroxides (LDHs): Experiments and mechanism analysis, Constr. Build. Mater. 176 (2018) 228–240. doi:10.1016/j.conbuildmat.2018.04.222.

[64] C. Shi, T.S. He, G. Zhang, X. Wang, Y. Hu, Effects of superplasticizers on carbonation resistance of concrete, Constr. Build. Mater. 108 (2016) 48–55. doi:10.1016/j.conbuildmat.2016.01.037.

[65] S. Steiner, B. Lothenbach, T. Proske, A. Borgschulte, F. Winnefeld, Effect of relative humidity on the carbonation rate of portlandite, calcium silicate hydrates and ettringite, Cem. Concr. Res. 135 (2020) 106116. doi:10.1016/j.cemconres.2020.106116.

[66] H. Cui, W. Tang, W. Liu, Z. Dong, F. Xing, Experimental study on effects of CO2 concentrations on concrete carbonation and diffusion mechanisms, Constr. Build. Mater. 93 (2015) 522–527. doi:10.1016/j.conbuildmat.2015.06.007.

[67] G. Villain, M. Thiery, G. Platret, Measurement methods of carbonation profiles in concrete: Thermogravimetry, chemical analysis and gammadensimetry, Cem. Concr. Res. 37 (2007) 1182–1192. doi:10.1016/j.cemconres.2007.04.015.

[68] T. K., Corrosion of steel in concrete, Swedish Cem. Concr. Res. Institute, Stock. (1982).

[69] P. Ghods, O. Burkan Isgor, F. Bensebaa, D. Kingston, Angle-resolved XPS study of carbon steel passivity and chloride-induced depassivation in simulated concrete pore solution, Corros. Sci. 58 (2012) 159–167. doi:10.1016/j.corsci.2012.01.019.

[70] B. Lin, R. Hu, C. Ye, Y. Li, C. Lin, A study on the initiation of pitting corrosion in carbon steel in chloride-containing media using scanning electrochemical probes, Electrochim. Acta. 55 (2010) 6542–6545. doi:10.1016/j.electacta.2010.06.024.

[71] R.E. Beddoe, H.W. Dorner, Modelling acid attack on concrete: Part I. The essential mechanisms, Cem. Concr. Res. 35 (2005) 2333–2339. doi:10.1016/j.cemconres.2005.04.002.

[72] R. Talero, L. Trusilewicz, A. Delgado, C. Pedrajas, R. Lannegrand, V. Rahhal, R. Mejía, S. Delvasto, Comparative and semi-quantitative XRD analysis of Friedel' s salt originating from pozzolan and Portland cement, Constr. Build. Mater. 25 (2011) 2370–2380. doi:10.1016/j.conbuildmat.2010.11.037.

[73] G. Paul, E. Boccaleri, L. Buzzi, F. Canonico, D. Gastaldi, Cement and Concrete Research Friedel' s salt formation in sulfoaluminate cements: A combined XRD and Al MAS NMR study, Cem. Concr. Res. 67 (2015) 93–102. doi:10.1016/j.cemconres.2014.08.004.

[74] Z. Shi, M. Rica, B. Lothenbach, K. De Weerdt, K. Enemark-rasmussen, J. Skibsted, S. Ferreiro, Friedel' s salt profiles from thermogravimetric analysis and thermodynamic modelling of Portland cement-based mortars exposed to sodium chloride solution, 78 (2017). doi:10.1016/j.cemconcomp.2017.01.002.

[75] M. Chen, F. Wu, L. Yu, Y. Cai, H. Chen, M. Zhang, Chloride binding capacity of LDHs with various divalent cations and divalent to trivalent cation ratios in different solutions, CrystEngComm. 21 (2019) 6790–6800. doi:10.1039/c9ce01322a.

[76] G.K. Glass, B. Reddy, N.R. Buenfeld, The participation of bound chloride in passive film breakdown on steel in concrete, Corros. Sci. 42 (2000) 2013–2021. doi:10.1016/S0010-938X(00)00040-8.

[77] V. Zivica, A. Bajza, Acidic attack of cement based materials - A review. Part 1. Principle of acidic attack, Constr. Build. Mater. 15 (2001) 331–340. doi:10.1016/S0950-0618(01)00012-5.

[78] S. Irico, L. De Meyst, D. Qvaeschning, M.C. Alonso, K. Villar, N. De Belie, Severe sulfuric

acid attack on self-compacting concrete with granulometrically optimized blast-furnace slag-comparison of different test methods, Materials (Basel). 13 (2020). doi:10.3390/ma13061431.

[79] T. Gutberlet, H. Hilbig, R.E. Beddoe, Acid attack on hydrated cement - Effect of mineral acids on the degradation process, Cem. Concr. Res. 74 (2015) 35–43. doi:10.1016/j.cemconres.2015.03.011.

[80] H. Gay, T. Meynet, J. Colombani, Local study of the corrosion kinetics of hardened Portland cement under acid attack, Cem. Concr. Res. 90 (2016) 36–42. doi:10.1016/j.cemconres.2016.09.007.

[81] O. Oueslati, J. Duchesne, The effect of SCMs and curing time on resistance of mortars subjected to organic acids, Cem. Concr. Res. 42 (2012) 205–214. doi:10.1016/j.cemconres.2011.09.017.

[82] E.O. Nnadi, J. Lizarazo-Marriaga, Acid Corrosion of Plain and Reinforced Concrete Sewage Systems, J. Mater. Civ. Eng. 25 (2013) 1353–1356. doi:10.1061/(asce)mt.1943-5533.0000641.

[83] H. Yuan, P. Dangla, P. Chatellier, T. Chaussadent, Degradation modelling of concrete submitted to sulfuric acid attack, Cem. Concr. Res. 53 (2013) 267–277. doi:10.1016/j.cemconres.2013.08.002.

[84] L. Gu, P. Visintin, T. Bennett, Evaluation of accelerated degradation test methods for cementitious composites subject to sulfuric acid attack; application to conventional and alkali-activated concretes, Cem. Concr. Compos. 87 (2018) 187–204. doi:10.1016/j.cemconcomp.2017.12.015.

[85] R.G. Du, R.G. Hu, R.S. Huang, C.J. Lin, In situ measurement of Cl- concentrations and pH at the reinforcing steel/concrete interface by combination sensors, Anal. Chem. 78 (2006) 3179–3185.

[86] W. Vonau, U. Guth, pH Monitoring: A review, J. Solid State Electrochem. 10 (2006) 746–752.

[87] Y. Abbas, F. Pargar, D.A. Koleva, K. van Breugel, W. Olthuis, A. van den Berg, Non-destructive measurement of chloride ions concentration in concrete – A comparative analysis of limitations and prospects, Constr. Build. Mater. 174 (2018) 376–387.

[88] F. Schoefs, M. Torres-Luque, M. Sánchez-Silva, J.F. Osma, E. Bastidas-Arteaga, Non-destructive methods for measuring chloride ingress into concrete: State-of-the-art and future challenges, Constr. Build. Mater. 68 (2014) 68–81.

[89] A. Behnood, K. Van Tittelboom, N. De Belie, Methods for measuring pH in concrete: A review, Constr. Build. Mater. 105 (2016) 176–188.

[90] A. Hulanicki, S. Geab, F. Ingman, Chemical sensors definitions and classification, Pure Appl. Chern. 63 (1991) 1247–1250.

[91] L.M. Moretto, K. Kalcher, Environmental Analysis by Electrochemical Sensors and Biosensors, Springer, 2014.

[92] P. Gründler, Chemical sensors: An introduction for scientists and engineers, Springer, 2007. doi:10.1007/978-3-540-45743-5.

[93] C.P. Atkins, J.D. Scantlebury, P.J. Nedwell, S.P. Blatch, Monitoring Chloride Concentrations in Hardened Cement Pastes Using Ion Selective Electrodes, Cem. Concr. Compos. 26 (1995) 319–324.

[94] M.A. Climent-Llorca, E. Viqueira-Pérez, M.M. López-Atalaya, Embeddable Ag/AgCl

sensors for in-situ monitoring chloride contents in concrete, Cem. Concr. Res. 26 (1996) 1157–1161.

[95] M.F. Montemor, J.H. Alves, A.M. Simões, J.C.S. Fernandes, Z. Lourenço, A.J.S. Costa, A.J. Appleton, M.G.S. Ferreira, Multiprobe chloride sensor for in situ monitoring of reinforced concrete structures, Cem. Concr. Compos. 28 (2006) 233–236.

[96] R. Greef, R. Peat, L.M. Peter, D. Pletcher, J. Robinson, Instrumental Methods in Electrochemistry, Woodhead Publishing Limited, 2011.

[97] L. Guo, P.C. Searson, Evolution of surface width in electrochemical nucleation and growth, Electrochem. Commun. 12 (2010) 431–434. doi:10.1016/j.elecom.2010.01.011.

[98] L. Guo, P.C. Searson, On the influence of the nucleation overpotential on island growth in electrodeposition, Electrochim. Acta. 55 (2010) 4086–4091. doi:10.1016/j.electacta.2010.02.038.

[99] B.R. Scharifker, J. Mostany, Electrochemical Nucleation and Growth, in: Encycl. Electrochem., 2003. doi:10.1002/9783527610426.bard020503.

[100] B. Scharifker, Theoretical and experimental studies of multiple nucleation, Electrochim. Acta. 28 (1982) 879–889.

[101] P. Sjöberg-Eerola, J. Bobacka, A. Lewenstam, A. Ivaska, All-solid-state chloride sensors based on electronically conducting, semiconducting and insulating polymer membranes, Sensors Actuators, B Chem. 127 (2007) 545–553.

[102] N.M. Kocherginsky, Z. Wang, Polyaniline membrane based potentiometric sensor for ascorbic acid, other redox active species and chloride, J. Electroanal. Chem. 611 (2007) 162–168.

[103] P.L. Fuhr, B. MacCraith, D.R. Huston, M. Guerrina, M. Nelson, Fiber Optic Chloride Sensing, (n.d.).

[104] F. Laferrière, D. Inaudi, P. Kronenberg, I.F.C. Smith, A new system for early chloride detection in concrete, Smart Mater. Struct. 17 (2008) 045017. doi:10.1088/0964-1726/17/4/045017.

[105] P.J. Brewer, A.S. Leach, R.J.C. Brown, The Role of the Electrolyte in the Fabrication of Ag|AgCl Reference Electrodes for pH Measurement, Electrochim. Acta. 161 (2015) 80–83.

[106] D. Stoica, P.J. Brewer, R.J.C. Brown, P. Fisicaro, Influence of fabrication procedure on the electrochemical performance of Ag/AgCl reference electrodes, Electrochim. Acta. 56 (2011) 10009–10015.

[107] S. Zhao, Y. Zhang, Y. Zhou, K. Qiu, C. Zhang, J. Fang, X. Sheng, Reactable polyelectrolyte-assisted preparation of flower-like Ag/AgCl/BiOCl composite with enhanced photocatalytic activity, J. Photochem. Photobiol. A Chem. 350 (2018) 94–102.

[108] X. Lin, H. Liu, B. Guo, X. Zhang, Synthesis of AgCl/Ag/AgCl core-shell microstructures with enhanced photocatalytic activity under sunlight irradiation, J. Environ. Chem. Eng. 4 (2016) 4021–4028.

[109] C.P. Atkins, M.A. Carter, J.D. Scantlebury, Sources of error in using silver/silver chloride electrodes to monitor chloride activity in concrete, Cem. Concr. Res. 31 (2001) 1207–1211. doi:10.1016/S0008-8846(01)00544-0.

[110] R.G. Compton, G.H.W. Sanders, Electrode potentials, Oxford Science Publications, 1996.

[111] G. Inzelt, A. Lewenstam, F. Scholz, Handbook of Reference Electrodes, Springer, 2013.

[112] M.F.L. Demele, R.C. Salvarezza, V.D. V Moll, H.A. Videla, A.J. Arvia, Kinetics and

Mechanism of Silver-Chloride Electroformation during the Localized Electrodissolution of Silver in Solutions Containing Sodium-Chloride, J. Electrochem. Soc. 133 (1986) 746–752. doi:10.1149/1.2108667.

[113] H. Ha, J. Payer, The effect of silver chloride formation on the kinetics of silver dissolution in chloride solution, Electrochim. Acta. 56 (2011) 2781–2791. doi:10.1016/j.electacta.2010.12.050.

[114] G.J. Janz, H. Taniguchi, The Silver-Silver halide Electrodes: Preparation, Stability, and Standard Potentials in Aqueous and non-Aqueous Media, Chem. Rev. 53 (1953) 397–437.

[115] Y. Seguí Femenias, U. Angst, F. Caruso, B. Elsener, Ag/AgCl ion-selective electrodes in neutral and alkaline environments containing interfering ions, Mater. Struct. Constr. 49 (2016) 2637–2651. doi:10.1617/s11527-015-0673-8.

[116] M.J. Ruedas-Rama, A. Orte, E.A.H. Hall, J.M. Alvarez-Pez, E.M. Talavera, A chloride ion nanosensor for time-resolved fluorimetry and fluorescence lifetime imaging, Analyst. 137 (2012) 1500–1508. doi:10.1039/c2an15851e.

[117] W. Xiao, L. Ding, J. He, J. Huang, Preparation of lucigenin-doped silica nanoparticles and their application in fiber optic chloride ion sensor, Opt. Mater. (Amst). 98 (2019) 109467. doi:10.1016/j.optmat.2019.109467.

[118] J.I. Millán, J. V. García-Ramos, S. Sanchez-Cortes, Study of the adsorption and electrochemical reduction of lucigenin on Ag electrodes by surface-enhanced Raman spectroscopy, J. Electroanal. Chem. 556 (2003) 83–92. doi:10.1016/S0022-0728(03)00332-2.

[119] S. Kakooei, C. Ismail, B. Ari-Wahjoedi, An overview of pH Sensors Based on Iridium Oxide: Fabrication and Application, Int. J. Mater. Sci. Innov. 1 (2013) 62–72.

[120] Z. Zhu, X. Liu, Z. Ye, J. Zhang, F. Cao, J. Zhang, A fabrication of iridium oxide film pH micro-sensor on Pt ultramicroelectrode and its application on in-situ pH distribution of 316L stainless steel corrosion at open circuit potential, Sensors Actuators, B Chem. 255 (2018) 1974–1982.

[121] C.C.M. Martinez, R.E. Madrid, C.J. Felice, A pH sensor based on a stainless steel electrode electrodeposited with iridium oxide, IEEE Trans. Educ. 52 (2009) 133–136.

[122] N. Cherchour, C. Deslouis, B. Messaoudi, A. Pailleret, pH sensing in aqueous solutions using a MnO2 thin film electrodeposited on a glassy carbon electrode, Electrochim. Acta. 56 (2011) 9746–9755.

[123] S. Muralidharan, T.H. Ha, J.H. Bae, Y.C. Ha, H.G. Lee, D.K. Kim, A promising potential embeddable sensor for corrosion monitoring application in concrete structures, Measurement. 40 (2007) 600–606.

[124] F. Yue, T.S. Ngin, G. Hailin, A novel paper pH sensor based on polypyrrole, Sensors Actuators B. 32 (1996) 33–39.

[125] K.K. Shiu, F.Y. Song, K.W. Lau, Effects of polymer thickness on the potentiometric pH responses of polypyrrole modified glassy carbon electrodes, J. Electroanal. Chem. 476 (1999) 109–117.

[126] X. Mo, J. Wang, Z. Wang, S. Wang, Potentiometric pH responses of fibrillar polypyrrole modified electrodes, Sensors Actuators B. 96 (2003) 533–536.

[127] A.E. Taouil, F. Lallemand, J.M. Melot, J. Husson, J.Y. Hihn, B. Lakard, Effects of polypyrrole modified electrode functionalization on potentiometric pH responses, Synth. Met. 160 (2010) 1073–1080.

[128] H.J.N.P.D. Mello, M. Mulato, Influence of galvanostatic electrodeposition parameters on the structure-property relationships of polyaniline thin films and their use as potentiometric and optical pH sensors, Thin Solid Films. 656 (2018) 14–21.

[129] A. Fog, R.P. Buck, Electronic semiconducting oxides as pH sensors, Sensors and Actuators. 5 (1984) 137–146. doi:10.1016/0250-6874(84)80004-9.

[130] P. Steegstra, E. Ahlberg, Involvement of nanoparticles in the electrodeposition of hydrous iridium oxide films, Electrochim. Acta. 68 (2012) 206–213.

[131] R.D. Meyer, S.F. Cogan, T.H. Nguyen, R.D. Rauh, Electrodeposited iridium oxide for neural stimulation and recording electrodes, IEEE Trans. Neural Syst. Rehabil. Eng. 9 (2001) 2–11. doi:10.1109/7333.918271.

[132] Y. Lu, T. Wang, Z. Cai, Y. Cao, H. Yang, Y.Y. Duan, Anodically electrodeposited iridium oxide films microelectrodes for neural microstimulation and recording, Sensors Actuators, B Chem. 137 (2009) 334–339. doi:10.1016/j.snb.2008.11.036.

[133] R. Badam, M. Hara, H.H. Huang, M. Yoshimura, Synthesis and electrochemical analysis of novel IrO2 nanoparticle catalysts supported on carbon nanotube for oxygen evolution reaction, Int. J. Hydrogen Energy. 43 (2018) 18095–18104. doi:10.1016/j.ijhydene.2018.08.034.

[134] B. Tian, F. Liu, Y. Liu, C. Wang, J. Wang, Y. Lei, Investigation of high-performance IrO2 electrocatalysts prepared by Adams method, Int. J. Hydrogen Energy. 43 (2018) 19460–19467. doi:10.1016/j.ijhydene.2018.08.196.

[135] A. Papaderakis, D. Tsiplakides, S. Balomenou, S. Sotiropoulos, Electrochemical impedance studies of IrO2 catalysts for oxygen evolution, J. Electroanal. Chem. 757 (2015) 216–224. doi:10.1016/j.jelechem.2015.09.033.

[136] A. Savan, B. Ratna, S. Merzlikin, B. Breitbach, A. Ludwig, K.J.J.J. Mayrhofer, S. Cherevko, S. Geiger, O. Kasian, N. Kulyk, J.-P. Grote, A. Savan, B.R. Shrestha, S. Merzlikin, B. Breitbach, A. Ludwig, K.J.J.J. Mayrhofer, Oxygen and hydrogen evolution reactions on Ru, RuO_2, Ir, and IrO_2 thin film electrodes in acidic and alkaline electrolytes: A comparative study on activity and stability, Catal. Today. 262 (2015) 170–180. doi:10.1016/j.cattod.2015.08.014.

[137] T.N. Wu, Electrochemical removal of MTBE from water using the iridium dioxide coated electrode, Sep. Purif. Technol. 79 (2011) 216–220. doi:10.1016/j.seppur.2011.02.008.

[138] S. Korkmaz, F.M. Tezel, A. Kariper, Synthesis and Characterization of GO/IrO2 Thin Film Supercapacitor, Synth. Met. 242 (2018) 37–48. doi:10.1016/j.synthmet.2018.05.002.

[139] R.M. Ianniello, A.M. Yacynch, Urea sensor based on iridium dioxide electrodes with immobilized urease, Anal. Chim. Acta. 146 (1983) 249–253. doi:10.1016/S0003-2670(00)80612-1.

[140] W. Olthuis, M.A.M. Robben, P. Bergveld, M. Bos, W.E. van der Linden, pH sensor properties of electrochemically grown iridium oxide, Sensors Actuators B. Chem. 2 (1990) 247–256. doi:10.1016/0925-4005(90)80150-X.

[141] M.A. Petit, V. Plichon, Anodic electrodeposition of iridium oxide films, J. Electroanal. Chem. 444 (1998) 247–252. doi:10.1016/S0022-0728(97)00570-6.

[142] Y. Chen, P.L. Taylor, D. Scherson, Electrochemical and In Situ Optical Studies of Supported Iridium Oxide Films in Aqueous Solutions, J. Electrochem. Soc. 156 (2009) F14. doi:10.1149/1.2999092.

[143] H.A. Elsen, C.F. Monson, M. Majda, Effects of Electrodeposition Conditions and Protocol

on the Properties of Iridium Oxide pH Sensor Electrodes, J. Electrochem. Soc. 156 (2009) F1–F6. doi:10.1149/1.3001924.

[144] I.G. Casella, M. Contursi, R. Toniolo, Anodic electrodeposition of iridium oxide particles on glassy carbon surfaces and their electrochemical/SEM/XPS characterization, J. Electroanal. Chem. 736 (2015) 147–152. doi:10.1016/j.jelechem.2014.11.012.

[145] M. Wang, S. Yao, M. Madou, A long-term stable iridium oxide pH electrode, Sensors Actuators, B Chem. 81 (2002) 313–315. doi:10.1016/S0925-4005(01)00972-8.

[146] S. Yao, M. Wang, M. Madou, A pH Electrode Based on Melt-Oxidized Iridium Oxide, J. Electrochem. Soc. 148 (2001) H29–H36. doi:10.1149/1.1353582.

[147] H.Y. Wang, Y.C. Hsieh, K.C. Tso, C.K. Chang, Y.T. Cheng, P.W. Wu, J.F. Lee, Combination of electrophoresis and electro-flocculation for the formation of adhering IrO2 pH sensing films, Electrochim. Acta. 312 (2019) 291–298. doi:10.1016/j.electacta.2019.05.006.

[148] C.M. Nguyen, S. Rao, X. Yang, S. Dubey, J. Mays, H. Cao, J.C. Chiao, Sol-gel deposition of iridium oxide for biomedical micro-devices, Sensors (Switzerland). 15 (2015) 4212–4228. doi:10.3390/s150204212.

[149] M.A. El Khakani, M. Chaker, Reactive pulsed laser deposition of iridium oxide thin films, Thin Solid Films. 335 (1998) 6–12. doi:10.1016/S0040-6090(98)00862-1.

[150] J. Backholm, E. Avendano, A. Azens, G. de M Azevedo, E. Coronel, G.A. Niklasson, C.G. Granqvist, Iridium-based oxides: Recent advances in coloration mechanism, structural and morphological characterization, Sol. Energy Mater. Sol. Cells. 92 (2008) 91–96. doi:10.1016/j.solmat.2007.03.029.

[151] L.D. Burke, J.K. Mulcahy, D.P. Whelan, Preparation of an oxidized iridium electrode and the variation of its potential with pH, J. Electroanal. Chem. 163 (1984) 117–128. doi:10.1016/S0022-0728(84)80045-5.

[152] E.E.D.M. El-Giar, D.O. Wipf, Microparticle-based iridium oxide ultramicroelectrodes for pH sensing and imaging, J. Electroanal. Chem. 609 (2007) 147–154.

[153] C.C. Mayorga Martinez, R.E. Madrid, C.J. Felice, Electrochemical and geometrical characterization of iridium oxide electrodes in stainless steel substrate, Sensors Actuators B. 133 (2008) 682–686.

[154] K. Yamanaka, Anodically electrodeposited Iridium Oxide Films, Jpn. J. Appl. Phys. 28 (1989) 632–637.

[155] S.A.M. Marzouk, S. Ufer, R.P. Buck, T.A. Johnson, L.A. Dunlap, W.E. Cascio, Electrodeposited iridium oxide pH electrode for measurement of extracellular myocardial acidosis during acute ischemia, Anal. Chem. 70 (1998) 5054–5061. doi:10.1021/ac980608e.

[156] A. Cross, A. Morel, A. Cormie, T. Hollenkamp, S. Donne, Enhanced manganese dioxide supercapacitor electrodes produced by electrodeposition, J. Power Sources. 196 (2011) 7847–7853.

[157] M.F. Dupont, S.W. Donne, Nucleation and growth of electrodeposited manganese dioxide for electrochemical capacitors, Electrochim. Acta. 120 (2014) 219–225. doi:10.1016/j.electacta.2013.12.014.

[158] D.P. Dubal, D.S. Dhawale, T.P. Gujar, C.D. Lokhande, Effect of different modes of electrodeposition on supercapacitive properties of MnO2thin films, Appl. Surf. Sci. 257 (2011) 3378–3382. doi:10.1016/j.apsusc.2010.11.028.

[159] B. Babakhani, D.G. Ivey, Effect of electrodeposition conditions on the electrochemical capacitive behavior of synthesized manganese oxide electrodes, J. Power Sources. 196 (2011)

10762–10774. doi:10.1016/j.jpowsour.2011.08.102.

[160] N. Palaniyandy, F.P. Nkosi, K. Raju, K.I. Ozoemena, Conversion of electrolytic MnO2 to Mn3O4 nanowires for high-performance anode materials for lithium-ion batteries, J. Electroanal. Chem. 833 (2019) 79–92.

[161] M. Chamoun, W.R. Brant, C.W. Tai, G. Karlsson, D. Noréus, Rechargeability of aqueous sulfate Zn/MnO2 batteries enhanced by accessible Mn2+ ions, Energy Storage Mater. 15 (2018) 351–360.

[162] M. Raupach, J. Mietz, B. Elsener, R. Polder, Corrosion of Reinforcement in Concrete - Monitoring , Prevention and Rehabilitation, Woodhead Publishing Limited, 2006.

[163] Y. Wei, L. Ni, M. Li, J. Zhao, A template-free method for preparation of MnO2 catalysts with high surface areas, Catal. Today. 297 (2017) 188–192.

[164] J. Li, I. Zhitomirsky, Cathodic electrophoretic deposition of manganese dioxide films, Colloids Surfaces A Physicochem. Eng. Asp. 348 (2009) 248–253. doi:10.1016/j.colsurfa.2009.07.035.

[165] Z. Rogulski, H. Siwek, I. Paleska, A. Czerwiński, Electrochemical behavior of manganese dioxide on a gold electrode, J. Electroanal. Chem. 543 (2003) 175–185.

[166] X. Hu, X. Lin, Z. Ling, Y. Li, X. Fu, Fabrication and characteristics of galvanostatic electrodeposited MnO 2 on porous nickel from etched aluminium, Electrochim. Acta. 138 (2014) 132–138. doi:10.1016/j.electacta.2014.06.109.

[167] M.P. Owen, G.A. Lawrance, S.W. Donne, An electrochemical quartz crystal microbalance study into the deposition of manganese dioxide, Electrochim. Acta. 52 (2007) 4630–4639. doi:10.1016/j.electacta.2007.01.012.

[168] A.J. Gibson, R.C. Burns, M.F. Dupont, S.W. Donne, Mesoscale morphological control of electrodeposited manganese dioxide films, Electrochim. Acta. 170 (2015) 343–352. doi:10.1016/j.electacta.2015.04.036.

[169] S. Bodoardo, J. Brenet, M. Maja, P. Spinelli, Electrochemical behaviour of MnO2 electrodes in sulphuric acid solutions, Electrochim. Acta. 39 (1994) 1999–2004. doi:10.1016/0013-4686(94)85080-1.

[170] S. Nijjer, J. Thonstad, G.M. Haarberg, Oxidation of manganese(II) and reduction of manganese dioxide in sulphuric acid, Electrochim. Acta. 46 (2000) 395–399. doi:10.1016/S0013-4686(00)00597-1.

[171] R.L. Paul, A. Cartwright, The mechanism of the deposition of manganese dioxide. Part II. Electrode impedance studies, J. Electroanal. Chem. 201 (1986) 113–122. doi:10.1016/0022-0728(86)90091-4.

[172] R.L. Paul, A. Cartwright, The mechanism of the deposition of manganese dioxide, J. Electroanal. Chem. Interfacial Electrochem. 201 (1986) 123–131. doi:10.1016/0022-0728(86)90092-6.

[173] G. Davies, Some aspects of the chemistry of manganese(III) in aqueous solution, Coord. Chem. Rev. 4 (1969) 199–224. doi:10.1016/S0010-8545(00)80086-7.

[174] A. Sardarinejad, D.K. Maurya, K. Alameh, The effects of sensing electrode thickness on ruthenium oxide thin-film pH sensor, Sensors Actuators, A Phys. 214 (2014) 15–19. doi:10.1016/j.sna.2014.04.007.

[175] B. Xu, W. De Zhang, Modification of vertically aligned carbon nanotubes with RuO2 for a solid-state pH sensor, Electrochim. Acta. 55 (2010) 2859–2864. doi:10.1016/j.electacta.2009.12.099.

[176] Y.H. Liao, J.C. Chou, Preparation and characteristics of ruthenium dioxide for pH array sensors with real-time measurement system, Sensors Actuators, B Chem. 128 (2008) 603–612. doi:10.1016/j.snb.2007.07.023.

[177] W. Lonsdale, D.K. Maurya, M. Wajrak, C.Y. Tay, B.J. Marshall, K. Alameh, Rapid measurement of urease activity using a potentiometric RuO2 pH sensor for detection of Helicobacter pylori, Sensors Actuators, B Chem. 242 (2017) 1305–1308. doi:10.1016/j.snb.2016.06.024.

[178] D.K. Maurya, A. Sardarinejad, K. Alameh, High-sensitivity pH sensor employing a sub-micron ruthenium oxide thin-film in conjunction with a thick reference electrode, Sensors Actuators, A Phys. 203 (2013) 300–303. doi:10.1016/j.sna.2013.09.003.

[179] J.J. Jow, H.J. Lee, H.R. Chen, M.S. Wu, T.Y. Wei, Anodic, cathodic and cyclic voltammetric deposition of ruthenium oxides from aqueous RuCl3 solutions, Electrochim. Acta. 52 (2007) 2625–2633. doi:10.1016/j.electacta.2006.09.018.

[180] C.C. Hu, K.H. Chang, Cyclic voltammetric deposition of hydrous ruthenium oxide for electrochemical supercapacitors: Effects of the chloride precursor transformation, J. Power Sources. 112 (2002) 401–409. doi:10.1016/S0378-7753(02)00397-X.

[181] C.C. Hu, K.H. Chang, Cyclic voltammetric deposition of hydrous ruthenium oxide for electrochemical capacitors: Effects of codepositing iridium oxide, Electrochim. Acta. 45 (2000) 2685–2696. doi:10.1016/S0013-4686(00)00386-8.

[182] R.K.V. Prataap, R. Arunachalam, R. Pavul Raj, S. Mohan, L. Peter, Effect of electrodeposition modes on ruthenium oxide electrodes for supercapacitors, Curr. Appl. Phys. 18 (2018) 1143–1148. doi:10.1016/j.cap.2018.06.015.

[183] D.J. Lee, S.W. Kang, S.W. Rhee, Chemical vapor deposition of ruthenium oxide thin films from Ru(tmhd)3 using direct liquid injection, Thin Solid Films. 413 (2002) 237–242. doi:10.1016/S0040-6090(02)00439-X.

[184] H.N. McMurray, P. Douglas, D. Abbot, Novel thick-film pH sensors based on ruthenium dioxide-glass composites, Sensors Actuators B. Chem. 28 (1995) 9–15.

[185] M. Vuković, D. Čukman, Electrochemical quartz crystal microbalance study of electrodeposited ruthenium, J. Electroanal. Chem. 474 (1999) 167–173. doi:10.1016/S0022-0728(99)00332-0.

[186] P. Kurzweil, Precious metal oxides for electrochemical energy converters: Pseudocapacitance and pH dependence of redox processes, J. Power Sources. 190 (2009) 189–200. doi:10.1016/j.jpowsour.2008.08.033.

[187] R. Balint, N.J. Cassidy, S.H. Cartmell, Conductive polymers: Towards a smart biomaterial for tissue engineering, Acta Biomater. 10 (2014) 2341–2353. doi:10.1016/j.actbio.2014.02.015.

[188] H. Nguyen Thi Le, B. Garcia, C. Deslouis, Q. Le Xuan, Corrosion protection and conducting polymers: Polypyrrole films on iron, Electrochim. Acta. 46 (2001) 4259–4272. doi:10.1016/S0013-4686(01)00699-5.

[189] P. Herrasti, A.I. del Rio, J. Recio, Electrodeposition of homogeneous and adherent polypyrrole on copper for corrosion protection, Electrochim. Acta. 52 (2007) 6496–6501. doi:10.1016/j.electacta.2007.04.074.

[190] M.B. Gonz??lez, S.B. Saidman, Electrodeposition of polypyrrole on 316L stainless steel for corrosion prevention, Corros. Sci. 53 (2011) 276–282. doi:10.1016/j.corsci.2010.09.021.

[191] R.H. Baughman, Conducting polymer artificial muscles, Synth. Met. 78 (1996) 339–353.

doi:10.1016/0379-6779(96)80158-5.

[192] T.F. Otero, J.G. Martinez, J. Arias-Pardilla, Biomimetic electrochemistry from conducting polymers. A review: Artificial muscles, smart membranes, smart drug delivery and computer/neuron interfaces, Electrochim. Acta. 84 (2012) 112–128. doi:10.1016/j.electacta.2012.03.097.

[193] T.F. Otero, J.G. Martinez, Physical and chemical awareness from sensing polymeric artificial muscles. Experiments and modeling, Prog. Polym. Sci. 44 (2015) 62–78. doi:10.1016/j.progpolymsci.2014.09.002.

[194] K.K.C. Lee, N.R. Munce, T. Shoa, L.G. Charron, G.A. Wright, J.D. Madden, V.X.D. Yang, Fabrication and characterization of laser-micromachined polypyrrole-based artificial muscle actuated catheters, Sensors Actuators, A Phys. 153 (2009) 230–236. doi:10.1016/j.sna.2009.05.005.

[195] M. Itik, E. Sahin, M.S. Ayas, Fractional order control of conducting polymer artificial muscles, Expert Syst. Appl. 42 (2015) 8212–8220. doi:10.1016/j.eswa.2015.06.033.

[196] A. Mourato, A.S. Viana, J.P. Correia, H. Siegenthaler, L.M. Abrantes, Polyaniline films containing electrolessly precipitated palladium, Electrochim. Acta. 49 (2004) 2249–2257. doi:10.1016/j.electacta.2004.01.006.

[197] M.H. Naveen, N.G. Gurudatt, Y.B. Shim, Applications of conducting polymer composites to electrochemical sensors: A review, Appl. Mater. Today. 9 (2017) 419–433. doi:10.1016/j.apmt.2017.09.001.

[198] S. Nambiar, J.T.W. Yeow, Conductive polymer-based sensors for biomedical applications, Biosens. Bioelectron. 26 (2011) 1825–1832. doi:10.1016/j.bios.2010.09.046.

[199] J.M. Moon, N. Thapliyal, K.K. Hussain, R.N. Goyal, Y.B. Shim, Conducting polymer-based electrochemical biosensors for neurotransmitters: A review, Biosens. Bioelectron. 102 (2018) 540–552. doi:10.1016/j.bios.2017.11.069.

[200] T. Abidin, Q. Zhang, K.L. Wang, D.J. Liaw, Recent advances in electrochromic polymers, Polymer (Guildf). 55 (2014) 5293–5304. doi:10.1016/j.polymer.2014.08.046.

[201] H. Wang, M. Barrett, B. Duane, J. Gu, F. Zenhausern, Materials and processing of polymer-based electrochromic devices, Mater. Sci. Eng. B Solid-State Mater. Adv. Technol. 228 (2018) 167–174. doi:10.1016/j.mseb.2017.11.016.

[202] L. Zhang, G. Xia, X. Li, G. Xu, B. Wang, D. Li, A. Gavrilyuk, J. Zhao, Y. Li, Fabrication of the infrared variable emissivity electrochromic film based on polyaniline conducting polymer, Synth. Met. 248 (2019) 88–93. doi:10.1016/j.synthmet.2019.01.007.

[203] B. Lakard, G. Herlem, S. Lakard, R. Guyetant, B. Fahys, Potentiometric pH sensors based on electrodeposited polymers, Polymer (Guildf). 46 (2005) 12233–12239. doi:10.1016/j.polymer.2005.10.095.

[204] J. Migdilski, T. Blaz, A. Lewenstam, Conducting polymer-based ion-selective electrodes, 322 (1996) 141–149.

[205] W. Prissanaroon-Ouajai, P.J. Pigram, R. Jones, A. Sirivat, A sensitive and highly stable polypyrrole-based pH sensor with hydroquinone monosulfonate and oxalate co-doping, Sensors Actuators, B Chem. 138 (2009) 504–511. doi:10.1016/j.snb.2009.01.037.

[206] G. Inzelt, Conducting Polymers: A New Era in Electrochemistry, 2nd ed., Springer, 2011.

[207] J.M. Ribo, C. Acero, M.C. Anglada, A. Dicko, On the Structure and Transport Properties of Polypyrroles, Bull. Soc. Cat. Cien. 13 (1992). https://publicacions.iec.cat/repository/pdf/00000122/00000079.pdf.

[208] D.A. Kaplin, S. Qutubuddin, Electrochemically synthesized polypyrrole films: effects of polymerization potencial and electrolyte type, Polymer (Guildf). 36 (1995) 1275–1286.

[209] M. Li, H. Zhu, X. Mao, W. Xiao, D. Wang, Electropolymerization of polypyrrole at the three-phase interline: Influence of polymerization conditions, Electrochim. Acta. 92 (2013) 108–116. doi:10.1016/j.electacta.2013.01.016.

[210] A. Kaynak, L. Rintoul, G.A. George, Change of mechanical and electrical properties of polypyrrole films with dopant concentration and oxidative aging, Mater. Res. Bull. 35 (2000) 813–824. doi:10.1016/S0025-5408(00)00280-4.

[211] T. Patois, B. Lakard, S. Monney, X. Roizard, P. Fievet, Characterization of the surface properties of polypyrrole films: Influence of electrodeposition parameters, Synth. Met. 161 (2011) 2498–2505. doi:10.1016/j.synthmet.2011.10.003.

[212] E. Kupila, J. Kankare, Influence of electrode pretreatment, counter anions and additives on the electropolymerization of pyrrole in aqueous solutions, Synth. Met. 74 (1995) 241–249.

[213] T. Silk, Q. Hong, J. Tamm, R.G. Compton, AFM studies of polypyrrole film surface morphology II. Roughness characterization by the fractal dimension analysis, Synth. Met. 93 (1998) 65–71. doi:10.1016/S0379-6779(98)80132-X.

[214] T. Silk, Q. Hong, J. Tamm, R.G. Compton, AFM studies of polypyrrole film surface morphology I. The influence of film thickness and dopant nature, Synth. Met. 93 (1998) 59–64. doi:10.1016/S0379-6779(98)80131-8.

[215] J.B. Schlenoff, Evolution of Physical and Electrochemical Properties of Polypyrrole during Extended Oxidation, J. Electrochem. Soc. 139 (1992) 2397–2401. doi:10.1149/1.2221238.

[216] S. Gentil, E. Crespo, I. Rojo, A. Friang, C. Vinas, F. Teixidor, B. Gruner, D. Gabel, Polypyrrole materials doped with weakly coordinating anions: Influence of substituents and the fate of the doping anion during the overoxidation process, Polymer (Guildf). 46 (2005) 12218–12225. doi:10.1016/j.polymer.2005.10.092.

[217] Y. Li, R. Qian, Electrochemical overoxidation of conducting polypyrrole nitrate film in aqueous solutions, Electrochim. Acta. 45 (2000) 1727–1731. doi:10.1016/S0013-4686(99)00392-8.

[218] C. Debiemme-Chouvy, T.T.M. Tran, An insight into the overoxidation of polypyrrole materials, Electrochem. Commun. 10 (2008) 947–950. doi:10.1016/j.elecom.2008.04.024.

[219] T.W. Lewis, G.G. Wallace, C.Y. Kim, D.Y. Kim, Studies of the overoxidation of polypyrrole, Synth. Met. 84 (1997) 403–404. doi:10.1016/S0379-6779(97)80803-X.

[220] X. Li, I. Zhitomirsky, Capacitive behaviour of polypyrrole films prepared on stainless steel substrates by electropolymerization, Mater. Lett. 76 (2012) 15–17. doi:10.1016/j.matlet.2012.02.058.

[221] D.K. Ariyanayagamkumarappa, I. Zhitomirsky, Electropolymerization of polypyrrole films on stainless steel substrates for electrodes of electrochemical supercapacitors, Synth. Met. 162 (2012) 868–872. doi:10.1016/j.synthmet.2012.03.020.

[222] A.J. Bard, L.R. Faulkner, Electrochemical Methods: Fundamentals and Applications, John Wiley & Sons, Inc, 2001.

[223] Y. Wang, J.G. Limon-Petersen, R.G. Compton, Measurement of the diffusion coefficients of [Ru(NH3)6]3+ and [Ru(NH3)6]2+ in aqueous solution using microelectrode double potential step chronoamperometry, J. Electroanal. Chem. 652 (2011) 13–17. doi:10.1016/j.jelechem.2010.12.011.

[224] F.M. de Oliveira, L.M. Da Silva, W.T.P. dos Santos, Double-pulse chronoamperometry using

short times for the kinetic study of simple quasi-reversible electrochemical reactions at low overpotentials, J. Electroanal. Chem. 848 (2019) 113291. doi:10.1016/j.jelechem.2019.113291.

[225] Á. Molina, R.G. Compton, C. Serna, F. Martínez-ortiz, E. Laborda, Theory for double potential step chronoamperometry for any potential values at spherical electrodes Simultaneous determination of the diffusion coefficients of the electroactive species, Electrochim. Acta. 54 (2009) 2320–2328. doi:10.1016/j.electacta.2008.10.053.

[226] Y. Yang, Y. Li, M. Pritzker, Control of Cu2O Film Morphology Using Potentiostatic Pulsed Electrodeposition, Electrochim. Acta. 213 (2016) 225–235. doi:10.1016/j.electacta.2016.07.116.

[227] M.S. Chandrasekar, M. Pushpavanam, Pulse and pulse reverse plating-Conceptual, advantages and applications, Electrochim. Acta. 53 (2008) 3313–3322. doi:10.1016/j.electacta.2007.11.054.

[228] N.R. Chowdhury, R. Kumar, R. Kant, Theory for the chronopotentiometry on rough and finite fractal electrode: Generalized Sand equation, J. Electroanal. Chem. 802 (2017) 64–77. doi:10.1016/j.jelechem.2017.08.039.

[229] M. Cremer, Über die Ursache der elektromotorischen Eigenschaften der Gewebe, zugleich ein Beitrag zur Lehre von polyphasischen Elektrolytke, Z. Biol. 47 (1906) 562–569.

[230] A.J. Bard, M. V. Mirkin, Scanning Electrochemical Microscopy, CRC Press, 2012.

[231] R.P. Buck, E. Lindner, Recomendations for nomenclature of ion-selective electrodes (IUPAC recommendations 1994), Pure Appl. Chem. 66 (1994) 2527–2536. doi:10.1351/pac199466122527.

[232] A.K. Covington, Ion-Selective Electrode Methodology. Volume I, 1979.

[233] Y. Umezawa, K. Umezawa, H. Sato, Selectivity Coefficients for Ion-Selective Electrodes - Recommended Methods for Reporting Ka,b Values, Pure Appl. Chern. 67 (1995) 507–518.

[234] M.E. Orazem, B. Tribollet, Electrochemical Impedance Spectroscopy, Wiley-VCH, 2008.

[235] M.F. Montemor, A.M.P. Simões, M.M. Salta, Effect of fly ash on concrete reinforcement corrosion studied by EIS, Cem. Concr. Compos. 22 (2000) 175–185. doi:10.1016/S0958-9465(00)00003-2.

[236] S. Rengaraju, L. Neelakantan, R.G. Pillai, Investigation on the polarization resistance of steel embedded in highly resistive cementitious systems – An attempt and challenges, Electrochim. Acta. 308 (2019) 131–141. doi:10.1016/j.electacta.2019.03.200.

[237] C.Q. Ye, R.G. Hu, S.G. Dong, X.J. Zhang, R.Q. Hou, R.G. Du, C.J. Lin, J.S. Pan, EIS analysis on chloride-induced corrosion behavior of reinforcement steel in simulated carbonated concrete pore solutions, J. Electroanal. Chem. 688 (2013) 275–281. doi:10.1016/j.jelechem.2012.09.012.

[238] X. Hu, C. Shi, X. Liu, J. Zhang, G. de Schutter, A review on microstructural characterization of cement-based materials by AC impedance spectroscopy, Cem. Concr. Compos. 100 (2019) 1–14. doi:10.1016/j.cemconcomp.2019.03.018.

[239] S. Wang, J. Zhang, O. Gharbi, V. Vivier, M. Gao, M.E. Orazem, Electrochemical impedance spectroscopy, Nat. Rev. 1 (2021) 1–21. doi:10.5189/revpolarography.65.87.

[240] D. V. Ribeiro, J.C.C. Abrantes, Application of electrochemical impedance spectroscopy (EIS) to monitor the corrosion of reinforced concrete: A new approach, Constr. Build. Mater. 111 (2016) 98–104. doi:10.1016/j.conbuildmat.2016.02.047.

[241] H.G. Tompkins, A User ' s Guide to Ellipsometry, Academic Press, Inc, 1993.

[242] H.G. Tompkins, Handbook of Ellipsometry, 2005. doi:10.1007/3-540-27488-X.

[243] R. Greef, Ellipsometry in electrochemistry: a spectrum of applications, Thin Solid Films. 233 (1993) 32–39. doi:10.1016/0040-6090(93)90056-U.

[244] J.L. Ord, Z.Q. Huang, An Optical Study of the Deposition, Discharge, and Recharge of Manganese Dioxide Films, J. Electrochem. Soc. 132 (1985) 1183–1186.

[245] J.P. Correia, L.M. Abrantes, In situ ellipsometric studies on the electrochemically induced structural modifications during poly(3-methylthiophene) formation, Synth. Met. 156 (2006) 287–292. doi:10.1016/j.synthmet.2005.12.013.

[246] L.M. Abrantes, J.P. Correia, A.I. Melato, An ellipsometric study of poly(3,4-ethylenedioxythiophene) electrosynthesis - From the initial stages to thick layers formation, J. Electroanal. Chem. 646 (2010) 75–84. doi:10.1016/j.jelechem.2010.02.025.

[247] H.N. Dinh, J. Ding, S.J. Xia, V.I. Birss, Multi-technique study of the anodic degradation of polyaniline films, J. Electroanal. Chem. 459 (1998) 45–56. doi:10.1016/S0022-0728(98)00286-1.

[248] O. Yavuz, L.E.A. Berlouis, M.L. Hitchman, A.S. Sarac, Optical, thermal and electrochemical properties of co-electropolymerized films of acrylamide and carbazole, Synth. Met. 110 (2000) 165–174. doi:10.1016/S0379-6779(99)00296-9.

[249] A. Ul-Hamid, A Beginners' Guide to Scanning Electron Microscopy, 2018. doi:10.1007/978-3-319-98482-7.

[250] B.J. Inkson, Scanning Electron Microscopy (SEM) and Transmission Electron Microscopy (TEM) for Materials Characterization, Elsevier Ltd, 2016. doi:10.1016/B978-0-08-100040-3.00002-X.

[251] A.M. Paredes, Microscopy: Scanning Electron Microscopy, Second Edi, Elsevier, 2014. doi:10.1016/B978-0-12-384730-0.00215-9.

[252] E. Zolotoyabko, Basic concepts of X-ray diffraction, Wiley-VCH, 2014.

[253] J.L. Rosa, A. Robin, M.B. Silva, C.A. Baldan, M.P. Peres, Electrodeposition of copper on titanium wires: Taguchi experimental design approach, J. Mater. Process. Technol. 209 (2009) 1181–1188.

[254] S.M. Pourmortazavi, M. Rahimi-Nasrabadi, Y. Fazli, M. Mohammad-Zadeh, Taguchi method assisted optimization of electrochemical synthesis and structural characterization of copper tungstate nanoparticles, Int. J. Refract. Met. Hard Mater. 51 (2015) 29–34. doi:10.1016/j.ijrmhm.2015.02.013.

[255] B. J.O, A. Reddy, Modern Electrochemistry v.2A Fundamentals of Electrodics, 2nd ed., Kluwer Academic Publishers, 2002.

[256] J.W. Dini, Electrodeposition: The Materials Science of Coatings and Substrates, Noyes Publications, 1993.

[257] M. Eyraud, Z. Hanane, J. Crousier, Galvanostatic study of the electrocrystallization of binary nickel-base alloys. I: Zn-Ni alloy on glassy carbon, Surf. Coatings Technol. 67 (1994) 35–42. doi:10.1016/S0257-8972(05)80024-6.

[258] M. Hernández Ubeda, H. Herrera, H.T. Mishima, B.A. De López Mishima, H.M. Villullas, M. López Teijelo, The electrochemical response of manganese hydroxide-oxide films in slightly alkaline solutions. II. Voltammetric and ellipsometric studies, Electrochim. Acta. 44 (1998) 513–519. doi:10.1016/S0013-4686(98)00068-1.

[259] R. Kötz, C. Barbero, O. Haas, Probe beam deflection investigation of the charge storage reaction in anodic iridium and tungsten oxide films, J. Electroanal. Chem. 296 (1990) 37–49.

doi:10.1016/0022-0728(90)87231-8.

[260] P.G. Pickup, V.I. Birss, The kinetics of charging and discharging of iridium oxide films in aqueous and non-aqueous media, J. Electroanal. Chem. 240 (1988) 185–199. doi:10.1016/0022-0728(88)80322-X.

[261] L.D. Burke, D.P. Whelan, A voltammetric investigation of the charge storage reactions of hydrous iridium oxide layers, J. Electroanal. Chem. 162 (1984) 121–141.

[262] R.H.G. Mingels, S. Kalsi, Y. Cheong, H. Morgan, Iridium and Ruthenium oxide miniature pH sensors: Long-term performance, Sensors Actuators, B Chem. 297 (2019) 126779. doi:10.1016/j.snb.2019.126779.

[263] L.E. Owe, M. Tsypkin, K.S. Wallwork, R.G. Haverkamp, S. Sunde, Iridium-ruthenium single phase mixed oxides for oxygen evolution: Composition dependence of electrocatalytic activity, Electrochim. Acta. 70 (2012) 158–164. doi:10.1016/j.electacta.2012.03.041.

[264] C.C. Hu, Y.H. Huang, Effects of preparation variables on the deposition rate and physicochemical properties of hydrous ruthenium oxide for electrochemical capacitors, Electrochim. Acta. 46 (2001) 3431–3444. doi:10.1016/S0013-4686(01)00543-6.

[265] G. Gunawardena, G. Hills, I. Montenegro, Electrochemical nucleation. Part IV. Electrodeposition of copper onto vitreous carbon, J. Electroanal. Chem. 184 (1985) 357–369. doi:10.1016/0368-1874(85)85539-8.

[266] J. Park, M. Kim, S. Kim, Surface renewable nano-iridium oxide polymeric composite pH electrodes, Sensors Actuators, B Chem. 204 (2014) 197–202. doi:10.1016/j.snb.2014.07.104.

[267] L. Sziráki, L. Bóbics, Impedance study of electrochromism in anodic Ir oxide films, Electrochim. Acta. 47 (2002) 2189–2197. doi:10.1016/S0013-4686(02)00055-5.

[268] J.D.E. McIntyre, Oxidation State Changes and Structure of Electrochromic Iridium Oxide Films, J. Electrochem. Soc. 127 (1980) 1264–1268. doi:10.1149/1.2129868.

[269] C. Kollia, Z. Loizos, N. Spyrellis, Influence of pulse reversed current technique on the crystalline orientation and surface morphology of nickel electrodeposits, Surf. Coatings Technol. 45 (1991) 155–160. doi:10.1016/0257-8972(91)90218-L.

[270] A.M. Alfantazi, G. Brehaut, U. Erb, The effects of substrate material on the micro structure of pulse-plated Zn-Ni alloys, Surf. Coatings Technol. 89 (1997) 239–244. doi:10.1016/S0257-8972(96)02894-0.

[271] P.G. Pickup, V.I. Birss, Chemical analysis of the ionic content of hydrous iridium oxide films, J. Electroanal. Chem. 240 (1988) 171–183. doi:10.1016/0022-0728(88)80321-8.

[272] T.M. Christensen, J.M. Blakely, Ellipsometric investigation of Be(0001) oxidation, J. Vac. Sci. Technol. A Vacuum, Surfaces, Film. 3 (1985) 1607–1612. doi:10.1116/1.573144.

[273] J.O.M. Bockris, M.A. Genshaw, V. Brusic, H. Wroblowa, The mechanism of the passivation of iron in neutral solutions: An ellipsometric and coulometric investigation, Electrochim. Acta. 16 (1971) 1859–1894. doi:10.1016/0013-4686(71)85144-7.

[274] H. Oranowska, Z. Szklarska-Smialowska, An electrochemical and ellipsometric investigation of surface films grown on iron in saturated calcium hydroxide solutions with or without chloride ions, Corros. Sci. 21 (1981) 735–747. doi:10.1016/0010-938X(81)90085-8.

[275] C. Gomes, Z. Mir, R. Sampaio, A. Bastos, J. Tedim, F. Maia, C. Rocha, M. Ferreira, Use of ZnAl-Layered double Hydroxide (LDH) to extend the service life of reinforced concrete, Materials (Basel). 13 (2020) 1–19. doi:10.3390/MA13071769.